

# **Experimental Investigation of Bassoon Acoustics**

Experimentelle Untersuchung der Akustik des Fagotts

Von der Fakultät Maschinenwesen  
der Technischen Universität Dresden  
zur Erlangung des akademischen Grades  
Doktoringenieur (Dr.-Ing)  
angenommene

**Dissertation**

von

**Dipl.-Ing. Timo Grothe**

geboren am  
7. August 1978 in Boppard

Tag der Einreichung: 25. November 2013

Tag der Verteidigung: 3. Juni 2014

1. Gutachter:

Prof. (em.) Dr.-Ing. Roger Grundmann

2. Gutachter:

Prof. Dr. Ir. Avraham Hirschberg

3. Gutachter:

Dr. Ir. Cornelis J. Nederveen



# Abstract

The bassoon is a conical woodwind instrument blown with a double-reed mouthpiece. The sound is generated by the periodic oscillation of the mouthpiece which excites the air column. The fundamental frequency of this oscillation is determined to a large extent by the resonances of the air column. These can be varied by opening or closing tone-holes. For any given tone hole setting a fine-tuning in pitch is necessary during playing. Musicians adjust the slit opening of the double-reed by pressing their lips against the opposing reed blades. These so-called embouchure corrections are required to tune the pitch, loudness and sound color of single notes. They may be tedious, especially if successive notes require inverse corrections. However, such corrections are essential: Due to the very high frequency sensitivity of the human ear playing in tune is the paramount requirement when playing music. This implies, that embouchure actions provide an important insight into a subjective quality assessment of reed wind instruments from the viewpoint of the musician: An instrument requiring only small corrections will be comfortable to play.

Theoretical investigations of the whole system of resonator, reed, and musician by use of a physical model nowadays still seem insufficient with respect to the required precision [129]. Therefore the path of well-described artificial mouth measurements has been chosen here. For the separate treatment of the resonator and the double-reed, existing classical models have been used. Modifications to these models are suggested and verified experimentally. The influence of the musician is incorporated by the lip force-dependent initial reed slit height. For this investigation a measurement setup has been built that allows precise adjustment of lip force during playing. With measurements of the artificial mouth parameters blowing pressure, mouthpiece pressure, volume-flow rate and axial lip position on reed, the experiment is fully described for a given resonator setting represented by an input impedance curve. By use of the suggested empirical model the adjustment parameters can be turned into model parameters. A large data set from blowing experiments covering the full tonal and dynamical range on five modern German bassoons of different make is given and interpreted.

The experimental data presented with this work can be a basis for extending the knowledge and understanding of the interaction of instrument, mouthpiece and player. On the one hand, they provide an objective insight into tuning aspects of the studied bassoons. On the other hand the experiments define working points of the coupled system by means of quasi-static model parameters. These may be useful to validate dynamical physical models in further studies.

The experimental data provide an important prerequisite for scientific proposals of optimizations of the bassoon and other reed wind instruments. It can further serve as a fundament for the interdisciplinary communication between musicians, musical instrument makers and scientists [174].



# Contents

<b>Abstract</b>	<b>iii</b>
<b>1 Introduction</b>	<b>1</b>
1.1 Motivation . . . . .	1
1.2 Scientific Approaches to Woodwind Musical Instruments . . . . .	3
1.3 Organization of the Thesis . . . . .	6
<b>2 Acoustical Properties of the Bassoon Air Column</b>	<b>7</b>
2.1 Wave propagation in tubes . . . . .	7
2.1.1 Theory . . . . .	7
2.1.2 Transmission Line Modeling . . . . .	8
2.1.3 Implementation . . . . .	18
2.1.4 Remarks on Modeling Wall Losses in a Conical Waveguide . . . . .	19
2.2 Input Impedance Measurement . . . . .	23
2.2.1 Principle . . . . .	23
2.2.2 Device . . . . .	23
2.2.3 Calibration and Correction . . . . .	24
2.3 Comparison of Theory and Experiment . . . . .	27
2.3.1 Repeatability and Measurement Uncertainty . . . . .	27
2.3.2 Comparison of numerical and experimental Impedance Curves . . . . .	32
2.4 Harmonicity Analysis of the Resonator . . . . .	35
2.4.1 The Role of the Resonator . . . . .	35
2.4.2 The reed equivalent Volume . . . . .	35
2.4.3 Harmonicity Map . . . . .	36
2.5 Summary . . . . .	38
<b>3 Characterization of the Double Reed Mouthpiece</b>	<b>41</b>
3.1 Physical Model of the Double-Reed . . . . .	41
3.1.1 Working Principle . . . . .	41
3.1.2 Structural Mechanical Characteristics . . . . .	42
3.1.3 Fluid Mechanical Characteristics . . . . .	44
3.2 Measurement of Reed Parameters . . . . .	49
3.2.1 Quasi-stationary Measurement . . . . .	49
3.2.2 Dynamic Measurement . . . . .	50
3.3 Construction of an Artificial Mouth . . . . .	52
3.3.1 Requirements Profile . . . . .	52
3.3.2 Generic Design . . . . .	53
3.3.3 The artificial Lip . . . . .	54
3.3.4 Air Supply . . . . .	55
3.3.5 Sensors and Data Acquisition . . . . .	57
3.3.6 Experimental setup . . . . .	59
3.4 Summary . . . . .	59

<b>4</b>	<b>Modeling Realistic Embouchures with Reed Parameters</b>	<b>61</b>
4.1	Reed Channel Geometry and Flow Characteristics . . . . .	61
4.1.1	The Double-Reed as a Flow Duct . . . . .	61
4.1.2	Bernoulli Flow-Model with Pressure Losses . . . . .	65
4.1.3	Discussion of the Model . . . . .	68
4.2	Quasi-static Interaction of Flow and Reed-Channel . . . . .	72
4.2.1	Pressure-driven Deformation of the Duct Intake . . . . .	72
4.2.2	Reed-Flow Model including Channel Deformation . . . . .	75
4.2.3	Influence of Model Parameters . . . . .	76
4.2.4	Experimental Verification . . . . .	78
4.3	Effect of the Embouchure on the Reed-Flow . . . . .	81
4.3.1	Adjustment of the Initial Slit Height . . . . .	81
4.3.2	Quasi-static Flow in the Deformed Reed-Channel . . . . .	83
4.3.3	Simplified empirical Model including a Lip Force . . . . .	85
4.4	Summary . . . . .	93
<b>5</b>	<b>Survey of Performance Characteristics of the Modern German Bassoon</b>	<b>95</b>
5.1	Experimental Procedure and Data Analysis . . . . .	95
5.1.1	Description of the Experiment . . . . .	95
5.1.2	Time Domain Analysis . . . . .	97
5.1.3	Spectral Analysis – Period Synchronized Sampling . . . . .	98
5.1.4	Spectral Centroid and Formants . . . . .	99
5.1.5	Embouchure parameters . . . . .	100
5.2	Observations on the Bassoon under Operating Conditions . . . . .	105
5.2.1	Excitation Parameter Ranges . . . . .	106
5.2.2	Characteristics of the radiated Sound . . . . .	110
5.2.3	Reed Pressure Waveform Analysis . . . . .	115
5.2.4	Summarizing Overview . . . . .	118
5.3	Performance Control with the Embouchure . . . . .	120
5.3.1	Register-dependent Embouchure Characteristics . . . . .	120
5.3.2	Intonation Corrections . . . . .	123
5.3.3	Sound Color Adjustments . . . . .	127
5.3.4	Relation to the acoustical Properties of the Resonator . . . . .	129
5.4	Summary . . . . .	137
<b>6</b>	<b>Conclusion</b>	<b>139</b>
6.1	Summary . . . . .	139
6.2	Outlook . . . . .	141
	<b>Acknowledgements</b>	<b>143</b>
	<b>Bibliography</b>	<b>155</b>
	<b>List of Figures</b>	<b>163</b>
	<b>List of Tables</b>	<b>165</b>
	<b>Appendix</b>	<b>167</b>
	A1: Remarks on Modeling Wall Losses in a Conical Waveguide . . . . .	167
	A2: Influence of Model Parameters . . . . .	171

## Roman Symbols

Symbol	Units	Description
A,B	[Pa]	Pressure amplitude
a	[-]	Dimensionless number defined in section 2.1.4
A, B, C, D	[-]	Transfer matrix elements
$a_0, a_1, a_2, a_3, a_4$		Regression model coefficients
b	[m]	Tone hole radius
B1, B2, B3, B4	[Hz]	Formant bandwidth (first, second, third, fourth)
c	[m/s]	Speed of Sound
C	[(mm/kPa) <sup>2</sup> ]	Empirical constant in section 2.2.1
$C_c$	[-]	Jet contraction coefficient
$C_p$	[J/(kg K)]	Heat capacity under isobaric conditions
$C_v$	[J/(kg K)]	Heat capacity under isochoric conditions
d	[m]	diameter
d	[kg/s]	Damping coefficient
E, F, G, H	[-]	Stiffness matrix elements
f	[Hz]	Frequency
<b>f, g</b>	[-]	Numbers defined in [125]
$f_0$	[Hz]	Fundamental frequency
$\tilde{f}$	[-]	Dimensionless frequency
$f_{ref}$	[Hz]	Frequency reference
$f_s$	[Hz]	Sampling frequency
$F_l$	[N]	Lip force
$F_i$	[N]	Inertial force
$F_d$	[N]	Damping force
$F_s$	[N]	Restoring force
$\mathcal{F}1, \mathcal{F}2, \mathcal{F}3, \mathcal{F}4$	[Hz]	Formant center frequency (first, second, third, fourth)
g <sub>r</sub>	[1/s]	Damping factor
h	[m]	Reed slit height
h <sub>sc</sub>	[Hz]	Harmonic spectral centroid
h <sub>sd</sub>	[-]	Harmonic spectral deviation
h <sub>ss</sub>	[-]	Harmonic spectral spread
I	[Cent]	Interval in Cent (logarithmic frequency ratio)
j	-	Imaginary unit
k	[1/m]	Wave number
$k_c$	[1/m]	Complex wavenumber
$\bar{k}_c$	[1/m]	Effective complex wavenumber
k	[kg/s <sup>2</sup> ]	Stiffness
K	[Pa/m]	Equivalent stiffness per unit area
$K_s$	[Pa/m <sup>2</sup> ]	Equivalent stiffness per unit volume
L	[m]	Length
m	[-]	Cross section ratio
m	[kg]	Mass
n		Count
N	[Sone]	Loudness
p	[Pa]	Pressure
$p_M$	[Pa]	Pressure needed to close the reed
P	[Pa]	Spectral pressure magnitude
Pr	[-]	Prandtl number
q	[m <sup>3</sup> /s]	Volume flow-rate, acoustic volume velocity
q <sub>A</sub>	[m <sup>3</sup> /s]	Flow parameter defined in section 3.1.3

$Q_r$	[-]	Reed quality factor
$r$	[m]	Inner radius
$R$	[m]	Outer radius
$R^2$	[-]	Coefficient of determination
$Re$	[-]	Reynolds number
$S$	[m <sup>2</sup> ]	Area
$S_{12}$		Stiffness matrix of a two-port with ends $(\cdot)_1$ and $(\cdot)_2$ .
$s$	[m]	Displacement of the reed's neutral axis
$sf$	[-]	Shape factor
$S_r$	[m <sup>2</sup> ]	Equivalent reed surface area
$S_{in}$	[m <sup>2</sup> ]	Reed intake cross section
$S_{\infty}$	[m <sup>2</sup> ]	Reed initial intake cross section
$SPL$	[dB SPL]	Sound pressure level
$St$	[-]	Strouhal number
$SS_{resid}$		Residual sum of squares
$t$	[s]	Time
$T_{12}$		Transfer matrix of a two-port with ends $(\cdot)_1$ and $(\cdot)_2$ .
$T_{1n}$		Transfer matrix of a two-port with ends $(\cdot)_1$ and $(\cdot)_n$ .
$t$	[m]	Tone hole chimney height
$T$	[K]	Temperature
$t_a$	[m]	Intersection length correction
$t_i$	[m]	Inertial length correction
$t_m$	[m]	Volumetric length correction
$t_r$	[m]	Radiation length correction
$u$	[m/s]	Particle velocity
$U$	[m <sup>3</sup> /s]	Acoustical volume flow
$V$	[m <sup>3</sup> ]	Volume
$v$	[-]	Dimensionless number defined in section 2.1.2
$V_{eq}$	[m <sup>3</sup> ]	Equivalent volume
$w$	[m]	Reed width at the tip
$x$	[m]	Cartesian Coordinate
$x_l, x_{cl}$	[m]	Distance from reed tip
$y$	[m]	Cartesian Coordinate
$Y$	[m <sup>3</sup> /(Pa s)]	Acoustic admittance
$Y_{cav}$	[m <sup>3</sup> /(Pa s)]	Acoustic admittance of a cavity
$z$	[-]	Taper
$Z$	[(Pa s)/m <sup>3</sup> ]	Acoustic Impedance
$Z_a$	[-]	Tone hole series impedance
$Z_c$	[(Pa s)/m <sup>3</sup> ]	Characteristical Impedance (with regard to a cross sectional area)
$Z_h$	[-]	Tone hole shunt impedance



## Greek Symbols

Symbol	Units	Description
$\alpha$	[-]	Acoustic boundary layer loss coefficient
$\bar{\alpha}$	[-]	Effective acoustic boundary layer loss coefficient
$\tilde{\alpha}, \tilde{\alpha}_f, \tilde{\alpha}_g$	[-]	Loss coefficients defined in section 2.1.4
$\alpha'$	[m]	Equivalent acoustic boundary layer thickness
$\alpha$	[-]	Global quasi-static flow parameter defined in section 4.1.2
$\beta$		Loss parameter defined in [125]
$\gamma$	[-]	Ratio of heat capacities under isobaric and isochoric conditions
$\gamma$	[-]	Dimensionless blowing pressure
$\gamma_E$		Euler-Mascheroni-constant
$\delta$	[-]	Radius ratio in section 2.1.2
$\delta t$	[s]	Time Step
$\delta_v$	[m]	Viscous boundary layer thickness
$\delta_t$	[m]	Thermal boundary layer thickness
$\epsilon_v$		Loss parameter defined in [125]
$\varepsilon$	[-]	Squared ratio of cross sections
$\zeta$	[-]	Hydraulic loss coefficient
$\zeta$	[-]	Dimensionless embouchure parameter
$\eta$	[N s/m <sup>2</sup> ]	Dynamic viscosity
$\theta$		Trigonometric term defined in section 2.1.2
$\kappa$	[-]	Reed stiffness exponent
$\kappa$	[J/s /(m K)]	Thermal conductivity
$\lambda$	[m]	Wavelength
$\mu$		Mean value
$\mu_r$	[kg/m <sup>2</sup> ]	Effective mass
$\nu$	[m <sup>2</sup> /s]	kinematic viscosity
$\xi$	[-]	Dimensionless length correction section 2.1.4
$\rho$	[kg/m <sup>3</sup> ]	Density
$\tau$	[s]	Periodic time
$\sigma$	Standard deviation	
$\Phi$	[-]	Rotation angle
$\Psi$	[-]	Dimensionless length correction defined in [128]
$\omega$	[1/s]	Angular frequency
$\omega_r$	[1/s]	Reed angular resonance frequency

## Operators

$\dot{(\cdot)}$	First time derivative
$\ddot{(\cdot)}$	Second time derivative
$\partial(\cdot)$	Partial derivative
$d(\cdot)$	Infinitesimal variation
$\hat{(\cdot)}$	Amplitude value
$\Delta(\cdot)$	Differential value
$\bar{(\cdot)}$	Mean value
$\tilde{(\cdot)}$	Non-dimensional value
$ \cdot $	Modulus

## Subscripts

$(\cdot)_0$	Offset value at zero frequency
$(\cdot)_\infty$	Initial, time independent value
$(\cdot)_1$	Input end
$(\cdot)_2$	Output end
$(\cdot)_A$	Depending on the axial position
$(\cdot)_a$	Re-attachment point
$(\cdot)_{av}$	Average
$(\cdot)_{adp}$	Adapater
$(\cdot)_{cyl}$	Cylindrical
$(\cdot)_{con}$	Conical
$(\cdot)_{circ}$	Circular
$(\cdot)_c$	Closed
$(\cdot)_o$	Open
$(\cdot)_d$	Dynamic
$(\cdot)_{decr.}$	Decreasing
$(\cdot)_{incr.}$	Increasing
$(\cdot)_e$	Elliptic
$(\cdot)_p$	Parabolic
$(\cdot)_F, (\cdot)_B$	given by Fletcher, Benade, respectively
$(\cdot)_h$	Associated with the reed slit height $h$
$(\cdot)_{hole}$	Tone hole
$(\cdot)_{in}$	Intake
$(\cdot)_j$	Jet
$(\cdot)_m$	Mouth
$(\cdot)_r$	Reed
$(\cdot)_{max}$	Maximum value
$(\cdot)_{min}$	Minimum value
$(\cdot)_{meas}$	Measurement value
$(\cdot)_{model}$	Model estimate
$(\cdot)_{nom}$	Nominal
$(\cdot)_{p_M}$	associated with the pressure parameter $p_M$
$(\cdot)_{q_A}$	associated with the flow parameter $q_A$
$(\cdot)_{res}$	Residual
$(\cdot)_{read}$	Reading
$(\cdot)_{RMS}$	Root-Mean-Square
$(\cdot)_s$	Sound
$(\cdot)_{sat}$	Saturation

## Other symbols

$\mathfrak{F}$	Periodic function
$\Re$	Real part
$\mathcal{N}$	Numerator
$\mathcal{D}$	Denominator

# 1 Introduction

## 1.1 Motivation

The bassoon is a woodwind instrument blown with a double-reed mouthpiece. The conical air column is sharply bent inside the instrument, at the bottom of the wooden corpus. At its small end a thin curved metal tube, the so-called bocal (or crook), connects the corpus and the mouthpiece.



**Figure 1.1** Corpus and bocal of a modern German bassoon. Picture taken from [171]

The stimulus for this thesis was the question of how the bocal of a bassoon affects its sound. Many bassoonists report a life-time spent searching for the optimal bocal, yet their requirements are simple: It should just complement their instrument. That means that the bocal should be suited to their playing and reed-making habits and provide perfect intonation together with an even, pleasant tone colour throughout the playing range. It should not itself have any bad notes, and it should compensate for any bad notes in the body of the bassoon. Musical instrument makers, who are able to manufacture nominally identical bocals within very small geometrical tolerances, find it hard to understand the large variation in bocal quality that musicians apparently are able to detect.

Against this complex background, the work of Grundmann *et al.* generated much interest. By carrying out purely numerical studies based on fluid dynamics, they proposed a new design for the bassoon bocal [82, 83, 81]. This development, once put into practice by an associated woodwind instrument maker, raised many questions regarding the correlation between the design of a wind instrument and its acoustical performance, and on the consequences and relevance of subtle geometric changes for its playability. The quest for answers or partial explanations to these kinds of questions is one of the major fascinations in the research discipline of musical acoustics, and it has been an inspiration to highly gifted scientists for many decades.

It seems paradoxical, however, that the greatest achievements have undoubtedly been made by craftsmen. The tremendous degree of maturity in today's orchestral musical instruments has been reached predominantly without scientific assistance, and rather through experience and intuition.

The present author is strongly aware of this fact and it is far beyond the scope of this thesis to try to develop a new theory or a new musical instrument design. The general objective is to provide an inventory of performance characteristics as observed on bassoons of given design under controlled and realistic conditions, using state-of-the-art measuring equipment. This inventory, together with a suited experimental apparatus and the measurement strategies may be used as tools for the suggestion and validation of modifications on the reed wind instruments.

As an introduction to the complexity of this task, a brief overview of the construction of the bassoon and its playing technique will be given here<sup>1</sup> to point to the acoustical peculiarities of this instrument.

Like most musical instruments, the bassoon has undergone a development process over several decades, mainly by trial and error. The design of today's modern German bassoon was developed in the workshop of Wilhelm Heckel in the late 19<sup>th</sup> century and has barely changed since then. The bassoon's body consists of four joints: the *wing joint*; the *butt*; the *bass joint*; and the *bell*. The main bore generally is conical with a gradient in diameter of approximately 1/70. At the foot of the butt joint this bore is turned through 180 degrees by means of a U-bend in order to make an instrument with an acoustic length of more than 2.5 meters easier to handle. The *bocal* is a narrow curved metal tube connecting the body of the instrument with the double-reed mouthpiece held between the lips of the player. Depending on construction, the body of the instrument has about 30 tone holes. The chromatically playable standard tonal range covers the notes between B♭1 ( $f_0 = 58$  Hz) and D5 ( $f_0 = 622$  Hz)<sup>2</sup>; skilled bassoonists can play even higher notes.

It is a historical hangover that the first five tone holes in the wing and butt joints are stopped directly by fingers. Acoustics however demand greater distances between the holes than fingers can stretch. For that reason these holes are bored at an angle to the main bore-axis of the instrument. Their length in turn necessitates greater thickness of the instrument wall, giving rise to the characteristic form of the wing joint and hence to its name. These long, narrow tone holes are an important reason for the bassoon's acoustic unevenness, with far-reaching consequences regarding the location of the remaining tone holes, the way they are operated by means of the keywork, the special fingering system, and lastly also for the player's fingering and breath techniques.

When a current of air is blown through the narrow double-reed channel, the mouthpiece pressure decreases and the two reed-blades deflect until they touch. Inertia in the flow arising from this complete interruption causes a negative pressure pulse to travel down the air column of the instrument. It is reflected back at an opening in the bore and returns to the reed as a positive pressure impulse. The time of flight depends mostly on the position and size of that opening. However, in passing both ways through the irregular bassoon bore with local variations in taper and closed tone holes, the reflected pressure contains information about the complete bore when arriving back at the reed. Taking this into account, it is evident that any of the tone holes to some extent influences every single fingering to some extent, not only those resonator opening(s) which determine the effective acoustic length.

In the light of this complexity, the reform of the acoustical design of the resonator which the bassoonist Carl Almenröder initiated in 1825, and which came to fruition in the late 19<sup>th</sup> century in the workshop of Wilhelm Heckel [85], cannot be valued highly enough. These two master instrument makers developed a system of tone holes which retains the historic construction of the body of the bassoon and, taking account of its ergonomic limitations, makes it possible to play chromatically. Inspired by the discoveries of Gottfried Weber [165, 166], a compromise was worked out which rests extensively on empirical experience and works reasonably well for all notes. This compromise consists of localized adjustments to the taper of the main bore, and of a multiplicity of large and small, long and short, vertical and diagonal tone holes, which are operated through a complex keywork system. Despite some attempts at new and experimental designs, the

<sup>1</sup>Parts of this overview have been published by the author in [74, 76]. The translation into English is courtesy of Michael Johnson.

<sup>2</sup>In this thesis, the note scale is referenced to A4 = 443 Hz, adopting the convention that is, to the knowledge of the author, currently agreed along German bassoonists.

acoustic concept of the modern German bassoon has barely changed since then [170, 105]. Its fingering system mirrors the complicated and acoustically irregular construction. To play some notes, in particular in the upper, but also in the lower register, additional holes downstream the “active” open tone hole must be opened or closed, to correct the tone for tuning, stability or sound color. Some of those additional holes are included in what is called a standard fingering pattern [53], others are fingered involuntarily, because they are operated automatically by clutches in the keywork. Many players even use individual “helper holes”, required according to their skills and habits, in special dynamic regimes or to correct the tuning of individual notes on an individual instrument. These peculiarities obscure the underlying logic [104] in the bassoon fingering system, which requires intensive practice and a high degree of finger dexterity.

So far, the reed has not been considered. From the point of view of the musician, it is the most important part of the story. The fingering sets up a blend of air column modes which favors an oscillation in a certain frequency range that is small with respect to the tonal range of the instrument. In the light of the extreme sensitivity of the human ears in frequency detection, however, a deviation of 0.5 % may be unacceptably large in a musical context. As a consequence, intonation has to be corrected during performance. The player must use his embouchure and fine-tune the slit height of the vibrating reed with his lips to adjust the pitch of each note individually. The required tightness of embouchure is far from being static like the fingering pattern. It largely depends on the desired dynamic level and further on the properties of the reed, such as the shape, the material properties, the age and so on.

In the light of the engineering scope of this thesis, the main objectives are the following:

- Create experimental environments featuring repeatability and precision in proper degrees.
- Identify parameters describing realistic experimental situations in the context of basic existing models.
- Characterize the system by the totality of musically relevant regimes, i.e. covering the tonal and dynamic range.
- Reveal underlying systematics where possible.
- Find indications for the relevance of the results with regard to experiences reported by practitioners.

Model parameters derived from such experiments might be a valuable contribution to further investigations into the physical modeling of self-sustained oscillations in reed wind instruments. A long-term goal could then be to develop suggestions for targeted modifications of the instrument. Following the presented methodology, this goal can be reached subsequent to proving the relevance of laboratory results in the artistic and musical context.

## 1.2 Scientific Approaches to Woodwind Musical Instruments

Early scientific descriptions of musical woodwind instruments date back to 1816, when the musicologist Gottfried Weber published a comprehensive set of four articles entitled “Versuch einer praktischen Akustik der Blasinstrumente” (An Attempt at Functional Wind Instruments Acoustics) [164]. From phenomenological observations, he identified of the fundamental differences in the excitation mechanism of flue, free reed and beating reed organ pipes, and he further describes the basic principles of woodwind tone-hole design. Interestingly, it was his work that inspired the pioneering bassoonist Carl Almenröder who proposed his new, and at that time revolutionary, bassoon design just a few years later [165, 166, 7]. In principle, this is the bassoon design which has subsisted until today.

One may speculate whether Weber's treatise served also as an inspiration to his namesake, the physicist Wilhelm Weber. However, it was the latter who investigated free reed organ pipes and ten years later, in 1829, presented a theory concerning the coupled motion of reed and air-column. This led him to a "pitch compensating" design of a reed for a reed organ pipe whose fundamental frequency does not change with the blowing pressure<sup>3</sup> [168]. In this study Wilhelm Weber is fully aware of the greatly increased complexity of reed wind instrument mouthpieces (namely clarinet, bassoon and oboe), but he attributes this complexity to their geometry, material properties and clamping, rather than to the fundamental difference, that those reeds are usually beating. Weber concludes his treatise with a very remarkable note, which is pragmatic and clear-sighted at the same time:

*"As soon as one fixes the reeds of clarinet, oboe or bassoon in the same manner as a free reed in the lingual organ pipe, the same theory (...) applies and one could fairly hope to solve one of the most complex and useful tasks that one can imagine when applying a theory to experience, namely to build a large number of musical instruments according to well-established theoretical rules, as is possible for optical instruments."*

Another forty years later it was the pioneering acoustician Hermann von Helmholtz who presented a full description of a beating reed coupled to a resonating air column, in an appendix of his classic book "Die Lehre von Tonempfindungen" (On the Sensation of Tone) [163], added to the fourth edition in 1877 [15]. The application of scientific results in instrument making was at that time advanced by Theobald Böhm who invented a new, systematic design for flute, oboe and clarinet<sup>4</sup> [22]

Based on the results of Weber and von Helmholtz, Henri Bouasse presented a set of fundamental studies in his two volume book "Instruments à Vent" (Wind Instruments) [24, 25].

In the middle of the 20<sup>th</sup> century, when bassoon design apparently reached the mature status of what is known today as the modern German bassoon (Heckel-type), wind instrument research started to go increasingly into detail.

A pioneering comprehensive study of woodwind acoustics has been presented by Nederveen [125], who, based on analytical considerations, provided a framework for tone hole calculations taking into account bore perturbation and the flow induced by the reed motion. Considering many practical issues of woodwind instrument design and performance, his study, supported and validated by detailed measurements of woodwind geometries, is still a classic today.

Refinements of theories for calculations on the resonator were proposed out at the same time by Benade, who derived an analytic model of woodwind tone holes [14] and exploited the electro-acoustical analogy to model woodwind air columns as a network of lumped impedances [19].

Simultaneously, the basis for research into the action of the reed, and its interaction with the resonator, was elaborated. Backus presented one of the first detailed experimental studies of the coupled oscillations in a clarinet [8], and refined the theory for small amplitude non-beating regimes. With the incorporation of this in an experimental apparatus [169] by Backus, the measurement of input impedance of musical wind instruments and thus quantitative studies of resonators became possible [9, 30]. These inspired fundamental physical models of the coupled reed-resonator, like those by Wilson and Beavers in the frequency domain [172] and by Schumacher [147] in the time domain.

The research of Benade and his co-workers yielded many important results especially in reed wind instruments [178, 156, 96, 17, 20], most of which are collected in his comprehensive classic textbook "Fundamentals of Musical Acoustics" [16].

A basic non-dimensional model of the reed-resonator interaction, along with a profound theoretical

<sup>3</sup>Wilhelm Weber in the same year published an abridged comprehensive version of his article in Gottfried Weber's musical journal, preceded by a foreword by the latter [167].

<sup>4</sup>A bassoon design of his based on the same acoustic principles, and being more systematic than the classical Almenäder/Heckel layout, was however rejected by practitioners because of its inbeautiful timbre [105].

analysis of the aeroacoustics of the flow in the reed channel is elaborated by Kergomard [102] and Hirschberg [86] in the book *Mechanics of Musical Instruments*, jointly edited with Weinreich. Since then, many important works have contributed to the present state of the art in musical acoustics research. Portable input impedance measurement systems for wind instruments are nowadays available [138, 48], with commercial software for musical instrument makers' workshops.

Methodologies to use simple air-column models for woodwind design have been proposed [100, 109] and applied [122, 132, 76] with some success.

Fundamental experiments on the valve characteristics of the reed exciter have been carried out [40, 161, 4] which have confirmed earlier analytical predictions [89]. The classic single-reed model has been proven to be useful in general also for double-reeds under quasi-static conditions [4], and has been applied in sound synthesis physical models [1]. With time-domain modeling it has been possible to show mode-locking effects [129] on a clarinet. Periodic steady-state solutions for the non-linearly coupled reed-resonator system can be obtained from hybrid modeling techniques such as the harmonic balance method [72]. Other researchers have set up two-dimensional models for detailed numerical investigations in the fluid-structure interaction at the single reed [39]. The present state of the art in modeling the complete system is to use an extended analytical model [152] to predict a static solution and apply a numerical continuation technique [94], to explore the blowing pressure ranges for a given resonator setting. Applications which are ready to use are freely available online.

Experimental research on wind instruments in playing conditions has developed greatly, in two directions: the *in vitro* approach using artificial mouths [11, 150, 119, 42, 3, 115, 75, 2] on the one hand, and the *in vivo* approach on the other, which encompasses measurements at the reed or player's mouth during musical performances [68, 32, 84, 113]. The first approach has revealed many fundamental aspects of the reed excitation mechanism, e.g. detailed knowledge of the flow-field inside a saxophone mouthpiece [115], but the imitation of realistic embouchures by a technical device is still problematic. With the latter approach, enlightening observations on the interaction of musician and musical instruments have been made, e.g. on the role of the vocal tract in saxophone playing [32], but it is very difficult to set up experiments in which the interaction between musicians and sensors does not disturb their performance.

Quite a number of questions remain open, especially on the respective roles of resonator, reed and embouchure in the settling of a fundamental frequency. Even though numerical physical models do generally explain the coupling process, fundamental frequency estimates often match the expected pitch poorly. *In vivo* measurements at the reed, e.g. flow field measurements or reed motion measurements, are still extremely difficult and their repeatability may be biased by large geometric differences between reeds and, in addition, changes in material properties in the course of the experiment, in particular due to changes in the moisture content.

More than 150 years ago, Weber was already aware of this complexity and very pessimistic about it:

*"There is such a great amount of indeterminacy in the manufacture of those instruments, namely, that (...) the reed blades (...) are simply tied together, that a detailed investigation of the reed's influence is impossible, unless its assembly is changed."*  
[168]

Even though Weber was not completely correct in that point, most researchers interested in double-reeds may indeed agree, that investigations into these most delicate parts are intricate and tedious. It is the sincere hope of the author, that this present work will provide valuable steps on the way for anyone aspiring to go further.

## 1.3 Organization of the Thesis

The thesis is organized in six parts:

**Chapter 1** is an introduction.

In **Chapter 2** the acoustic properties of the bassoon's resonator are investigated. A résumé of a one-dimensional air column model is presented, along with measurements of acoustic impedance spectra including estimations of experimental uncertainty.

**Chapter 3** is dedicated to the double-reed mouthpiece, which is described in a simplistic way as a harmonic oscillator with the tip displacement as a single degree of freedom and a non-linear pressure-flow characteristic. An experimental setup is presented to measure the corresponding parameters according to this model in relation to real reeds.

In **Chapter 4**, the influence of a lip force exerted on the reed-blade is investigated, by use of an adapted analytical model and measurements of characteristics in a set of realistic embouchure situations. An empirical model is derived to assign reed model parameters to any embouchure situation given by a pair of values of lip force and blowing pressure.

The behavior of the coupled system of resonator, reed and embouchure under playing conditions is discussed in **Chapter 5**, by analyzing a set of experiments with an artificial mouth. For the tonal and dynamical range of the bassoon, benchmarking values are given and the performance characteristics are analyzed in view of the harmonicity of the resonator.

Each of these chapters is presented with a short introduction and a concluding summary.

Finally **Chapter 6** summarizes the main results and provides some possible directions for future research.



## 2 Acoustical Properties of the Bassoon Air Column

### 2.1 Wave propagation in tubes

The aim of this Chapter is to introduce a basic analytic model of the air-column of a woodwind instrument. The discussion starts from the fundamentals of plane-wave propagation in a duct with the one-dimensional wave equation [141]. The transmission-line terminology to calculate air-column resonances from impedance networks models is presented, formula of most relevant elements are revisited and wall losses are introduced. Model calculations and measurements are juxtaposed and practical aspects of the measurement, such as repeatability and accuracy are discussed. A rescaled graphical representation of measurement results is introduced. This helps to understand the acoustical layout of the bassoon and to relate the harmonic properties of the resonator to aspects of bassoon performance, which will be the focus of Chapter 5.

#### 2.1.1 Theory

The propagation of sound waves in air in absence of wall losses is described by the wave equation. The case of a sound wave propagating in a tube of uniform cross section can be treated at low frequencies as a one-dimensional problem. In this case, the wave equation reads

$$\frac{\partial^2 p}{\partial t^2} = c^2 \frac{\partial^2 p}{\partial x^2}, \quad (2.1)$$

where  $p(x, t)$  is the pressure, at the time  $t$  at the location  $x$ . The D'Alembert general solution to this equation is a superposition of two arbitrary functions  $\mathcal{F}_1$  and  $\mathcal{F}_2$  of the argument  $(ct \pm x)$

$$p(x, t) = \mathcal{F}_1(ct - x) + \mathcal{F}_2(ct + x). \quad (2.2)$$

A harmonic motion in the complex notation of the type

$$\mathcal{F} = \Re\{e^{j\omega(t \pm \frac{x}{c})}\} \quad (2.3)$$

satisfies Eq. (2.1) [103]. This expression can be interpreted as a pressure wave traveling at the speed  $c$  forward (+) or backward (-) in  $x$ - direction, oscillating with the angular frequency  $\omega$ . Consequently, the superposition of these waves is also a solution to Eq. (2.1)

$$p(x, t) = A e^{j\omega t - jkx} + B e^{j\omega t + jkx} \quad (2.4)$$

where  $k = \omega/c$  is the wave number and A and B are the pressure amplitudes of the waves depending on  $\omega$ . The physically relevant solution is the real part of Eq. (2.4).

The velocity  $u$  is linked to the pressure  $p$  by the one-dimensional equation of motion

$$-\frac{\partial p}{\partial x} = \rho \frac{\partial u}{\partial t}, \quad (2.5)$$

where  $\rho$  is the density. Thus the velocity  $u$  in space and time becomes

$$u(x, t) = -\frac{1}{\rho c} \left( -A e^{j\omega t - jkx} + B e^{j\omega t + jkx} \right). \quad (2.6)$$

The quantities of interest are the resonance frequencies, therefore it is most useful to treat the tube problem in the frequency domain as a function of  $\omega$  and examine the acoustic impedance  $Z$ , which is for any location  $x$  defined as the ratio of pressure  $p$  to volume flow  $u S$

$$Z(x, \omega) = \frac{\rho c}{S} \frac{A e^{-jkx} + B e^{jkx}}{A e^{-jkx} - B e^{jkx}} \quad (2.7)$$

where  $S$  is the cross section of the tube.

A tubular element of length  $L$  is defined, whose impedances at the input  $Z_1 = Z(0, \omega)$  and output end  $Z_2 = Z(L, \omega)$  are

$$Z_1 = Z_c \frac{A + B}{A - B} \quad (2.8a)$$

$$Z_2 = Z_c \frac{A e^{-jkL} + B e^{jkL}}{A e^{-jkL} - B e^{jkL}}, \quad (2.8b)$$

where  $Z_c$  is the characteristic impedance of the tube<sup>1</sup>.

For the modeling of acoustical ducts it will be very useful to relate the input impedance  $Z_1$  of the duct to its output impedance  $Z_2$ . Rearranging Eqs.(2.8) yields [103, 59]

$$Z_1 = Z_c \frac{Z_2 \cos(kL) + j Z_c \sin(kL)}{j Z_2 \sin(kL) + Z_c \cos(kL)}. \quad (2.9)$$

The basic example of an open cylindrical tube with radius  $r$  and length  $L$  with characteristic impedance  $Z_c = \rho c / (\pi r^2)$  and output impedance  $Z_2 = 0$  yields

$$Z_{1,cyl,open,ideal} = j Z_c \tan(kL). \quad (2.10)$$

This is the analytical solution for the input impedance of a circular tube with an ideally open termination.

### 2.1.2 Transmission Line Modeling

Applying the electro-acoustical analogy, the one-dimensional plane-wave propagation in a duct can be represented as an equivalent electrical circuit. The transmission of waves through the elements of such a circuit can formally be described by a series of 4-pole elements, a so-called transmission line.

It will be shown here, how the elementary equation Eq. (2.9) can be rewritten in the transmission-line formalism in order to calculate plane-wave propagation in musical wind instruments.

First of all, the unbranched one-dimensional waveguide with a varying cross section is separated into a sequence of uniform tubular elements. Starting with the output impedance of the last element at the far end of such a compound model geometry, by successive solving of Eq. (2.9) the input impedance of the first element at the input can be calculated. In wind instrument research, this approach has been proposed first by Plitnik [142] to calculate the input impedance spectrum of an oboe and many modifications and extensions have been documented since then [30, 96, 118, 130, 46, 108].

For the numerical concatenation of acoustical elements to model a complex waveguide, the trans-

<sup>1</sup>The characteristic impedance of the tube  $Z_c$  is the specific characteristic impedance of air  $\rho c$  divided by the cross section  $S$  of the tube

mission line formalism

$$\begin{bmatrix} p_1 \\ U_1 \end{bmatrix} = T_{12} \begin{bmatrix} p_2 \\ U_2 \end{bmatrix}, \quad (2.11)$$

is useful, where a (2x2) matrix  $T_{12}$  links the pressure amplitude  $p$  and the acoustical volume flow amplitude  $U$  at the input  $(\cdot)_1$  and output  $(\cdot)_2$  end of the duct.

The matrix  $T_{12}$  is called *transmission matrix* and is given by

$$T_{12} = \begin{bmatrix} A_{12} & B_{12} \\ C_{12} & D_{12} \end{bmatrix}, \quad (2.12)$$

which represents the sound transmission behavior of the duct by means of the matrix coefficients  $A_{12}$ ,  $B_{12}$ ,  $C_{12}$  and  $D_{12}$ , whose values depend upon the physical boundaries.

In analogy to electrical network engineering, an acoustical waveguide can be treated as a lumped element model represented by a series of perfectly joined duct segments, each of which is described by Eq. (2.12). The transfer matrix of a waveguide separated into  $n$  duct segments between input  $(\cdot)_1$  and output  $(\cdot)_n$  writes

$$T_{1n} = \prod_{i=1}^n T_{i,i+1} = \begin{bmatrix} A_{1n} & B_{1n} \\ C_{1n} & D_{1n} \end{bmatrix} \quad (2.13)$$

In duct acoustics, the formalism introduced with Eqs.(2.11),(2.12),(2.13) is referred to as the *Transfer Matrix Method* [124] (TMM). It is useful in musical acoustics to model the plane-wave propagation in tubular resonators of wind instruments and obtain their resonance frequencies from the calculated input impedance spectrum.

Given the output impedance  $Z_n$  of the  $n^{th}$  element of a composed waveguide characterized by the transmission matrix  $T_{1n}$ , the input impedance  $Z_1$  can be calculated from

$$Z_1 = \frac{A_{1n} Z_n + B_{1n}}{C_{1n} Z_n + D_{1n}}. \quad (2.14)$$

It should be noticed, that the resulting input impedance  $Z_1$  obtained from solving Eq. (2.14) with Eq. (2.13) is numerically identical to the input impedance  $Z_1$  obtained from  $n$ -times successive solving of Eq. (2.9), starting from the  $n^{th}$  elementwise backwards to the first element, as proposed by Plitnik [142]. This approach is called the *Transmission Line Method*.

The transmission matrix formulation Eq. (2.11) is generally very convenient, since any waveguide segment whose transmission behavior can be represented by matrix coefficients according to Eq. (2.11) can be included into Eq. (2.13). Therefore the approach allows to model the wave propagation in a complex composite waveguide, by segmenting it into basic elements.

For the case of a woodwind resonator, which is schematically shown in Fig.2.1, there are four aspects that have to be considered for the modeling:

**duct:** waveguide element of main bore

**radiation:** duct termination, closed or open to the ambiance

**tone hole:** side branch to the main bore, open or closed

**losses:** visco-thermal losses at the wall

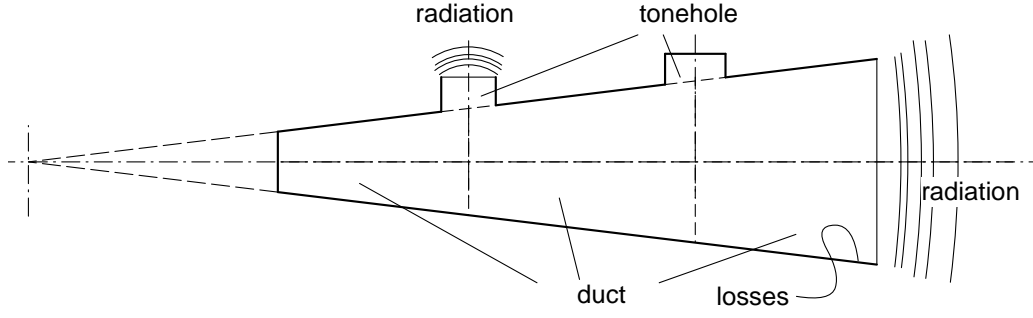


Figure 2.1 Schematic view of a conical woodwind instrument

### Cylindrical Duct Element

A basic lumped element is a cylindrical duct segment with length  $L$  and radius  $r$ . The matrix formulation is derived from Eq. (2.9), by replacing  $Z_{1,2}$  by the ratios  $(p/U)_{1,2}$ , at the input and output end, respectively

$$\frac{p_1}{U_1} = Z_c \frac{\frac{p_2}{U_2} \cos(kL) + j Z_c \sin(kL)}{j \frac{p_2}{U_2} \sin(kL) + Z_c \cos(kL)}, \quad (2.15)$$

where  $U$  is the volume flow  $uS$ . Separating nominator and denominator yields a set of equations

$$\begin{aligned} p_1 &= p_2 \cos(kL) + U_2 Z_c j \sin(kL), \\ U_1 &= p_2 \frac{1}{Z_c} j \sin(kL) + U_2 \cos(kL). \end{aligned} \quad (2.16)$$

Bringing this equation into the TMM formalism, the coefficients of the transmission matrix  $T_{cyl}$  of the cylindrical acoustical duct segment

$$T_{cyl} = \begin{bmatrix} A_{cyl} & B_{cyl} \\ C_{cyl} & D_{cyl} \end{bmatrix} \quad (2.17)$$

are found to be

$$\begin{aligned} A_{cyl} &= \cos(kL) \\ B_{cyl} &= Z_c j \sin(kL) \\ C_{cyl} &= \frac{1}{Z_c} j \sin(kL) \\ D_{cyl} &= \cos(kL). \end{aligned} \quad (2.18)$$

With the cylindrical duct element, it is possible to approximate a cone, if the taper is small enough that the bulging height  $s$  of the wavefront (Fig. 2.2) can be neglected. In that case an equivalent cylindrical element with mean radius is a good first order approximation, although the pressure iso-surfaces are spherical, not planar. A tubular waveguide with smoothly varying taper along the main axis can be approximated by a stepped tube concatenated of cylindrical duct segments described by Eq. (2.18).

### Conical Duct Element

A duct segment which is better suited to model a tapered waveguide is a conical frustum, described by the input and output radii  $r_1$  and  $r_2$ , and length  $L$ , as shown in Fig. 2.2. By using elements of this type, the number of segments needed to model the plane-wave propagation in a tapered waveguide can be reduced.

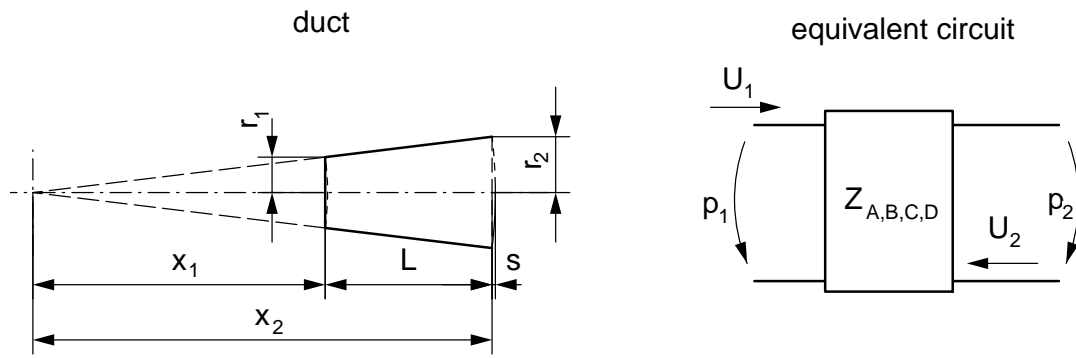


Figure 2.2 Schematic view of a conical duct element

Analogous to the above derivation of transfer matrix coefficients for the plane-wave propagation in a cylindrical element from the wave equation (Eq. (2.1)), the transfer matrix coefficients for the spherical wave propagation in a conical element can be derived with some calculus [61] from the one-dimensional Webster-equation

$$\frac{\partial^2 p}{\partial t^2} = c^2 \frac{\partial^2 p}{\partial x^2} + \frac{c^2}{S} \frac{dS}{dx} \frac{\partial p}{\partial x}, \quad (2.19)$$

where  $S$  is the surface area of an isophase surface that crosses the duct center axis at  $x$ .

The solution for the input impedance from this equation is given in the literature [137, 59]. Rearranged to match the TMM formalism, the coefficients of the transmission matrix  $T_{con}$  of the conical acoustical duct segment

$$T_{con} = \begin{bmatrix} A_{con} & B_{con} \\ C_{con} & D_{con} \end{bmatrix} \quad (2.20)$$

are found to be

$$\begin{aligned} A_{con} &= \frac{r_2}{r_1} \cos \left( kL - \left( \theta_2 - \frac{\pi}{2} \right) \right) (\sin \theta_2)^{-1} \\ B_{con} &= Z_{c2} \frac{r_2}{r_1} j \sin(kL) \\ C_{con} &= \frac{1}{Z_{c1}} \frac{r_2}{r_1} j \sin(kL + \theta_1 - \theta_2) (\sin \theta_1 \sin \theta_2)^{-1} \\ D_{con} &= \frac{Z_{c2}}{Z_{c1}} \frac{r_2}{r_1} \cos \left( kL + \left( \theta_1 - \frac{\pi}{2} \right) \right) (\sin \theta_1)^{-1}. \end{aligned} \quad (2.21)$$

where  $\theta_1 = \arctan(k x_1)$  and  $\theta_2 = \arctan(k x_2)$ .

The analogy to the formulation of the cylinder (Eq. (2.18)) is obvious. The effect of taper is represented by the terms in  $\theta_{1,2}$  and the duct radius ratio  $r_2/r_1$  ( $Z_{c1}/Z_{c2} = r_2^2/r_1^2$ ).

It can be seen, that the cylindrical duct segment is a special case of the conical segment with vanishing taper:

As  $r_2/r_1 \rightarrow 1$ , for a fixed segment length  $L$ , it follows  $x_1, x_2 \rightarrow \infty$ ,  $1/(k x_1) \rightarrow 0$ , and  $\theta_1, \theta_2 \rightarrow \pi/2$  and therefore Eq. (2.18) is part of Eq. (2.21), for vanishing taper.

No distinction between conical and cylindrical waveguides is necessary, and the TMM-formulation for the conical waveguide Eq. (2.21) can be used universally.

Whereas the duct segment is a distributed element, whose transmission characteristics depend upon its length, radiation boundaries and tone-holes can be modeled as lumped acoustic elements[96]. These have no physical length, although the term *correction length* will be used to model the effective lengthening of the bore at a termination [130].

Previous to the discussion of tone-holes, the representation of duct openings as zero-dimensional radiation impedances will be outlined.

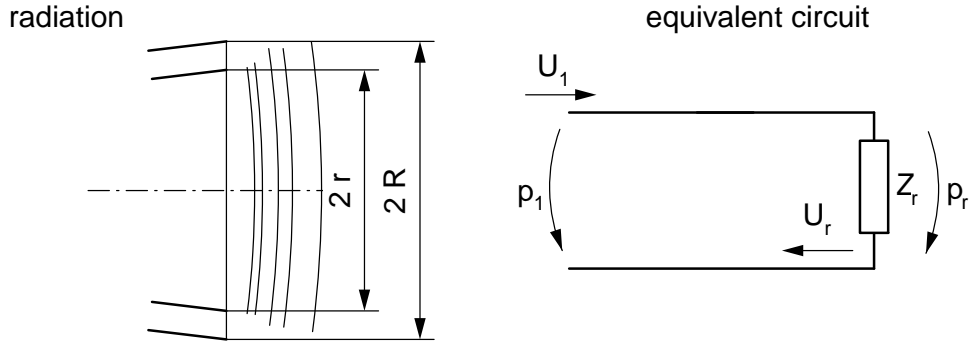


Figure 2.3 Schematic representation of a radiation boundary

### Radiation at a duct termination

At the termination of a duct, the air-flow from the duct is suddenly expanded. A part of the energy is radiated, as the pressure wave-front travels away from the termination. Another part of the energy is reflected and a pressure wave travels back into the pipe. This behavior can be represented in terms of the transmission-line theory by a lumped element representing the radiation impedance  $Z_r$  of the duct

$$Z_r = j Z_c \tan(kt_r), \quad (2.22)$$

where  $t_r$  is an equivalent length accounting for the inertia of the flow outside the tube by a hypothetical effective prolongation of the tube. The analogy to Eq. (2.10) is obvious, and the impedance of the non-ideally terminated pipe of length  $L$  is simply  $Z_{cyl,open,real} = j Z_c \tan(k(L + t_r))$ . Therefore  $t_r$  is called a length correction. Details of the geometry of the termination are important in the determination of  $t_r$ . A broad variety of configurations has been studied experimentally in detail [47], but here the focus is only on five termination configurations typically found in woodwind instrument resonators. For a tube of radius  $r$  the length corrections are [47]

$$t_r = \begin{cases} r \left( 0.613 \frac{1+0.044(kr)^2}{1+0.19(kr)^2} - 0.012 \sin^2(2kr) \right) & \text{open, unflanged } (R \rightarrow r) \\ r \left( 0.822 \frac{1+0.77kr}{1+0.77kr+(0.77kr)^2} \right) & \text{open, infinitely flanged } (R \rightarrow \infty) \\ r \left( 0.822 - 0.156 \left( \frac{r}{R_{circ}} \right) - 0.057 \left( \frac{r}{R_{circ}} \right)^6 \right) & \text{open, circularly flanged } (R_{circ} = R) \\ r \left( 0.822 - 0.47 \left( \frac{r}{R_{cyl}} \right)^{0.8} \right) & \text{open, cylindrically flanged} \\ \frac{\pi}{2k} & \text{closed,} \end{cases} \quad (2.23)$$

where  $R_{circ}$  and  $R_{cyl}$  are the outer flange radius and the radius of the cylindrical flange of the termination (Fig. 2.3). The cylindrical flange corresponds to situation where a hole is perpendicular to the main bore, and  $R_{cyl}$  is the outer radius of the main bore.

For the closed termination  $t_r$  is not a length correction. The above formulation uses the symmetry  $\tan\left(x + \frac{\pi}{2}\right) = -\cot(x)$  to assure the ideal pressure reflection at a closed boundary.

### Tone holes

A tone hole is a side branch of the main bore that can be interpreted as a shunt pathway for the oscillating pressure. In terms of TMM, this can be modeled by the transmission matrix of a lumped

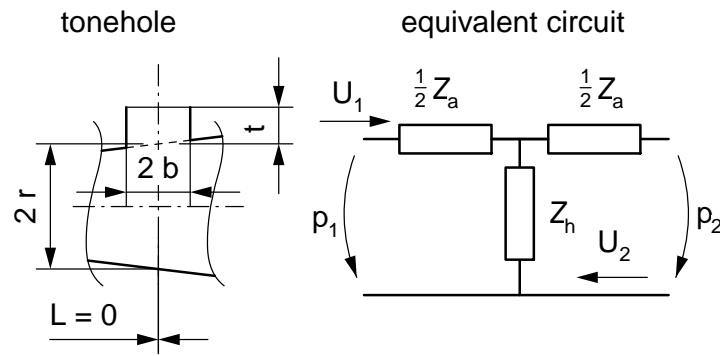


**Figure 2.4** Schematic representation of a tone-hole in a woodwind instrument and its equivalent circuit.

element T-circuit<sup>2</sup> including additional equivalent shunt and series impedances [96, 97]. A sketch of the tone hole its equivalent circuit is shown in Fig. 2.4 The oscillation of pressure into the tone hole chimney effectively acts as an acoustic compliance in the main duct, represented by a shunt impedance  $Z_h$ . The effective widening of the duct at the perforation leads to an apparent shortening [130] of the main duct, which is represented by the series impedances  $Z_{a1,2}$ .

Using the Kirchhoff's circuit laws, the set of equations for the equivalent T-circuit is

$$\begin{aligned} p_1 &= p_2 \left( 1 + \frac{Z_{a1}}{Z_h} \right) + U_2 \left( Z_{a1} + Z_{a2} + \frac{Z_{a1}Z_{a2}}{Z_h} \right), \\ U_1 &= p_2 \left( \frac{1}{Z_h} \right) + U_2 \left( 1 + \frac{Z_{a2}}{Z_h} \right). \end{aligned} \quad (2.24)$$

Considerations on the equivalent T-circuit of a tone hole are based on the assumption of the symmetry  $Z_{a1} = Z_{a2} = Z_a/2$  [96]. The transmission matrix for the tone-hole then becomes

$$T_{hole} = \begin{bmatrix} A_{hole} & B_{hole} \\ C_{hole} & D_{hole} \end{bmatrix} \quad (2.25)$$

with the elements

$$\begin{aligned} A_{hole} &= 1 + \frac{Z_a}{2Z_h} \\ B_{hole} &= Z_a + \frac{Z_a^2}{4Z_h} \\ C_{hole} &= \frac{1}{Z_h} \\ D_{hole} &= 1 + \frac{Z_a}{2Z_h}. \end{aligned} \quad (2.26)$$

The series and shunt impedances for the tone hole of radius  $b$  and height  $t$  are given by [46]

$$Z_a = j Z_c (k t_a) \quad (2.27a)$$

$$Z_h = j Z_{ch} (k t_i + \tan(k(t_m + t + t_r))) \quad (2.27b)$$

where  $Z_c = \pi r^2$  and  $Z_{ch} = \pi b^2$  are the characteristic impedances of the main duct and the tone hole chimney and

$$\begin{aligned} t_a &= -b 0.282 \delta^2 \\ t_i &= b(0.75 \delta^{2.7} - 1.4 \delta^2 + 0.82) \\ t_m &= b(0.026 \delta^3 + 0.125 \delta) \end{aligned} \quad (2.28)$$

<sup>2</sup>In contrast to the tone hole, the main bore is represented as a *distributed* transmission line element, whose parameters depend on the physical length of the duct segment

are length corrections to include the effects of the penetration of the pressure field into the hole ( $t_a$ ), the increased inertia of the air entering the hole ( $t_i$ ), the underestimation of the duct volume at the tone hole junction ( $t_m$ ) [130],[46]. The ratio of the tone hole radius  $b$  at the tone-hole position and the main duct radius  $r$  is  $\delta = b/r$ . The radiation length correction  $t_r$  is given by Eq. (2.23), by replacing the pipe radius  $r$  in this equation by the tone hole radius  $b$ .

The matrices of lumped (tone hole) and distributed (main duct) elements can be multiplied to characterize the transmission of a perforated duct [96, 124].

Note that open and closed tone holes can be modeled analogously. In the case of the closed tone hole, the radiation parameter  $t_r$  is set to  $\pi/(2k)$ , such that the tangent in the tone hole shunt impedance (Eq. (2.27b)) becomes a negative cotangent. Then,  $t_r$  is not a length correction: The inversion models a pressure antinode at the reflecting closed end of the chimney instead of representing an effectively prolongation to the chimney with a pressure node reflection at the open boundary.

This seemingly simplistic approach of converting an essentially three-dimensional acoustical situation into a one-dimensional impedance model has been theoretically proven to be valid, as long as the tone hole radius is small compared to the main duct radius, which must also be small compared to the spacing between the tone holes [112]. This is indeed the case for the majority of tone holes on the bassoon.

At this point, all basic<sup>3</sup> elements to model woodwind bores of small taper with tone-holes have been introduced. So far, ideal boundaries for the fluid at the wall have been assumed. In the next section, an approach to include the effect of wall losses is outlined.

### Visco-thermal losses at the wall

Friction and heat exchange between wall and fluid lead to velocity and temperature gradients along the duct radius. A simplified approach to account for these effects has been derived from acoustical boundary layer theory [114, 141].

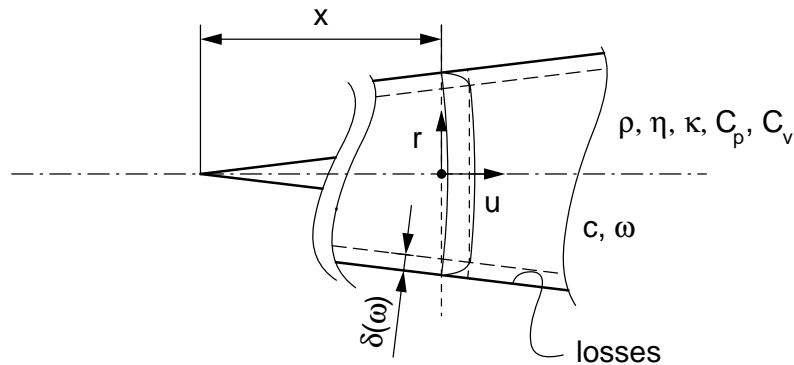


**Figure 2.5** Schematic representation of velocity profile and boundary layer in a conical duct

The existence of boundary layers reduces the effective radius of the duct (Fig. 2.5). Due to mass conservation, the apparent density of the fluid is then increased and the wave propagation speed is lowered. Besides this, energy is dissipated in the boundary layers and the pressure amplitude of

<sup>3</sup>For more complex geometrical elements such as rapidly flaring sections, expansion chambers, or bends of the main duct, in which the plane-wave approximation is questionable, approximate 1-D descriptions are given in the literature (e.g. [128, 159, 62]).



the wave is reduced. These effects can be directly included into the solution of the wave-equation Eq. (2.4) by replacing the wavenumber  $k$  with the complex quantity  $k_c$  defined as

$$k_c = k(1 + \alpha_1 - j\alpha_2), \quad (2.29)$$

where  $\alpha_{1,2}$  are dimensionless loss coefficients related to the viscous and thermal boundary layer thickness. This dispersion relation [114, 141] can be interpreted as follows: The real part of  $k_c$  lowers the wave-propagation speed by the factor  $1/(1 + \alpha_1)$  to account for the increased effective inertia and the additional imaginary term in  $\alpha_2$  introduces wave attenuation<sup>4</sup> due to frictional resistance.

The magnitude of the loss coefficients  $\alpha_{1,2}$  depends on the impact of the boundary layer effects on the wave propagation in the duct, which can be quantified through the ratios  $\delta_v/r$  and  $\delta_t/r$ , with  $r$  being the duct radius and  $\delta_v$  and  $\delta_t$  being the viscous and thermal boundary layer thicknesses

$$\begin{aligned} \delta_v &= \sqrt{\frac{\eta}{\omega\rho}}, \\ \delta_r &= \sqrt{\frac{\eta}{\omega\rho}} \sqrt{\frac{\kappa}{\eta C_p}}, \end{aligned} \quad (2.30)$$

where  $\eta$ ,  $\rho$ ,  $C_p$ , and  $\kappa$  are the dynamic viscosity, density, isobaric specific heat and thermal conductivity of the fluid, and  $\omega = 2\pi f$  is the angular frequency [19].

For the loss coefficients  $\alpha_{1,2}$  approximation formula are given in the literature which stem from series expansions to approximate Bessel functions [99]. The validity and accuracy of these approximations depends upon the frequency-dependent ratio  $\delta_v/r$ .

For the case of the small diameter duct with  $r \leq 2\delta_v$  approximations for the loss coefficients are [99]<sup>5</sup>

$$\begin{aligned} \alpha_1 &= 2\sqrt{\gamma} \left[ \frac{\delta_v}{r} + \frac{r}{\delta_v} \left( \frac{1}{12} - \frac{1}{16} Pr^{\frac{\gamma-1}{\gamma}} \right) \right] - 1, \\ \alpha_2 &= 2\sqrt{\gamma} \left[ \frac{\delta_v}{r} - \frac{r}{\delta_v} \left( \frac{1}{12} - \frac{1}{16} Pr^{\frac{\gamma-1}{\gamma}} \right) \right], \end{aligned} \quad (2.31)$$

where  $Pr$  is the Prandtl Number  $Pr = (\eta C_p)/\kappa$ , and  $\gamma$  is the ratio of the specific heat in isobaric and isochoric conditions  $\gamma = C_p/C_v$ .

For the case of the large diameter duct with  $r > 2\delta_v$  approximations for the loss coefficients are [99]<sup>6</sup>

$$\begin{aligned} \alpha_1 &= \frac{1}{2} \sqrt{2} \frac{\delta_v}{r} \left( 1 + \frac{\gamma-1}{\sqrt{Pr}} \right) + O(3), \\ \alpha_2 &= \frac{1}{2} \sqrt{2} \frac{\delta_v}{r} \left( 1 + \frac{\gamma-1}{\sqrt{Pr}} \right) + \left( \frac{\delta_v}{r} \right)^2 \left( 1 + \frac{\gamma-1}{\sqrt{Pr}} - \frac{1}{2} \frac{\gamma-1}{Pr} - \frac{1}{2} \frac{(\gamma-1)^2}{Pr} \right) + O(3), \end{aligned} \quad (2.32)$$

to second order accuracy<sup>7</sup>. Within the scope of the present work, first order accuracy is sufficient, which leads to some simplifications outlined subsequently.

### Effective Loss Coefficient for any tubular Duct

Since the loss coefficients depend upon the radius,  $\alpha_{1,2} = \alpha_{1,2}(r)$ , for the case of a duct segment with varying radius along its main axis, integral mean values over the segment length [18, 157, 108]

<sup>4</sup>The solutions to the wave-equations have the form  $p(x, t) = A e^{j\omega t - jkx}$  which, by replacing  $k$  with  $k_c$ , becomes  $p(x, t) = e^{-\alpha_2} A e^{j\omega t - j\frac{\omega}{c}(1+\alpha_1)x}$ . Here,  $e^{-\alpha_2}$  is an attenuation coefficient scaling the pressure amplitude  $A$ .

<sup>5</sup>Eqs. (11.h) and (11.g) in [99] correspond to  $\alpha_1$  and  $\alpha_2$ , respectively.

<sup>6</sup>Eqs. (12.h) and (12.g) in [99] correspond to  $\alpha_1$  and  $\alpha_2$ , respectively.

<sup>7</sup>Third order terms are given in [99]. Considering higher order effects would consequently require to take viscous dissipation in the main flow into account, which is clearly beyond the scope of this work.

can be used as *effective* loss coefficients  $\bar{\alpha}_{1,2}$

$$\bar{\alpha}_{1,2} = \frac{1}{x_2 - x_1} \int_{x_1}^{x_2} \alpha_{1,2}(x) dx. \quad (2.33)$$

In most waveguides considered in music acoustics, in the frequency range of interest,  $\delta_v$  is small compared to the duct radius: In case of a bassoon bore, at the fundamental frequency of the lowest note  $f_0 = 58$  Hz, the smallest radius<sup>8</sup> at the bocal tip ( $r \approx 2$  mm) is about ten times larger than the viscous boundary layer thickness. Therefore it is justified to use the approximation for the large diameter duct Eq. (2.31) and neglect the terms in  $(\delta_v/r)^2$ .

To first order accuracy the loss coefficients are then

$$\alpha_1 = \alpha_2 = \alpha \approx \frac{\alpha'(\omega)}{r}, \quad (2.34)$$

where  $\alpha'(\omega)$  is an frequency dependent thickness accounting for both viscous and thermal boundary layer effects. This *equivalent* boundary layer thickness  $\alpha'$  is about 5% larger than the viscous boundary layer thickness  $\delta_v$  at 20°C and atmospheric pressure [99, 31].

With respect to lumped element modeling, an *effective* boundary layer thickness of a tubular duct segment with constant taper can be calculated, according to Eq. (2.33), from the integral mean of the local *equivalent* boundary layer thickness  $\alpha'$ , as

$$\bar{\alpha} = \frac{1}{L} \int_{x_1}^{x_2} \frac{\alpha'}{z} \frac{1}{x} dx = \frac{\alpha'}{Lz} \ln \frac{x_2}{x_1} = \frac{\alpha'}{r_2 - r_1} \ln \frac{r_2}{r_1} \quad (2.35)$$

where  $x_1 = r_1/z$  and  $x_2 = r_2/z$  are the apical distances of input and output cross sections of the duct,  $L = x_2 - x_1$  is the length and  $z = (r_2 - r_1)/L$  is the taper.

Now the effective complex wavenumber for any tubular duct segment with constant taper can be written

$$\bar{k}_c = \begin{cases} k \left( 1 + \frac{\alpha'}{r_2 - r_1} \ln \frac{r_2}{r_1} (1 - j) \right), & \text{for } r_2 \neq r_1 \\ k \left( 1 + \frac{\alpha'}{r} (1 - j) \right), & \text{for } r_2 = r_1 \end{cases} \quad (2.36)$$

In standard music acoustics literature [59] another formulation for effective wavenumber of the cylindrical duct is given<sup>9</sup>, which assumes that  $(\alpha')^2$  can be neglected.

The formulation Eq. (2.36) is valid for any waveguide segment with constant taper. For vanishing taper ( $z \rightarrow 0$ ) the function smoothly approaches the singularity which characterizes the cylindrical case. This can be proven by evaluating the limit  $r_2 \rightarrow r_1$  by use of l'Hospital's rule:

$$\lim_{r_2 \rightarrow r_1} \frac{\ln \left( \frac{r_2}{r_1} \right)}{r_2 - r_1} = \lim_{r_2 \rightarrow r_1} \frac{\frac{\partial}{\partial r_2} \ln \left( \frac{r_2}{r_1} \right)}{\frac{\partial}{\partial r_2} (r_2 - r_1)} = \frac{\frac{1}{r_1}}{1} = \frac{1}{r_1}. \quad (2.37)$$

Although elsewhere stated [108], the effective wavenumber of the cone does not depend upon the segment length.

<sup>8</sup>Exceptions are the register holes, which may have radii down to  $r = 0.4$  mm. The boundary layer thickness is then comparable to the duct radius at low frequencies and these holes appear to be closed.

<sup>9</sup>Fletcher and Rossing give  $k_c \approx k \left( \frac{1}{1 - \alpha'} - j \alpha' \right)$  (Eqs.(8.14),(8.15) in [59]), repeating an approximation by Benade [19] which is based on the assumption  $1/(1 - \varepsilon) \approx 1 + \varepsilon$ . This assumption appears to be needless to the present author, as it does not lead to any helpful simplification.

It should be noted here, that the integrand in Eq. (2.33) has been derived explicitly for ducts with *uniform* cross section [141]. A more sophisticated approach to incorporate wall losses in conical waveguides has been presented by Nederveen [125] (see section 2.1.4).

### Approximations for the Loss Coefficient

If a first order accuracy is sufficient, both loss coefficients  $\alpha_{1,2} = \alpha$  can be approximated by  $\alpha'/r$ , with

$$\alpha'(\omega) = \frac{1}{2} \sqrt{2} \delta_v \left( 1 + \frac{\gamma - 1}{\sqrt{Pr}} \right) = \frac{1}{2} \sqrt{2} \sqrt{\frac{\eta}{\omega \rho}} \left( 1 + \left( \frac{C_p}{C_v} - 1 \right) \sqrt{\frac{\kappa}{\eta C_p}} \right). \quad (2.38)$$

The first term  $1/2 \sqrt{2} \delta_v$  accounts for viscous losses<sup>10</sup>, the second term  $(1 + (\gamma - 1)/\sqrt{Pr})$  accounts for thermal losses.

In the temperature range of  $T = 300 \pm 10$  K and atmospheric pressure Benade [19] gives linear approximations for the physical properties of air which are repeated here:

$$\begin{aligned} c &= 347.23 \left( 1 + 0.00166 \frac{1}{^\circ\text{C}} \Delta T \right) \frac{\text{m}}{\text{s}} \\ \eta &= 1.8460 \left( 1 + 0.00250 \frac{1}{^\circ\text{C}} \Delta T \right) \frac{\text{Ns}}{\text{m}^2} \cdot 10^{-5} \\ \rho &= 1.1769 \left( 1 - 0.00335 \frac{1}{^\circ\text{C}} \Delta T \right) \frac{\text{kg}}{\text{m}^3} \\ \gamma = \frac{C_p}{C_v} &= 1.4017 \left( 1 - 0.00002 \frac{1}{^\circ\text{C}} \Delta T \right) \\ \sqrt{Pr} = \sqrt{\frac{\eta C_p}{\kappa}} &= 0.8410 \left( 1 - 0.00002 \frac{1}{^\circ\text{C}} \Delta T \right), \end{aligned} \quad (2.39)$$

where  $\Delta T = T - T_0$  is the temperature difference between the actual temperature  $T$  and the reference temperature  $T_0 = 300$  K.

The temperature dependent constants in expression Eq. (2.38) can be lumped into a factor  $v$  to give

$$\alpha' = \frac{v(\Delta T)}{\sqrt{f}}, \quad (2.40)$$

where  $v$  is

$$v = \frac{1}{2} \sqrt{\frac{\eta}{\pi \rho}} \left( 1 + \left( \frac{C_p}{C_v} - 1 \right) \sqrt{\frac{\kappa}{\eta C_p}} \right) \quad (2.41)$$

At  $20^\circ\text{C}$ ,  $v = 1.617 \cdot 10^{-3}$ . In the literature  $\alpha'$  is often expressed in terms of the loss free wave number  $k = \omega/c$ . Near  $20^\circ\text{C}$ , as a rule of thumb, the following expressions are given [46, 59, 31]

$$\alpha' \approx 2.96 \cdot 10^{-5} \sqrt{\frac{f}{\text{Hz}}} \frac{1}{k} \approx 3 \cdot 10^{-5} \sqrt{\frac{f}{\text{Hz}}} \frac{1}{k}. \quad (2.42)$$

The approach outlined above provides a simple method to include the effect of wall-losses in the one-dimensional model of sound propagation in a tubular waveguide. All boundary layer effects are lumped in one non-dimensional, frequency-dependent parameter in an expression for the *effective* wavenumber, which becomes complex. To model the lossy case, the formula derived for the ideal, loss-free case can be used straightforward by replacing the occurrences of the free-space wave number  $k$  with the effective wavenumber  $\bar{k}_c$  of the duct segment.

The approach is very convenient, as the calculus remains the same for both cases. Replacing  $k$  by the effective, complex wavenumber  $k_c$ , the originally loss-free theory can be used to model the real situation<sup>11</sup>. This approach has been successfully used, and it applies for the main duct, as well as for tone holes [130, 46].

<sup>10</sup>Lighthill presents a derivation of this coefficient from an energy balance, stating that the mean rate of a pressure force per unit volume does an amount of work to the fluid per unit area, which must equal the mean rate of viscous dissipation energy [114], p.128-136

<sup>11</sup>This approach implies that also the characteristic impedance  $Z_c$  becomes a complex quantity. Formula are given e.g. in [19, 99, 30, 31]

### 2.1.3 Implementation

In musical instruments research, the input impedance spectrum of a duct with known geometry and radiation impedance can be obtained by successive solving of Eq. (2.9) for each element starting from the radiating boundary at the output end [142, 130, 149] or, equivalently, by multiplying the transmission matrices of the segments Eq. (2.13) and solve Eq. (2.14) [96, 118, 111].

When studying the interactions of the musical instruments geometry and its resonance frequencies, it is interesting to obtain the distributed pressure amplitude along the main axis of the duct. This information can generally be obtained by the transmission-line approach, but in the case of a perforated duct, both classical methods of solving include numerical problems, as the tone-hole matrices are usually badly conditioned. To overcome this, an alternative implementation will be used here<sup>12</sup>. The basic transfer matrix formulation Eq. (2.11) of an arbitrary element can be rearranged as follows

$$\begin{bmatrix} p_1 \\ U_1 \end{bmatrix} = T_{12} \begin{bmatrix} p_2 \\ U_2 \end{bmatrix} \Rightarrow \begin{bmatrix} p_1 \\ p_2 \end{bmatrix} = S_{12} \begin{bmatrix} U_1 \\ U_2 \end{bmatrix}. \quad (2.43)$$

The transfer matrix  $T_{12}$  is transformed into a stiffness matrix  $S_{12}$  [36]

$$T_{12} = \begin{bmatrix} A_{12} & B_{12} \\ C_{12} & D_{12} \end{bmatrix} \Rightarrow S_{12} = \begin{bmatrix} E_{12} & F_{12} \\ G_{12} & H_{12} \end{bmatrix}, \quad (2.44)$$

with

$$\begin{aligned} E_{12} &= \frac{A_{12}}{C_{12}}, \\ F_{12} &= B_{12} - \frac{A_{12}D_{12}}{C_{12}}, \\ G_{12} &= \frac{1}{C_{12}}, \\ H_{12} &= -\frac{D_{12}}{C_{12}}. \end{aligned} \quad (2.45)$$

Equivalently to  $T_{12}$ , the stiffness matrix  $S_{12}$  characterizes an acoustical duct element, with input pressure  $p_1$  and output pressure  $p_2$ . The conjunction of  $n$  elements requires the balance of forces at the joining cross sections. Assuring mass conservation at the connections, i.e.  $U_{i-,i} = -U_{i,i+1}$ , a set of  $n$  linear equations is obtained, that can be written as a matrix equation

$$\begin{bmatrix} p_1 \\ 0 \\ 0 \\ \vdots \\ 0 \\ 0 \end{bmatrix} = \begin{bmatrix} -E_{12} & F_{12} & 0 & 0 & \cdots & 0 \\ -G_{12} & H_{12} - E_{23} & F_{23} & 0 & & 0 \\ 0 & -G_{23} & H_{23} - E_{34} & F_{34} & & 0 \\ \vdots & \vdots & \ddots & \vdots & \ddots & \vdots \\ 0 & 0 & 0 & -G_{n-1,n} & H_{n-1,n} - E_{n,n+1} & F_{n,n+1} \\ 0 & 0 & 0 & 0 & -G_{n,n+1} & H_{n,n+1} - Z_r \end{bmatrix} \begin{bmatrix} U_1 \\ U_2 \\ U_3 \\ \vdots \\ U_{n-1} \\ U_n \end{bmatrix}, \quad (2.46)$$

where the boundary conditions at the input and output are given by an input volume velocity  $U_1$  and an output impedance  $Z_r$ . This equation can be solved for the input pressure  $p_1$  and the unknown volume velocities  $U_2, U_3 \cdots U_n$ . The input impedance is then given by  $Z_1 = p_1/U_1$ .

This approach is equivalent to classical transmission line assembly Eq. (2.13) and the subsequent solving of Eq. (2.14).

The advantage of this implementation, however, is that in the post-processing the unknown pressures  $p_2, p_3 \cdots p_n$  at the junctions can be calculated<sup>13</sup> from the volume velocities  $U_1, U_2 \cdots U_n$  according

<sup>12</sup>This approach has been proposed to the author by Johannes Baumgart

<sup>13</sup>The condition number of the tone hole transmission matrix is small, and numerical errors grow rapidly when multiplying inverse matrices to calculate the pressures at the intersections using the classical transmission line approach Eq. (2.13)

to the law of conservation of energy. This can be written as a matrix equation to give

$$\begin{bmatrix} p_2 \\ p_3 \\ \vdots \\ p_n \end{bmatrix} = \begin{bmatrix} -G_{12} & H_{12} & 0 & \cdots & 0 \\ 0 & -G_{23} & H_{23} & & 0 \\ \vdots & & & & \vdots \\ 0 & 0 & \cdots & -G_{n-1,n} & H_{n-1,n} \end{bmatrix} \cdot \begin{bmatrix} U_1 \\ U_2 \\ U_3 \\ \vdots \\ U_n \end{bmatrix}. \quad (2.47)$$

The numerical problems of badly conditioned (2x2) tone hole transfer matrices can be avoided by solving this matrix equation. The pressure distribution along a duct with sideholes can be shown for the complete length, in particular downstream of the first open tone hole.

## Summary

The brief overview provided in this sections illustrates a simple and robust method to model the sound wave propagation in tubular ducts with slowly varying cross section along the main axis and an arbitrary number of side branches. Resonators of woodwind instruments can be modeled as such ducts.

This theory has been proven to be useful to calculate the input impedance of woodwind resonators, and the effect of geometry changes of the resonator on the air column resonances [125, 142, 100]. The well-known theory has been restructured and a simplified notation is given here.

The calculus of the transmission-line model based on one stiffness matrix for the complete system, as presented here, allows to compute standing pressure wave patterns in a duct with tone holes, over the complete length.

### 2.1.4 Remarks on Modeling Wall Losses in a Conical Waveguide

The inclusion of losses by means of an effective wavenumber deserves some discussion for the case of a conical duct.

A derivation for the modified, complex wavenumber to consider viscous and thermal effects at the walls of a cylindrical waveguide is given by Pierce [141]. It is not obvious, that this formulation of a complex wavenumber can be used for the case of the conical duct with varying cross section. In contrast to the cylindrical duct segment, for the case of the cone loss-dependent pressure gradient in propagation direction occur.

Many authors (e.g. [30, 20, 118, 55]) have used this approximation for conical waveguides to model them with the Transmission Line Method with the equations given in the preceding sections. They used an average radius  $\bar{r}$  to calculate an effective wavenumber for a conical duct segment with  $r_1 \neq r_2$ .

Instead of modifying the wavenumber in the solution of the ideal case, it appears to be more elaborate to include loss terms in the wave-equation, and derive solutions to satisfy this modified equation. This path has been followed by Nederveen, who scaled flow and pressure in the equation of motion and continuity by means of loss coefficients [125]. The result is a modified Webster-equation, extended by loss terms. From solving this, an explicit formula for the input impedance of the conical waveguide is obtained, based on several assumptions.

Nederveen [128] gives a formula<sup>14</sup> for the admittance  $Y = 1/Z$  of a cross section within a conical duct for the loss-free case. Rearranging this to match the notation of present work his can be

---

<sup>14</sup>(Eq.(8) in [128])

rewritten for the input impedance of the loss-free cone

$$Z_1 = \left( \frac{1}{jZ_{c1}} \left[ \frac{1}{kx_1} - \frac{\left( \frac{1}{kx_2} - j\frac{Z_{c2}}{Z_2} \right) + \tan(kL)}{1 - \left( \frac{1}{kx_2} - j\frac{Z_{c2}}{Z_2} \right) \tan(kL)} \right] \right)^{-1}, \quad (2.48)$$

This equation can be further rearranged to match the transmission-line formalism for the cone (Eq. (2.21) in the present work), so both approaches are mathematically identical. The rearrangement<sup>15</sup> is shown in Appendix A1.

Including loss terms into the Webster-equation, Nederveen [125] derived an explicit analytical formula for the lossy cone<sup>16</sup> which after some rearrangement to match the notation of the present work can be written for the input impedance of the lossy cone

$$Z_1 = \left( \frac{1}{jZ_{c1}} \left[ \frac{1 - \tilde{\alpha}_{g1}}{kx_1} - \frac{(1 + \tilde{\alpha}_{f1}) \left( \frac{1 - \tilde{\alpha}_{g2}}{kx_2} - j\frac{Z_{c2}}{Z_2} \right) + (1 + \tilde{\alpha}_{f1})(1 + \tilde{\alpha}_{f2}) \tan(kL + \tilde{\alpha}_2 \Delta\xi)}{(1 + \tilde{\alpha}_{f2}) - \left( \frac{1 - \tilde{\alpha}_{g2}}{kx_2} - j\frac{Z_{c2}}{Z_2} \right) \tan(kL + \tilde{\alpha}_2 \Delta\xi)} \right] \right)^{-1}, \quad (2.49)$$

where  $\Delta\xi = \xi_2 - \xi_1 = \ln(r_2/r_1) + g_2 - g_1$  (see Appendix A1 for details) Here,  $\tilde{\alpha}$  are frequency and position dependent loss terms given by

$$\begin{aligned} \tilde{\alpha}(r) &= kx \frac{\alpha'}{r} \\ \tilde{\alpha}_f(r, x) &= kx \frac{\alpha'_f}{r} (1 - j), \\ \tilde{\alpha}_g(r, x) &= (kx)^2 \frac{\alpha'_g}{r} (1 - j) \\ \text{and} \\ \xi &= \ln(kx) + g. \end{aligned} \quad (2.50)$$

There are three loss parameters  $\alpha'$  which analogously to Eq. (2.38) represent effective boundary layer thicknesses

$$\begin{aligned} \alpha'(\omega) &= \frac{1}{2} \sqrt{2} \delta_v \left( 1 + \frac{\gamma-1}{\sqrt{Pr}} \right), \\ \alpha'_f(\omega, x) &= f \sqrt{2} \delta_v \left( 1 + \frac{1}{f \cdot (kx)} + \frac{\gamma-1}{\sqrt{Pr}} \right), \\ \alpha'_g(\omega, x) &= g \sqrt{2} \delta_v \left( 1 + \frac{1}{2g \cdot (kx)^2} + \frac{\gamma-1}{\sqrt{Pr}} \right), \end{aligned} \quad (2.51)$$

where  $f$  and  $g$  are factors from a combination of with sinus cardinalis and Cosine integral<sup>17</sup> functions evaluated at the position  $2kx$  given by

$$\begin{aligned} f &= \text{Ci}(2kx) \sin(2kx) - \text{si}(2kx) \cos(2kx), \\ g &= -\text{Ci}(2kx) \cos(2kx) - \text{si}(2kx) \sin(2kx), \end{aligned} \quad (2.52)$$

which stem from approximations to solutions of the extended wave-equation.

It can be shown that for the loss free case with  $\delta_v = 0$  the loss terms  $\tilde{\alpha}$ ,  $\tilde{\alpha}_f$ ,  $\tilde{\alpha}_g$  become zero and Eq. (2.49) becomes Eq. (2.48)

## Discussion

Rearranging the well-known formula by Nederveen [125] reveals the analogy of Eq. (2.38) and the loss parameters  $\tilde{\alpha}$  in Eq. (18) which represent boundary layer thicknesses [114]. In the line of this

<sup>15</sup>An interesting side product of this rearrangement is a reconsideration of the transmission matrix coefficients that Benade gave to describe the transmission characteristics of an “equivalent circuit for conical waveguides” [19]. Although Benades approach and his equations are sometimes regarded as an approximate solution [59], they are in fact mathematically identical with the analytic solution Eq. (2.21) given by Fletcher [61].

<sup>16</sup>(Eq.(23.36) in [125])

<sup>17</sup> $\text{si}(x) = \frac{\sin x}{x}$  and  $\text{Ci}(x) = \gamma_E + \ln x + \int_0^x \frac{\cos t - 1}{t} dt$ , with  $\gamma_E = 0.57721$  being the Euler-Mascheroni-constant.

argumentation Eq. (2.29) compares with the loss terms Eq. (17).

It becomes obvious, that in Nederveens derivation, due to the extension of the Webster-equation by loss terms, additional derivatives occur which lead to linear and quadratic terms in  $(kx)$ , to scale the losses. The difference to Eq. (2.29) is obvious.

From the formal analogy observed here between the loss-free and the lossy case, Nederveens formula Eq. (2.49) may be used as a reference solution, as his derivation of the loss terms from the wave-equation is certainly more elaborate, than using the corrective terms to the wavenumber originally derived for a cylindrical duct<sup>18</sup>. The latter approach, which is often used [157, 108, 110], may be straightforward for cylindrical ducts, but the application to conical ducts is not obvious.

Kulik [108] claimed, that increased precision in the modeling of conical ducts could be achieved by regarding the wavenumber as a local complex quantity  $k = k_c(x)$ . This argumentation leads to two consequences in his transmission-line formulation. The integral mean of  $\bar{k}_c(x)$  along the duct element is used as an effective wavenumber (compare Eq. (2.33)), and for the terms in  $\theta$ , which represents the widening of the duct, different wave-numbers  $k_{c,1,2} = k_c(x_{1,2})$  are used within one equation, as is

$$\begin{aligned}\theta_1 &= \arctan(k_{c,1} x_1) \\ \theta_2 &= \arctan(k_{c,2} x_2)\end{aligned}\tag{2.53}$$

Under this assumption, Kulik showed that the segmentation of a macroscopical conical waveguide of input radius  $r_{in}$ , output radius  $r_{out}$  and length  $L$  according to (Eq.2.13) into  $n$  conical segments  $i$ , with input radius  $r_1^i$ , output radius  $r_2^i$  and length  $L_{12}^i$  does not affect the global transfer matrix  $T_{in,out}$ . This is a consequence of Eq. (2.53) according to which

$$k_{c2}^i = k_{c1}^{i+1}.\tag{2.54}$$

All conicity terms at the junctions between segments  $i$  and  $i+1$  cancel each other out for  $i = 1 \dots n-1$ .

The only remaining terms are  $\theta_1 = \theta_{in}$  and  $\theta_2 = \theta_{out}$ .

This is mathematically elegant and seems to make the segmentation of a cone unnecessary.

However, one may argue, that Eq. (2.53) is a misinterpretation, as it causes a spatial dependence of the wave-propagation speed, which is by definition a constant in the wave-equation Eq. (2.2).

To include the effect of wall losses into the transmission matrix of a cone, it is possible to regard the effective wavenumber  $\bar{k}_c$  as an elementwise constant property, thus

$$\begin{aligned}\theta_1 &= \arctan(\bar{k}_c x_1) \\ \theta_2 &= \arctan(\bar{k}_c x_2),\end{aligned}\tag{2.55}$$

where the effective wavenumber  $\bar{k}_c$  is based on an integral mean of the *effective* boundary layer thickness, but itself is constant within the element. This is justified as it is the intrinsic character of the TMM approach to elementwise convert the physical problem into the model domain.

In this case, as

$$\bar{k}_c^i \neq \bar{k}_c^{i+1},\tag{2.56}$$

the corrective terms at the junctions do not cancel out and consequently, the segmentation does affect the global transfer matrix  $T_{in,out}$ .

The conformance of the problem and the model depends upon the model assumptions, i.e. the conical segments should be chosen small enough, that the assumption of a constant wave-propagation speed within the element is met. Consequently, the model can only be improved by segmenting the duct into segments with a smaller ratio  $r_2/r_1$  where the model assumptions are met better.

Generally, as  $r_2^i \rightarrow r_1^i$  or  $L_{12}^i \rightarrow 0$ , the model geometry approaches the real geometry and the

<sup>18</sup>see Pierce [141], p. 533 ff

conicity terms cancel out. Therefore the results of piecewise modeling with cylindrical and conical elements converge with decreasing element length. Kuliks approach is insensitive to segmentation, but his result does not equal the result of the piecewise approach for vanishing element lengths.

### Summary

The results of three different approaches to model the wave propagation in a cone will be compared. One approach requires segmentation of the macroscopical conical waveguide into smaller conical segments, the other two are direct solutions independent of segment length. While being identical for the loss free case, there are significant differences assuming wall-losses. For comparison, results are given for the cone modeled as a sequence of short cylindrical segments.

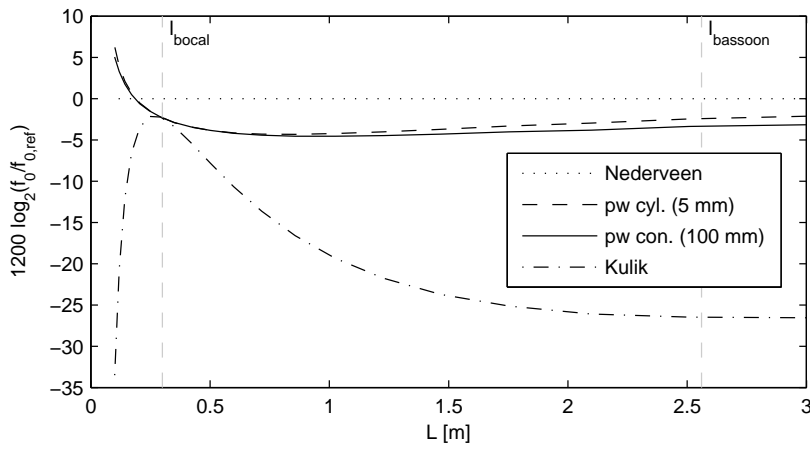


**Figure 2.6** Deviation of fundamental frequency of the air column predicted by 4 plane-wave approximations. Conical waveguides with bassoon-like taper  $z = 140$  and input radius  $r = 2$  mm, and lengths  $L$  within  $100 \text{ mm} < L < 3000 \text{ mm}$ .

Fig. 2.6 shows the deviation of fundamental frequencies of lossy cones of varying length, as predicted by four different plane-wave approximations: Nederveens approach without segmentation Eq. (2.49), piecewise modeling with short cylinders (pw cyl. (5 mm)) and with cones (pw con. (100 mm)), both calculated from Eq. (2.21) with Eq. (2.55), and Kuliks approach without segmentation calculated from Eq. (2.21) with Eq. (2.53).

From this plot and the above considerations, the discussion of the plane-wave propagation modeling in conical waveguides with respect to wall losses can be summarized in three statements:

- Nederveens approach to include loss terms into the Webster equation is the most promising to provide a correct model of the physics, and is therefore regarded as a reference solution. It provides a direct solution without the need of segmentation.
- A good approximation to the reference solution is provided by piecewise modeling. Cylindrical or conical duct elements may be used as for sufficiently small elements, both approaches converge. With conical elements, convergence is achieved faster, but a systematic deviation remains.
- Kuliks suggestion of a “Transfer matrix of conical waveguides with any geometric parameters for increased precision in computer modeling” is perfectly consistent in the mathematical sense, but the results differ largely from the reference solution.

Concerning the frequency of the fundamental air column mode, for a cone of small input radius and slight taper, comparable to a bassoon ( $r_1 = 2$  mm,  $m = 1/140$ ), discrepancies between the three approaches are found, which are large enough to be relevant in the context of musical instruments



[41] and require further investigations (Fig. 2.6).

These should be carried out using precise impedance measurement setups [50, 41], and very accurately manufactured conical waveguides with small input diameter, where the boundary layer effects become important.

An analytical approach to address the cone problem would be to derive a formula for the complex wave-number taking friction into account from a modified Webster equation<sup>19</sup>.

A alternative, promising approach for a numerical verification is the Finite-Element Modeling with visco-acoustic elements [13].

Given a geometry with tone holes, such a model would allow to investigate viscous effects due to local losses at the sharp edges, which are expected to be crucial [88].

## 2.2 Input Impedance Measurement

### 2.2.1 Principle

The input impedance measurement of the resonator is a standard technique in wind instruments acoustics. Peaks in the input impedance spectrum correspond to frequencies, at which a high pressure amplitude can be obtained by a small volume velocity excitation.

Beginning in the 1960s, several experimental setups have been developed. As the impedance is the ratio of pressure and volume flow at a given cross section of the duct, both quantities are to be measured simultaneously. In contrast to the sound pressure, the acoustical volume flow cannot easily be measured and various setups have been developed to overcome this problem. In the following, only a very short review of the main principles is given, a thorough discussion can be found in the literature, [17] and more recently [50].

While few researchers have accepted the challenge of measuring both sound pressure and acoustical volume flow at the time [52], most struggles have been put into the development a reflection-free volume velocity source to sinusoidally excite the air column. A measurement of the resulting sound pressure is then sufficient, since it will be proportional to the impedance. Successful realizations of such a source have been constructed from a loudspeaker driven pressure chamber with a very narrow outflow channel [173, 9, 30, 138, 149]. However, these setups require an efficient mechanical decoupling of loudspeaker and measurement object, because otherwise wall vibrations can dramatically influence the results. The latter must be long and thin enough to acoustically decouple pressures at the outflow end and inside the pressure chamber by means of wall friction. Alternatively, the air column can be excited by a piezo-electric element, which can be designed to work as a reflection free source [17, 41].

Another method, which does not require a decoupling from the source, consists of an connection duct that is equipped with two or more spaced microphones. By the use of calibration geometries with a known acoustical response, the volume velocity information can be obtained from the pressure signals and their delays [71, 93, 50]. The connection duct must have the same input cross section as the calibration objects and the object under test.

### 2.2.2 Device

For the impedance measurements in this study, the commercially available impedance measurement system “BIAS” [138] has been used. The impedance head uses the principle of a constant volume flow source. A bundle of capillaries provides the high acoustical resistance that decouples the pressure chamber from the measurement object. The setup comprises two microphones, one in the pressure chamber and one at the measurement cross section<sup>20</sup>. The measurement software uses

<sup>19</sup>E.g. Eq. (10-5.6) in [141]

<sup>20</sup>For details on the BIAS measurement head see <http://www.bias.at/> (last viewed Nov. 23rd 2013)

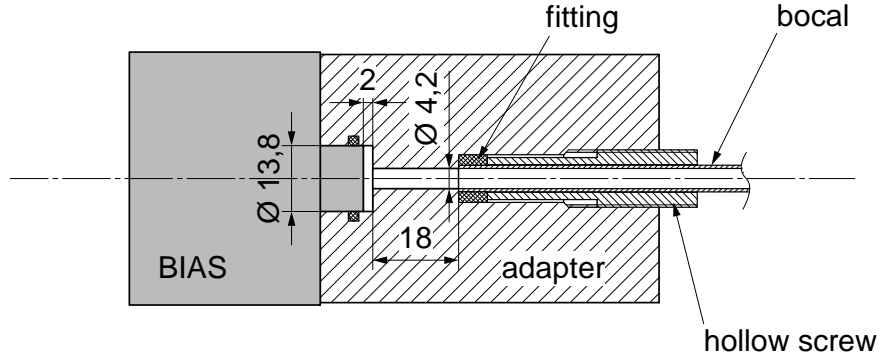


**Figure 2.7** Sketch the adapter to connect a bassoon bocal to the BIAS measurement head.

a factory calibration on two cylindrical calibration cavities with different lengths, the calibration procedure is described in [149]. For this study, the factory calibration has been successfully verified on cylindrical tubes of various lengths in an anechoic chamber.

The impedance measurement system has recently been used several scientific studies on brass wind instruments [29, 27, 95, 26], and woodwinds [149, 117].

As it is designed for brass instruments, the cross section where input impedance is measured is 12 mm in diameter. In order to measure bassoons with an input diameter of approximately 4 mm, an adapter has been built.

### 2.2.3 Calibration and Correction

All impedance data shown in this study rely on the factory calibration of the “BIAS” software. However, in the post-processing of the obtained impedance curves an additional correction procedure has been performed, to numerically eliminate the acoustical effect of the adapter.

As seen from the bocal, the adapter must be a diverging duct to match the impedance head’s diameter. Such an enlargement acts as an acoustical compliance in parallel to the measurement object and introduces additional damping. As the volume is critical the adapter should be a short stepped tube, rather than a long conical waveguide with a smooth diameter transition.

The adapter was designed to have a very short cylindrical section of 13.8 mm diameter and 2 mm length, that merges abruptly into a second smaller cylindrical section of 4.2 mm diameter and 18 mm length (Fig. 2.7).

To correct for the errors introduced by a diameter mismatch Fletcher [60] proposed to subtract an impedance correction of the form  $\bar{A} \sqrt{\omega} + j \bar{B} \omega$  from the measurement result of a calibrated setup. In contrast to the cases discussed there, in this study the diameter of the impedance head is *larger* than that of the measurement object. To correct for the errors introduced by this situation, a similar approach of using an empirical impedance correction has been chosen. Instead of a series impedance  $Z_{\text{ser}} = j \bar{B} \omega$ , a parallel impedance  $Z_{\text{par}} = -j \bar{B} / \omega$  was used to correct for the discrepancies between measured and theoretical impedance peak frequencies.

Adding a negative impedance  $Z_{\text{par}}$  in parallel eliminates the compliant effect of a cavity with a volume  $V_{\text{adp}}$  and an acoustic compliance  $V_{\text{adp}} / (\rho c^2) = 1 / \bar{B}$ . This correction is used to remove the effect of the first wide and short section from the measurement.

The second thin and long section is modeled as a cylindrical duct segment with radius  $r_{\text{adp}}$  and length  $l_{\text{adp}}$  characterized by the transmission matrix  $T_{\text{adp}}$  according to Eq. (2.17). By rearranging Eq. (2.9), the effect of this second section is subsequently removed from the measurement result.

The two step correction procedure is written

$$Z' = \frac{Z_{\text{meas}} \cdot (-Z_{\text{par}})}{Z_{\text{meas}} + (-Z_{\text{par}})} \quad (2.57a)$$

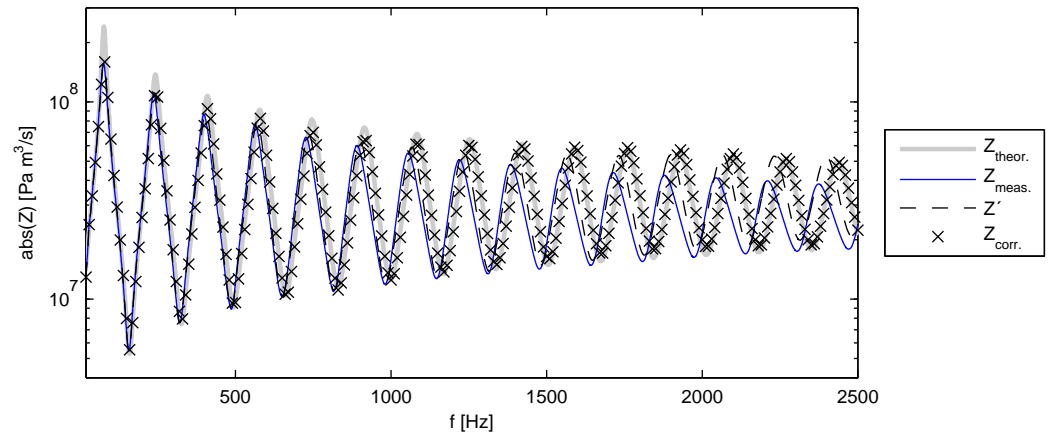
$$Z_{\text{corr}} = \frac{B_{\text{adp}} - Z' D_{\text{adp}}}{Z' C_{\text{adp}} - A_{\text{adp}}}, \quad (2.57b)$$

where  $Z_{\text{meas}}$  is the measured impedance of the object with attached adapter as obtained by the “BIAS” system, and  $Z_{\text{corr}}$  is the corrected impedance, that is assumed to be equal to the input impedance of the object alone.

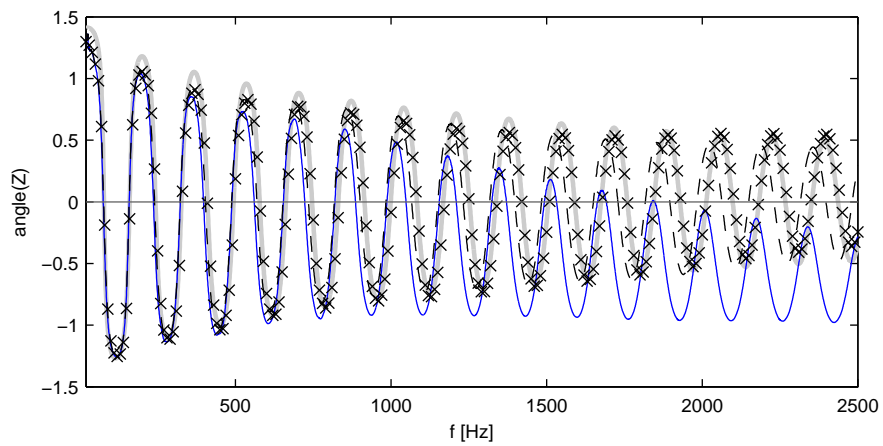
According to the above considerations, the correction is completely defined by a corrective volume  $V_{\text{adp}}$  and the radius and length  $r_{\text{adp}}$ ,  $l_{\text{adp}}$  of the equivalent connector. Assuming  $r_{\text{adp}}$  to equal the actual physical radius of the adapter, the other two parameters  $V_{\text{adp}}$  and  $l_{\text{adp}}$  have been determined by fitting theoretical impedance curves to measurement data of simple well-defined reference objects. The trial and error procedure that Fletcher proposed [60] has been used and the calibration objects were cylindrical tubes with an inner diameter of 4.2 mm. This is very close to the actual input diameter of a bassoon bocal. The steps of the correction procedure for a tube of 1 m length is illustrated in Fig. 2.8. Using open tubes of different lengths, the correction parameters  $V_{\text{adp}}$  and  $l_{\text{adp}}$  have been determined to be  $V_{\text{adp}} = 213.7 \text{ mm}^3 \pm 8\%$  and  $l_{\text{adp}} = 15.7 \text{ mm} \pm 9\%$ .

After the correction with these parameters, the discrepancy of the impedance peak frequencies was  $\pm 15$  Cent in frequency range from 70 Hz to 2.5 kHz (Fig. 2.9). This is a small, but certainly significant discrepancy which is critical in the estimation of the fundamental frequency of a musical instrument. A way to overcome this problem might be the design of an impedance probe with a smaller or no diameter mismatch [101], or probably to employ a more elaborate technique [159, 128, 110] in the modeling of the adapter in the correction procedure.

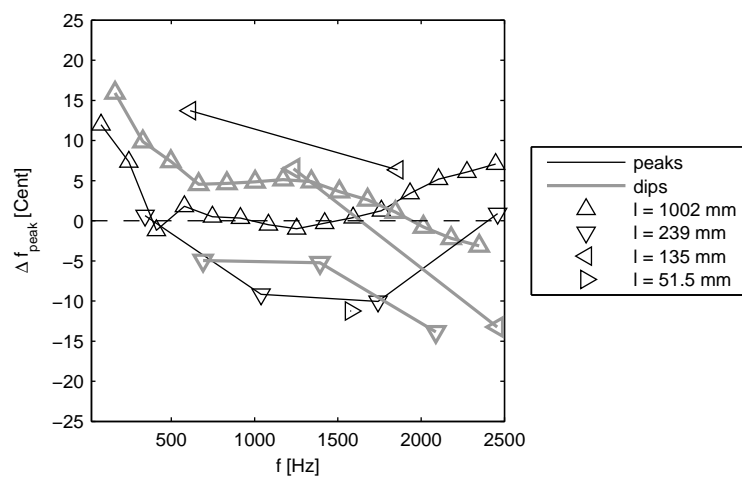
Nevertheless, the impedance measurement setup used here is suited to study general characteristics of the bassoons air column, to show differences between instruments and to monitor relative changes in the impedance spectrum due to geometrical modifications. Practical issues of the measurement with respect to possible causes of error are discussed in the next section.



(a) Magnitude



(b) Phase

**Figure 2.8 Steps of the Calibration Procedure****Figure 2.9 Deviation between measured and theoretical impedance extrema, from four cylindrical open tubes with radius  $r = 2.1$  mm and varying length  $l$ .**

## 2.3 Comparison of Theory and Experiment

This section is dedicated to compare theoretical and measured acoustic impedance spectra of several duct geometries.

First, the accuracy of the measurement is addressed, with respect to real woodwind geometries. With the knowledge of experimental uncertainty, numerical calculations of the input impedance basing on precise measurements are juxtaposed and the discrepancies are discussed.

### 2.3.1 Repeatability and Measurement Uncertainty

In a practical situation the result of an input impedance measurement is influenced by many factors. Regarding a bassoon measurement important influencing factors are

**tiny leaks** : imprecisely fitted joints, badly closed keypads

**mounting offsets** : joint of measurement device and measurement object

**climate** : temperature and humidity of the air column

**noise** : acoustical noise in the ambiance

Noise can easily be avoided in a laboratory measurement. Furthermore, the “BIAS” impedance head is a system designed for the use in musical instrument workshops. It features a high excitation level and low sensitivity of the measured impedance to moderate acoustic noise above 40 Hz outside of the instrument.

### Avoiding Temperature Gradients in the Air Column

The temperature, moisture content and gas composition of the air column have an effect on the speed of sound and thus on the peak frequencies in the impedance measurement. The moisture content of the air has a small effect on the plane wave attenuation in a tube [159]. The O<sub>2</sub> content in exhaled air varies between 20 to 15 %, while the CO<sub>2</sub> content varies from 2.5 to 8.5 % during exhaling, which introduces a frequency decrease around 20 % [67]. However, these effects occurring during the performance are not studied here. In fact, the temperature is of interest here mainly to avoid systematic errors in measurements of acoustic impedance peak frequencies, due variations in the speed of sound, and to estimate times of acclimatization for an instrument air column after a climate change. If the radius of the duct is about ten times larger than the viscous boundary layer thickness  $\delta_v$ , this effect can be neglected.

The air temperature, on the other hand, is important. As the wavelength  $\lambda = c/f$  is constant, the frequency shift due to a temperature change is given by  $f(T_1) = f_0 \cdot (c(T_1)/c_0)$ , where  $f_0, c_0$  are frequency and speed of sound in an arbitrary reference condition. This relation must be used to rescale the frequency axis when comparing impedance curves measured at different temperatures. Benades linear approximations [19] for the speed of sound (see Eq. (2.39)) predict a relative pitch change of 2.85 Cent/°C.

As the viscous boundary layer thickness increases with temperature, damping of the impedance peaks increases as well. By means of transmission line simulation, the relative change in impedance magnitude is estimated to be approximately -0.3%/°C, for impedance maxima at low frequencies<sup>21</sup>. To assure consistency in repeated measurements, there should be no temperature gradients within the air column. As a bassoon is typically manufactured from wood and thin metal sheets, it will take some time, until the instrument and air column are in temperature equilibrium with the surrounding

<sup>21</sup>On a simple cone of  $l = 2.56$  m,  $r_1 = 2.6$  mm and  $r_2 = 20.2$  mm, the deviation from linearity in the impedance magnitude is  $\pm 0.01\%$  within the frequency range from 50 to 3000 Hz.

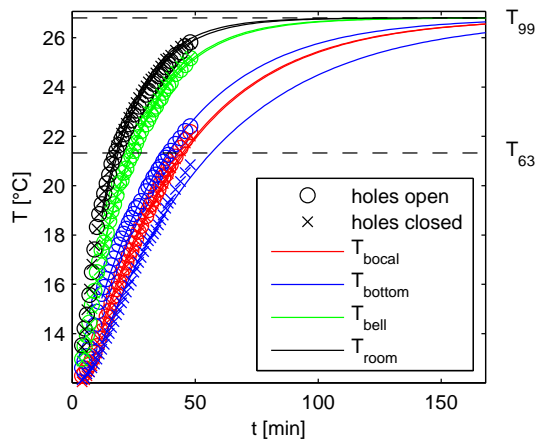


**Figure 2.10** Temperature change at different positions in a bassoon bore after a temperature jump of the ambient temperature from 12 to 27 °C°

air. For a quite drastic temperature change of 15 °C, from 12 to 27 °C, the temperature 100% rise time has been estimated to be about 7 hours, based on measurements of the first 60 minutes after the temperature jump (Fig.2.10). This experiment was performed twice, on a bassoon with all holes open (fingering F3) and all holes closed (fingering Bb1), with sensors at different locations inside the air column, and one reference measurement in the room. The temperature inside the instrument was measured using small PT-100 resistance temperature detectors hanging into the air column. Compared to the reference temperature change in the room, the temperature in the bell is only slightly retarded, whereas inside the bocal, the temperature change time constant is approximately doubled. In the butt, at the position of the u-shaped bend, the temperature changed even slower than in the bocal, for the closed-holes fingering.

Any mounting offsets will have a large effect on the consistency of the measurement. Especially for high impedance objects with a small diameter, such as a bassoon bocal, it is critical to place the object precisely at the same position relative to the reference plane, to which the impedance head is calibrated. Another typical problem in bassoon impedance measurements associated with the mounting, is the occurrence of tiny leaks at the junction of bocal and measurement head.

To minimize these possible causes of error, the impedance adapter used here has a dead stop for the bocal tip and a squeeze-type gasket to seal the joint, assure a centered position and air-tight mounting (Fig. 2.7).

### Influence of Temperature on the Input Impedance

The influence of temperature on the impedance peaks has been tested by a study of repeated measurements [135].

Throughout a period of two months, impedance measurements of five fingerings (Bb1, Eb3, Eb3 + Eb-Key, F3, and F4) on four bassoons were carried out at random temperatures between 19.3 °C and 24.8 °C. All instruments were stored in the measurement room throughout the complete study. The room climate changed slowly, such that temperature equilibrium in the air column was assumed for each single measurement.

From 50 independent measurements on each bassoon and fingering, the impedance peaks were analyzed. A binning routine was used to concatenate the scattered measurement values of each impedance peak and subsequently the linear correlation of peak frequency and magnitude with the air temperature in the room was calculated. Averaged over the observed frequency range from

50 Hz to 3 kHz, the pitch shift per  $^{\circ}\text{C}$  temperature change was  $2.85 \text{ Cent}/^{\circ}\text{C}$  ( $\sigma = 0.54 \text{ Cent}/^{\circ}\text{C}$ ), which is in very good agreement with theory (see Fig 2.11(a)).

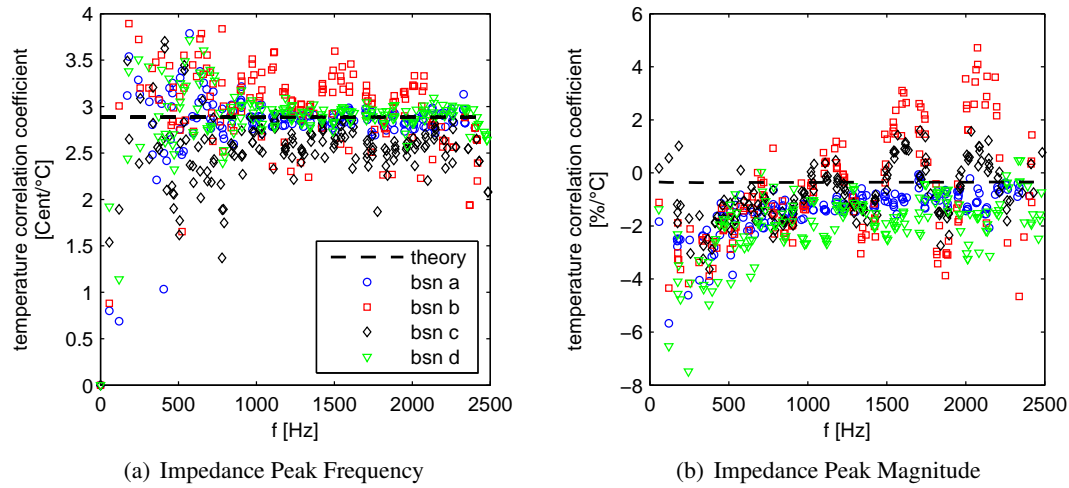


**Figure 2.11 Influence of Temperature on the Input Impedance of Bassoons**

With the same procedure, an influence of temperature on the impedance peak magnitudes has been observed (Fig 2.11(b)). In the lowest frequency range, up to 1 kHz, the correlation coefficient was preponderantly observed to be negative, which means that the peak magnitudes decrease with increasing temperature. This is generally in agreement with theory, but the observed correlation is much larger. On the other hand, some peak magnitudes above 1 kHz were observed to *increase* with temperature. A frequency dependent pattern was especially apparent for two bassoons, independently of the fingering, whereas the other two did not show this behavior. A possible superimposing or masking effect is unclear. Ignoring the obviously non-random effects and averaging over all measurements, the mean peak magnitude change is  $-1.14 \text{ } \%/^{\circ}\text{C}$  ( $\sigma = 1.41 \text{ } \%/^{\circ}\text{C}$ ).

In any case, the measured correlation of impedance peak magnitude is significantly stronger than predicted by transmission line theory.

### Study of Repeatability

A measure for the repeatability is the observed dispersion of peak frequencies. To verify this, all measured peak frequencies have been related to a reference temperature of  $21.7^{\circ}\text{C}$ , which was the median from 50 measurements within a range of  $19.3^{\circ}\text{C}$  to  $24.8^{\circ}\text{C}$ . After this correction procedure, most of the observed peak frequencies and magnitudes were normally distributed. The maximum standard deviation observed is 6.5 Cent for the peak frequencies and 13 % for the peak magnitudes. Concerning the peak frequencies, a frequency dependence is clearly observed (Fig. 2.12): The dispersion decays with frequency. The decay however, seems to be related with the ordinal number of the resonances, rather than with the absolute frequency, as can be seen from comparison Figs. 2.12(a) and 2.12(b), which show measurement results of bassoon bores with different acoustic lengths. At frequencies above 500 Hz, the standard deviation is  $< 3 \text{ Cent}$ .

The frequency dependence of the magnitude dispersion is similar to that of the frequency dispersion, but much larger: Averaging over frequencies the standard deviation is 4.60 % ( $\sigma = 2.18 \text{ } \%$ ).

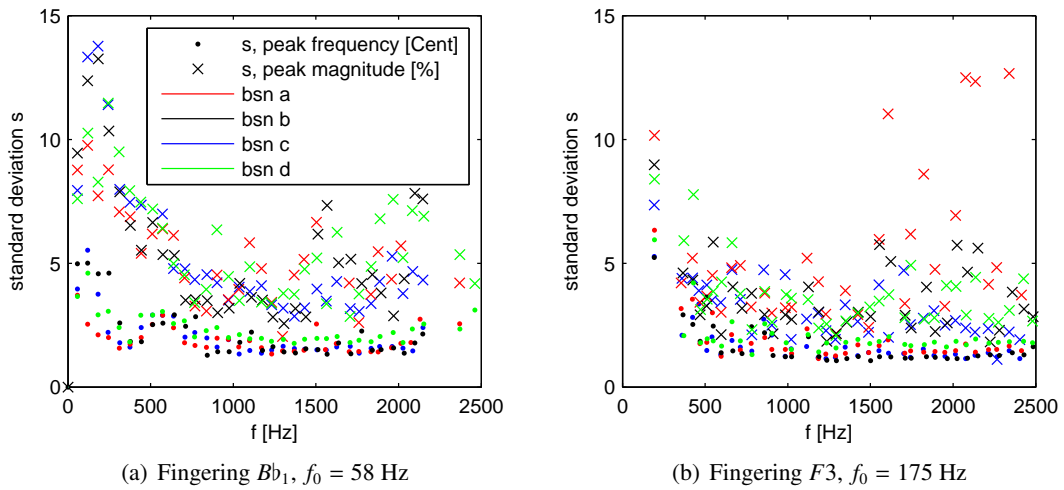


Figure 2.12 Dispersion of Input Impedance Peak Data (Frequency (·), Magnitude (x))

### Variance between Instruments

In the light of this measurement uncertainty, it is interesting to compare the variability of impedance curves measured on bassoons of the same type made by different manufacturers. Since the acoustic impedance spectra of musical wind instrument's resonators provide an objective measure of the instrument alone, it is tempting to relate the produced sound or performance characteristics to the measured input impedance and try to obtain objective measures for the “quality” of a musical instrument from it. Many researchers have tried and still try to tackle this topic, as a progress in this problem would provide specific guidance how to build good instruments.

This however seems to be very difficult, as it has been observed, that musical wind instruments of the same type, which greatly differ in their musical performance, seem to have very similar acoustic properties [9].

Although the measurement and calculation of input impedance is a standard technique in the research of musical wind instruments, only very little experimental data were published the literature, and discussed with respect to the inherent measurement uncertainty.

The aim of this subsection is to give an idea about the order magnitude of variability found in the acoustical design of bassoons from different manufacturers. This comparison further allows to estimate the reliability of the *complete experiment*, as a combination of measurement device, mounting, measurement object and measurement conditions with respect to the frequency dependent standard deviations.

Scientific studies focusing on the measurement technique provide some discussion of measurement errors [148, 50, 41], but are mostly focused on simple calibration objects, such as cylindrical tubes. This may be sufficient when measuring simple unbranched wind instrument resonators. For woodwind instruments with tone-holes, the measurement uncertainty may be significantly larger.

Keefe [96] and Dalmont *et. al* [46] have carried out careful experimental studies on single tone-hole configurations in a cylindrical main duct and determined correction parameters for a simplified tone-hole representation in a one-dimensional model of plane-wave propagation. Their results have been verified to some extent by Lefebvre [110], by use of a three-dimensional Finite-Element Model.

Papers with a detailed discussion of impedance measurements on real woodwind instruments are relatively rare.

In a pioneering study, Backus [9] compared three bassoons and stated that the impedance “curves for the three instruments were quite similar for a given note” and the differences “may be musically



significant, but at this time we cannot say”. Cronin and Keefe [37] have carried out measurements on bassoons to investigate the role of auxiliary fingerings. Although not focusing on differences between specific instruments, their work is interesting as it provides experimental evidence of the general functioning of auxiliary fingerings, which shift dedicated higher air column modes such that a change in the oscillating regimes of reed and resonator is favored and a desired pitch and/or tone-color change is achieved.

Wolfe *et. al* [177] provide a comparison of flute impedance spectra together with sound files [175]. They explicitly mention the limited possibilities to interpret impedance spectra with respect to details in instrument performance or sound characteristics. In this context, their data has informative character.

Later, Wolfe and Smith [176] have extended their investigation of flute impedance spectra to a discussion of cut-off frequencies of several flute designs and point out possible causes for timbre differences. They give impedance curves with standard deviations, but their work does not aim to reveal sensitive differences between individual instruments of the same type, due to their making. This objective has been tackled in an excellent comprehensive study on didjeridoos by Smith *et. al* [154], who were able to relate acoustical properties of the resonator to a subjective quality ranking by a broad panel of musicians. This complex task was facilitated by the largely differing design of individual didjeridoos which are usually shaped in a natural process.

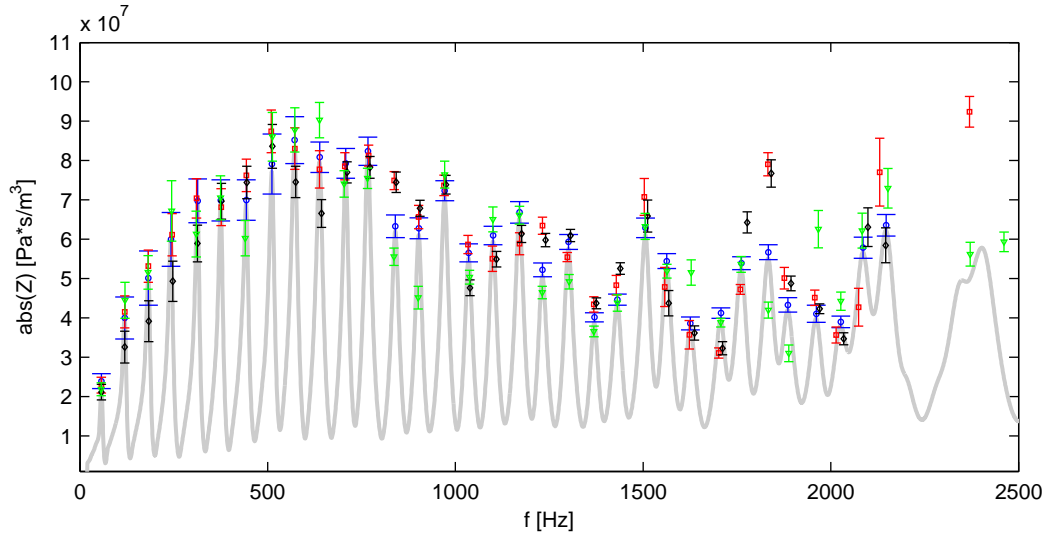
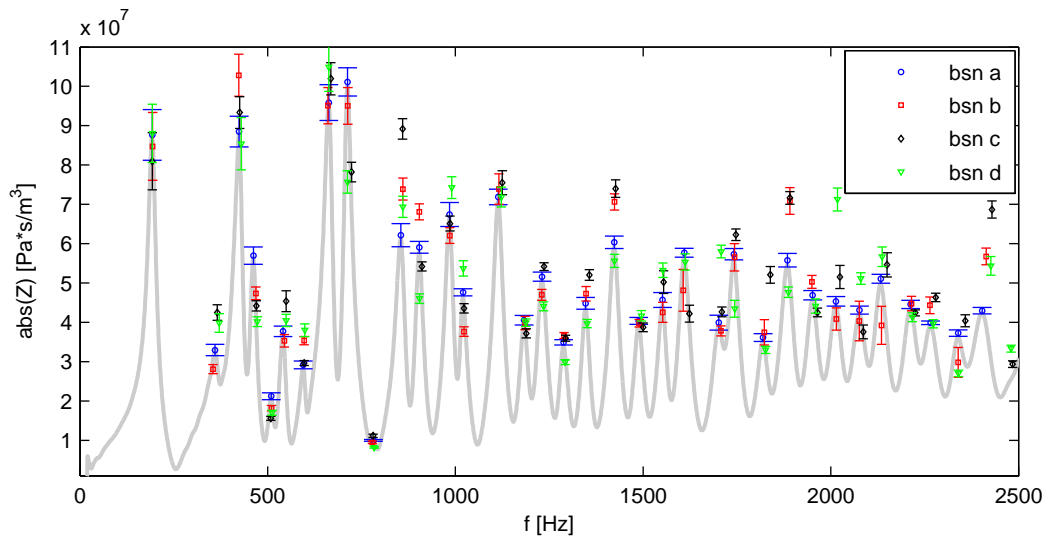
Macaluso and Dalmont have reviewed acoustic design principles for wind instruments and presented a trumpet air column design featuring near-perfect harmonicity [116].

For air columns in case of the modern German bassoons, regardless of which manufacturer, only subtle differences are found. The generic acoustic design of this instrument has not changed since 1920 [10, 170].

In this context, the consistency of woodwind instrument manufacturing has been studied by Mamou-Mani *et. al* [117], who compared the impedance curves of five nominally identical oboes and stated that these differed by 2% in peak frequency and 30 % in impedance peak magnitude. In this paper, however, an analysis of experimental uncertainty is missing.

From the set of 50 repeated measurements recorded over a period of two months within the present work, the impedance peaks mean values and standard deviations are plotted in Fig. 2.13. As mentioned above, all measurements were obtained at various temperatures and subsequently rescaled to the same reference temperature.

The plot reveals that all curves are generally similar and the fundamental air column mode is well aligned for all four bassoons. In detail, however, differences are observed, as single peaks deviate largely from the mean curve. These large individual discrepancies are for most peaks greater than the standard deviation, which implies that only a few measurement repetitions are needed to confirm the peak magnitude, whereas the measured peak frequency is quite consistent, apart from the temperature effect.

(a) Fingering  $Bb_1$ ,  $f_0 = 58$  Hz(b) Fingering  $F3$ ,  $f_0 = 175$  Hz**Figure 2.13 Comparison of Input Impedance curves of 4 different Bassoons**

### 2.3.2 Comparison of numerical and experimental Impedance Curves

For narrow cylindrical tubes of various lengths, the discrepancy between measured resonance frequencies and those predicted by plane-wave theory has been determined to be  $\pm 15$  Cent with the setup used in this study. The random error of the experiment has been verified in a study of repeated measurements ( $n=50$ ) to be  $< 5$  Cent for the peak frequencies and  $< 15\%$  for the peak magnitudes. In this section, the discrepancy between theoretical and measured impedance curves is discussed, for few selected fingerings on a modern german bassoon.

#### Geometrical measurements

The theoretical approach requires a precise information on the geometry of the duct, which is difficult to obtain for real musical instruments. The numerical bassoon impedance curves that will be presented in this section are based on precision measurements of the inner diameter of the

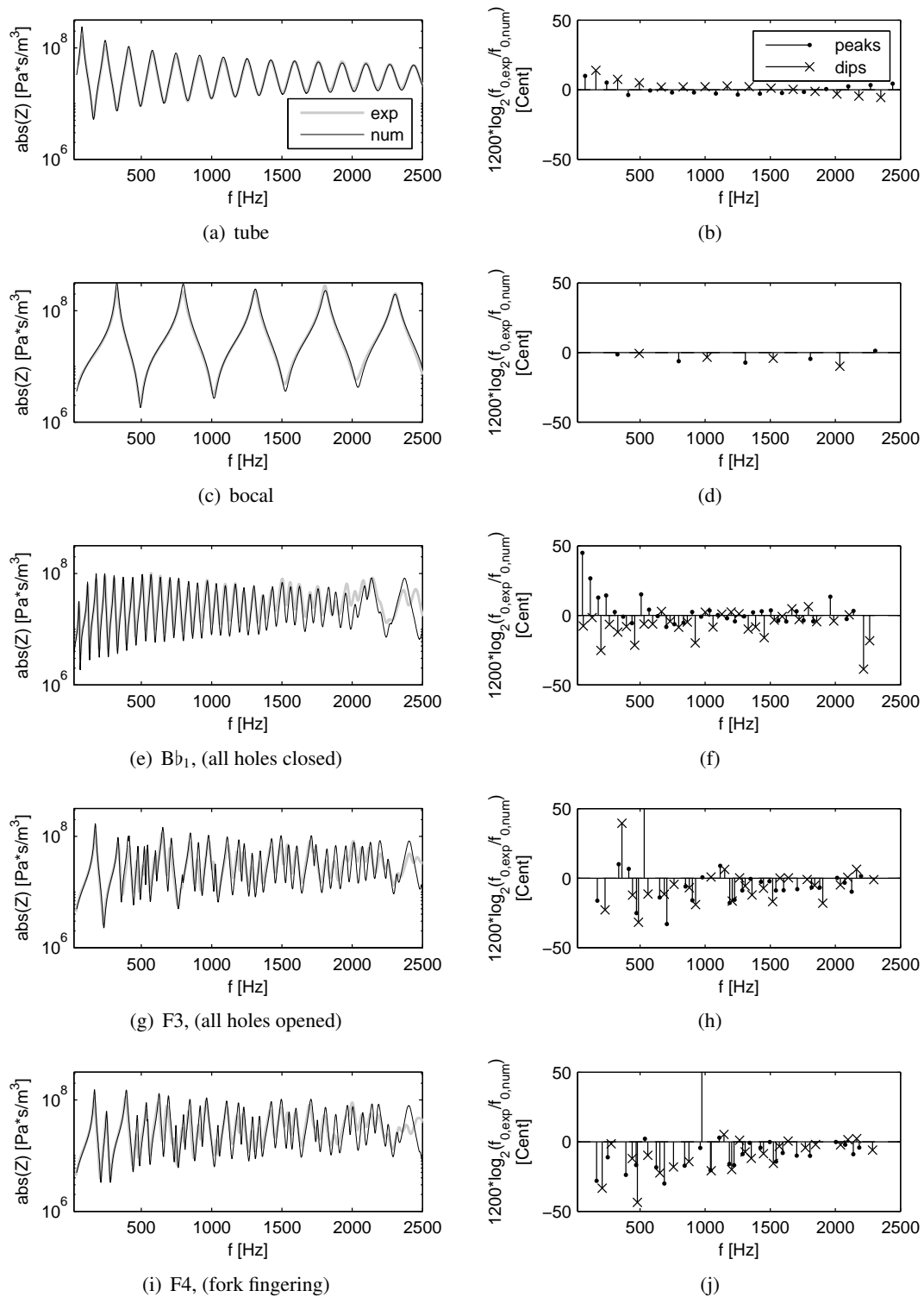


**Figure 2.14** Comparison of numerical and experimental input impedance spectra of (a,b) a thin tube ( $r = 2.1$  mm,  $l = 1002$  mm), (c,d) a straight bocal ( $r_1 = 2.1$  mm,  $r_2 = 4.4$  mm  $l = 328$  mm), (e,f) a bassoon with all holes closed (Bb<sub>1</sub>,  $f_0 = 58$  Hz), (g,h) a bassoon with all holes open (F3,  $f_0 = 175$  Hz), and (i,j) a bassoon with a fork fingering (F4,  $f_0 = 353$  Hz). The impedance modulus is shown in the left column of graphs (a),(c),(d),(g),(i), the frequency deviation in Cent between the numerical and experimental impedance extrema is shown in the right column of graphs (b),(d),(f),(h),(j), for the respective cases.

bore with a spatial resolution of 5 mm along the main axis. Precision split-ball probes<sup>22</sup> with a repeatability of 1  $\mu\text{m}$ , have been used to measure the diameter  $d$  of the bassoon bore in the range of  $4\text{ mm} < d < 20\text{ mm}$ . This corresponds to the bocal (a straight bocal was measured), the wing and half of the butt down to the u-bend. The accuracy of the split-ball measurement is estimated to be  $\pm 5\text{ }\mu\text{m}$ . To estimate the diameter of rest of the bore down to the bell, a bassoon of the same type<sup>23</sup> was sawn into two halves and the diameter has been obtained from a laser surface scan [146]. The tone-hole dimensions were determined by diameter gages. If the tone-hole axis was not perpendicular to the main axis of the bore, the average chimney height has been used for the TMM model. The bore and all holes were assumed to be cylindrical, although this does not hold true, strictly speaking: The measurements revealed discrepancies from the circular cross sections in the bocal, due to the soldered seam and in the wooden parts, due to warping. Some hole chimneys are rather cones than cylinders. All these discrepancies were neglected here, for reasons of simplicity. However, their influence may be non-negligible: A measurement error of 50  $\mu\text{m}$  in diameter near the bocal tip with a diameter of 4 mm introduces a local error of 1.25 % which corresponds to 22 Cent.

A juxtaposition of measured and calculated results is provided in Fig. 2.14, for geometries with increasing complexity. Starting with a narrow cylindrical tube (Fig. 2.14(a)), which was used as a calibration object (see section 2.2.3), results for a bocal (Fig. 2.14(c)), a bassoon with all holes closed (Fig. 2.14(e)), all holes opened (Fig. 2.14(g)) and with a fork fingering (Fig. 2.14(i)) are presented.

For simple geometries without side-branches, the agreement between numerical and experimental impedance maxima is fairly good Fig. 2.14(a) and 2.14(c). For more complex geometries with toneholes, the observed discrepancies are much larger than the measurement uncertainty, especially in the low frequency range, below 500 Hz. A possible reason might be the simplistic approach of tone-hole modelling: At the junctions of main bore and tone-holes, the air is suddenly expanded. Details such as oblique tone-hole chimneys and interactions of open tone-holes are not modeled, but may be important as well [98]. At the junctions of main bore and tone-holes, the air is suddenly expanded. Details such as oblique tone-hole chimneys and interactions of open tone-holes are not modelled, but may be important as well [98]. At higher frequencies, in particular, the damping of the air-column modes appears to be underestimated in the model. This may be due to the fact that the viscous effects have been estimated by use of acoustic boundary layer theory which assumes perfectly smooth walls. For the case of the bassoon, this assumption is clearly not met in all parts of the bore. Whereas the wing and upper butt usually have a very smooth, polished surface, the bocal, the wooden parts of the butt, the long joint and bell, as well as most tone-holes have rather rough surfaces. This might be taken into account by increased effective boundary layer thicknesses. Apart from that, the humidified air from the players lungs will condense at the walls in playing conditions. Further sources of error might be viscous losses at sharp edges where the tone hole chimneys penetrate the main bore.

However, a general family resemblance is observed for a broad frequency range, and the envelopes of the curves are similar. This gives confidence in using the simple modeling approach to predict relative changes in the air column resonances due to geometrical changes of the bore. With some efforts in calibration, the technique can be successfully used for the design of woodwind instruments [100, 74]. Due to its low computational complexity it is very well suited for the use in optimization routines [143, 140, 26, 110].

<sup>22</sup>DIATEST M2-T, courtesy of DIATEST Herrmann Koeltgen GmbH, Darmstadt, Germany

<sup>23</sup>Standard Model Wolf S2000

## 2.4 Harmonicity Analysis of the Resonator

In the previous sections it has been shown, that the impedance curve obtained from measurements and a simple one-dimensional waveguide model match well. The importance of the acoustical properties of resonator for the sound generation depends strongly on the harmonicity of the air-column resonances. These will be crucial for the resulting pitch and spectral coloration of the stationary sound. Furthermore, very subtle differences in resonance frequencies may play a crucial role for the transient evolvement of a stationary sound.

In this section attempts are made to analyze the “harmonic content” of the bassoon air column. This will be helpful in subsequent discussions of the interplay of musician, reed and resonator in Chapter 5.

### 2.4.1 The Role of the Resonator

The effective acoustic length of the air-column of woodwinds is shortened by opening sideholes in the main bore. For cylindrical woodwinds, it is attractive to describe the air-column as one or more harmonic oscillators, depending only on the effective length. This however fails for conical woodwinds, and especially for the bassoon which has an irregular bore profile, and various tone holes of very different shape. The composition of air-column resonances is therefore quite complex and the system behind the fingering is difficult to comprehend in the higher registers [104].

In Fig. 2.13 measured impedance spectra are shown in which the air-column resonances appear as peaks. The resonance frequencies clearly visible in these plots, however, do not provide a precise estimation of the sound fundamental frequency, for two reasons. Firstly the reed has been taken off the bocal to measure the impedance at the input cross section of the tube. As an approximation, a reed-equivalent volume is taken into account, which is larger than the geometrical volume [125, 43]. This shifts the resonances downward in frequency.

Secondly it is not necessarily one resonance, that determines the fundamental frequency, but it is the result of a compromise between a few resonances. If there are pronounced, nearly harmonic, damped resonances present in a linear oscillator which is coupled to a highly nonlinear excitation, the complete system settles in a stable phase-locked periodic oscillation [58] with a contribution of all resonances. Benade called this mode-locked case a *regime of oscillation*.

Many attempts have been made for a frequency domain based estimation of the sounding frequency of a wind instruments [125, 173, 43, 101], but these two aspects are still not well established. On the other hand, more elaborate numerical techniques used for sound synthesis also fail to model the excitation with the precision required for the determination of the fundamental frequency [172, 147, 72, 102, 153].

### 2.4.2 The reed equivalent Volume

The discussion of harmonicity based on impedance measurements starts with the proper choice of a reed equivalent volume. For the case of the bassoon, an equivalent volume of  $1.9 \text{ cm}^3$  is reasonable [125, 107, 55]. This volume is approximately twice its geometric volume. The increase accounts to the fact that the reed blades are not rigid boundaries, their motion induces an additional air-flow, which can be considered an additional effective volume.

A reed equivalent cylindrical volume of 3.6 mm in diameter and 47 mm length is “added” numerically to the measured input impedance in the bocal cross section by use of Eq. 2.9. This volume prolongs the air column and lowers the resonances. Further it damps the higher resonances above 500 Hz (Fig. 2.15). Due to this correction for the reed equivalent volume, not only the fundamental

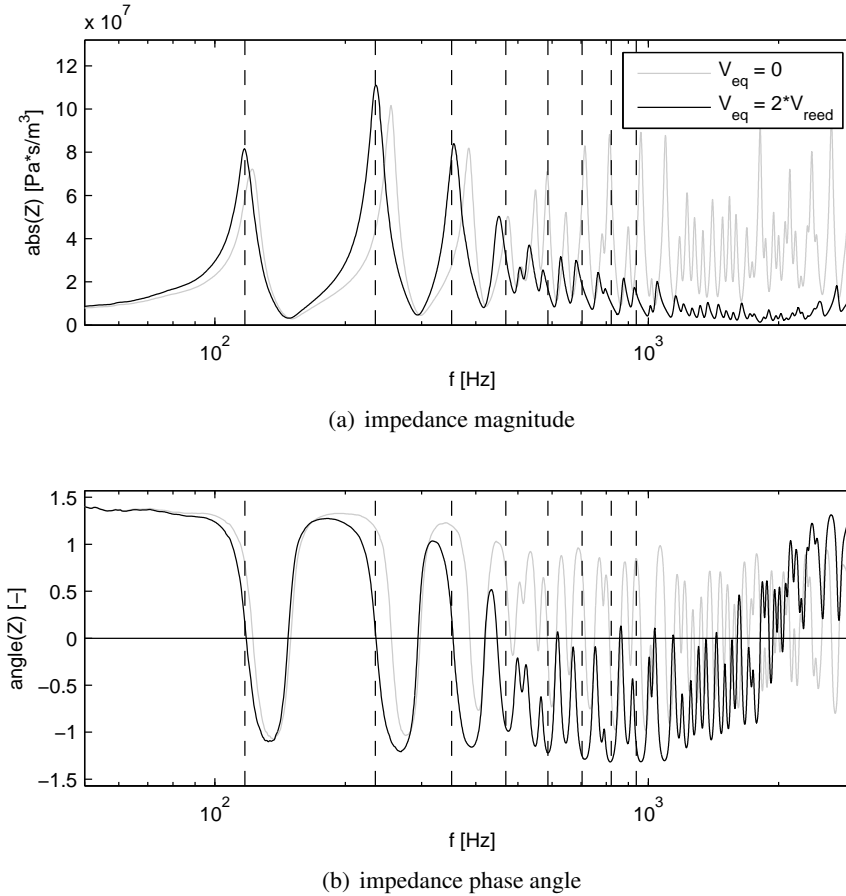


**Figure 2.15** Effect of the reed equivalent volume  $V_{eq}$ .  
**gray:** measured input impedance at the bocal tip;  
**black:** measurement corrected by a reed equivalent volume.  
 The vertical dashed lines mark the harmonic frequencies for Bb2,  $f_0 = 117.3 \text{ Hz}$

resonance frequency fits better the nominal<sup>24</sup> sounding frequency  $f_0$ , but also the harmonicity of the air-column is increased for the first three resonances.

### 2.4.3 Harmonicity Map

To represent the resonance properties of a woodwind over its tonal range, i.e. for all standard fingerings corresponding to notes of the equally tempered scale, it is useful, to rescale the frequency axis. A good overview gives a contourplot plot of impedance modulus  $|Z|$  over non-dimensional harmonic frequencies  $\tilde{f}$  over the logarithmic nominal sounding frequency  $f_0$ , corresponding to this fingering. The harmonic frequencies  $\tilde{f} = f/f_0$  are the measured frequencies  $f$  normalized by the fundamental frequency  $f_0$ . The magnitude of the impedance is plotted in a grayscale. The dark regions in this plot indicate the impedance peaks and their alignment with the harmonic frequencies  $n f_0$ . Air-column resonances close to harmonics can support the regime of oscillation. Another condition for this so-called mode-locking is, that the impedance magnitudes of these modes must be sufficiently large [58].

The resulting graphical representation (Fig. 2.16) is called “impedance map” here. It gives a qualitative overview on how many impedance peaks are potentially contributing to the regime of

<sup>24</sup>This is the expected frequency corresponding to the fingering

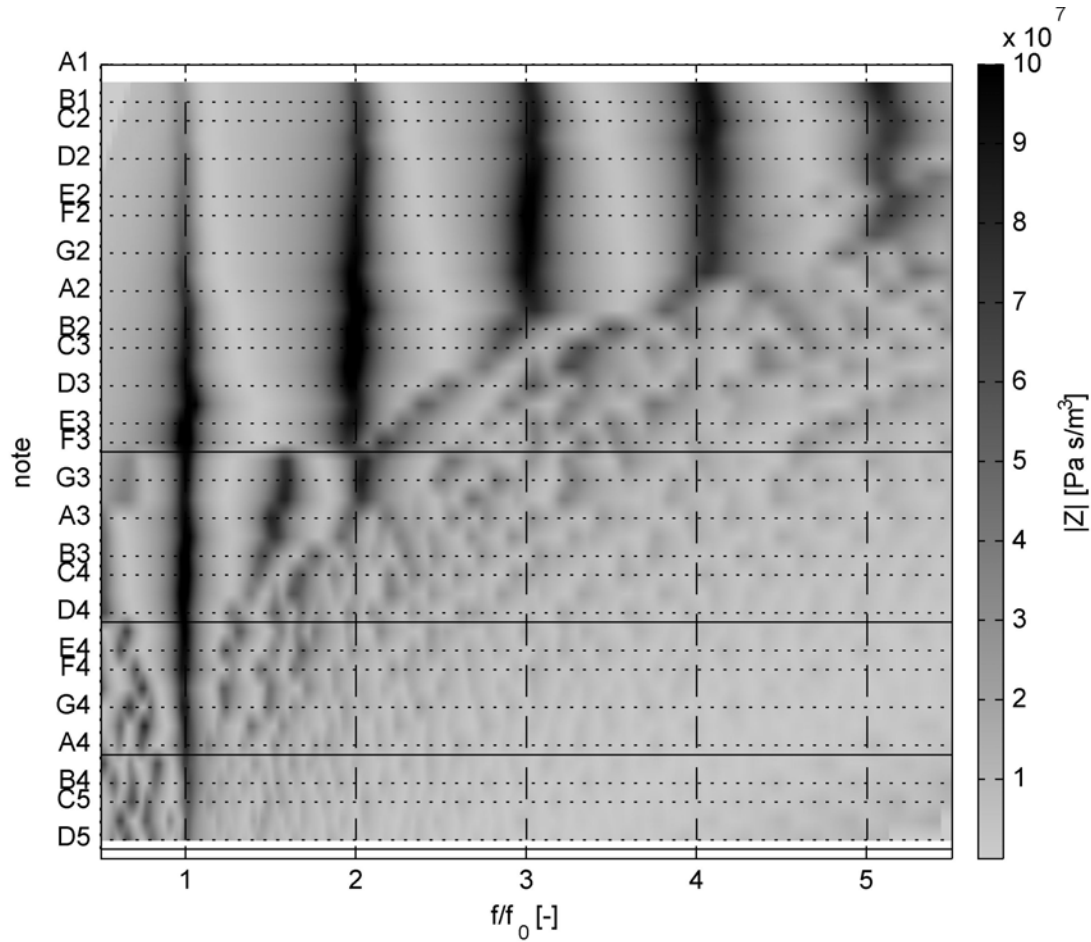


**Figure 2.16** Impedance map. The gray scale provides information about the magnitude of the impedance  $|Z|$

oscillation at a given frequency  $f_0$ . Harmonicity is usually measured as the logarithm of a frequency ratio. To better display the deviations of the impedance peak frequencies from the integer harmonic frequencies, the impedance map is rescaled, such that only the range of  $\pm 100$  Cent<sup>25</sup> around each harmonic frequency is shown. In the light of another condition for mode-locking, that the modes involved must be “nearly harmonically related” [58], this provides a zoomed view into each harmonic and visualizes more clearly the inharmonicity of the impedance peaks. To qualitatively meet the previous condition that the mode amplitudes must be large, the dynamic range of the plot in  $|Z|$ -dimension is limited to 6 dB. In a work on bore optimization of brasses, a similar plot has been proposed by Braden *et al.* [26], which was called an inharmonicity plot<sup>26</sup>. In line with this idea, the plot in fig. 2.17 is called a *harmonicity map* here, because it maps the harmonicity of all fingerings corresponding to the chromatic tonal range of the woodwind.

In Chapter 5 will be shown, that the harmonicity map is useful to understand several aspects of bassoon performance by the analysis of detailed and comprehensive artificial mouth measurements.

<sup>25</sup>Cent is the unit of the logarithm of a frequency ratio  $\Delta f = 1200 \log_2 \frac{f}{f_{ref}}$ . It is used in musical terms to describe a pitch difference between a sounding frequency  $f$  and a nominal frequency  $f_{ref}$ . 1200 Cent correspond to an octave (frequency doubling), 100 Cent corresponds to one semitone. For trained listeners pitch differences of 5..10 Cent are perceivable.

<sup>26</sup>There, the ordinal number of air column modes is plotted vs their tuning discrepancy in Cent

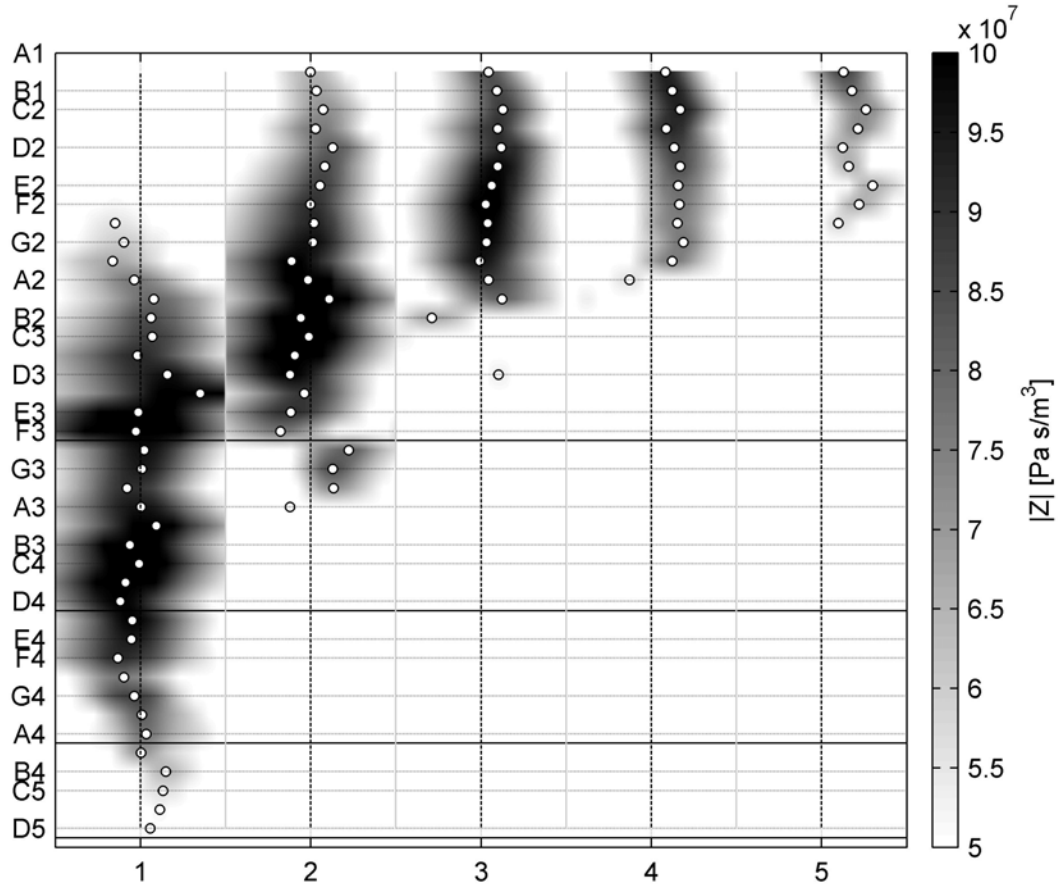


**Figure 2.17** Harmonicity map. The vertical gray lines margin a frequency range of  $\pm 100$  Cent left and right to each harmonic. The white dots mark the impedance peak frequencies and the grayscale provide information on the quality of the resonances. The dynamic range of the  $|Z|$ -axis is limited to 6 dB.

## 2.5 Summary

In this chapter the elementary theory of plane-wave propagation in wind instruments has been presented. Formulations well-known from the literature have been rearranged, compared and formally simplified. A consistent formulation is presented for the basic model elements to compose a musical woodwind resonator, in the formalism of an acoustical transmission-line. An implementation that allows to calculate the pressure standing wave patterns in a woodwind with tone-holes is presented. Experiments have been performed with a commercial impedance measurement system for brass instruments. A connection adapter constricting the measurement cross section to match the bocal of bassoons was constructed, and a correction procedure was applied to compensate for the effect of the adapter on the measured impedance curve in the post-processing. Comparing with theoretical impedance spectra of narrow calibration tubes, the setup with adapter is accurate within  $\pm 15$  Cent in peak frequencies. In a study of repeated measurements on bassoons, the repeatability of the setup has been determined to be  $< 5$  Cent in the peak frequencies and  $< 15\%$  in the peak magnitude. The random variation decreases with the ordinal number of the air column modes. The variability between measurements on bassoons of four different manufacturers has been observed to be fairly small in general, some specific peaks, however, reveal differences both in peak frequency and magnitude which are much larger than the random error.

The dimensions of one bassoon bore were determined accurately ( $\pm 5 \mu\text{m}$ ) and impedance measure-



ments on this bassoon were compared with predictions by the theory. A good agreement is found concerning the general shape of the curve, but the discrepancies in impedance peak positions are still in the range of  $\pm 20$  Cent and may reach up to over 50 Cent for single peaks.

The strong point of the numerical approach is its simple, fast, and robust concept, making it suitable for relative comparisons and optimization tasks.

In Chapter 5, relations between playing characteristics and the acoustical properties of the air-column will be shown. These performance-related aspects may be used to define optimization targets for woodwind instrument design. A first step into this direction has been undertaken with partial contribution of the present author [80].



## 3 Characterization of the Double Reed Mouthpiece

### 3.1 Physical Model of the Double-Reed

A short introduction on the general functioning of the double-reed is given in this section. Subsequently, the derivation of the basic physical model for the pressure induced reed motion will be presented. This introduces model parameters, that allow to characterize the experimental situations in this study.

The apparatus which has been constructed for this study, and two setups for experimental parameter estimation of the double-reed with this device are presented. Typical model parameters from measurements on bassoon double-reeds will be given.

#### 3.1.1 Working Principle

The double reed mouthpiece consists of two blades of reed cane that are tied up with wires at one end, to form a tubular channel. At this end, the reed is connected to the acoustic resonator of the musical instrument. At the other end, the reed *tip*, the opposing blades form a narrow oval slit through which the air flow from the musician enters the instrument. A bassoon reed is usually about

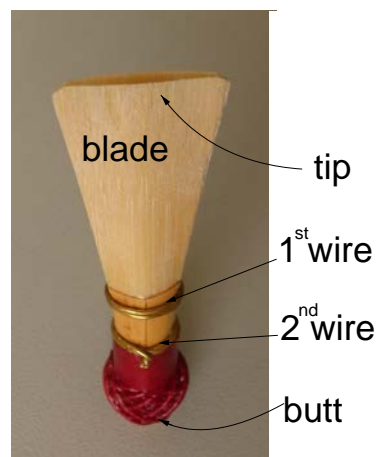


Figure 3.1 Terms used to describe double reeds

55 – 60 mm long and tied up by three wires, the last one of which at the *butt* is usually wrapped by yarn. The inner diameter at this rear end is approximately 5 mm. At the reed tip, the dimensions are typically a channel width of 12 – 15 mm and a height of 1 – 1.5 mm. From the first wire to the reed tip, the blades are progressively thinned out. In this part, the musician clasps his lips around the double-reed.

The interaction of the player and the mouthpiece is called the embouchure. This term encompasses the position of the lips, jaw and oral cavity, and the blowing pressure. The embouchure plays a

key-role in musical performance of double-reed instruments. During playing, the musician is able and advised to adjust the mechanical response of the reed with his embouchure in order to produce notes of proper tuning, dynamic level and sound color.

During this musical performance, the double-reed acts as a pressure controlled valve. The pressure difference between the blowing pressure in the mouth of the player and the pressure inside the mouthpiece acts on the reed blades. An air-flow through the narrow mouthpiece channel reduces the static pressure and results in a deflection of its elastic bounding walls. Consequently, the intake cross section will be reduced. At a certain threshold pressure, the reed blades touch each other and block the air-flow. Due to inertia, this sudden interruption induces a negative pressure pulse to travel downstream from the reed tip into the pipe. If a resonating pipe is attached to the mouthpiece, this pressure pulse will be reflected and self-sustained oscillations can occur.

In order to study the performance characteristics of the bassoon, an introduction of the physical characteristics of the double-reed is useful to provide a description of experiments in a model domain.

Although there are many differences between single and double-reeds, the classical model elaborated for a clarinet reed oscillations will be employed here to introduce the governing quantities and equations. As shown in recent literature [4], this model is suited for double-reeds oscillations as well, with minor modifications.

Throughout the study, synthetic bassoon reeds were used. These are made from non-hygroscopic materials and therefore yield a better reproducibility of the experiments, compared to bassoon reeds from natural reed cane (Giant Cane, *Arundo Donax (L.)*), which are most widely used by bassoonists.

### 3.1.2 Structural Mechanical Characteristics

In the following, the derivation of the classical physical model [144, 8, 172, 147, 102] for the excitation mechanism of reed woodwind instruments will be presented.

The balance of forces on a segment of the reed blade with the mass  $m$  and surface  $S_r$  yields, according to Fig. 3.2:

$$F_l + p_m S_r = F_i + F_d + F_s + p_r S_r, \quad (3.1)$$

where  $F_l$  is an external force, in particular a contact force applied by a lip,  $F_i$  is the inertial force of the accelerated mass,  $F_d$  is a damping force proportional to the velocity and  $F_s$  is a restoring force proportional to the displacement.  $p_m$  and  $p_r$  are pressure in the mouth of the player and inside the reed, respectively.

The equation of motion for the reed tip as a function of the pressures and forces acting on it writes:

$$F_l(t) + p_m(t) S_r = m \ddot{x}(t) + d \dot{x}(t) + k x(t) + p_r(t) S_r. \quad (3.2)$$

where  $d$  and  $k$  are constants for reed damping and reed stiffness.

By assuming that the spatially distributed reed/mouthpiece system is represented by a discrete model in which the reed tip displacement  $x(t)$  is the only degree of freedom, Eq. (3.2) is a *lumped model* of the reed. It should be noticed, that  $S_r$ ,  $m$ ,  $d$ , and  $k$  then become *equivalent* quantities representing the whole reed mouthpiece assembly. This concept of modeling the reed had already been suggested by Helmholtz [163] in 1877, and about 100 years later Wilson and Beavers first presented a numerical model [172].

Assuming that stiffness and damping are constant, and neglecting the external contact forces at reed closing allows to linearize the reed model: The reed blade is thought to oscillate periodically around a rest position, which is the result of a constant mouth pressure and lip force acting on it. The motion is driven by the reed pressure with an oscillation frequency  $\omega$  well below the reeds

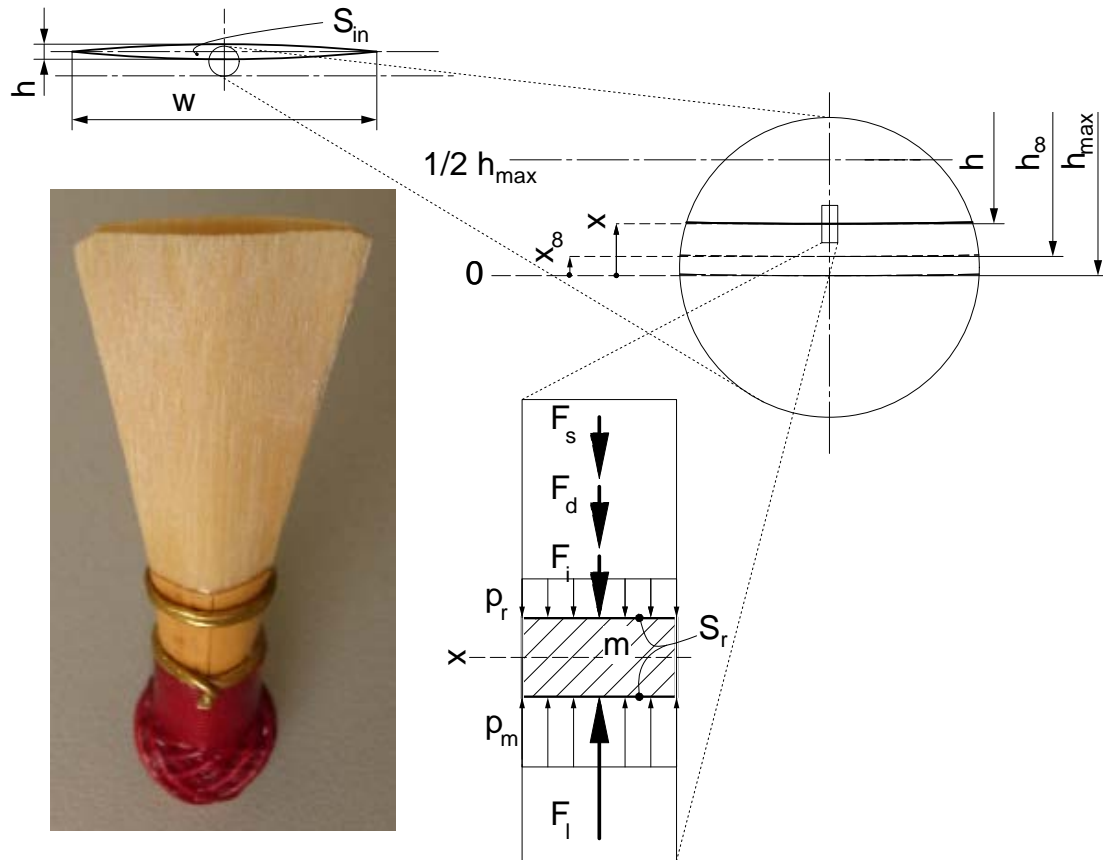


Figure 3.2 Notation of variables and balance of forces on a mass segment of a reed blade

natural frequency  $\sqrt{k/m}$ . The reed pressure fluctuations  $p_r(t)$  are therefore almost in phase with the reed tip displacement  $x(t)$ . Using the superposition principle, this is written:

- $x(t) = x_0 + \hat{x} e^{j\omega t}$
- $p_r(t) = p_{r,0} + \hat{p}_r e^{j\omega t}$

where  $j$  is the imaginary unit ( $j^2 = -1$ ) and  $\omega$  the angular frequency. One furthermore neglects fluctuations in the mouth pressure  $p_m(t)$  and lip force  $F_l(t)$ :

- $p_m(t) = p_{m,0} = \text{const.}$
- $F_l(t) = F_{l,\infty} = \text{const.}$

With  $\dot{x} = (j\omega)\hat{x} e^{j\omega t}$  and  $\ddot{x} = (j\omega)^2 \hat{x} e^{j\omega t}$ , the linearized form of Eq. (3.2) writes:

$$F_{l,\infty} + p_{m,0} S_r = ((j\omega)^2 m + (j\omega)d + k) \hat{x} e^{j\omega t} + k x_0 + \hat{p}_r e^{j\omega t} S_r + p_{r,0} S_r. \quad (3.3)$$

This motion can be separated into the steady and oscillatory parts, writing

$$F_{l,\infty} = kx_0 - (p_m - p_r)_0 S_r, \quad (3.4)$$

and, in the frequency domain, dividing by  $e^{j\omega t}$ ,

$$((j\omega)^2 m + (j\omega)d + k) \hat{x} = -\hat{p}_r S_r. \quad (3.5)$$

It is useful to normalize Eq. (3.5) with the equivalent mass  $m$  and simplify the expression using the following notation [102, 43]:

$$\begin{aligned}\omega_r &= \sqrt{\frac{k}{m}}, \\ g_r &= \frac{d}{m}, \\ \mu_r &= \frac{m}{S_r}, \\ K &= \frac{k}{S_r} = \omega_r^2 \mu_r,\end{aligned}\tag{3.6}$$

where  $\omega_r$ ,  $g_r$ ,  $\mu_r$  and  $K$  are the reed natural angular frequency, damping factor, effective mass and equivalent stiffness per unit area of the reed, respectively.

The tip displacement ranges<sup>1</sup> from  $x = 0$  (reed equilibrium rest position in absence of a lip force) to  $x = h_{\max}/2$  (reed closed), (see Fig. 4.11). The constant lip force  $F_{l,\infty}$  on the reed blade with the static stiffness  $k$  yields, in absence of a pressure difference across the reed (i.e. before starting to play a note), to an initial displacement  $x_\infty$ . With  $F_{l,\infty} = k x_\infty$  and introducing  $\Delta p = p_m - p_r$  as the pressure difference between the outer (mouth) and inner surface of the reed, the Eqs.(3.4) and (3.5) can be written

$$x_0 = x_\infty + \frac{\Delta p_0}{K},\tag{3.7}$$

for the rest position  $x_0$ , and

$$\hat{x} = \frac{\hat{p}_r}{\mu_r(-\omega^2 + j\omega g_r + \omega_r^2)}\tag{3.8}$$

for the oscillation amplitude  $\hat{x}$ .

The separation of the displacement  $x$  into a steady and oscillatory portion is helpful in order to determine the reed's static and dynamic parameters from separate experiments.

By use of Eqs.(3.6) and (3.8) the reed transfer function  $D$  is

$$\frac{\hat{x}}{\hat{p}_r}(\omega) = \frac{1}{\mu_r(-\omega^2 + j\omega g_r + \omega_r^2)} = \frac{\frac{1}{K}}{1 - (\frac{\omega}{\omega_r})^2 + j(\frac{\omega}{\omega_r})\frac{1}{Q_r}} = D(\omega)\tag{3.9}$$

where  $Q_r = \frac{\omega_r}{g_r}$  is the quality factor of the reed resonance.

To summarize, the reed is described as a damped harmonic oscillator, with the reed blade displacement at the tip as single degree of freedom. In the context of this lumped model description, the structural mechanical parameters of the reed are [172, 102]:

**K:** Reed stiffness per unit area

$\omega_r$ : Reed natural angular frequency

$Q_r$ : Reed quality factor.

These parameters are related to the material properties, as well as to the geometry of the reed blade.

### 3.1.3 Fluid Mechanical Characteristics

In the discussion above, the interaction between the fluid and the structure is implicitly included in terms of the pressure. A pressure difference acting on the surfaces of the elastic reed blades results in a deflection of the bounding surface and a change of the volume of the double-reed channel.

<sup>1</sup>In dynamic regimes  $x < 0$  is theoretically possible. Note that the equilibrium rest position with regard to a lip force  $F_{l,\infty}$  is denoted  $x_\infty$  here, and  $x_\infty > 0$ .

Analogously to the largely simplified description of the structural mechanics, the fluid mechanical characteristics are treated separately in the static and in the dynamic domain. Generally, the reed deformation has two consequences for the flow:

- A relative displacement of the two opposing reed tips changes the area of the intake cross section (see Fig. 4.11).
- The moving reed blades induce a flow transversal to the main flow direction.

According to this simplified model, the pressure induced static reed deflection (Eq. (3.7)) dominates the quasi-stationary flow-rate  $q$ , and the dynamic reed blade motion (Eq. (3.8)) induces a superimposed portion of “pumped flow” of alternating sign with the frequency dependent amplitude  $\hat{q}$ .

### Quasistatic regime

To a first approximation, the pressure induced change of intake cross section of the double-reed assumed linearly proportional to the reed displacement  $x$  [4].

Using the symmetry of the opposing reed blades, and assuming their curvature to be parabolic, the actual intake area  $S_{in}$  of the reed is

$$S_{in} = \frac{2}{3} w h \quad (3.10)$$

where  $w$  and  $h$  are the width and height of the reed channel at the tip. According to Fig. 4.11, the reed slit height at rest  $h$  can be divided into two parts

$$h = h_{\infty}(F_{l,\infty}) - \Delta h(\Delta p), \quad (3.11)$$

where  $h_{\infty}$  is the initial slit height due to the action of the lip force in absence of pressure and  $\Delta h$  is the additional narrowing of the slit if a static pressure difference is present.

With Eq. (3.7) the pressure induced area change can be written

$$S_{in} = \frac{2}{3} w (h_{\infty} - 2(x - x_{\infty})) = \frac{2}{3} w \left( h_{\infty} - 2 \frac{\Delta p}{K} \right). \quad (3.12)$$

From Eq. (3.12) the stiffness parameter  $K_s$

$$K_s = \frac{3}{4 w} K \quad (3.13)$$

can be introduced as a stiffness constant per unit volume, and Eq. (3.12) writes with the initial cross section  $S_{\infty} = 2/3 w h_{\infty}$

$$S_{in} = S_{\infty} - \frac{\Delta p}{K_s} = S_{\infty} \left( 1 - \frac{\Delta p}{p_M} \right) \quad (3.14)$$

where  $p_M = K_s S_{\infty}$  is the mouth pressure needed to close the reed completely ( $\Delta h = h_{\infty}$ ).

Denoting the velocities  $u$  in the mouth and in the reed with subscripts  $(\cdot)_r$  and  $(\cdot)_m$ , respectively, and assuming incompressibility of the fluid ( $\rho = \text{const.}$ ), a uniform velocity profile in the duct ( $u_r(y) = \bar{u}_r = \text{const.}$ ), and a very large mouth cavity ( $\bar{u}_r \gg u_m \approx 0$ ), the air flow-rate  $q$  through the reed open area  $S_{in}$  can, in a first approximation, be deduced from the dynamic pressure term in the quasi-static Bernoulli equation  $\Delta p = \frac{\rho \bar{u}_r^2}{2}$ . Thus

$$q = \bar{u}_r S_{in} = \sqrt{\frac{2 \Delta p}{\rho}} S_{in} \quad (3.15)$$

Combining Eqs.(3.14) and (3.15) leads to a nonlinear relation between any pressure difference  $\Delta p \leq p_M$  and the flow through the reed:

$$q = S_\infty \left(1 - \frac{\Delta p}{p_M}\right) \sqrt{\frac{2\Delta p}{\rho}} = q_A \left(1 - \frac{\Delta p}{p_M}\right) \sqrt{\frac{\Delta p}{p_M}}, \quad (3.16)$$

where  $q_A = S_\infty \sqrt{\frac{2p_M}{\rho}}$  is a flow-rate [102, 4].

This function reaches its maximum  $q_{\max}$  at the saturation pressure  $p_{m,s}$  which are given by

$$\begin{aligned} p_{m,s} &= \frac{1}{3}p_M, \\ q_{\max} &= \frac{2}{3\sqrt{3}}q_A. \end{aligned} \quad (3.17)$$

### Dynamic regime

An expression for the flow induced by an oscillating reverberant boundary with respect to its displacement will be derived for the double-reed mouthpiece in a dynamic regime [125, 156]. Again, the discussion is based on the balance of forces sketched in Fig. 4.11. Note, that in the following equations,  $m$  and  $S_r$  are *equivalent* properties representing the reed in a the context of a lumped model.

The volumetric displacement  $dV$  of air inside the double-reed mouthpiece due to a displacement  $dx$  of the reed blade segment with surface  $S_r$  writes

$$dV = 2S_r dx. \quad (3.18)$$

Consequently,

$$\frac{dV}{dt} = 2S_r \frac{dx}{dt} = q_d, \quad (3.19)$$

is volume flow-rate<sup>2</sup> induced by a dynamic motion of the boundary. For harmonic fluctuations of the flow  $q_d = \hat{q} e^{j\omega t}$  and the of reed velocity  $\dot{x} = j\omega \hat{x} e^{j\omega t}$  this can be written:

$$\hat{q} = 2S_r j\omega \hat{x}. \quad (3.20)$$

Inserting the ratio of reed tip displacement and reed pressure in the dynamic regime Eq. (3.9) into Eq. (3.20) yields

$$\hat{q} = 2S_r j\omega \hat{p}_r D(\omega). \quad (3.21)$$

With Eq. (3.9) the amplitude ratio of the motion induced flow and the pressure inside the mouthpiece is

$$\frac{\hat{q}}{\hat{p}_r}(\omega) = 2S_r j\omega \frac{\frac{1}{K}}{1 - (\frac{\omega}{\omega_r})^2 + j(\frac{\omega}{\omega_r})\frac{1}{Q_r}} = Y_r, \quad (3.22)$$

which can be called the reed's acoustic admittance  $Y_r$ .

For weak damping, the modulus of this function reaches its maximum  $|\hat{q}/\hat{p}_r|_{\max}$  near the reed's resonance frequency  $f_r$ , the corresponding function value is

$$\left| \frac{\hat{q}}{\hat{p}_r} \right|_{\max} = 4\pi S_r f_r \frac{Q_r}{K} \quad (3.23)$$

<sup>2</sup>subscript  $(\cdot)_d$  stands for dynamic



The reed admittance  $Y_r$  is sometimes interpreted as an acoustic compliance of an *equivalent volume*  $V_{eq}$ . With  $Y_r = 1/Z_{cav}$ , where  $Z_{cav} = -j\rho c^2/(V_{eq}\omega)$  is the acoustic impedance of a cavity, the equivalent volume  $V_{eq}$  becomes

$$V_{eq} = 2 S_r \rho c^2 \frac{\frac{1}{K}}{1 - (\frac{\omega}{\omega_r})^2 + j(\frac{\omega}{\omega_r})\frac{1}{Q_r}}. \quad (3.24)$$

$V_{eq}$  obviously is a frequency dependent quantity. However, its offset value  $V_{eq,0} = 2 S_r \rho c^2 Q_r / K$  is often used to calculate a frequency independent length correction  $\Delta L = V_{eq,0}/S$  [125, 43], where  $S$  is a cross section of the bore. This, however, implicitly assumes an inertial nature of the equivalent volume, which seems to be in contradiction with the statement that led to Eq. (3.24)<sup>3</sup>.

To summarize, the quasi-static and dynamic fluid-mechanical characteristics of a reed blade according to the basic model [102, 125] are:

$p_M$ : Static pressure to close the reed,

$q_{max}$ : Maximum flow through the maximally open reed,

$S_r$ : Reed effective surface.

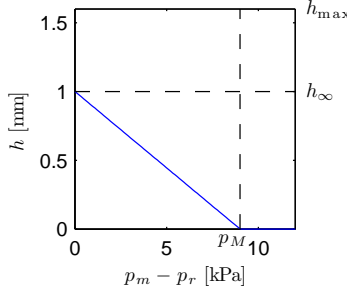
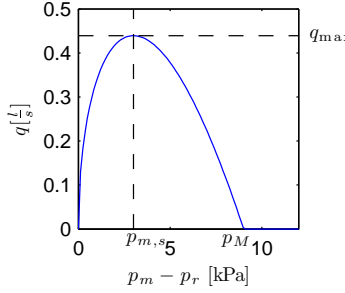
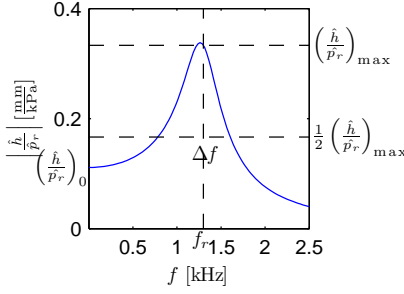
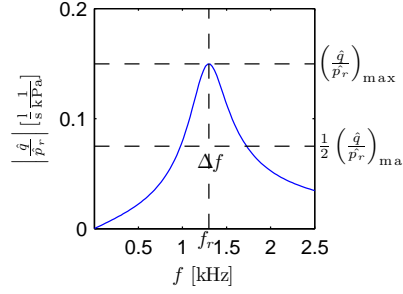
Additionally, the width of the reed channel  $w$  as a constant geometrical parameters is necessary to link the tip displacement  $x$  to the intake cross section  $S_{in}$ .

The set of equations given in this section and the assumptions which they are based on is referred to as the “Raman-Model” [42], after a pioneering treatise by Raman [144].

In Table 3.1 an overview on the model functions, the characteristic curve points and related reed parameters is given for typical values of a bassoon double reed. In contrast to the derivation above, the equations in this table for the reed displacement are written in terms of the reed slit height  $h$ , instead of reed tip position  $x$ , and in terms of frequency  $f$  in Hertz, instead of angular frequency  $\omega$ .

<sup>3</sup>The concept of a reed equivalent volume has recently been adapted by Dalmont *et al.* [45] for the non-linear beating-reed regime. The authors discriminate a *displaced* volume, corresponding to the reed motion, and an *equivalent* volume as a inertial correction to be applied to the resonator, which is sought to explain the discrepancy between its fundamental air column mode and the sounding frequency of the reed-resonator system in playing conditions.

**Table 3.1 An elementary physical model for the double-reed (“Raman-Model” [102])**  
**Model parameters**  $h_\infty = 1 \text{ mm}$ ,  $w = 14 \text{ mm}$ ,  $p_M = 9.5 \text{ kPa}$ ,  $f_r = 1300 \text{ Hz}$ ,  $Q_r = 3$ .

	structural-mechanical	fluid-mechanical	
quasi-static	function	$h(\Delta p) = h_\infty \left(1 - \frac{\Delta p}{p_M}\right)$	$q(\Delta p) = q_A \left(1 - \frac{\Delta p}{p_M}\right) \sqrt{\frac{\Delta p}{p_M}}$
	graph		
	characteristic values	$h_\infty$ $p_M$	$q_{\max}$ $p_{m,s}$ $p_M$
	related parameters	$S_\infty = \frac{2}{3} w h_\infty$ $K_s = \frac{p_M}{S_\infty}$ $K = \frac{4}{3} w K_s$	$q_A = \frac{3}{2} \sqrt{3} q_{\max}$ $p_M = 3 p_{m,s}$ $S_\infty = q_A \sqrt{\frac{\rho}{2 p_M}}$ $K_s = \frac{p_M}{S_\infty}$ $K = \frac{4}{3} w K_s$
dynamic	function	$\frac{\hat{h}}{\hat{p}_r}(f) = 2 \frac{\frac{1}{K}}{1 - (\frac{f}{f_r})^2 + j(\frac{f}{f_r})^{\frac{1}{Q_r}}}$	$\frac{\hat{q}}{\hat{p}_r}(f) = 2j \frac{\frac{1}{K}}{1 - (\frac{f}{f_r})^2 + j(\frac{f}{f_r})^{\frac{1}{Q_r}}} 2\pi f S_r$
	graph		
	characteristic values	$f_r = \frac{\omega_r}{2\pi}$ $\Delta f$ $\left(\frac{\hat{h}}{\hat{p}_r}\right)_{\max}, \left(\frac{\hat{h}}{\hat{p}_r}\right)_0$	$f_r$ $\Delta f$ $\left(\frac{\hat{h}}{\hat{p}_r}\right)_{\max}$
	related parameters	$Q_r = \frac{f_r}{\Delta f} = \left(\frac{\hat{h}}{\hat{p}_r}\right)_{\max} \left(\frac{\hat{h}}{\hat{p}_r}\right)_0^{-1}$ $K = 2 \left(\frac{\hat{h}}{\hat{p}_r}\right)_0^{-1} = 2 Q_r \left(\frac{\hat{h}}{\hat{p}_r}\right)_{\max}^{-1}$ $\mu_r = \frac{K}{(2\pi f_r)^2}$	$Q_r = \frac{f_r}{\Delta f}$ $S_r = \frac{1}{4\pi} \frac{K}{Q_r} \left(\frac{\hat{q}}{\hat{p}_r}\right)_{\max}$ $\mu_r = \frac{K}{(2\pi f_r)^2}$

## 3.2 Measurement of Reed Parameters

The measurement of the reed's behavior in the static and dynamic domain allows to estimate model parameters according to Table 3.1 by matching the specific model function to experimental data.

Two experiments have been performed:

From the first experiment the mechanical and flow-related parameters in the quasistatic regime can be obtained. In this basic experiment, the pressure difference across the reed and the resulting flow through it is measured in absence of reed oscillations [40, 4].

The second experiment is a measurement of the frequency dependent acoustic impedance of the reed taken off the bocal. This allows for a rough estimation of dynamic mechanical properties of the reed blades [101].

### 3.2.1 Quasi-stationary Measurement

The principle of this experiment is to measure the pressure difference  $\Delta p = p_m - p_r$  between the mouth and the inside of the reed channel, and the flow  $q$  through the reed, simultaneously. The reed blades will deflect due a pressure difference acting on them and the reed slit is narrowed. By a simultaneous optical measurement of the intake area  $S_{in}$ , slit height  $h$  and width  $w$ , it is possible to obtain the reed's static structural mechanical parameters in the same measurement run. To assure quasi-static conditions, auto-oscillations of the reed blades must be prevented.

### Experimental Setup

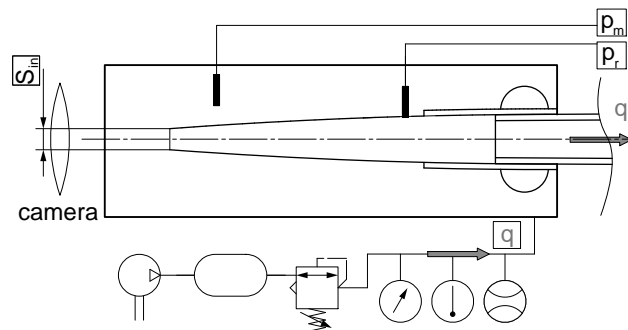


**Figure 3.3** Schematic representation of the experimental setup of the artificial mouth (not to scale)

The experimental setup is shown schematically in Fig. 3.3. In contrast to other measurement setups reported in the literature [40, 4], the volume flow is here measured with a thermal mass-flow meter in the air supply at the inlet of the artificial mouth. This setup was chosen since it allows for a direct measurement of the mean flow-rate in both quasi-static and oscillating regime. The leakage volume-flow rate of the setup is small enough to be neglected<sup>4</sup>.

As for the volume of the mouth cavity downstream of the flow-meter, the practical measurement procedure requires to adjust several steady-state regimes of constant mouth pressure. With the present setup, a steady flow regime was achieved approximately 2 seconds after a readjustment of the pressure-relief valve. At each of these states, a picture of the intake area was taken by use of a

<sup>4</sup>The leakage has been determined from a pressure decay measurement. The slope of the log-pressure decay vs. time is  $-0.002$  1/s. From the bulk modulus of air  $1.43$  Pa and a mouth cavity volume of  $3.5$  litre, this yields a leak coefficient of  $5 \cdot 10^{-11}$  ( $m^3/s$ )Pa. That is, the leak flow-rate at  $\Delta p = 10$  kPa is  $q_{leak} < 5 \cdot 10^{-4} \frac{\text{litre}}{s}$ , which is about 1% of the residual flow-rate which is measured, when the reed appears to be completely closed

camera equipped with a macro lens. A piece of reusable plastic sealing material (Bostik Blu-Tack) was stuck to the reed blade, to considerably increase its effective mass and damping to prevent auto-oscillations during the experiments.

From the characteristic curves obtained by plotting the flow-rate  $q$  and the reed slit height  $h$  versus the differential pressure  $\Delta p$ , the reed parameters  $p_{m,s}$ ,  $q_{\max}$ ,  $h_{\infty}$ , and  $p_M$  can be read. Subsequently, the reed parameters  $q_A$ ,  $S_{\infty}$ ,  $K_s$  and  $K$  can be calculated. Alternatively,  $S_{\infty}$  can be directly read from a respective curves, and  $p_M$  can be estimated from the pressure-flow characteristic, although the saturation pressure  $p_{m,s}$  may be more easily identified in practice.

An overview on the measured curves, the reading of characteristic values and the related reed parameters is provided in Table 3.2.

### 3.2.2 Dynamic Measurement

The principle of this measurement is an acoustical excitation of a reed blade motion and a measurement of the resulting air flow. This can be done with the acoustic impedance measurement setup introduced in the previous chapter. The impedance spectrum measured by a swept-sine pressure excitation will reveal a dip near the mechanical resonance of the double-reed assembly due to the additional “pumped flow” induced by the moving reed blades [101].

#### Experimental Setup

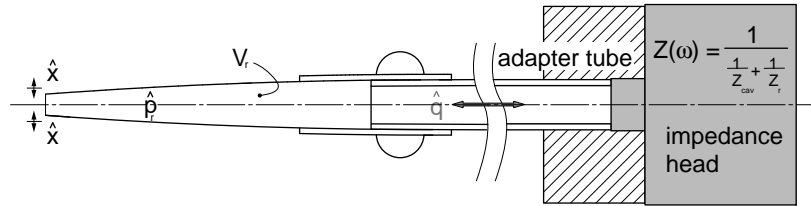


Figure 3.4 Schematic representation of the reed admittance measurement (not to scale)

The experimental setup consists of a narrow cylindrical tube of 139 mm length<sup>5</sup> and 4.2 mm diameter, which corresponds to the diameter of a bassoon bocal. The reed is stuck to this adapter tube like it were a bocal, and the impedance of the reed seen from the butt is measured (Fig. 3.4). The dip in the measured impedance spectrum corresponds to an admittance maximum of the reed assembly. It can be clearly detected in the spectrum when comparing two configurations with free and strongly damped reed blades.

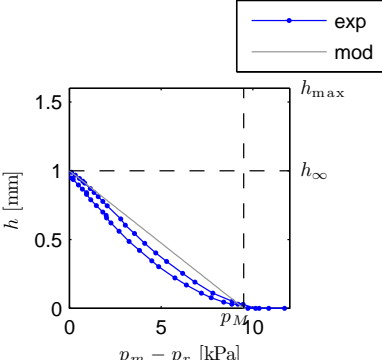
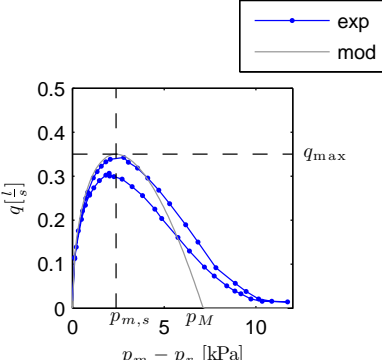
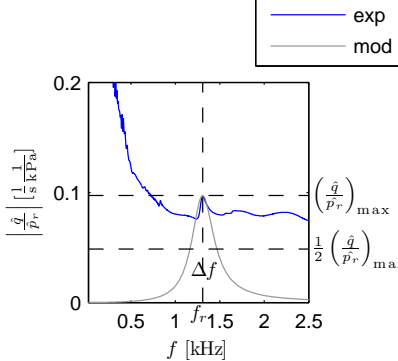
As the admittance measured in this way is a superposition of the admittance  $Y_{cav}$  of the air enclosed in the reed channel cavity, and the admittance due to the reed motion  $Y_r$ , the latter can be obtained by subtracting  $Y_{cav} = 1/(-j\rho c^2/(V_r\omega))$  from the measured admittance.  $V_r$  is the volume of the reed channel.

From the characteristic points of this curve  $f_r$ ,  $\Delta f$ , and  $|\hat{q}/\hat{p}|_{\max}$  can be read. This allows to determine the reed parameters  $Q_r$  and  $S_r$ , if the reed's stiffness  $K$  is known. As an estimate, the value for  $K$  obtained from the static measurement can be used.

It must be mentioned, that for this procedure to determine  $S_r$  and  $Q_r$  the correct measurement of the acoustic impedance magnitude is crucial. With the present setup, this aspect may be critical, as the damping in the measurement appears to be much larger than predicted by theory. The impedance peak magnitudes are measured smaller by up to 50%. The measured values for  $S_r$  and  $Q_r$  should be regarded as rough estimates, which may be greater ( $S_r$ ) or smaller ( $Q_r$ ) by factor 2. However, the

<sup>5</sup>This length has been chosen for practical reasons of the artificial mouth, in which the double-reed is rigidly mounted.

**Table 3.2** Parameter estimation for the “Raman-Model” [102] on the basis of measurements on the double-reed

	structural-mechanical	fluid-mechanical
quasi-static	model $h(\Delta p) = h_\infty \left(1 - \frac{\Delta p}{p_M}\right)$	model $q(\Delta p) = q_A \left(1 - \frac{\Delta p}{p_M}\right) \sqrt{\frac{\Delta p}{p_M}}$
		
	graph	
	characteristic values $h_\infty = 1 \text{ mm}$ $p_M = 9.5 \text{ kPa}$	$q_{\max} = 0.35 \frac{1}{s}$ $p_{m,s} = 2.4 \text{ kPa}$ $p_M$ not read
dynamic	related parameters $S_\infty = 9.3 \text{ mm}^2$ $K_s = 1.0 \cdot 10^9 \frac{N}{m^4}$ $K = 1.9 \cdot 10^7 \frac{N}{m^3} \quad (*)$	$q_A = 0.91 \frac{1}{s}$ $p_M = 7.1 \text{ kPa}$ $S_\infty = 8.4 \text{ mm}^2$ $K_s = 8.5 \cdot 10^8 \frac{N}{m^4}$ $K = 1.6 \cdot 10^7 \frac{N}{m^3}$
	model $\frac{\hat{h}}{\hat{p}_r}(f) = 2 \frac{\frac{1}{K}}{1 - (\frac{f}{f_r})^2 + j(\frac{f}{f_r})\frac{1}{Q_r}}$	model $\frac{\hat{q}}{\hat{p}_r}(f) = 2j \frac{\frac{1}{K}}{1 - (\frac{f}{f_r})^2 + j(\frac{f}{f_r})\frac{1}{Q_r}} 2\pi f S_r$
		
	graph	
	characteristic values $f_r = 1306 \text{ Hz}$ $\Delta f = 304 \text{ Hz}$ $\left(\frac{\hat{h}}{\hat{p}_r}\right)_{\max} = 0.1 \frac{1}{s \text{ kPa}}$	$f_r = 1306 \text{ Hz}$ $\Delta f = 304 \text{ Hz}$ $\left(\frac{\hat{h}}{\hat{p}_r}\right)_{\max} = 0.1 \frac{1}{s \text{ kPa}}$
	related parameters $\mu_r = 0.28 \frac{kg}{m^2}$	with $K$ from (*) $Q_r = 4.3$ $S_r = 26 \text{ mm}^2$ $\mu_r = 0.28 \frac{kg}{m^2}$

method will give a reasonable estimate for the resonance frequency  $f_r$ , and is probably still useful to provide a qualitative idea of the relative change of these parameters as the embouchure situation is varied.

An overview on the measured curves, the reading of characteristic values and the related reed parameters is provided in Table 3.2.

As can be seen in this table, some of reed parameters have been determined by different methods. The differences between the values for one and the same parameter obtained from different measurements are interesting. They allow for the estimation of the importance of flow effects in the double-reed. These aspects will be addressed in detail in the next chapter.

Previous to that, the next section gives an overview on the artificial mouth setup used in the experiments.

### 3.3 Construction of an Artificial Mouth

The performance characteristics of reed woodwind instruments are influenced by the player to a great extent. A musician can turn the output of a *coupled oscillating system* into a piece of art: music.

In reed woodwind this “conversion” requires delicate actions of the player by using his facial muscles to influence the double-reeds operation conditions.

It is not easy to observe this interaction in a real performance, since the excitation mechanism is very sensitive, and is most easily disturbed by the sensors. However, recent studies with instrumented mouthpieces were able to demonstrate the importance of *in vivo* experiments in understanding advanced playing techniques with single reed instruments [84, 33, 69]. To the authors knowledge, such studies have not been carried out for double-reed instruments, so far.

Here, a different approach has been chosen. The human player is replaced by a technical device, that is supposed to interact with the excitation mechanism in a very similar way as a musician does. This *in vitro* approach facilitates measurements describing the interaction player and instrument and has been widely used in the field of wind instruments musical acoustics. Experimental devices constructed for this purpose are called *artificial mouths*.

Being far from music, an artificial mouth is helpful to study the interaction of the player and instrument and provides some basic insight into the performance characteristics of the sounding instrument.

For this thesis, an artificial mouth for double-reed instruments has been constructed, which allows for both characteristic experiments describing the embouchure-reed system by model parameters, as well as for blowing experiments with a complete instrument in realistic playing conditions. A description of this device is given in the following.

#### 3.3.1 Requirements Profile

The approach of studying musical wind instruments by use of an artificial mouth has a long tradition. Several devices have been developed starting from about the 40s of the last century [120] and refined versions have been used for recent studies of various wind instruments (see, e.g. for brass instruments: [38, 131, 28]; flute: [12, 155, 57]; single-reed instruments: [92, 40, 119, 153, 3, 115, 21]; double-reed instruments: [150, 106, 6, 77, 75]). According to the specific subject of interest, each of these devices meets different demands.

In the present study, the main objective is to study the performance characteristics of bassoons with respect to the embouchure action of player, who, in a musical context, has to comply with one

paramount condition: playing in tune. The artificial mouth developed for this study should allow for a quantification of the efforts, a musician has to make to play in tune with a given instrument, i.e. a combination of double-reed, bocal and bassoon.

Such a device should allow for:

- Measurement of lip force, reed blade displacement, blowing pressure, mouth pressure and mean flow,
- Precise adjustment of lip position, lip force and blowing pressure,
- Individual adjustability of lip position, lip force and blowing pressure during playing,
- Optical access to the reeds front view, and
- Robust design for the possibility to swap between instruments without affecting the embouchure.

In order to ensure a reasonable repeatability of the experiments, it was chosen to use synthetic bassoon double-reeds, exclusively. These are made from non-hygroscopic materials and their dynamic properties are not affected by the humidity of the air. This facilitates the design of the experimental setup, since the artificial mouth can then be operated with dry air.

### 3.3.2 Generic Design

In musical acoustics, various attempts have been made to imitate human lips, and the different implementations according to different types of wind instruments reflect the broad range of mechanical function, that musicians lips can provide: Whereas in brass instruments playing the lips directly form an “outward-striking” valve, in reed-woodwinds each of the lips is pinched between the players teeth and the oscillating reed blades. This damps the “inward-striking” valve and avoids oscillations at the reed’s natural frequency.

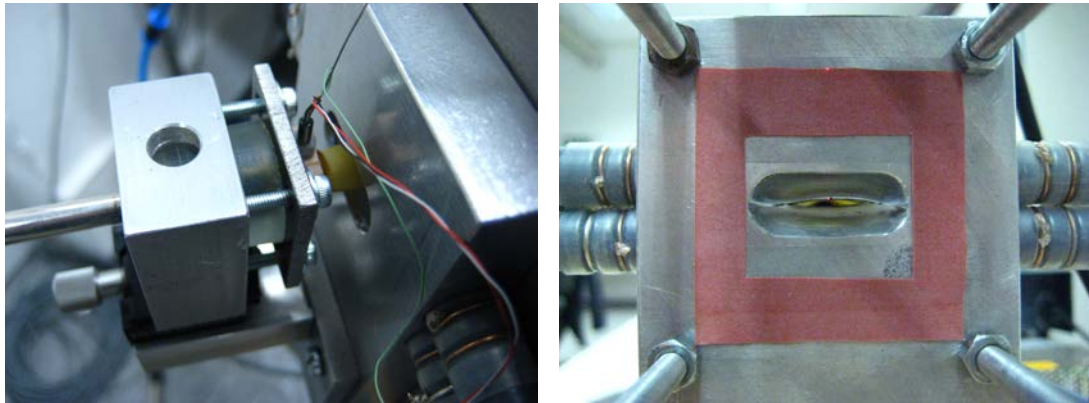
During the present study, two lip-configurations have been successfully used to mimic a double-reed embouchure.

#### Prototype I - fixed lip, adjustable reed

The first prototype is similar to artificial mouths used in brass instruments research (e.g. [131]). The lips are thin water filled silicon tubes enclosed by two adjoining bores in a rigid lip block. A thin sealing lip is glued to each of these tubes. If a double-reed is positioned between the tubes and the mouth cavity is pressurized, these thin sealing lips will lie against the reed blades and tighten the mouth cavity (see Fig. 3.5(b)). A few drips of silicone oil can be used additionally. This setup has the following advantages:

- Like in a human mouth, the lip assembly separates the mouth cavity and the ambience. The mouth pressure acts only on the surfaces of the reed blades protruding from the lips into the mouth cavity.
- A cavity of arbitrary size and wall stiffness can be attached to the lip block to mimic the vocal tract.
- The clamping of the double reed between the lips can be varied in a simple and robust manner by adjusting the water pressure inside the lips.

The characteristic details of Prototype I are shown in Fig. 3.5.



(a) Lip block with water-filled silicon tubes and double reed mounted in an axially shiftable support (b) Double-reed between the silicon tubes as seen from the mouth cavity (removed for the picture)

**Figure 3.5 Prototype I: Front perspective (a) and rear view (b)**

Yet, the main disadvantage of the setup is the incapability to precisely control the embouchure:

- The position of the reed-mouthpiece relative to the lips cannot be adjusted accurately, since the lips may stick or slip in case of transversal movement of the lip.
- The lip-force acting on the reed blades cannot be measured directly.
- A “biting” of the reed mouthpiece is not possible, whereas reed-woodwind players usually make use of their jaw and teeth control the reed.

To overcome these drawbacks, a second device has been developed.

### **Prototype II - fixed reed, adjustable lips**

The key feature of this setup is the precise adjustability of an exchangeable lip element relative to a rigidly fixed double-reed mouthpiece. The lip element is mounted on a load cell, which can be positioned by micrometer screws in two directions, longitudinal and perpendicular to the main axis of the double-reed (see Figs. 3.6 and 3.7).

In contrast to a real embouchure, the artificial lip does not provide an air-tight separation of the mouth cavity from the ambience. The artificial jaw is mounted inside a housing, which consequently is considerably larger than the human mouth cavity. Furthermore, for practical reasons, the housing is made of acrylic glass (PPMA) which is a hard-walled boundary of the mouth cavity. Compared to a real mouth cavity, these aspects are significant drawbacks, since it has been shown that the vocal tract can play a role in extended playing techniques in single reed instruments [33].

Nevertheless, the unrealistically large volume of the present artificial mouth does not affect its general function. Regarding this aspect, the claim to mimic the human mouth cavity has been released here for the sake of a precise adjustment of lip relative to the reed, which undoubtedly is very sensitive to mechanical interaction.

### **3.3.3 The artificial Lip**

In reed instrument performance, the lips are the interface by which the player can control the excitation of the instrument. Generally, they serve two important functions: On the one hand, the lips are clasped around the reed providing an air-tight sealing of the mouth and thus enable the buildup of mouth pressure. On the other hand, the lips are the medium of force transmission from the jaw to the reed.

The lip-reed interaction is complex since a number of facial muscles are employed, allowing



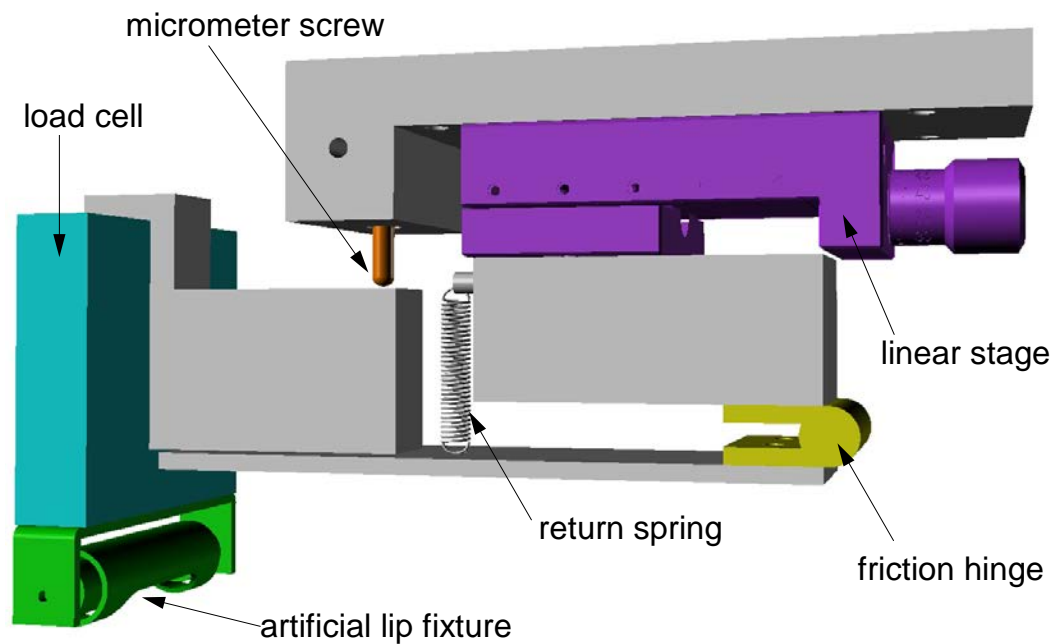


Figure 3.6 Setup of the adjustable artificial lip module for Prototype II

for great variation of the situation in terms of geometrical and mechanical characteristics: The human lip mainly consists of a very thin layer of skin that covers a circular muscle (*musculus orbicularis oris*). The lip rests on the reed blade like a cushion. The teeth are positioned on top of this lip cushion. The muscles of mastication (*musculus masseter*, *musculus temporalis*, *musculus pterygoideus medialis*, *musculus pterygoideus lateralis*) are used to press the teeth into the lip cushion and therefore exert force on the reed blade. Some of these muscles are also used to shift upper and lower jaw versus each other to adjust the position of interaction relative to the blade. The elasticity of the lip cushion can be adjusted by the tension of the circular muscle.

Recently, attempts have been made to characterize dynamical mechanical parameters of the human lip from the viewpoint of wind instrument performance [65, 70, 131]. It was found that their characteristics are represented best by a compound of an air balloon filled with foam and glycerin [70].

Inspired by this concept an artificial lip module has been created for the present study. It consists of a rigid rib, imitating the teeth, which is sheathed by a piece of 3 mm cellular rubber. On top of this, a glycerin filled air balloon is overlaid. This compound is fixed in a short steel tube which can be clamped onto the artificial jaw module by use of centering bolts (see Fig. 3.8).

This lip module can be positioned with micrometer screws in two dimensions to axially adjust the contact region of the lip on the reed as well as the forces exerted to the blades. The micrometer screws are actuated by 2 mm hex-wrenches, which are revolvably mounted in air-tight fittings in the housing of the artificial mouth. This makes it possible to independently adjust the lips in both dimensions during the experiment.

### 3.3.4 Air Supply

An important practical feature of the artificial mouth is the concept of air supply and pressure regulation. The pressure in the mouth of a performing bassoonist ranges approximately from 1 to 9 kPa [68]. Typically, the mean volume flow-rate into the instrument is in the range of 0.03 to 0.4 l/s during playing. In medical research it is common to use membrane pumps and control the

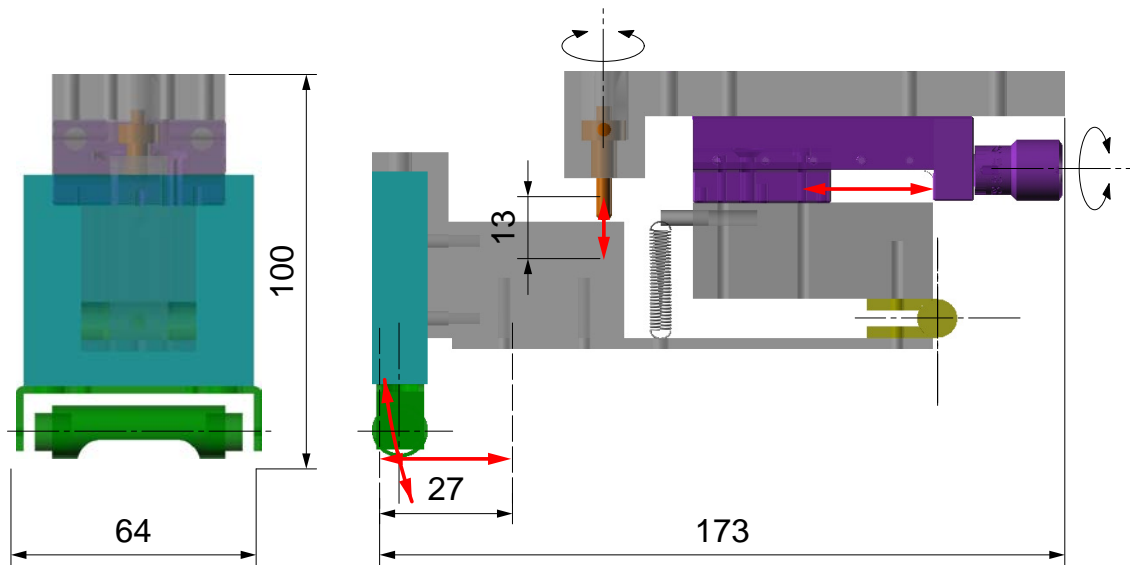


**Figure 3.7** Front and side view of the lip module with possibility to adjust the lip position in 2 directions. Dimensions are in mm.

air-flow to imitate the human respiratory system. In the present study, for practical reasons, it was decided to use a high overpressure reservoir and control the pressure in the mouth by means of a pressure-relief valve. This principle can lead to problems if the valve mechanism interacts with the double-reed which itself is a highly dynamic pressure regulated valve.

### Starting the oscillation

A delicate aspect of the air supply is the strategy to start the oscillations. The musician usually blocks the airflow by closing the reed with his tongue to build up the mouth pressure and then quickly releases the tongue to start the vibration of the reed. A mechanism providing the same function has recently been included in an artificial mouth for clarinets [3]. Yet, it is also possible, to start the oscillation by simply increasing the mouth pressure [21].

When a certain threshold pressure, depending on the reed and embouchure, is exceeded, the reed will close, and the mouth pressure will increase rapidly, depending on the mouth cavity volume. The delay<sup>6</sup> of the mouth pressure regulating system determines if the reed remains in this blocked position, or if it opens again and the system settles in an oscillating regime. In the present work, a large diaphragm pressure regulator has been used.

### Pressure Control

The computer aided control of the air supply of an artificial mouth is a demanding task<sup>7</sup> in terms of control technology and precision engineering [56, 57, 151]. For the focus of this work which

<sup>6</sup>The characteristic time of the pressure regulating system (mouth cavity, inlet pipe and valve) has to be short enough to release the mouth-pressure, once the reed has beaten. On the other hand, the inertia of the system must be large enough to prevent a coupling with double-reed valve.

<sup>7</sup>A direct control of the mouth-pressure at the inlet of the mouth cavity is delicate. Unlike the human mouth cavity the artificial mouth is hard-walled and acoustic reflections are likely to influence the control mechanism. Piezo-operated proportional pressure regulating valves in the given pressure range are available, but their maximum flow-rates are



**Figure 3.8** Assembling steps of the artificial lip. The air-balloon is subsequently filled with glycerin through tiny brass capillaries fitted in the PVC caps.

is a detailed monitoring of the sounding bassoon in various configurations, a manual control of the artificial mouth is sufficient. The air supply chain which was used is schematically shown in Fig. 3.3. The mouth cavity has outer dimensions of 200 mm × 180 mm × 80 mm and with respect to the equipment a cavity with a volume of approximately 2 l. A pipe of 6.5 m length and 12 mm diameter connects the artificial mouth and the valve. The mouth pressure is controlled by a manual precision pressure regulator without constant bleed (*AirCom Type R216-0E*). This device has a diaphragm of approximately 80 mm diameter and the pressure can be controlled in range from 100 Pa to 60 kPa, at maximum flows of 700 l/min. With this setup, it is possible to sound the bassoon throughout the complete playing range from 58 to 622 Hz.

### 3.3.5 Sensors and Data Acquisition

This section gives a brief overview on the measurement devices used in the artificial mouth.

#### Mouth pressure

The mouth pressure is sensed with an amplified differential pressure transducer (*sensortech Type HDIM200DBP5*) in a range of 0 to 20 kPa within an accuracy of 0.1% full scale output. The pressure sensor has been calibrated with a hydraulic deadweight tester in the range of -2 to 2 kPa, with an accuracy of 10 Pa. Assuming a constant mouth pressure, only the RMS-value of the measured pressure signal has been used in the postprocessing.

#### Reed pressure

The reed pressure is probed with a differential piezoresistive miniature transducer (*kulite Type XCQ-093*), with a maximum pressure amplitude of 35 kPa, a sensitivity of 2.85 mV/kPa and a natural frequency of 150 kHz. The sensor is mounted flush to the outer surface of the reed blade approximately 30 mm downstream of the reed tip. Access to the reed channel is given by a small, centered hole of 0.5 mm diameter in the blade. The reed pressure transducer is pre-amplified by a

---

small. For large cavities like the present artificial mouth, the pressurization times may be too long to maintain the double-reed oscillation, once it was started.

DC-coupled differential amplifier (*Brüel&Kjær Type 2697A*) and with a flat frequency response (+/- 10%) from DC to 100 kHz. The pressure sensor has been calibrated with a hydraulic deadweight tester in the range of -2 to 2 kPa, with an accuracy of 10 Pa.

### Sound pressure

The sound pressure was measured with an externally polarized 1/2" free-field microphone (*Brüel&Kjær Type 4190*) with a sensitivity of 52.7 mV/Pa. The frequency response is flat within a tolerance of 0.2 dB, for the frequency range of 10 Hz to 10 kHz. The microphone was placed at a distance of 1.5 m from the instrument. The experiments have been carried out in a laboratory room acoustically modified to suit musical instrument rehearsal (reverberation times around 0.8 s above 200 Hz).

### Volume flow-rate

The volume flow-rate is measured in the air supply at the entrance of the mouth cavity with a thermal mass-flow meter (*Voegtlin Type GSM-D9TA*) within a range of 0.3-30 nl/min with an accuracy of  $\pm 0.5\%$  of the measured value plus a tolerance of 0.09 nl/min. The factory calibration of the flow-meter is in standard litres (nl STP), that is a volume of 1 l at standard state (1.013  $\times 10^5$  Pa, 0 °C). The reading has to be corrected for actual pressure and temperature to give the actual volume flow. Using Boyle's law, the actual volume flow is calculated from the sensor reading  $q_{read}$  in nl/min, the pressure  $p$  in Pa and the temperature  $T$  in K by following relation:

$$q = \frac{1.013 \times 10^5 \text{ hPa}}{p} \frac{T}{273.15 \text{ K}} \frac{q_{read}}{\frac{\text{nl}}{\text{min}}} \frac{1}{\text{min}}. \quad (3.25)$$

In the airway, the absolute pressure is measured with an amplified barometric pressure transducer (*sensortronics Type HDI0811AR*) with a measurement range of 0.8 to 1.1  $\times 10^5$  Pa and an accuracy of  $\pm 0.01 \times 10^5$  Pa. The temperature is measured by a resistance temperature detector (*heräus Type M310Pt100*), which was operated by a 3-wire input module (*dataforth Type SCM5B34-01*) yielding an accuracy of  $\pm 0.12$  °C. These measurement uncertainties have been used to estimate the uncertainty in the volume flow-rate.

### Lip Force

To measure the lip force, the lip module described in section 3.3.3 is mounted on a precision load cell (*AST Type KAP-S/10N/0,1*) featuring a measurement range of 0-10 N and an accuracy of  $\pm 0.01$  N. The signal is conditioned and amplified by a 4.8 kHz carrier frequency amplifier system *HBM-MGC* (Modules *HBM Type AP14*, *Type MC55*).

### Lip Position

The position of the lip module in axial direction of the reed can be adjusted by means of a manual linear stage (*owis Type VT-45-25*) within a range of 25 mm. The accuracy of the adjustment screw is approximately 10  $\mu\text{m}$ ; a full spindle turn of 50 digits corresponds to an axial displacement of 0.5 mm.

### Reed opening area

A conventional digital single lens reflex camera (*Nikon D3000*, sensor size 23.6 mm  $\times$  15.8 mm, effective pixels 10.2 M) with macro optics (lens *Nikkor AF-S DX 18-55 1:3,5-5,6* with 14 mm extension tube) was mounted on a positioning slide outside of the transparent housing of the

artificial mouth, facing the reeds front view. The reed - lens distance is approximately 20 mm. In this configuration a distance of 1 mm corresponds to 120 pixels approximately. This setup is used to record the reed open area during steady-state flow regimes. The infrared remote control of the camera was triggered by the measurement software. An algorithm has been implemented to extract geometrical measures of the reed front view from a JPEG-grayscale image. A subpixel resolution is achieved by fitting third order polynomials to the detected edges of the reed blades.

### Data Interfacing

The measurement data (except for the optical data) is interfaced by means of two DAQ-systems. For highly dynamical data, i.e. the reed pressure and sound pressure measurements, a *Brüel&Kjær PULSE* measurement system (*Type 3109*) was used. The data was sampled at 65.536 Hz. The quasi-stationary data was interfaced with a 8 channel digital I/O board *National Instruments Type NI 6601 PCI* with a maximum sampling rate of 2 MHz. A pulse-train trigger signal from this unit was recorded by the *PULSE* - frontend to synchronize the time series recorded with different systems in the postprocessing. The data acquisition from the PCI-board was controlled by use of the software environment *MATLAB (Data Acquisition Toolbox)*. In the post processing, the time series of both measurement systems and, where required, the image data were concatenated in one result file for subsequent data visualization.

### 3.3.6 Experimental setup

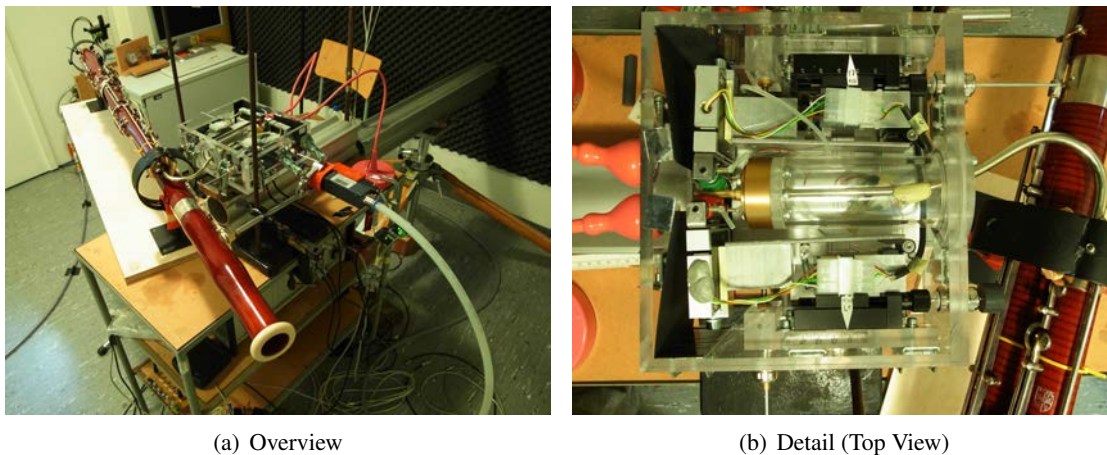


**Figure 3.9 Bassoon artificial mouth setup**

A picture of the experimental setup is shown in Figs. 3.9(a) and 3.9(b). The bassoon is mounted in a fixture, such that the main axis of the instrument is oriented horizontally. In this way, the instrument may be fingered easily with the typical handling used in musical performance.

## 3.4 Summary

In this chapter, an overview has been given on the basic physical model describing the pressure controlled reed motion in reed wind instruments. This single-degree of freedom model assumes, that the reed motion is governed by the reed displacement at its tip. Five independent parameters need to be determined for this lumped model description.

Two measurements are described to obtain the model parameters in the static and dynamic domain, and typical values are given.

A detailed overview is presented on the experimental setup constructed for this study. This artificial mouth allows to carry out characteristics measurements to determine the reed parameters, as well as blowing experiments with the sounding instrument. A key feature of the setup is the rigid fixture of the double-reed mouthpiece and a precisely adjustable lip block ( $\pm 10 \mu\text{m}$ ) to imitate realistic embouchures.

In the next chapter, details of the flow model will be discussed, and the effect of a pre-deflection of the reed due to the action of a lip force is investigated.

## 4 Modeling Realistic Embouchures with Reed Parameters

### 4.1 Reed Channel Geometry and Flow Characteristics

#### 4.1.1 The Double-Reed as a Flow Duct

Unlike in single-reeds, the cross section of the double-reed channel varies greatly along the main flow direction. This section addresses the reed's geometry in order to estimate some characteristic values of the flow, i.e. the mean velocity and Reynolds number along the main axis.

##### Geometry of the reed channel

To describe the cross section and perimeter change of the double-reed channel along the flow direction, a parametrized geometric model of the bassoon reed is introduced. It is based on several measures at characteristic cross sections of various bassoon double-reeds with a veneer caliper and does not claim to give a precise description of a specific bassoon reed.

For this representative model it is assumed that the cross section of a bassoon reed blade at any point along the reed's longitudinal axis is well approximated by either a parabolic or elliptic curve, or a linear combination of both. Thus, at any axial distance  $x$  from the reed tip, the cross section of the reed channel is described by three parameters:

The channels lateral and vertical elevation,  $w_A(x)$  and  $h_A(x)$  respectively, and a shape factor  $sf(x)$ , which determines if the curve is parabola ( $sf = 1$ ) or an ellipse ( $sf = 0$ ) or a weighted average of both.

With this linear combination, the elevation  $h(x, y)$  perpendicular to the reed's longitudinal axis is given by

$$h(x, y) = sf(x) h_p(x, y) + (1 - k(x)) h_e(x, y), \quad (4.1a)$$

where

$$h_p(x, y) = \left( 1 - \left( \frac{y}{w_A(x)} \right)^2 \right) h_A(x) \quad (4.1b)$$

and

$$h_e(x, y) = \sqrt{1 - \left( \frac{y}{w_A(x)} \right)^2} h_A(x) \quad (4.1c)$$

describe a parabolic and elliptic curve within a rectangular bounding box of dimensions  $h_A$  and  $w_A$ . A picture of a bassoon reed is given in Fig. 4.1. To model its geometry, the reed is divided into three sections

**front:** The reed blades, from tip (a) to the first wire (b), which have a parabolic shape ( $sf = 1$ );

**intermediate:** The section between first (b) and second wire (c), in which the curve is smoothly changed from parabolic to elliptical shape ( $1 < sf < 0$ );

**rear:** The lower part of the reed from the second wire (d) to the outlet end (d), where the reed halves have a elliptical shape ( $sf = 0$ ).

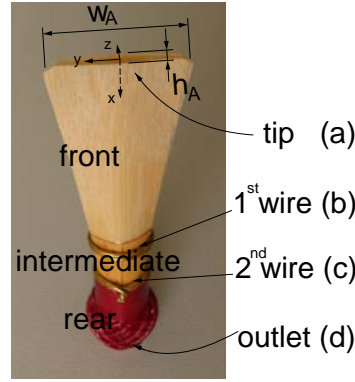


Figure 4.1 Characteristic measures on a Bassoon Double-Reed

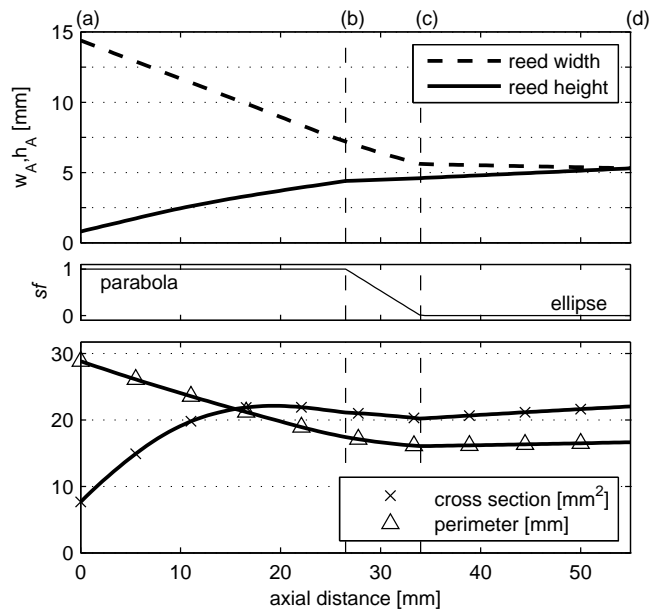


Figure 4.2 Model parameters  $w_A, h_A, s_f$  for a Bassoon Double-Reed

The following measures correspond to a synthetic bassoon reed (*Selmer Premium Plastic Medium 270M*) used in this study (in mm):

(a)	$x = 0$	$w_A = 14.4$	$h_A = 1.6$
(b)	$x = 26.5$	$w_A = 7.2$	$h_A = 4.4$
(c)	$x = 34$	$w_A = 5.6$	$h_A = 4.6$
(d)	$x = 55$	$w_A = 5.3$	$h_A = 5.3$

Using this data for the geometrical model introduced above yields an estimation of the cross section and of the perimeter along its longitudinal axis, as shown in Fig. 4.2. Note, that in the first region the reed's cross section has a local maximum, while the width and height of the reed channel are linear functions. The reed channel is subsequently constricted by the wires, between which the pressure sensor is mounted. A mesh plot of the bassoon reed blade corresponding to the above data is shown in Fig. 4.3, where the sensor position between the wires (b) and (c) is marked by a black dot.



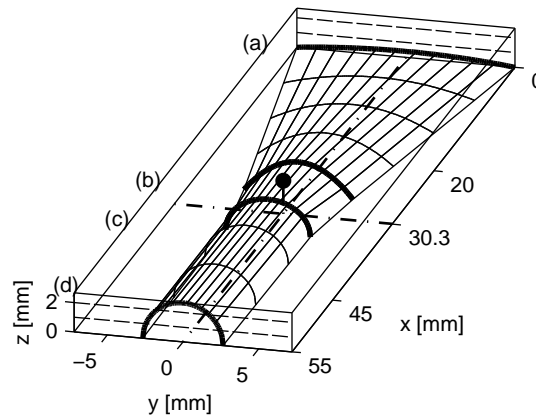


**Figure 4.3 Geometrical Model of a Bassoon Reed Blade**  
(measures taken from *Selmer Premium Plastic Medium 270M*)

The rear section of the reed ((c)-(d)) has a slightly widening cross section along the flow direction, steadily approaching a circular cross section at the outlet end ( $x = 55$  mm).

### Mean velocity and Reynolds number

The geometrical model can be used in order to estimate the change of the reed channel cross section while the blades are deflected. Here it is assumed, that the line of maximum elevation ( $y = 0$ ) of the reed can be described by the cubic function of a Bernoulli-Euler beam. The beam is clamped at  $x_{cl}$  and a force is acting on it at  $x_l$  yielding a deflection  $\Delta h$  at the tip. For the purpose of estimating the change of the flow duct dimensions the reed is closed at its tip, any intermediate state during the closure is defined simply by given values of  $x_{cl}$ ,  $x_l$  and  $h$ , instead of modeling load situation in terms of its physical properties. It is assumed further, that the reed's width  $y = f(x)$  is not affected by a change in the inlet cross section of the reed channel.

This model and the resulting cross section change of the closing reed defined in Fig. 4.2 is plotted in Fig. 4.4 for  $x_{cl} = (3/4) x_{(a)(b)}$  and  $x_l = (1/4) x_{(a)(b)}$  and  $0.1 \text{ mm} < h < 1.6 \text{ mm}$ . The measure (a)(b) is the axial distance between the section (a) and (b). With this approach, the volume and cross section along the main flow axis of the duct can be estimated roughly for any state of closure during a measurement of the reed's quasi-stationary flow characteristics.

In the following, a typical measurement run will be illustrated on the basis of Fig. 4.4: The unstressed situation is marked by the dashed line. Next, the reed is pre-deflected to a slit height  $h = 0.9 \text{ mm}$  by means of a force  $F$  imitating the embouchure of the player. The mouth pressure in this initial state is zero; this situation is marked by the dark solid line. As the mouth pressure is increased, the reed's blades deflect and the tip height decreases to zero (line colors change from dark to light). Once the critical pressure difference  $p_M$  has been reached, the reed closes completely ( $h = 0$ ). If the reed is maximally open (the dashed line), the cross section is nearly of the same size at any position along the main flow axis. For small slit heights  $h$ , however, the geometric model predicts a large change in cross section along the first 10 mm of the reed duct. To characterize the flow during the process of pressure driven reed closure in a quasi-stationary regime, the Reynolds number is calculated. It is the ratio of inertial and viscous forces in the flow and can be used to categorize flow regimes. The Reynolds number is calculated at three characteristic cross sections: Tip (a), pressure sensor position (halfway between (b) and (c)), and the outflow end (d), as shown in Fig. 4.5(a). At the tip (a), the cross section is variable, the other control points are assumed to be invariant.

The equivalent slit height  $h_{eq}$  used for the calculation of the Reynolds number  $Re$ , is the height of a rectangle with the same area  $S$  and aspect ratio  $h_{tip}/w_{tip}$  as the reed cross section measured

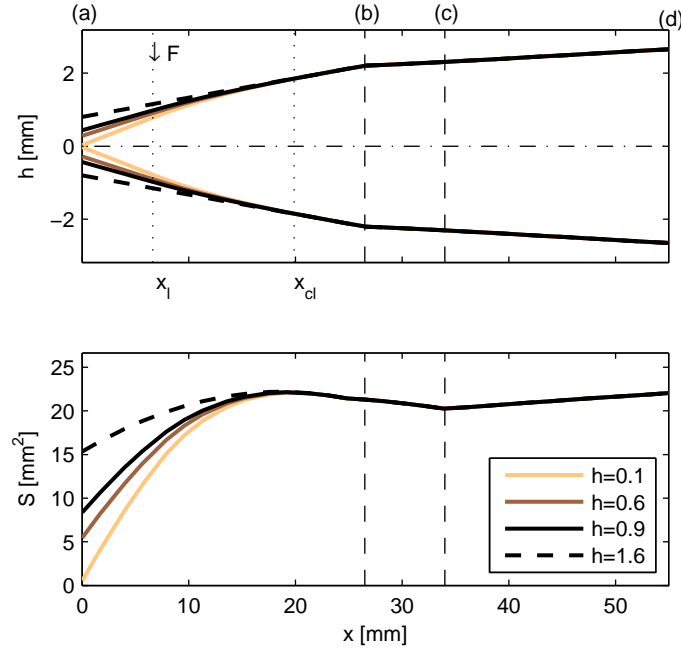


**Figure 4.4** Reed channel height and cross section profiles for several reed slit heights in the range  $0.1 \text{ mm} < h < 1.6 \text{ mm}$ .

optically. As a characteristic velocity, the mean velocity  $\bar{v} = q/S$  is calculated from the measured mean flow-rate and the respective cross section at the three control points. In Fig. 4.5 the Reynolds number and mean velocity are plotted versus the equivalent reed tip height  $h_{eq}$ , for values measured during the pressure driven quasi-stationary closure of the reed.

Throughout the closure of the reed, the velocities in the slit increase, whereas the Reynolds number has a maximum at  $h_{eq} \approx 0.5 \text{ mm}$ , at the maximum flow rate, reaching a value of 3500 at the sensor position and the reed outlet (d).

The mean flow velocity  $\bar{v} = q/S$  in the reed channel is estimated from the lower plot in Fig. 4.5 to be in the order of 10 m/s, whereas in the slit (a) the values cover a broad range from 20 to 180 m/s. In the quasi-stationary regime, the flow is laminar in the slit and in a transitional or turbulent regime at the sensor position, for mean velocities  $\bar{v}$  corresponding to reed slit heights larger than  $h_{eq} \approx 0.3 \text{ mm}$ .

Under these conditions, the following phenomena can appear in the quasi stationary flow [86]:

- flow separation at the sharp edges of the reed duct inlet forming a free jet
- turbulent mixing of the jet with the surrounding air in the reed duct on the way from the tip (a) to the sensor position (halfway between (b) and (c))
- detachment from the walls due to the change in taper of the reed duct
- friction at the channel walls

These phenomena incorporate energy dissipation that will be present as a flow-rate dependent pressure loss inside the reed, which can globally be taken into account. In the following sections, a model approach with respect to flow induced energy dissipation is derived to predict the flow-rate  $q$  from the pressure difference  $\Delta p$  measured inside and outside of the reed duct. Energy dissipation will be included in terms of coefficients scaling with the dynamic pressure and with the inlet cross section at the tip, respectively.

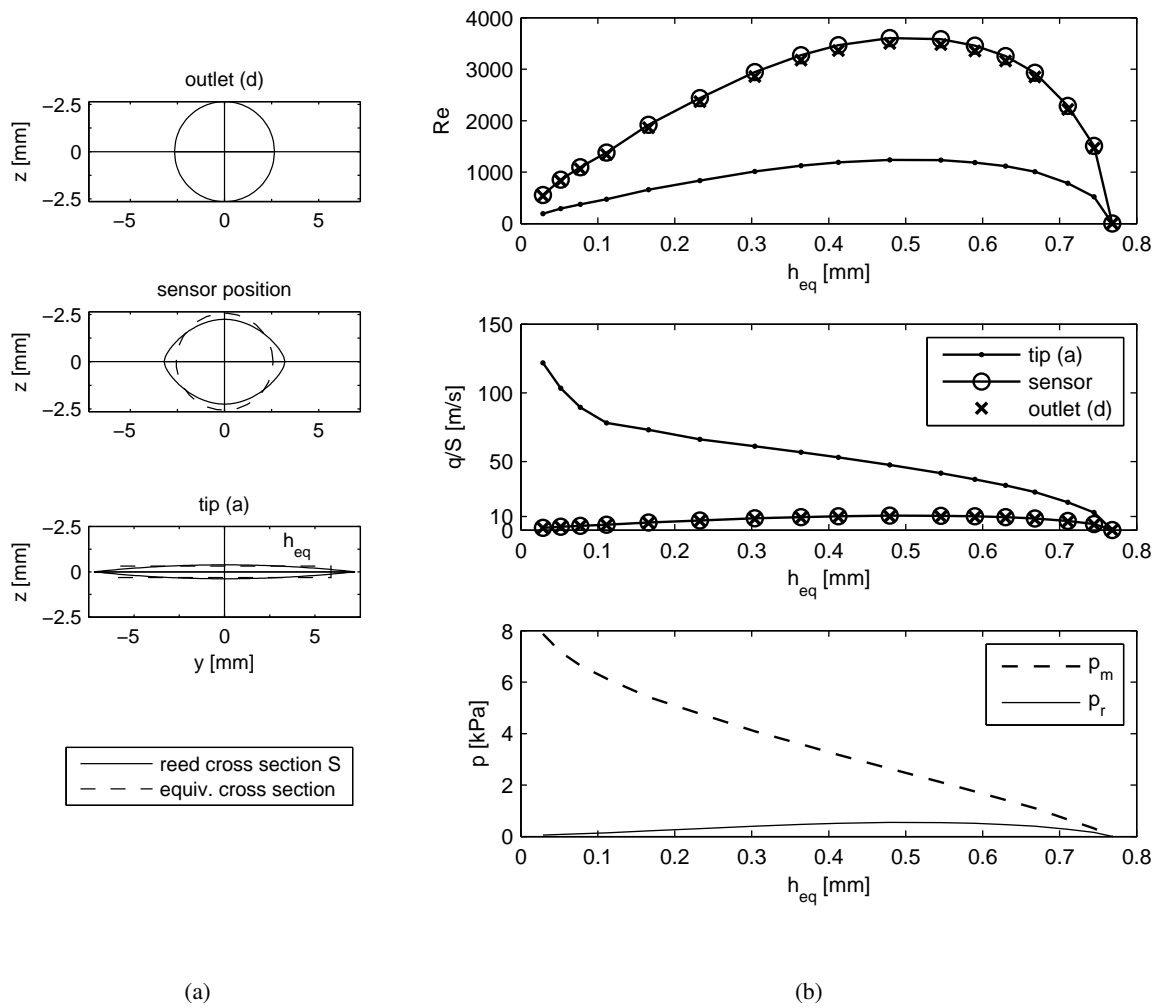


**Figure 4.5** Reynolds number  $Re$  and mean velocity  $\bar{v} = \frac{q}{S}$  at three cross sections of the reed duct, as a function of the equivalent reed slit height  $h_{eq}$  at the tip. The corresponding mouth pressure  $p_m$  and reed pressure  $p_r$  are given in the lower plot.

#### 4.1.2 Bernoulli Flow-Model with Pressure Losses

The flow phenomena given above are likely to occur in the quasi-stationary flow. As it is very difficult to directly measure the flow field inside the reed channel without disturbing it, a heuristic approach is used. The flow-related effects are included into a theoretical model for the pressure-dependence of the quasi-stationary flow-rate in a duct of a given, static geometry.

In this section, an analytical model for this duct flow based on the conservation of mass, energy, and momentum will be used and extended by including two coefficients accounting for flow-effects

$C_c$ : A constriction coefficient scaling with the duct inlet cross section accounting for flow separation at a sharp duct edges, which is referred to as the *vena contracta effect* [86].

$\zeta$ : A global pressure loss coefficient scaling with the dynamic pressure accounting for any dissipative effects such as detachment of the flow from the walls, and friction of the flow at the walls as it travels through the duct

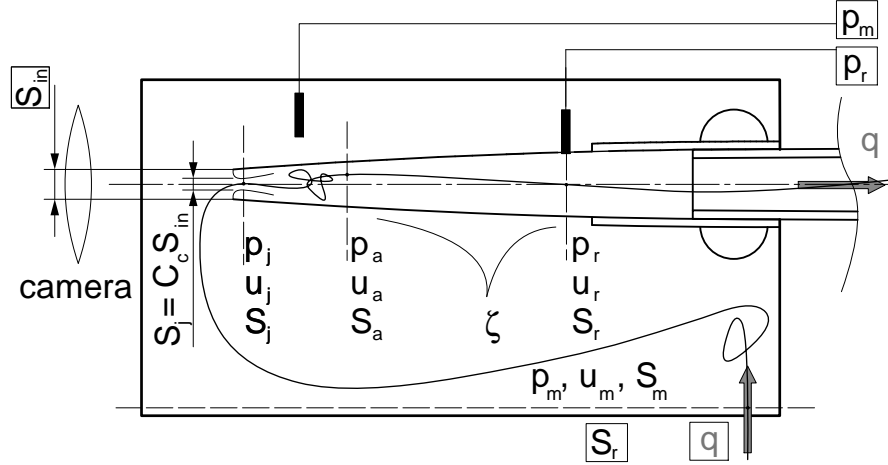


Figure 4.6 Sketch of the experimental setup

### Overview of the Measurement Setup

The measurement setup is shown in fig. 4.6. The quantities that are directly measured in the experiment are marked by a box. For practical reasons, the pressure transducer sensing the pressure inside the reed is placed some centimeters downstream of the reed tip<sup>1</sup> For the bassoon reeds in this study the sensor is mounted approximately 30 mm from the reed tip, between the wires (b) and (c) as shown in Fig. 4.3. Through a small<sup>2</sup> perpendicular hole in the channel wall about 30 mm from the reed tip, the static pressure is measured. In the following, this pressure will be denoted as the reed pressure  $p_r$ .

### Equations

As can be seen from Fig. 4.3, the reed channel is straight and has a smoothly diverging cross section. The flow entering the channel through the narrow intake cross section separates at the sharp edges of the reed to form a jet. At a short distance from the tip in the order of the reed tip height the flow expands and reattaches [160]. With the assumption that in the quasi-stationary regime the flow is uniform at the sensor position and that the air can be regarded as incompressible here, the flow can be treated as a stream tube in which Bernoulli's principle is applied.

According to energy conservation along the stream tube passing from the reed tip through the reed channel, Bernoulli's principle writes for the control sections  $S_m$ ,  $S_j$ ,  $S_a$  and  $S_r$ , as shown in Fig. 4.6:

$$p_m + \frac{\rho}{2}u_m^2 = p_j + \frac{\rho}{2}u_j^2 = p_a + \frac{\rho}{2}u_a^2 = p_r + \frac{\rho}{2}u_r^2. \quad (4.2)$$

where  $u_m$ ,  $u_j$ ,  $u_a$  and  $u_r$  are the velocities along the stream tube in the mouth  $(\cdot)_m$ , in the jet  $(\cdot)_j$ , in the reed inlet after reattachment  $(\cdot)_a$  and at the measurement point  $(\cdot)_r$ , respectively. The optically measured intake cross section  $S_{in}$  is implicitly included in the energy balance, in the jet cross section  $S_j$ . To account for possible flow separation  $S_j$  is written as a fraction of  $S_{in}$ .

The law of conservation of mass for the stream tube under the assumption of incompressibility yields

$$u_m S_m = u_j S_j = u_a S_a = u_r S_r = q. \quad (4.3)$$

<sup>1</sup>Here the channel walls are stiff enough that the dynamical properties of the reed are not influenced by the presence of the sensor. Thus it is possible to carry out dynamical measurements on the blown reed with the same setup.

<sup>2</sup>The diameter is 0.5 mm

The velocity in the mouth  $u_m$  is assumed to be negligible, as  $S_m \gg S_r$ . To account for the flow separation at the intake, the constriction coefficient  $C_c$  is introduced

$$C_c = \frac{S_j}{S_{in}}, \quad (4.4)$$

as the ratio of the jet cross section  $S_j$  and actual cross section  $S_{in}$ . Through the transparent housing of the artificial mouth,  $S_{in}$  is measured optically.

Since the flow reattaches shortly behind the intake, the duct cross section  $S_a$  is assumed to be equal to the intake cross section  $S_{in}$ :

$$S_a = S_{in}. \quad (4.5)$$

Whereas friction is neglected in the intake region due to the flow separation, a dissipative pressure drop  $\Delta p_{loss}$  is introduced to account for any pressure losses along the way from  $S_a$  to  $S_r$ , where the pressure is measured. The reed duct between these control sections is regarded as a non-ideal diffuser with the pressure loss

$$\Delta p_{loss} = \zeta \frac{\rho}{2} u_a^2. \quad (4.6)$$

where  $\zeta$  is a dimensionless loss coefficient<sup>3</sup>, which is zero in the loss-free case.

Implementing the dissipative term Eq. (4.6) in Eq. (4.2), and using the assumptions made above yields

$$p_m = p_j + \frac{\rho}{2 (C_c S_{in})^2} q^2 = p_r + m^2 \frac{\rho}{2 S_{in}^2} q^2 + \zeta \frac{\rho}{2 S_{in}^2} q^2, \quad (4.7)$$

where  $m$  is the cross section ratio

$$m = \frac{S_{in}}{S_r} \quad (4.8)$$

between inlet and outlet of the diffuser-equivalent part of the reed duct.

For the mixing zone of the jet between the intake  $(\cdot)_{in}$  and the reattachment point  $(\cdot)_a$  the conservation of momentum in the fluid is written as

$$p_j S_a + \rho u_j^2 S_j = p_a S_a + \rho u_a^2 S_a. \quad (4.9)$$

According to Eq. (4.7), the pressure  $p_1$  at the far end of the mixing zone is the static reed pressure  $p_r$  reduced by a term representing losses of kinetic energy. This pressure  $p_a$  therefore depends on the diffuser geometry and duct losses, represented by the coefficients  $m$  and  $\zeta$ , respectively, and writes

$$p_a = p_r + \frac{\rho}{2 S_{in}^2} q^2 (m^2 - 1 + \zeta). \quad (4.10)$$

Inserting Eq. (4.10) into Eq. (4.9) and solving for the pressure in the jet  $p_j$  yields

$$p_j = p_a + \rho \frac{q^2}{S_{in}^2} - \rho \frac{q^2}{S_j^2} C_c, \quad (4.11)$$

and with Eq. (4.10), the expression becomes

$$p_j = p_r + \frac{\rho}{2 S_{in}^2} q^2 \left( m^2 + 1 - \frac{2}{C_c} + \zeta \right). \quad (4.12)$$

<sup>3</sup>The diffuser converts kinetic energy into potential energy. The ideal diffuser has a vanishing mean velocity at the output, which means that the kinetic energy of the flow at the entrance is completely converted to potential energy. In practice, it is therefore useful to express the dissipative pressure drop as a fraction of the dynamic pressure at the intake, as it corresponds to the maximum amount of energy that can be converted to suite the purpose of the diffuser. Thus,  $\zeta = 1$  is the upper limit for complete dissipation and the lower limit  $\zeta = 0$  corresponds to complete conversion of kinetic energy in the ideal loss-free case

To express  $p_m$  as a function of  $p_r$ , Eq. (4.12) is used to eliminate  $p_j$  from Eq. (4.7) and a relation between the quantities determined in the experiment (marked by a box in Fig. 4.6) is obtained

$$p_m = p_r + \frac{\rho}{2 S_{in}^2} q^2 \left( m^2 + 1 - \frac{2}{C_c} + \frac{1}{C_c^2} + \zeta \right). \quad (4.13)$$

For conciseness, the coefficients  $C_c$  and  $\zeta$  representing the *vena contracta* effect and the duct loss, respectively are lumped into one scalar parameter

$$\alpha = 1 - \frac{2}{C_c} + \frac{1}{C_c^2} + \zeta, \quad (4.14)$$

and the pressure difference  $\Delta p = p_m - p_r$  is introduced to give

$$q = S_{in} \sqrt{\frac{2 \Delta p}{\rho (m^2 + \alpha)}}. \quad (4.15)$$

An interesting finding from this model is, that both the *vena contracta* coefficient  $C_c$  and the loss coefficient  $\zeta$  mainly scale the flow-curve  $q(\Delta p, S_{in})$ , but have only a small effect on its generic shape. In particular the saturation pressure is not lowered. For typical values of  $\Delta p$ ,  $S_{in}$  and  $q$  measured in a double-reed, the influence of the parameters  $m$ ,  $C_c$  and,  $\zeta$  is shown in the Appendix A2.

#### 4.1.3 Discussion of the Model

Other authors have used the modified Bernoulli equation in the form

$$q = C_{fit} S_{in} \sqrt{\frac{2 \Delta p}{\rho}} \quad (4.16)$$

with the empirical fit parameter  $C_{fit}$  to fit their measurements of the flow-rate  $q$  to the measured intake cross section  $S_{in}$  and pressure difference  $\Delta p$  [40, 4]. Adopting this strategy and applying it to measurements on a bassoon double-reed, we roughly find  $C_{fit} \approx 1$  for a wide range of reed openings (Fig. 4.7(a)). In this figure  $C_{fit}$  is plotted versus the centerline reed slit-height  $h_{max}$ , which was obtained from image analysis of the reed opening in various quasi-static regimes. Although the flow-curve  $q(\Delta p, S_{in})$  has a pronounced hysteresis<sup>4</sup>, no difference can be observed in  $C_{fit}$  between the increasing (incr.) and decreasing (decr.) pressure regime. If  $h_{max}$  becomes smaller than 0.3 mm,  $C_{fit}$  increases rapidly. Combining Eqs. 4.14, 4.15, and 4.16 the global fit parameter  $C_{fit}$  becomes

$$C_{fit} = \frac{1}{\sqrt{m^2 + 1 - \frac{2}{C_c} + \frac{1}{C_c^2} + \zeta}}. \quad (4.17)$$

This equation points out, that according to the model presented here,  $C_{fit}$  does not equal the jet contraction coefficient  $C_c$ . Besides the *vena-contracta* effect, also a change of the cross sectional area along the duct ( $m$ ) as well as other energy dissipating effects in the flow ( $\zeta$ ) are to be taken into account; the latter two are inversely related to  $C_{fit}$ .

From a measurement of the intake cross section, the parameter  $m$  is known and by fitting the parameter  $C_{fit}$  the coefficient  $\alpha$  for global energy dissipation ( $\alpha = (1/C_{fit}^2) - m^2$ ) is obtained. For slit heights smaller than 0.3 mm  $\alpha$  increases (Fig. 4.7(b)), indicating a change in the flow regime.

<sup>4</sup> Values of  $q(\Delta p)$  depend on the pressure history. The measurement run with a positive pressure gradient  $p_m = 0 \rightarrow p_M$  is called the *increasing* regime, the measurement run with a negative pressure gradient  $p_m = p_M \rightarrow 0$  is called the *decreasing* regime.

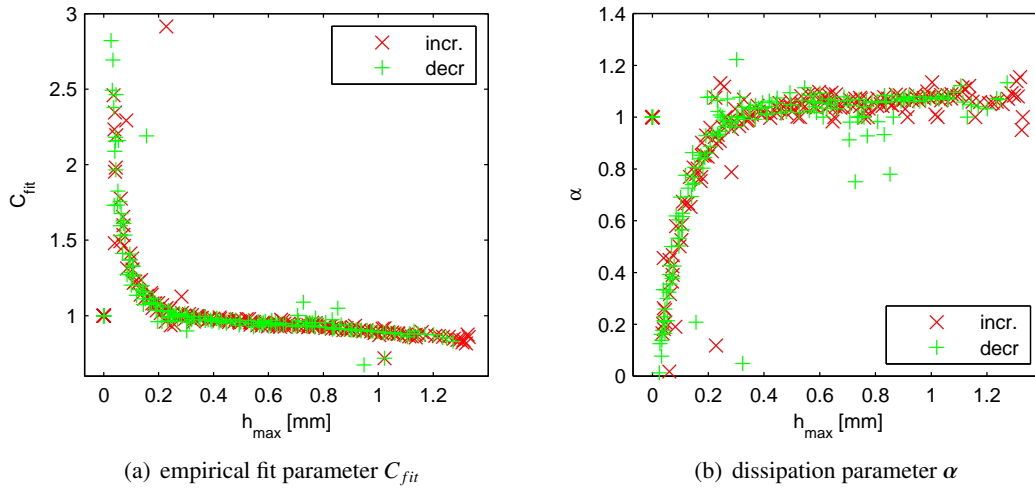


**Figure 4.7** Fit parameters for two writings of modified Bernoulli-equation describing the double-reed flow (Eqs. 4.15, 4.16).  $\alpha = \frac{1}{C_{fit}^2} - \frac{S_m^2}{S_r^2}$ .

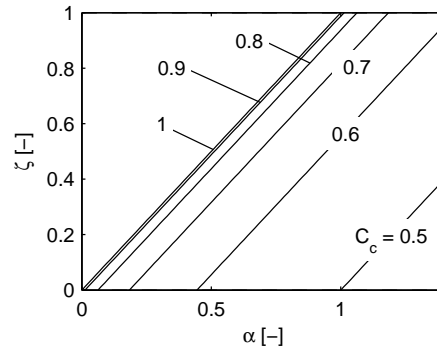


**Figure 4.8** Relations between global fit parameter  $\alpha$ , duct losses  $\zeta$  and vena contracta-effect  $C_c$  in double-reed flow.  $\zeta = \alpha - 1 + \frac{2}{C_c} - \frac{1}{C_c^2}$ . Colors correspond to a variation of  $C_c$ .

Possible combinations of the unknown parameters  $C_c$  and  $\zeta$  for a measured value of  $\alpha$  can be read from the graph in Fig. 4.8. The relevant range for the *vena contracta* effect is  $0 < C_c < 0.5$  [89] and the loss coefficient is valid within the range  $0 < \zeta < 1$ .

For  $\alpha \rightarrow 0$ , which is observed for slit heights  $h_{max}$  smaller than 0.3 mm, the model predicts, that both the jet contraction and the duct losses decrease ( $C_c \rightarrow 1, \zeta \rightarrow 0$ ).

This is due to the fact that the *vena contracta* effect vanishes, as the slit height  $h$  becomes comparable to the edge-radius  $R$  of the reed: Idelchik gives  $C_c = 0.96$  for  $R/d \approx 0.5$  [91].

For a circular intake of diameter  $d$ , Nurick [133] suggests the approximation

$$C_c(R/d) = \left( \frac{1}{C_{c,Ref}^2} - 11.4 \frac{R}{d} \right)^{-\frac{1}{2}}, \quad (4.18)$$

where  $C_{c,Ref}$  is the sharp edge value  $C_c(R/d = 0)$ .

Regarding  $d$  as a characteristic length and inserting the critical slit height  $h = 0.3$  mm, the jet contraction would vanish if the edge radius of the reed blade  $R$  were larger than 0.08 mm. According to Nurick, other authors state that for  $R/d \geq 0.14$ , no *vena contracta* can form [133], so that  $C_c = 1$ . For slit heights  $h_{max}$  larger than 0.3 mm, the edge of the reed blade can be considered sharp and flow separation occurs. For the case of reed woodwinds, Hirschberg *et al.* give  $0.5 < C_c < 0.61$

in quasi-stationary regimes [89] based on theoretical considerations. This has been confirmed experimentally by measurements of van Zon *et al.* [160]. For single-reeds in operating conditions, this range of values for  $C_c$  has recently been confirmed numerically [39] and experimentally [115]. For the case of a sharp-edged slit-like orifice in an plate mounted perpendicular to the flow direction in a tube, Durrieu *et al.* [51] found  $0.65 < C_c < 0.75$ .

A simple approach is to assume independently of the slit height  $C_c = 0.5$  for the jet contraction coefficient and neglecting further duct losses  $\zeta = 0$ . This yields  $\alpha = 1$ .

### Comparison of Measurement with Model

It is remarkable, that for the simple assumption  $C_c = 0.5$ ,  $\zeta = 0$  the experimental data is in very good qualitative and quantitative agreement with the model Eq. (4.15). This applies to both the increasing<sup>4</sup> and (Fig. 4.9(a)) and decreasing<sup>4</sup> (Fig. 4.9(b)) regime (Fig. 4.9). The fitting has been separately for increasing and decreasing regime, yielding a set of fit parameters  $(\cdot)_{incr.}$ ,  $(\cdot)_{decr.}$  for both regimes.

Note, that the ticks on the upper x-axis are not equidistant with respect to  $S_{in}$ , but indicate the instantaneous measurement value of  $S_{in}$  corresponding to the respective measurement point.

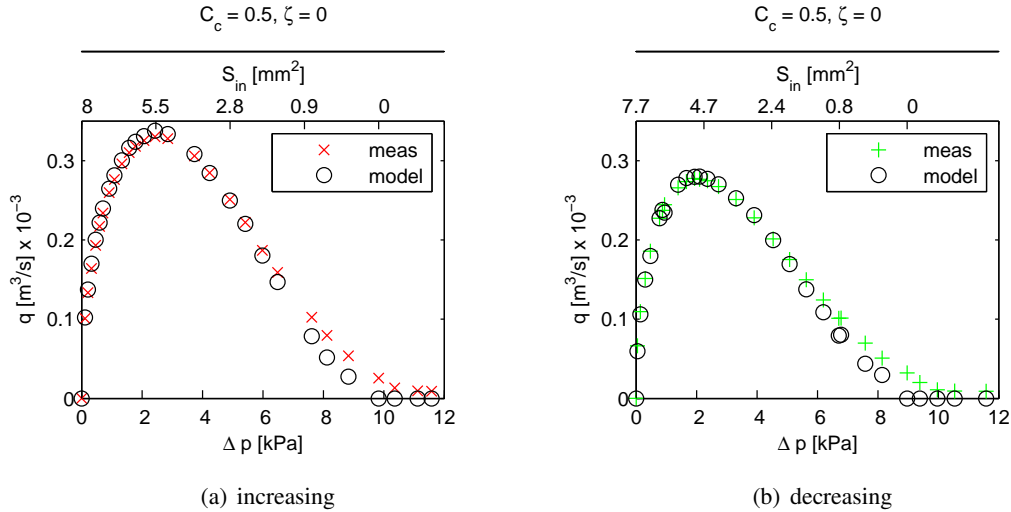


**Figure 4.9** Volume flow through a double-reed channel as a function of pressure difference  $\Delta p$  and inlet cross section  $S_{in}$ . Comparison of measurement and model Eq. (4.15), with  $\alpha = 1$ . Increasing (a) and decreasing (b) pressure regime.

The saturation pressure  $p_{m,sat}$  and the flow maximum  $q_{max}$  match well with the values predicted by the model. Expectedly, the assumption that  $\alpha$  is independent of the slit height results in a quite drastic underestimation of the flow as the pressures  $\Delta p$  exceed the saturation pressure and approach the reed closing pressure  $p_M$  ( $p_{M,incr.} = 9.8$  kPa,  $p_{M,decr.} = 8.9$  kPa). Here, also the measurement accuracy in  $S_{in}$  should be taken into account, estimations for the uncertainty will be given in the next section.

In the non-dimensional plot in Fig. 4.10 it can be seen that the flow-characteristics in the increasing and decreasing pressure regime do not reveal qualitative differences. The distinct hysteresis in the flow-curve is directly related to the hysteresis in the reed intake cross section ( $S_{\infty,incr.} = 8$   $\text{mm}^2$ ,  $S_{\infty,decr.} = 7.7$   $\text{mm}^2$ ). Other authors have related the hysteresis to a viscoelasticity in the reed material [1]. This creeping however is a long-term effect, and its role is not clear in the short time scale (minutes) of a quasi-static experimental run in which the hysteresis is observed. For a double-reed friction at the lateral contact areas of the reed blades seems to be a possible explanation as well.



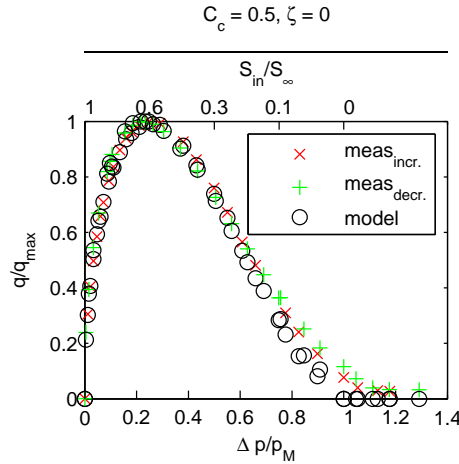


**Figure 4.10 Non-dimensional representation of the pressure-flow characteristics.**  
**The displayed measurement and model data correspond to Fig. 4.9**  
 $(p_{M,incr.} = 9.8 \text{ kPa}, p_{M,decr.} = 8.9 \text{ kPa}, S_{\infty,incr.} = 8 \text{ mm}^2, S_{\infty,decr.} = 7.7 \text{ mm}^2).$

### Comparison with an Oboe Double-Reed

It is remarkable, that there are distinct qualitative differences between the data obtained in this study for a bassoon double-reed and the data by Almeida *et al.* [4] for an oboe double-reed.

When comparing their data with the classical Bernoulli flow-model, they found that the measured saturation pressure was significantly lower ( $p_{m,sat}/p_M = 1/4$ ) than the theoretical prediction of the classical single-reed model ( $p_{m,sat}/p_M = 1/3$ ). Adhering to the assumption of a linear dependence of the intake cross section upon the pressure difference, they concluded, that the recovery of static pressure in the diffuser-like staple would introduce a change in the flow-curve, such that the location of the maximum is shifted to the lower pressure differences  $\Delta p$ .

In the present study of the bassoon reed,  $p_{m,sat}/p_M$  was also close to  $(1/4)$ . That is in good agreement with the presented model under the assumption of a constant *vena contracta* ( $C_c = 0.5$ ) and no additional friction losses ( $\zeta = 0$ ).

Besides the differences in the model that was used to predict  $p_M$ , differences in between the reeds and also some practical aspects measurement setup may further account for the discrepancy with the oboe study:

**Mean velocity:** As the intake cross section of an oboe reed is much smaller than that of a bassoon reed, and the pressure  $p_M$  needed to close the reed is about 5 times higher in the oboe. The mean velocities in the slit scales with  $\sqrt{2\Delta p/\rho}$  and thus are considerably larger. Besides the vanishing contraction for large ratios of edge radius to slit height, the constriction coefficient  $C_c$  also increases with the mean velocity [51]. This might be another reason for the less prominent jet constriction in the oboe reed.

**Sensing position:** The pressure sensor in the oboe-study [4] is mounted at the end of the staple, 70 mm behind the reed intake, where the cross section  $S_r$  is approximately 3 times larger than at the staple input; the staple itself is stiff. Here the sensor is mounted 30 mm behind the inlet. What is considered the diffuser input cross section here, is in the delectable front part of the reed. Therefore the taper of the “diffuser” depends upon the pressure.

**Flow measurement principle:** In the oboe study [4], the flow is decelerated by a diaphragm at the reed output end. Here, the reed pressure  $p_r$  is measured to determine the flow-rate from the pressure difference across the diaphragm. Here, in contrast, the flow-rate is measured by means of a thermal mass-flow meter and no diaphragm is used. Therefore, the situation is almost identical to the playing situation, as no significant resistances have been added to the flow path<sup>5</sup>.

<sup>5</sup>A conical resonator of 830 mm length (a bassoon bocal and wing) was connected to the reed during the characteristics measurement. A small resistance ( $\Delta p \approx 50 \text{ Pa}$ ) is incorporated by piece of foam, that has been loosely attached to the far end of the cone to prevent auto-oscillations of the reed.

With the setup presented in this study, the experiment and a model with a constant value  $\alpha$  are in good agreement, except for the systematic underestimation of the flow-rate when the slit height becomes very narrow.

## Conclusion

A quasi-static model for the flow-rate through a double-reed channel as a function of differential pressure and intake cross section has been derived. It is based on the Bernoulli-Equation, extended by two coefficients accounting for the constricted effective intake cross section ( $C_c$ ), due to flow separation at the sharp inlet-edges, and for pressure losses in the duct flow ( $\zeta$ ), due to dissipation. The existence of both effects increases the pressure inside the reed channel, but their respective fraction to the increase cannot be identified from a single point pressure measurement.

In the model Eq. (4.15), the coefficients  $C_c$  and  $\zeta$  are lumped into one global parameter  $\alpha$ , according to Eq. (4.14). Values for  $\alpha$  have been determined by fitting the model to experimental data, and for  $\alpha \approx 1$  a reasonably good fit is obtained for slit heights larger than 0.3 mm. For smaller slit heights,  $\alpha$  decreases which can be explained by the vanishing *vena contracta* effect as the slit height becomes comparable to the edge radius at the reed blade. Provided a reasonable guess on one of the two parameters in Eq. 4.14, the contribution of the jet contraction ( $C_c$ ) or other energy dissipating flow effects ( $\zeta$ ) can be estimated. Possible parameter combinations of  $\zeta$  and  $C_c$  for a given  $\alpha$  are shown in Fig. 4.8. The model presented here considers explicitly, that the reed pressure is measured at a distance from the reed tip. The possible occurrence of energy dissipating effects in the flow traveling into and through the reed channel are included. There are two key findings from this model:

- 1) The empirical fit factor  $C_{fit}$  in a model

$$q = C_{fit} S_{in} \sqrt{\frac{2\Delta p}{\rho}}$$

is not identical with the jet contraction coefficient  $C_c$ , also contributions of a change in the reed duct's cross sectional area and other energy dissipating effects have to be considered.

- 2) A pressure recovery in the duct does not significantly change the shape of the reed's quasi-static pressure vs. flow characteristics.

## 4.2 Quasi-static Interaction of Flow and Reed-Channel

### 4.2.1 Pressure-driven Deformation of the Duct Intake

The previous sections have dealt with the governing effects in the double-reed flow and an analytic description of the latter. For every quasi-stationary working point, the reed intake cross section  $S_{in}$  was assumed to be known from a measurement. However, since the mouth pressure driving the flow deflects the reed blades, the reed intake cross section of the duct can be expressed as a function of the differential pressure  $\Delta p$  across the reed. This interaction will qualitatively be analyzed in this section, based on optical measurements of the intake cross section  $S_{in}$  during quasi-static closure of the reed.

The double-reed reed intake cross section is formed by two opposing reed blades which have a parabolic shape, as shown in Fig. 4.11. Since the action of a lip force  $F_l$  will be taken into account in the next section, the following nomenclature is introduced here for to describe the deformation of the reed intake:

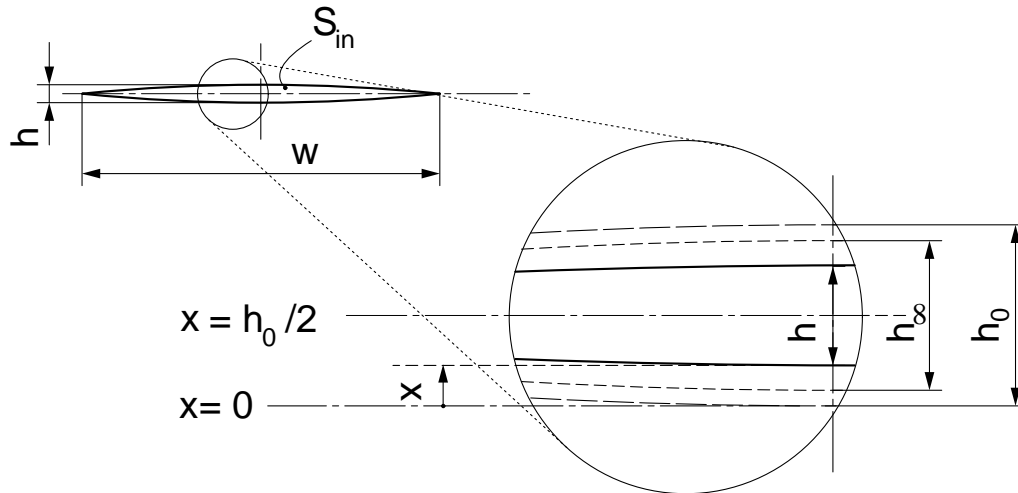


**Figure 4.11** Schematic of the reed intake and characteristic measures of the reed-slit height. Three different deformation stadia:  $h_0$ :  $F_l = 0$ ,  $\Delta p = 0$ ;  $h_\infty$ :  $F_l > 0$ ,  $\Delta p = 0$ ;  $h$ :  $F_l > 0$ ,  $\Delta p > 0$ .

$h$ : is the instantaneous reed slit height which is a result of both lip force and pressure difference ( $h = f(\Delta p, F_l)$ )

$h_\infty$ : is the reed slit height as adjusted by the mechanical action of lips, in absence of pressure difference ( $h_\infty = h(0, F_l)$ )

$h_0$ : is the maximum reed slit height in absence of differential pressure and lip force.

$x$ : is the instantaneous reed tip position which is a result of both lip force and pressure difference ( $x = f(\Delta p, F_l) = \frac{1}{2} (h_0 - h(\Delta p, F_l))$ ).

In absence of lip force and differential pressure  $x = 0$ .

Assuming that the reed blades at the tip are described by a parabola (Eq. 4.1b), the intake cross section  $S_{in}$  is

$$S_{in} = \frac{2}{3} w h, \quad (4.19)$$

where  $w$  is the reed channel width (Fig. 4.11), which is assumed to be constant as a first approximation.

In the classical model of single-reed flow, a linear relationship is assumed between the pressure and the position of the reed tip  $x(\Delta p)$ . In the double-reed case, however, there are some reasons to question the linearity: Firstly, double-reed blade has a convex surface and it is not obvious, that such a shape has a linear mechanical stiffness. Secondly, the reed-pressure  $p_r$  depends on the reed channel geometry and duct losses increase as the reed closes, which was addressed in the above section. The model proposed can be applied to any single or double-reed instrument. Practical issues of mounting pressure sensors on the reed and the reed dimensions, may be problematic when comparing the present results with that of an oboe reed. On the other hand, the linear relation between the deflection  $x$  at the reed tip and the input cross section  $S_{in}$  is questionable, as it is based on the assumption of a constant width  $W$  of the reed channel. This has been used in previous works on double-reeds [125, 101, 1], where the cross section has been estimated to be  $S_{in} = (1/2) wh$  (diamond-shaped) or  $S_{in} = (2/3) wh$  (parabola-shaped). The present experiments, however, reveal a non-linear relationship between the reed-slit height  $h$  and the reed's cross sectional area  $S_{in}$ :

As the reed closes, the contact points between upper and lower reed blade converge and the width  $w$  of the reed channel diminishes. In Fig. 4.12 a slight linear decrease of the equivalent reed channel

width  $\bar{w}$  can be observed as the slit height decreases from its initial value. For slit-heights smaller than 0.4 mm the curve progressively steepens. Since the value for the reed width  $w$  as determined by image analysis is most sensitive to lighting conditions, the hypothetical reed width  $\bar{w} = (3/2) S_{in}/h$  as calculated from measured values for  $S_{in}$  and  $h$ , is shown in Fig. 4.12.

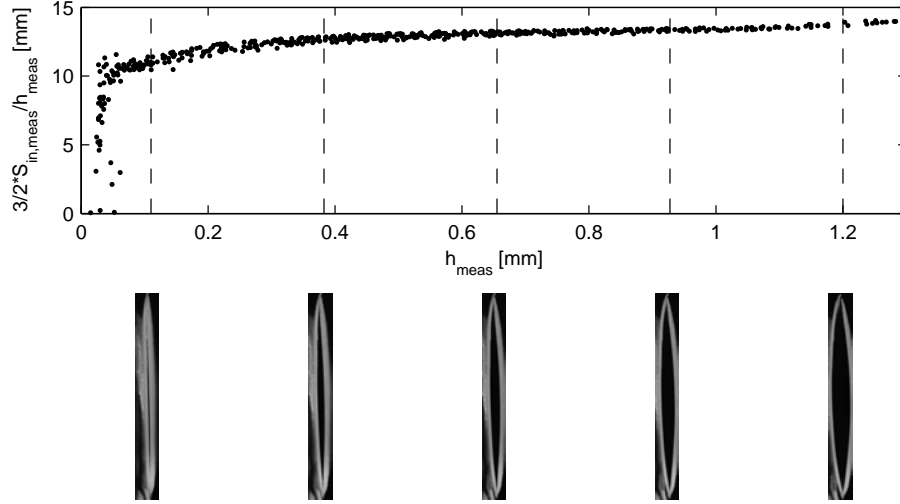


**Figure 4.12** Hypothetical reed width  $\bar{w} = \frac{3}{2} \frac{S_{in,meas}}{h_{meas}}$  versus measured reed slit height  $h_{meas}$ .  
Data from 12 independent measurements

In light of these uncertainties, a heuristic investigation of the double-reed behavior through fitting models to experimental data is a reasonable approach. Three models are employed to fit the measured data pairs  $\{S_{in}, \Delta p\}$ , where  $\Delta p = p_m - p_r$  according to Fig. 4.6.

$$S_{in} = S_{\infty} \left( 1 - \frac{\Delta p}{p_M} \right) \quad (4.20a)$$

$$S_{in} = S_{\infty} \left( 1 - \frac{\Delta p}{p_M} \right) + C (\Delta p)^2 \quad (4.20b)$$

$$S_{in} = S_{\infty} \left( 1 - \frac{\Delta p}{p_M} \right)^{\kappa} \quad (4.20c)$$

The linear model Eq. (4.20a) assumes a direct analogy to the single-reed flow [102] (see also Eq. (3.14)).

Model Eq. (4.20b) corrects the linear model Eq. (4.20a) by introducing a quadratic term. This reflects a stiffening of the reed as it approaches the complete closure. Model Eq. (4.20c) is a three-parameter ( $S_{\infty}$ ,  $p_M$ ,  $\kappa$ ) rational function, corresponding to a non-linear stiffness law. This approach has been used by Almeida *et al.* [5] in modelling an oboe reed.

Other approaches to considers the stiffening of the reed near closure have been used by Nederveen<sup>6</sup> [125, 127, 126, 129] and van Walstijn *et al.* [158].

When fitting these models to experimental data, the lower limit  $\min(S_{in}) = 0$  has been forced. The results of the fit are shown in Fig. 4.13(a).

<sup>6</sup>In contrast to Eq. (4.20b) Nederveen proposes a non-linear factor proportional to  $\frac{1}{h/2-x}$  for the reed stiffness. It then becomes infinitely large as the reed approaches complete closure ( $x \rightarrow \frac{h}{2}$ ), which is advantageous for physical dynamical modeling:  $S_{in}$  cannot become negative.

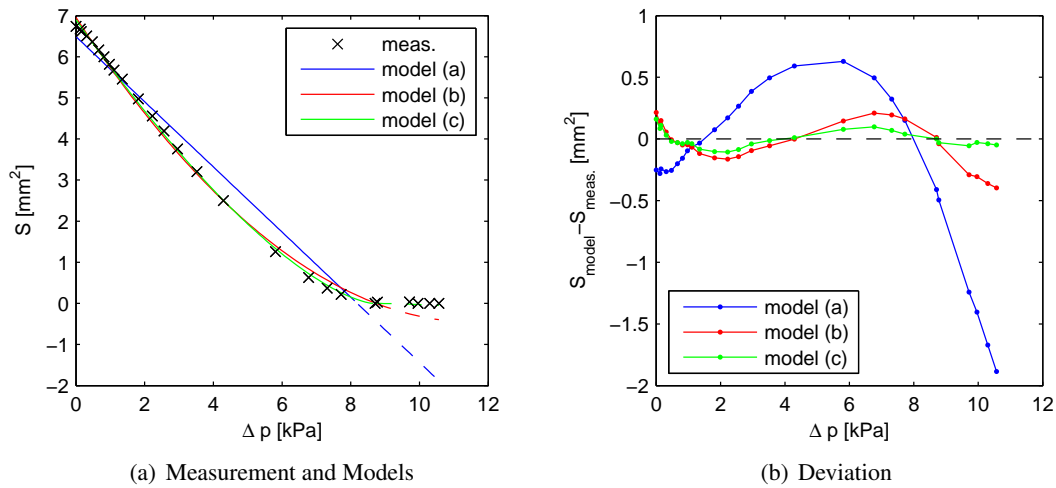


**Figure 4.13** Intake cross section  $S_{in}$  of a bassoon double-reed, as a function of a measured pressure difference  $\Delta p$ . Measurement and fit models

Eq. (4.20a), with  $S_{\infty} = 8.18 \text{ mm}^2$ ,  $p_M = 7.9 \text{ kPa}$

Eq. (4.20b), with  $S_{\infty} = 8.40 \text{ mm}^2$ ,  $p_M = 6.6 \text{ kPa}$  and  $C = 0.0336 \text{ (mm/kPa)}^2$

Eq. (4.20c), with  $S_{\infty} = 8.44 \text{ mm}^2$ ,  $p_M = 9.5 \text{ kPa}$  and  $\kappa = 1.47$

Note that for both models Eq. (4.20a) and Eq. (4.20b),  $S_{in}$  becomes negative for  $\Delta p > p_M$ . This range is indicated in Fig. 4.13(a) by dashed lines. For model Eq. (4.20c)  $S_{in}$  becomes complex due to the square-root in this pressure range. Fig. 4.13(a) shows the real part only<sup>7</sup>.

As illustrated in Fig. 4.13(b), the model Eq. (4.20c) provides the best overall fit to the experimental data, with  $\kappa \approx 1.5$ . With this model, analogously to the linear model Eq. (4.20a) and in contrast to the quadratic model Eq. (4.20b), the interpretation of the fit-parameter  $p_M$  is straightforward, as it denotes the pressure difference  $\Delta p$ , where the reed is completely closed.

The model parameter  $\kappa$  can be interpreted as a constant characterizing the progressive characteristics of a reed-blade equivalent spring.

#### 4.2.2 Reed-Flow Model including Channel Deformation

Two models have been derived in the previous sections 4.1.2 and 4.2.1, respectively.

**Eq. (4.15):** depicts the relation of the flow-rate  $q$  through a reed channel of known geometry ( $S_{in}, S_r$ ) as a function of differential pressure  $\Delta p$ .

**Eq. (4.20c):** characterizes the dependence of the intake cross section  $S_{in}$  upon the differential pressure  $\Delta p$ .

With these two equations, an explicit expression can be given for the flow-rate  $q$  through the double-reed channel, as a function of differential pressure  $\Delta p$  and invariant scalars. Inserting Eq. (4.20c) into Eq. (4.15), yields

$$q = S_{\infty} \left(1 - \frac{\Delta p}{p_M}\right)^{\kappa} \sqrt{\rho \left( \left(\frac{S_{\infty}}{S_r}\right)^2 \left(1 - \frac{\Delta p}{p_M}\right)^{2\kappa} + \alpha \right)}, \quad (4.21)$$

<sup>7</sup>For physical modeling purposes it would be useful to implement  $S_{in} = \Re\{S_{\infty} \left(1 - \frac{\Delta p}{p_M}\right)^{\kappa}\}$  and further adopt Nederveens implicit approach [129] of using a  $\frac{1}{S_{in}}$ -proportional term for the reed stiffness.

where  $S_r$  is the reed cross section at the sensor position. With the substitutions

$$q_A = S_\infty \sqrt{\frac{2 p_M}{\rho}}, \quad (4.22)$$

and

$$\epsilon = \left( \frac{S_\infty}{S_r} \right)^2, \quad (4.23)$$

this can be simplified to give

$$q = q_A \left( 1 - \frac{\Delta p}{p_M} \right)^\kappa \left( \frac{\Delta p}{p_M} \right)^{\frac{1}{2}} \left( \epsilon \left( 1 - \frac{\Delta p}{p_M} \right)^{2\kappa} + \alpha \right)^{-\frac{1}{2}}. \quad (4.24)$$

. This model is a generalization of the classical reed model. Besides the critical pressure to close the reed  $p_M$  and the flow parameter  $q_A$ , it includes three additional non-dimensional parameters

**Flow parameter  $\alpha$** , accounting globally for energy dissipation in the flow (Eq. (4.14)),

**Stiffness parameter  $\kappa$** , representing the spring-characteristics of the reed (Eq. (4.20c)), and

**Geometrical parameter  $\epsilon$** , regarding the pressure-recovery in the tapering reed channel.

Note, that the parameter  $m = \frac{S_{in}}{S_r}$  introduced in Eq. (4.15) does not appear here. The taper of the duct is represented here by the parameter  $\epsilon$ . In contrast to  $m = f(\Delta p)$ , which depends on the instantaneous value of the reed intake cross section  $S_{in}$ , the parameter  $\epsilon = \text{const.}$  represents the pre-deflection of the reed in absence of pressure.<sup>8</sup>

The single-reed flow model [102, 40], based on the assumption of Bernoulli-flow and a linear relationship between differential pressure and reed-intake cross section is part of this formulation, if  $\alpha = \kappa = 1$  and  $\epsilon = 0$  are selected. Note that, to avoid  $q$  become complex, a distinction of cases should be made in Eq. (4.24), such that  $q = 0$  for complete closure  $p_m > p_M$ .

### 4.2.3 Influence of Model Parameters

The discussion of the qualitative influence of the additional parameters  $\alpha$ ,  $\epsilon$  and  $\kappa$  on the shape of the pressure-flow characteristics starts with considerations on their limiting values:

**Flow parameter  $\alpha$ :** From a curve-fitting problem, where  $\alpha$  is the only free fit parameter (using Eq. (4.15) and experimental data), a range of  $0.8 < \alpha < 1.2$  has been determined experimentally. An exemplary juxtaposition of experimentally determined flow-rates and theoretical prediction for  $\alpha = 1$  is shown in Fig. 4.9; other confirming examples will be discussed last section of this chapter (Fig. 4.20).

**Stiffness parameter  $\kappa$ :** In the same manner, the spring parameter  $\kappa$  has been estimated to be  $\kappa \approx 1.5$  in section 4.2.1. A linear stiffness, which is often assumed for the single-reed corresponds to  $\kappa = 1$ .

**Geometrical parameter  $\epsilon$ :** The geometrical parameter  $\epsilon$  maps the role of the pre-constriction of the reed intake by the embouchure, as the musician presses his lips against the blades. The upper limit for  $\epsilon$  corresponds to a complete retraction of the lips from the reed. The reed is in its initial position, with a maximum slit height  $h_0$  (see Fig. 4.11). The lower limit is given by the smallest intake cross section, where oscillations of the reed are still possible. From

<sup>8</sup>Similar to the geometrical parameter  $m = \frac{S_{in}}{S_r}$  defined in section 4.1.2, the geometrical parameter  $\epsilon$  maps the role of the diffuser-like double-reed geometry. In contrast to  $m$ , which depends upon the instantaneous value of the reed intake cross section  $S_{in}$ , the parameter  $\epsilon$  is constant during reed closure.

blowing experiments with realistic embouchures the limits regarding the reed slit height are found to be  $0.2 \text{ mm} < h_\infty < 1.6 \text{ mm} = h_0$  which corresponds to an intake cross section ratio  $0.2 < S_{in}/S_r < 0.8$  and therefore  $0.04 < \epsilon < 0.64$ .

To illustrate the impact of these model parameters on the pressure-flow characteristics Eq. (4.24) is written in a non-dimensional form, using  $q_A$  and  $p_M$  to normalize  $q$  and  $\Delta p_{meas}$ :

$$\tilde{q} = (1 - \tilde{p})^\kappa \tilde{p}^{\frac{1}{2}} \left( \epsilon (1 - \tilde{p})^{2\kappa} + \alpha \right)^{-\frac{1}{2}}, \quad (4.25)$$

where the numeric values in the case of a bassoon reed may vary within the following limits

$0.7 < \alpha < 1.3$  for the flow parameter,

$1 < \kappa < 2.5$  for the stiffness parameter, and

$0.04 < \epsilon < 0.64$  for the geometrical parameter,

according to the considerations above.

The impact of these parameters on the non-dimensional pressure-flow characteristics are plotted in Fig. 4.14, for typical channel dimensions of a bassoon double reed ( $S_\infty = 8.2 \text{ mm}^2$ ,  $S_r = 21 \text{ mm}^2$ ). For comparison, the plot also shows the characteristic curve of the classical single-reed model ( $\alpha = \kappa = 1$  and  $\epsilon = 0$ ) and all curves are normalized to the maximum flow-rate  $\tilde{q}_{max}$  of the single-reed, which is  $\tilde{q}_{max} = 2/(3\sqrt{3})$ .

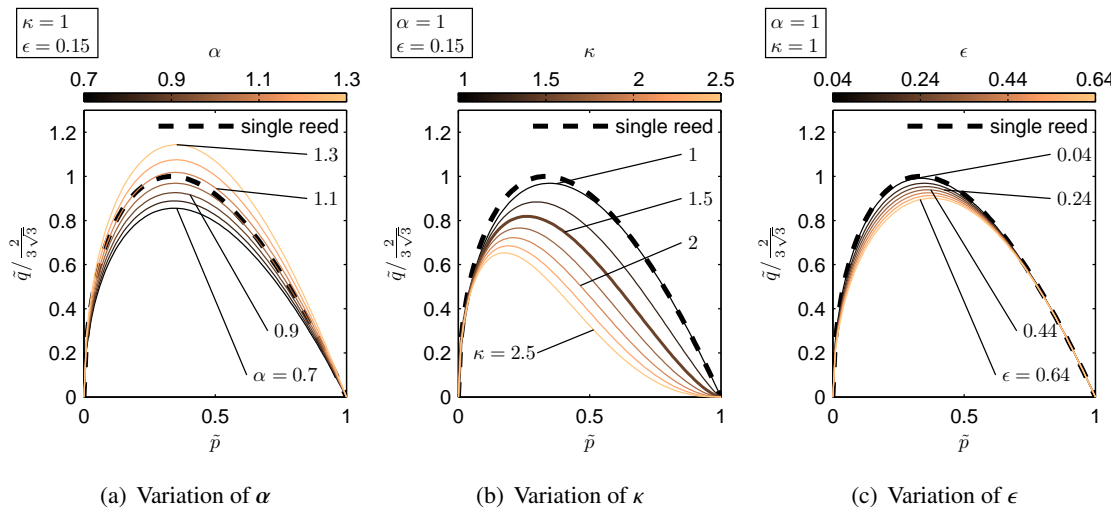


**Figure 4.14** Impact of the model parameters  $\alpha$ ,  $\kappa$  and  $\epsilon$  on the non-dimensional pressure-flow characteristics according to a general model for the reed-flow Eq. (4.25). The classical single-reed flow curve corresponds to  $\alpha = \kappa = 1$  and  $\epsilon = 0$  (dashed line)

It can be seen, that  $\kappa$  has the greatest qualitative influence on the pressure-flow characteristics. For  $\kappa > 1$ , the saturation pressure  $\tilde{p}_{m,sat}$  and corresponding flow-rate  $\tilde{q}_{max}$  are lowered. Further, a smooth decay of the flow-rate is introduced as the differential pressure approaches the reed-closing pressure threshold. In this region, the uncertainty in the measurement of the intake cross section  $S_{in}$  is a large source of error for the pressure-flow characteristic. It has been observed earlier, that  $\kappa \approx 1.5$  is a reasonable estimate for the non-linearity of the  $S_{in}$  vs.  $\Delta p$  characteristics (see section 4.2.1, Fig. 4.13). For that reason, the curve for  $\kappa = 1.5$  is printed with a thick linewidth in Fig. 4.14(b).

Another observation from Fig. 4.14 is, that the neither the flow parameter  $\alpha$  nor the geometrical parameter  $\epsilon$  lowers the saturation pressure  $\tilde{p}_{m,sat}$ , compared to the single reed curve with  $\tilde{p}_{m,sat} = 1/3$ .

Within its limits valid for the bassoon double-reed, the geometrical parameter scales the maximum flow  $\tilde{q}_{max}$  within  $0.9 \cdot 2/(3\sqrt{3}) < \tilde{q}_{max} < 0.99 \cdot 2/(3\sqrt{3})$ , with a slight increase of the saturation pressure  $\tilde{p}_{m,sat}$  for increasing  $\epsilon$ .

On the other hand, the flow parameter  $\alpha$  scales the maximum flow  $\tilde{q}_{max}$  within  $0.85 \cdot 2/(3\sqrt{3}) < \tilde{q}_{max} < 1.15 \cdot 2/(3\sqrt{3})$ , with negligible impact on the saturation pressure  $\tilde{p}_{m,sat}$ .

The model predicts, that flow-related phenomena, such as the *vena-contracta* effect at the inlet, kinetic energy loss due to friction and kinetic energy conversion in the diffuser-like double-reed have a very small impact on the shape of the flow-characteristics.

In fact significant qualitative changes in the flow-curve can be ascribed to the non-linear stiffness of the reed blades. The conclusion of these observations is, that for curve fitting purposes  $\alpha$  and  $\epsilon$  can be lumped into one parameter scaling the flow maximum  $\tilde{q}_{max}$ , and only  $\kappa$  has to be retained to qualitatively change the flow-characteristics.

#### 4.2.4 Experimental Verification

The quantities governing the reed-flow are measured directly and independently in the experiment (see Fig. 4.6). To verify the theory, the experimental results will be discussed with respect to the measurement uncertainty.

##### Measurement Uncertainties

The sensor for the reed pressure measurement is accurate within 0.1 % of the full-scale measurement range. The uncertainty corresponds to  $\pm 35$  Pa, which is very small compared to the measurement values in the range of several kPa and will be neglected in the following.

The accuracy of the flow meter is within  $0.09 \text{ nl/min} \pm 0.3 \%$  of the reading, which corresponds to a fairly large relative error at small flow-rates<sup>9</sup>.

The largest uncertainty, however, is due in the measurement of the reed intake cross section. Though the spatial resolution of the image is as large as 100 pixels per mm, the algorithm to determine the cross section from a gray-scale image of the reeds front view is very sensitive to lighting conditions. As discussed in the previous section, precise information on the intake cross section is crucial, when estimating the flow in a coupled reed-model from the differential pressure, solely: A non-linear dependence of intake cross section and differential pressure greatly influences the pressure-flow characteristics of the reed-valve.

To estimate the inherent uncertainty in the cross section analysis, for each gray-scale image of the reed's front view the edge-detection algorithm was run several times at different black/white binarization thresholds between zero and unity. After removal of outliers by means of Grubbs' test, the median of the remaining threshold dependent values of  $S_{in}$  is presumed to be the actual physical value of the intake cross section. The measurement uncertainty can be estimated from the 25<sup>th</sup> and 75<sup>th</sup> percentiles of the empirical distribution function. This procedure has been performed for each single image, which represents one measurement point in the quasi-stationary pressure-flow characteristics.

With the knowledge of these uncertainties, the validity of the models introduced in the above sections can be discussed.

<sup>9</sup> 1 nl is 1 litre at standard normal conditions  $T = 273.15 \text{ K}$ ,  $p_{abs} = 1013.25 \text{ mbar}$  (DIN 1343).



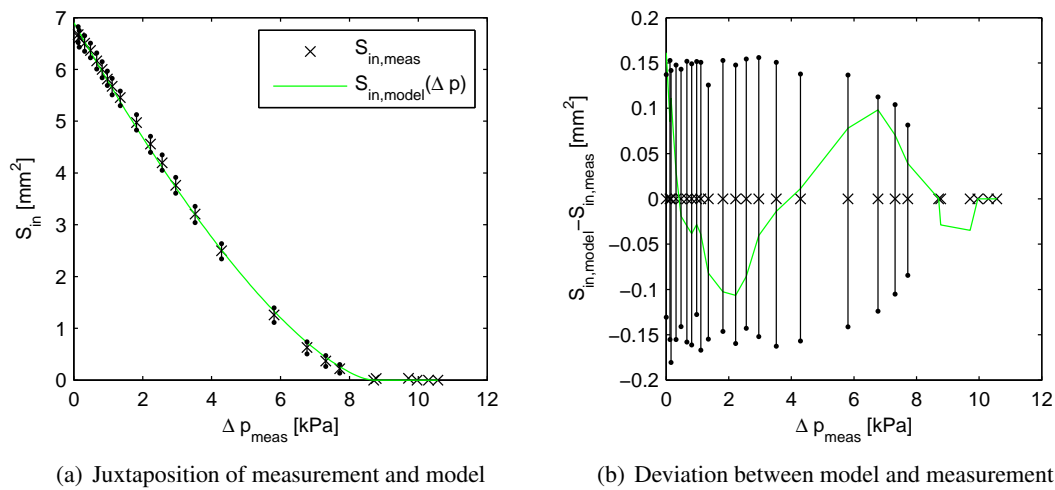


**Figure 4.15** Experimental data and fitted models for the intake cross section  $S_{in}$ . Model parameters obtained by least-squares fitting are  $S_{\infty} = 6.90 \text{ mm}^2$ ,  $p_M = 8.66 \text{ kPa}$  and  $\kappa = 1.48$ . The points  $S_{in,meas}$  are measured values (crosses), vertical lines show the uncertainty in  $S_{in}$  (25<sup>th</sup> and 75<sup>th</sup> percentiles).  $S_{in,model}(\Delta p)$  is calculated with identified model parameters for the range  $0 < \Delta p < 10.8 \text{ kPa}$  (green solid line). Data from the increasing pressure regime.

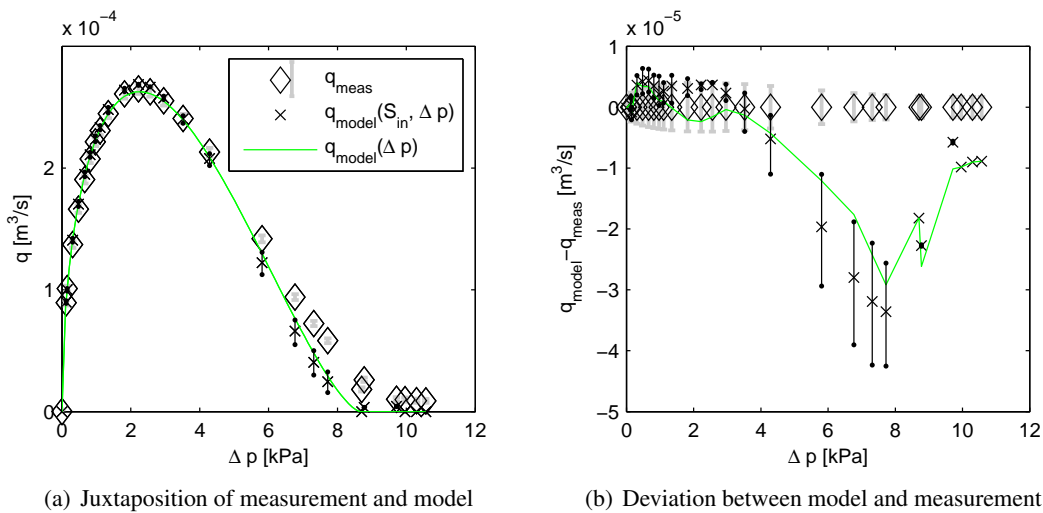


**Figure 4.16** Experimental data and fitted models for the flow-rate  $q$ . The points  $q_{meas}$  are measured values (crosses), vertical lines show the measurement uncertainty of the flow-meter. The model parameter obtained by least-squares fitting is  $\alpha = 1.016$ .  $q_{model}(S_{in}, \Delta p)$  is calculated with measured values for  $S_{in}$  and  $\Delta p$  (crosses), vertical lines show propagated uncertainty in  $q$  due the uncertainty in  $S_{in}$ .  $q_{model}(\Delta p)$  is calculated with the model parameters  $S_{\infty} = 6.90 \text{ mm}^2$ ,  $p_M = 8.66 \text{ kPa}$ ,  $\kappa = 1.48$ ,  $\alpha = 1.016$  for the range  $0 < \Delta p < 10.8 \text{ kPa}$  (green solid line). Data from the increasing pressure regime.

### Comparison of Experiment and Model

Both models Eq. (4.20c) for the intake cross section and Eq. (4.15) for the flow-rate are fitted to measured experimental data, in separate fitting routines. The fit-results are shown in Figs. 4.15 and 4.16, in comparison with the directly measured values and the respective measurement error estimates. The plot in Fig. 4.15 shows the data for the intake cross section  $S_{in}$ , obtained from evaluation of Eq. (4.20c) and the measurement uncertainties due to the image analysis procedure. From this

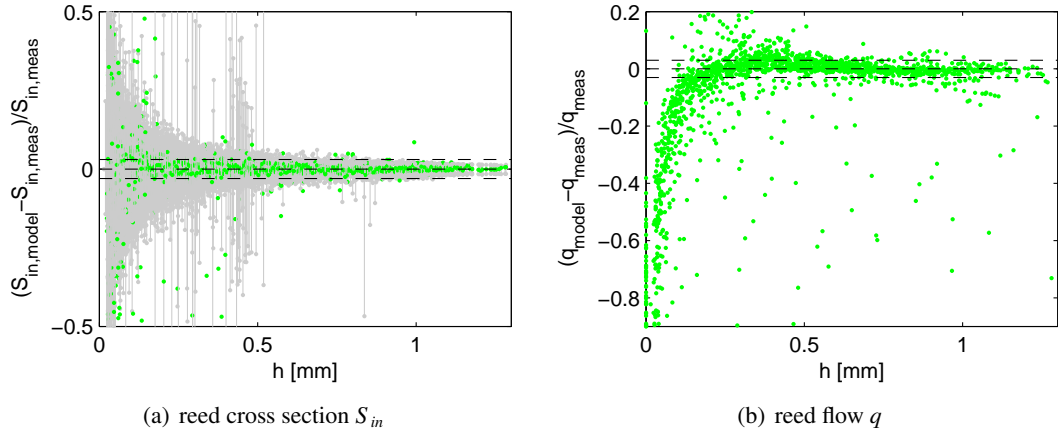


**Figure 4.17** Relative deviation of measurement and model prediction versus reed-slit height  $h$  for (a) the reed cross section  $S$  and (b) the quasi stationary flow  $q$ . The dashed lines mark the a 3% deviation, vertical gray lines in (a) mark the relative uncertainty incorporated in the measurement of  $S_{in,meas}$  due to the area detection algorithm. Data from 12 independent measurement series

fit, the model parameters  $S_\infty$ ,  $p_M$  and  $\kappa$  are determined to be  $S_\infty = 6.90 \text{ mm}^2$ ,  $p_M = 8.66 \text{ kPa}$ ,  $\kappa = 1.48$ .

The plots in Fig.4.16 show the measured and predicted values for the flow-rate  $q$ . Measured values for  $q$  are marked by diamonds with gray errorbars depicting the uncertainty of the flow-meter. The flow parameter  $\alpha$  was adjusted to be  $\alpha = 1.016$  by fitting Eq. (4.15) with measured data for  $\Delta p$ ,  $S_{in}$  to the measured flow-rate  $q$ . The predicted values for  $q$  are plotted as crosses for each measurement point; the errorbars mark the propagated uncertainty in the flow-prediction due to the measurement uncertainty of  $S_{in}$ .

After two separate fitting procedures, the parameters  $S_\infty$ ,  $p_M$ ,  $\kappa$  and  $\alpha$  are known. By use of these parameters, Eq. (4.21) provides an explicit formulation for the flow-rate  $q$  depending solely on the differential pressure  $\Delta p$ . For comparison, the data predicted by Eq. (4.21) are shown as a continuous green line by use of the previously identified model parameters. This comparison reveals, that the model systematically underpredicts the flow-rate, for pressures the above the saturation pressure.

In Fig. 4.17, the relative deviation of model prediction and measured values for the intake cross section  $S_{in}$  (Eq. (4.20c)) and the flow-rate  $q$  (Eq. (4.15)) are plotted versus the slit height  $h$ . In general, the model predictions are in reasonably good agreement with experimental data for large slit heights  $h$ .

The deviation for the cross section is within  $\pm 3 \%$ , as long as the slight height were larger than  $0.15 \text{ mm}$ . The measurement uncertainty in the intake cross section due to lighting conditions is within  $\pm 0.15 \text{ mm}^2$ , which is comparable to the measurement value at small reed openings: The smallest detectable cross section is about  $0.2 \text{ mm}^2$ . In Fig. 4.17 no errorbars are shown for measurements where the area detection algorithm failed, here  $S_{in} = 0$  has been assumed.

Concerning the prediction of the flow-rate, the deviation is within  $\pm 3 \%$  if the slit height  $h$  is larger than  $0.75 \text{ mm}$ . For  $0.25 < h < 0.75 \text{ mm}$ , the model tends to a slight overprediction, with a maximum at  $h \approx 0.4 \text{ mm}$ . The systematic underprediction of  $q$  mentioned above occurs for reed-slit heights smaller than  $0.25 \text{ mm}$  and becomes dramatic as  $h$  approaches the detection threshold<sup>10</sup>, which is about  $0.03 \text{ mm}$ .

<sup>10</sup>undetectable slight heights have been assumed to be zero

## Discussion

The conclusion to be drawn from Fig. 4.16 is, that the observed underprediction cannot be accounted to a measurement error of the intake cross section, despite the relatively large uncertainties in the determination of this property. The fit-model to estimate  $S_{in}$  from  $\Delta p$  tends to overpredict the intake cross section at pressures above saturation, but even this overprediction does not compensate for the underestimation of the flow-rate.

This confirms the statements of the previous section, that for small slit heights  $h < 0.3$  mm the edge radius becomes large, the Reynolds number is significantly lowered (Fig. 4.5) and the *vena contracta* effect vanishes. According to the presented model, in the case of no jet contraction ( $C_c \rightarrow 1$ ) and a very small input cross section ( $m \rightarrow 0$ ), the duct losses represented by  $\zeta$  must gain importance, otherwise the model would be undetermined as  $\alpha$  in Eq. (4.14) becomes zero. The loss coefficient  $\zeta$  for the double-reed channel can be compared to that of an equivalent cylindrical tube of 5 mm diameter and of 58 mm length (see section 4.1.1). For the case of a fully developed turbulent flow the loss coefficient according to the Blasius approximation at Reynolds numbers  $Re \approx 4000$  is  $\zeta \approx 0.5$ .

For the small slit heights observed at pressure differences  $\Delta p > 0.5p_M$  a Poiseuille-flow model [160, 89], or a model taking Reynolds lubrication into account [49] might be more adequate to model the gap-flow.

Another explanation for the underestimation of the flow at small slit heights might be a misinterpretation of the term “intake cross section”. It has been assumed, that the latter is equivalent to the gap between the reed blades, as seen from the reeds front view. There might, however, be lateral gaps at the sides of the reed blades, which are not detectable in the front view, which effectively increase the intake cross section: The measured integral flow-rate then incorporates a portion of gap flow through this lateral leaks.

To be more general, it can be said that the existence of any non-deformable set of capillaries introduces a rest-leakage, whose contribution is not incorporated in the model. An indication for the existence of leaks is the fact that a residual flow can be measured well above the closing pressure threshold  $p_M$ , where the reed appears to be completely closed. This is in agreement with previous experiments [40, 4] on single- and double-reeds. The measurements carried out in the present study suggest a linear relation of this gap flow on the driving pressure difference.

## 4.3 Effect of the Embouchure on the Reed-Flow

### 4.3.1 Adjustment of the Initial Slit Height

In a realistic situation, the reed-channel is pre-deformed. The musician presses his lips to the reed which results in a narrowing of the reed slit height.

The artificial mouth setup used in this experiments aims to mimic this situation in a controlled way. The double-reed is rigidly clamped at its tail, and the slit height  $h$  can be adjusted by moving a lip module against each of the opposing reed blades.

### Artificial embouchure configuration

In the practice of blowing experiments to be discussed in detail in the next chapter, evidence has been found for the hypothesis, that for a fixed axial position<sup>11</sup>  $x_l$  of the lips and a given blowing

<sup>11</sup> $x_l$  is defined as the distance of the lips center axis from the reed tip (Fig. 4.18)

pressure  $p_m$ , the sounding frequency depends *only* on the slit height  $h$ , but not on the respective contribution of each of the two lip modules on the adjustment of  $h$ .

This observation lead to a fundamental simplification of the experimental procedures by using an asymmetrical embouchure situation, with only one lip pressed to one of the reed blades.

The two configurations with one and two lips pressed to the reed, which result in the same initial slit height  $h$  are shown in Fig. 4.18.

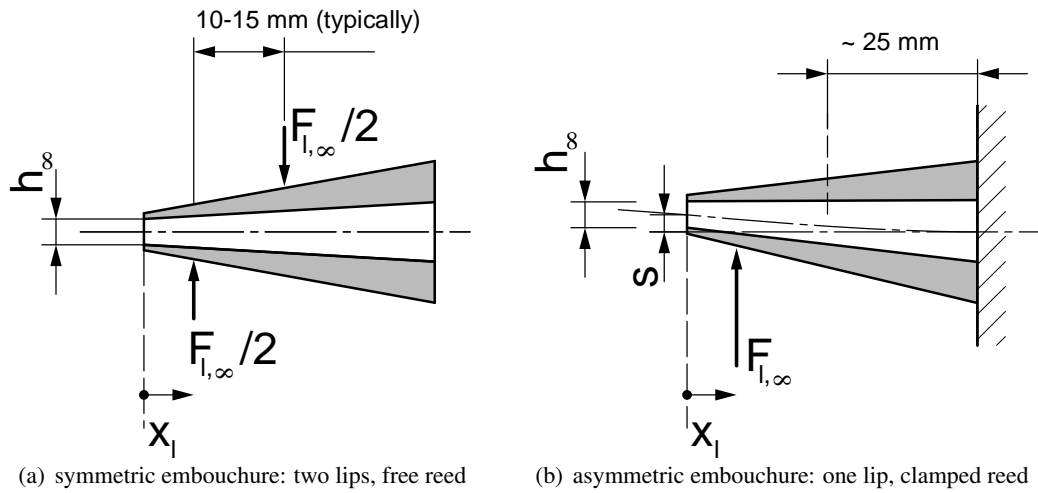


**Figure 4.18** Schematic representation of lip forces in a double-reed embouchure (longitudinal section)

This configuration might look unrealistic and improper at first glance. A real bassoon embouchure, however, is not so far from this situation: Bassoonists have an overbite on the reed. The upper jaw is used as a support against the action of the lower jaw on the double-reed. The contact point of upper and lower teeth on the reed have an offset with respect to the reed tip, and bassoonists even exaggerate the natural overbite by drawing back the lower jaw. The resulting offset of 10-15 mm provides a finer control of the reed slit height at the tip. This embouchure configuration is schematically shown in Fig. 4.18(a).

In the artificial mouth, the support against the action of the lower jaw is provided to the reed by means of a rigid frame at its rear end, and the upper lip can be released. This changes the mechanical configuration, as the support provided by the frame is shifted about 25 mm downstream, compared to the position of the upper teeth of a player, as shown in Fig. 4.18(b). The basic functioning of the reed in playing conditions, however, is not affected. Therefore this configuration is very useful for experimental studies: A well defined double-reed configuration can be adjusted with only one lip. The fact that all notes were actually playable at reasonable sound pressure levels confirms that this is a proper way to imitate a real double-reed embouchure<sup>12</sup>, at least for the purpose of a scientific study.

For the following, the embouchure configurations in Fig. 4.18 are considered to be equivalent, and all experiments (except stated otherwise) are performed with “asymmetrical embouchures” (Fig. 4.18(b)), for five different lip positions  $x_l$ , within the range of  $7 \text{ mm} < x_l < 12 \text{ mm}$ .

<sup>12</sup>Obviously, the dynamical properties, most notably damping, of the upper lip play a role in fine-tuning of the sound color. Although the upper reed-blade is not in contact with a lip, it is also not “free”. The bending of the whole reed assembly due to the asymmetry of the embouchure configuration will provide damping to the upper reed blade as well.

### Reed Deflection

The asymmetrical situation with one lip force  $F_l$  exerted to a reed clamped at its tail has two effects: A shift  $s$  of the center axis of the reed assembly<sup>13</sup>, and a narrowing of the reed slit inlet height  $h_\infty$ . Both can be characterized by effective stiffnesses, as obtained from the force vs displacement characteristics.

Due to the construction and wall thickness of the double-reed, the axial position  $x_l$  of the lip force relative to the reed tip obviously has a great influence on the characteristics. With a synthetic bassoon reed (*Selmer Premium Plastic 270M*), it could be shown that the centerline shift  $s$  depends linearly upon the applied lip force  $F_l$ , at least for the moderate range of forces, which is of interest here (Fig. 4.19(a)). The maximum force is the force needed to close the reed completely, which is smaller than 12 N depending on the lip position  $x_l$ . The equivalent stiffness of the double-reed assembly increases with  $x_l$  and range from 2.5 ( $x_l = 7$  mm) to 4.5 N/mm ( $x_l = 12$  mm).

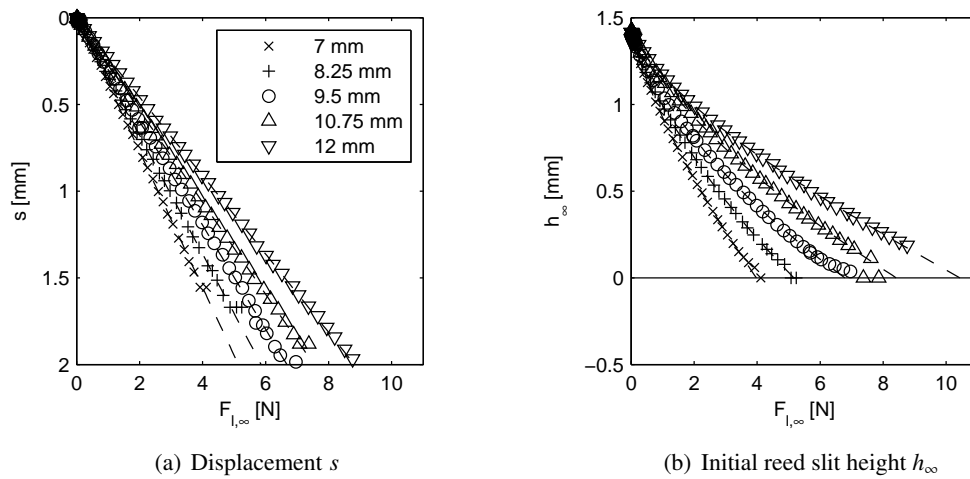


**Figure 4.19** Effect of a static lip-force  $F_{l,\infty}$  exerted to the reed in 5 different axial positions  $x_l$  (measured from the reed-tip)

The dependence of the initial slit height  $h_\infty$  on the applied lip force  $F_l$  is weakly non-linear. For small slit heights, approaching the reed closure, a significant increase in the equivalent stiffness is observed (Fig. 4.19(b)). The linear part of the equivalent reed-slit stiffness increases with  $x_l$  and ranges from 2.5 ( $x_l = 7$  mm) to 6.5 N/mm ( $x_l = 12$  mm).

The equivalent reed-slit stiffness is not the same as the stiffness of the reed-blade in the context of the one-parameter lumped reed model discussed in the previous chapter. This reed parameter is obtained from the quasi-stationary pressure-flow characteristics.

The purpose of the static reed deflection measurement is to characterize the embouchure situation. The governing parameter here is the initial reed slit-height  $h_\infty$ . Using a characteristic such as shown in Fig. 4.19(b), the slit-height can be monitored, by means of measuring the lip-force  $F_l$  and lip-position  $x_l$ .

#### 4.3.2 Quasi-static Flow in the Deformed Reed-Channel

The artificial embouchure situation is characterized by an axial lip position  $x_l$  and an initial slit height  $h_\infty$ . The position  $x_l$  of the lip might not only affect the lever arm and lip force needed to adjust the slit. One might guess, that the deformation of the blades' curvature could affect the flow

<sup>13</sup>comparable to the neutral axis of an Euler-Bernoulli beam

inside the reed channel. To test this, several quasi-stationary pressure-flow characteristics have been recorded for each of five axial lip positions, with varying initial slit heights between 1.6 and 0.2 mm. To each of these measurement curves, the models from the previous sections for the reed cross section and for the flow were fitted: In the first step, from fitting Eq. (4.20c) to measured data  $\Delta p, S_{in}$ , the parameters  $S_{\infty}$ ,  $p_M$  and  $\kappa$  were obtained. In the second step the flow parameter  $\alpha$  is determined from fitting Eq. (4.15) to measured data  $\Delta p, S_{in}, q$ . In Fig. 4.20, these fitting parameters are plotted in versus the initial slit height  $h_{\infty}$ , where markers correspond to the lip position  $x_l$  and colors mark the increasing (red) and decreasing (green) pressure regime, respectively.

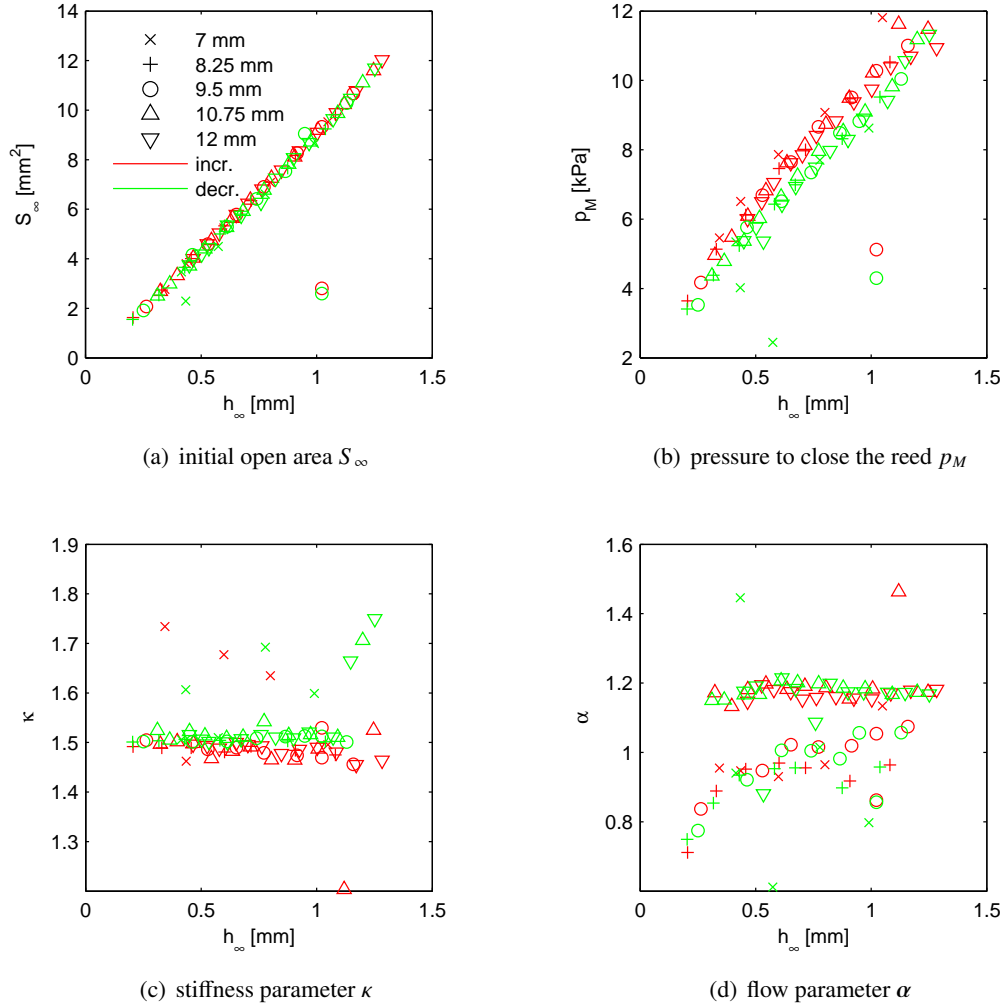


**Figure 4.20** Fitted model parameters  $S_{\infty}$ ,  $p_M$ ,  $\alpha$  and  $\kappa$  versus the initial reed-slit height  $h_{\infty}$ . Experiments were performed with an axially and vertically adjustable artificial lip. Markers depict the axial lip positions  $x_l$  with respect to the reed tip, vertical positions correspond to the initial slit height  $h_{\infty}$ .

A realistic embouchure situation is characterized by a pre-deflection of the reed blades. The effect of this initial reed deformation on the quasi-stationary pressure-flow characteristics can be discussed by means of the dependence of the reed model parameters upon  $h_{\infty}$ .

$S_{\infty}$ : The initial open area  $S_{\infty}$  depends approximately linearly<sup>14</sup> on the slit height  $h_{\infty}$ . The lip position has no influence.

<sup>14</sup>In detail, a slightly non-linear relation is observed (Fig. 4.12). Only for reed-slits smaller than 0.3 mm, the nonlinearity becomes drastic. However, a pre-deflection to such small slits is not reasonable, as it will be impossible to start and sustain an oscillation. These small slits occur during the pressure-induced closure of the reed.

$S_\infty$  is a measure limiting the maximum flow through the reed, and therefore the pressure amplitude and the dynamic level of a sounded note. Tight embouchures, with small slit heights  $h_\infty$ , are required to play softly.

$p_M$ : The pressure  $p_M$  to close the reed is proportional to the initial slit height  $h_\infty$ , but independent of the lip position  $x_l$ , where the force is applied. The observed values for the increasing and decreasing pressure regime differ from each other. This hysteresis is possibly due to friction between the lateral contact areas of the reed blades<sup>15</sup>. The present study reveals no significant relation between the magnitude of this hysteresis and the initial slit height. The discrepancy between the  $p_{M,incr.}$  and  $p_{M,decr.}$  is for any embouchure approximately 1 kPa.

$\kappa$ : The parameter  $\kappa$  appears to be a constant of the reed, as it is independent of the initial slit-height and the same for most lip positions. In this study, a value of 1.5 +/-0.05 is obtained, except for the lip position which is closest to the reed tip ( $x_l = 7$  mm).

This parameter stands for the mechanical spring characteristics of the reed. It appears as an exponent, any value greater than unity represents a non-linear continuous stiffening of the reed blade as the slit height decreases.

$\alpha$ : The parameter  $\alpha$  lumps flow induced pressure losses due to the vena contracta effect ( $C_c$ ) and dissipation inside the reed channel ( $\zeta$ ), according to  $\alpha = 1 - 1/C_c + 1/C_c^2 + \zeta$  derived in section 6.2. This flow coefficient  $\alpha$  is the only parameter of the model which apparently depends on the axial lip position  $x_l$ . The vena contracta coefficient  $C_c$  is constant, for any slit height large compared to the edge-radius of the blade [87]. Consequently  $\zeta$  increases with the lip position  $x_l$ . Increased dissipation can be understood by the different deformations of the reed channel, to result in a given slit height change by lip force application at various positions  $x_l$ . The reed is very thin and soft at its tip and for small  $x_l$  the flow channel will be deflected only near the intake, leaving the rear end of the channel unchanged. Shifting the lip in flow axis towards the bocal and thus increasing  $x_l$ , the effective stiffness increases Fig. 4.19 and the reed channel will be narrowed over a longer distance. This may be the reason for increased dissipation.

These results give some insight into the change of reed model parameters, as lips interact with the double-reed to form embouchure configurations typical for a musical performance. A convenient one-lip asymmetrical embouchure has been introduced for the double-reed and any embouchure configuration has been characterized by the initial slight height  $h_\infty$  and the lip position  $x_l$ , so far. In the operating regime, however, it is difficult to measure  $h_\infty$ , as it assumes the absence of pressure. Therefore, in the next section a minimalistic heuristic model will be proposed, which allows, for a given lip-position  $x_l$ , to estimate the reed model parameters corresponding to any embouchure configuration from the actual values of lip force  $F_l$  and the differential pressure  $\Delta p$ , which are easily captured state-variables of the artificial mouth.

### 4.3.3 Simplified empirical Model including a Lip Force

In the previous section, the details of the reed-flow were characterized by model parameters  $\kappa$ ,  $\alpha$  and  $\epsilon$ . In order to model realistic embouchures, this section aims to further reduce the general five parameter reed-model Eq. (4.24) and to empirically include a lip force  $F_l$  narrowing the slit at the reed channel intake. The result will be a three-parameter model similar to classical single-reed model with the parameters  $q_A$  and  $p_M$ , into which the lip force  $F_l$  is included by means of empirically obtained polynomials  $q_A = q_A(F_l, \Delta p)$  and  $p_M = p_M(F_l, \Delta p)$ .

<sup>15</sup>Other authors have attributed the hysteresis to viscoelastic effects they found in single [40] and double-reeds [6]

### Pressure induced Lip Force Reduction

In the artificial mouth the lip force  $F_l$  is exerted to the reed by a shift of the lip module perpendicular to the reeds main axis. In the absence of pressure, the static deflection-force characteristic describes the interaction (see Fig. 4.19). However, a pressure difference acting on the reed blades causes a reed deflection and the initially exerted force is reduced significantly.

This can be illustrated by means of a set of measurements with various embouchures: In each of five lip positions  $x_l$ , in absence of pressure difference, the initial reed slit height has been adjusted to several values within the range  $0.3 < h_\infty < 1.4$  mm by means of a lip force  $F_{l,\infty}$ . The force change  $\Delta F_l = F_l(\Delta p) - F_{l,\infty}$  as the mouth pressure is increased is shown in Fig. 4.21, where  $\Delta F_l$  is plotted versus the pressure difference  $\Delta p$ .

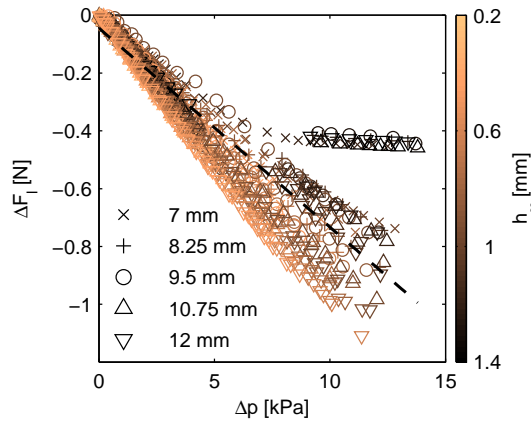


**Figure 4.21** Lip force change  $\Delta F_l$  due to the pressure induced reed blade deflection, for several embouchure configurations. Markers correspond to the lip position  $x_l$ , colors correspond to the initial slit height  $h_\infty$ .

From the slope  $\Delta p/\Delta F_l$ , the effective area  $S_r$  of the double-reed can be estimated to be  $S_r \approx 140 \text{ mm}^2$ , indicated by the dashed line. This value should be handled with care, however, due to the asymmetric embouchure configuration, where the artificial lip covers a broad region on the one reed-blade, while the surface of the other blade is completely free. Furthermore, due to the elasticity of the lip, the contact area of reed and lip module increases with  $F_l$  and the surface, on which the differential pressure  $\Delta p$  acts, is decreased. Hence, the estimate of  $S_r$  through the slope  $\Delta p/\Delta F_l$  apparently *increases* for tight embouchures with small  $h_\infty$ . This observation would deserve a more detailed description of the elastic properties and the three-dimensional geometry of the interaction of lip and reed, which is beyond the scope of this work.

Another observation is, that the slope  $\Delta p/\Delta F_l$  of the characteristics appears to be independent of the lip position  $x_l$ .

For very loose embouchures, where  $h_\infty \rightarrow h_0 = 1.4$  mm, a kink in the characteristics marks the retraction of the blade from the spatially fixed lip module.

The lip force significantly changes with the mouth pressure, and therefore both lip force and mouth pressure are needed to describe the embouchure configuration.

### Simplified Three-Parameter Model for the reed-flow

As was shown theoretically (Fig. 4.14), the parameters  $\alpha$  and  $\epsilon$  in the general reed model Eq. (4.24) have a negligible impact on the shape of the pressure-flow characteristics and mainly scale the curve. Whereas these parameters were important to discuss a possible impact of the corresponding effects on the flow-curve, they can be neglected in the context of a fitting model, in which another



scaling parameter ( $q_A$ ) is already included. Setting

$$\left( \epsilon \left( 1 - \frac{\Delta p_{meas}}{p_M} \right)^{2\kappa} + \alpha \right)^{-\frac{1}{2}} = 1. \quad (4.26)$$

in Eq. (4.24) eliminates the influence of parameters  $\alpha$  and  $\epsilon$ .

Concerning the stiffness parameter  $\kappa$ , Fig. 4.20 implies that  $\kappa = 1.5$  provides a good fit for the utmost embouchure configurations. Using this as a fixed value and with Eq. (4.26) the general model Eq. (4.24) can be written

$$q = q_A \left( 1 - \frac{\Delta p_{meas}}{p_M} \right)^{\frac{3}{2}} \left( \frac{\Delta p_{meas}}{p_M} \right)^{\frac{1}{2}}, \quad (4.27)$$

which is similar to the classical single-reed model, except for a non-linear spring characteristics expressed in the exponent  $3/2$ .

The general shape of the curve is determined by this fixed exponent, and the free parameters  $p_M$  and  $q_A$  stretch and scale the curve along the abscissa and the ordinate, respectively. Pressure-flow characteristics of this type have their flow-rate maximum  $\tilde{q}_{max} = 3/16 \sqrt{3} \approx 0.32$  at the saturation pressure  $\tilde{p}_{m,sat} = 1/4$ , in normalized coordinates  $\tilde{q} = q/q_A$ ,  $\tilde{p} = p/p_M$ .

Note that, to avoid  $q$  become complex, a distinction of cases should be made in Eq. (4.27), such that  $q = 0$  for complete closure  $p_m > p_M$ .

### Inclusion of the Lip Force into the Reed Model

In Fig. 4.20 the relation between model parameters and the initial slit height  $h_\infty$  for a broad variety of embouchures has been shown. In particular, the model parameters  $p_M$  and  $q_A$  are linear functions of  $h_\infty$ . Introducing a relation for  $h_\infty$  as a function of the lip force  $F_l$  and position  $x_l$  is a suitable way to include the lip force into the reed model<sup>16</sup>.

Any details of the quasi-static lip-reed interaction like the size of the contact area and the stiffness of the lip material are excluded by this simplistic approach. Only a calibration is needed to link the measured value of the integral lip force to the geometric measures at the reed intake, depending on the differential pressure acting on the reed.

For the asymmetric embouchure used in this study, all relevant information is found in the static characteristics of slit height versus lip force (see Fig. 4.19), the reduction of lip force due to pressure induced reed deformation (see Fig. 4.21) and the dependence of the reed parameters upon the initial slit height  $h_\infty$  (see Fig. 4.20).

Instead of separately evaluating these three relationships, the coefficients for a linear regression model will be derived directly from experimental data.

### Determination of Regression Coefficients

First, for each of five different lip positions  $x_l$  the pressure-flow characteristics have been measured, starting from various initial slit heights  $h_\infty$  within  $0.3 \text{ mm} < h_\infty < 1.4 \text{ mm}$ . During the characteristics measurement, the lip force  $F_l$  was recorded. The raw data of the measurement is shown in Fig. 4.22.

<sup>16</sup>This approach has been proposed by Nederveen [125], but quantitative data for double-reeds is missing.

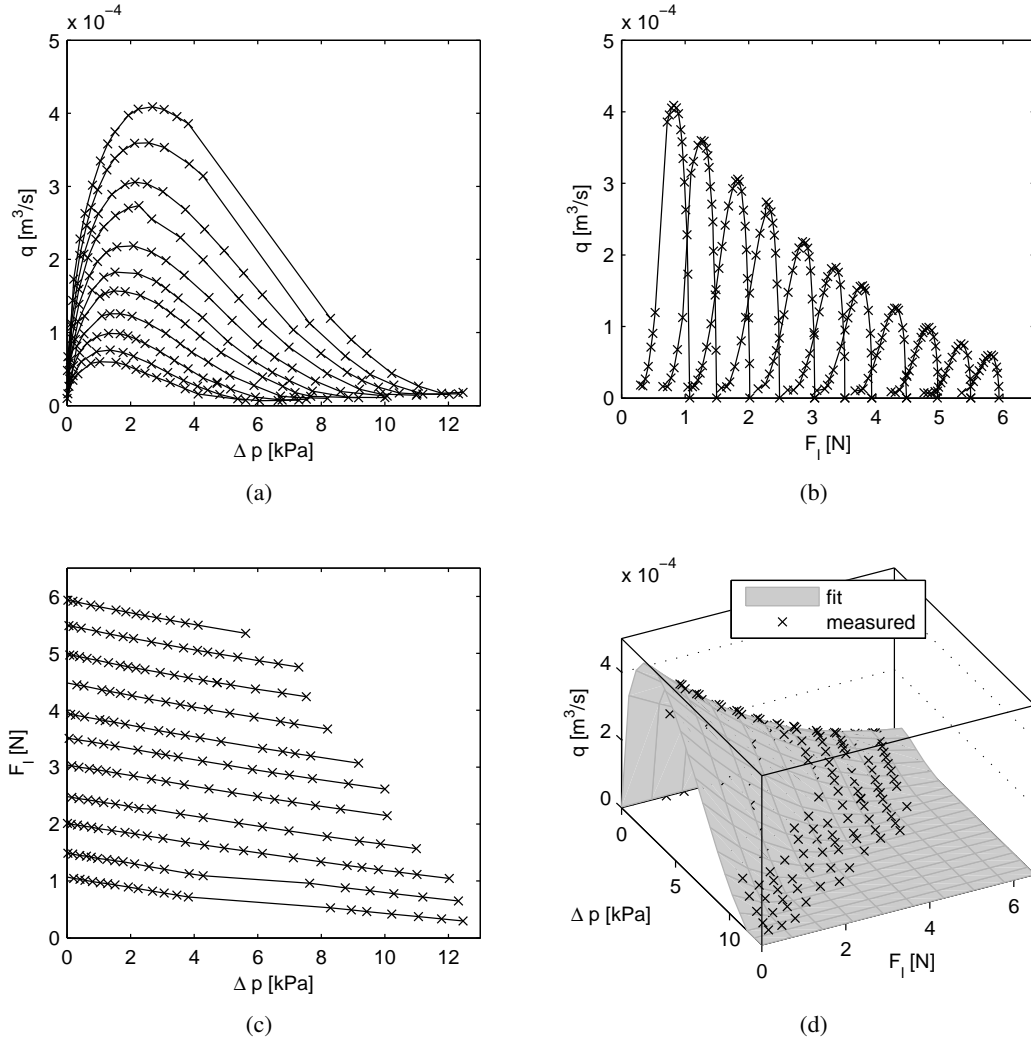


**Figure 4.22** Quasi stationary flow  $q$  through a bassoon double-reed as a function of differential pressure  $\Delta p$  and lip force  $F_{lip}$  for several initial slit heights  $h_{\infty}$ . Lip position  $x_l = 10.75$  mm. Only the decreasing branch of the characteristics is shown.

The quasi-stationary flow curve is a trace on a surface in the three-dimensional space with a pressure-, flow- and lip force-dimension of the form

$$q(\Delta p, F_l) = q_A(\Delta p, F_l) \left( 1 - \frac{\Delta p}{p_M(\Delta p, F_l)} \right)^{\frac{3}{2}} \left( \frac{\Delta p}{p_M(\Delta p, F_l)} \right)^{\frac{1}{2}}, \quad (4.28)$$

which is shown in Fig.4.22(d).

The functions  $q_A(\Delta p, F_l)$  and  $p_M(\Delta p, F_l)$  are found by fitting the simplified reed model Eq. (4.27) to the experimental data.

Previous to this second step, the model is extended by an empirical term to account for a phenomenon that has been deliberately excluded in the considerations on theoretical flow models: So far, it has been assumed that the flow is completely stopped when the reed is closed. The measurements reveal, however, the existence of a residual flow in the case of complete reed closure (Fig. 4.22(a)). This is in agreement with previous studies in this field, e.g. [40, 4]. A detailed view of the residual flow  $q_{res}$  observed in the present experiments provides Fig. 4.23 for several arbitrary

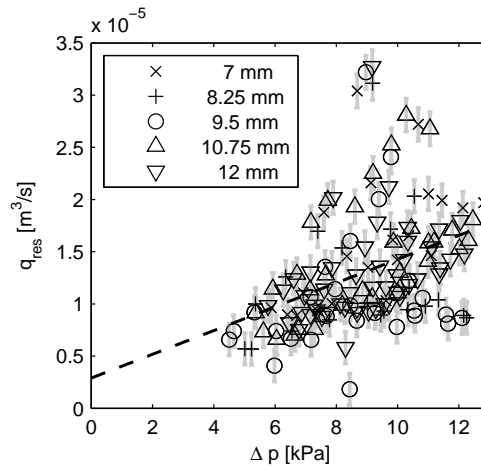


**Figure 4.23** Residual flow  $q_{res}$  as a function of mouth pressure. For the data shown here, the reed is assumed to be closed, i.e the image analysis algorithm failed to detect an intake area from the reeds front view.

values of  $h_\infty$  in five different lip positions  $x_l$ . The empirical linear relation

$$q_{res} = 1.138 \cdot 10^{-9} \frac{\text{m}^3}{\text{s Pa}} \Delta p + 0.289 \cdot 10^{-5} \frac{\text{m}^3}{\text{s}} \quad (4.29)$$

describes the residual flow as a function of the differential pressure  $\Delta p$ , independently of the embouchure adjustment. This is represented by the fit straight line in Fig. 4.23. Note, that  $\Delta p$  in Fig. 4.29 actually is the mouth pressure  $p_m$  because the reed is closed, and  $p_r = 0$ . To account for this effect, the simplified model Eq. (4.27) is extended by the correction term Eq. (4.29), thus

$$q_{corr.} = q_{model} + q_{res}. \quad (4.30)$$

For simplicity this equation can be used for any value  $\Delta p > 0$ , such that also for the open reed  $\Delta p < p_M$  a (very small) residual flow is added. Indeed, it can be assumed, that what is called  $S_{in}$  here is smaller than the real intake cross section, because the lateral contact area of the reed blade most probably is not air-tight and a gap flow from the sides may also play a role. For double-reeds however, this effect might be regarded less important than for single reeds.

The fitting procedure is now performed with the corrected two parameter model and for each embouchure configuration defined by  $x_l$  and  $h_\infty$  a pair of fit parameters  $q_{A,fit}$ ,  $p_{M,fit}$  is obtained. In the last step, the empirical functions  $q_A(\Delta p, F_l)$  and  $p_M(\Delta p, F_l)$  are determined by multiple linear regression of the measurement values for  $\Delta p$  and  $F_l$  on the fit parameters  $q_{A,fit}$  and  $p_{M,fit}$ . For this regression, the linear models

$$q_A(\Delta p, F_l) = a_{0,q_A} + a_{1,q_A} \Delta p + a_{2,q_A} F_l + a_{3,q_A} (\Delta p)^2 + a_{4,q_A} F_l^2 \quad (4.31a)$$

$$p_M(\Delta p, F_l) = a_{0,p_M} + a_{1,p_M} \Delta p + a_{2,p_M} F_l + a_{3,p_M} (\Delta p)^2 + a_{4,p_M} F_l^2 \quad (4.31b)$$

have been used. The coefficients thus obtained for five different axial lip positions are listed in tables 4.1 and 4.2.

**Table 4.1 Regression coefficients for  $q_A$ ; Eq. (4.31a)**

$q_A$	Lip distance from reed tip				
	7 mm	8.25 mm	9.5 mm	10.75 mm	12 mm
$a_0$ [l/s]	1.633	1.667	1.591	1.588	1.558
$a_1$ [(l/s)/kPa]	-0.032	-0.026	-0.022	-0.019	-0.017
$a_2$ [(l/s)/N]	-0.734	-0.639	-0.462	-0.383	-0.301
$a_3$ [(l/s)/kPa <sup>2</sup> ] · 10 <sup>-3</sup>	-0.336	-0.583	-0.316	-0.236	0.012
$a_4$ [(l/s)/N <sup>2</sup> ]	0.081	0.064	0.035	0.025	0.017

**Table 4.2 Regression coefficients for  $p_M$ ; Eq. (4.31b)**

$p_M$	Lip distance from reed tip				
	7 mm	8.25 mm	9.5 mm	10.75 mm	12 mm
$a_0$ [kPa]	13.245	12.696	12.325	12.284	12.189
$a_1$ [kPa/kPa]	-0.197	-0.192	-0.148	-0.131	-0.097
$a_2$ [kPa/N]	-3.469	-2.402	-1.801	-1.483	-1.333
$a_3$ [kPa/kPa <sup>2</sup> ] · 10 <sup>-3</sup>	0.923	3.151	2.314	2.561	1.115
$a_4$ [kPa/N <sup>2</sup> ]	0.259	0.073	0.045	0.037	0.053

## Residuals

The quality of the empirical reed model Eq. (4.28) can be assessed by means of the residual plot in Fig. 4.24, where the normalized residuals  $(q_{model} - q_{meas})/q_{meas}$  are plotted. This reveals a significant systematic deviation depending on the normalized differential pressure  $\tilde{p} = \Delta p/p_M$ :

- $0 < \tilde{p} < 0.25$ : The deviation between measurement and model is smaller than 5% below the saturation pressure  $\tilde{p}_{m,sat} = 0.25$ . The model accurately predicts the volume-flow maximum and the saturation pressure.
- $0.25 < \tilde{p} < 0.75$ : Above saturation, the model tends to systematically overpredict the flow-rate by up to 15 %.
- $0.75 < \tilde{p} < 1$ : Approaching the reed closure, the model drastically underestimates the flow by up to -80 %. It has been previously discussed in section 4.2.4, that this systematic deviation is possibly due to the fact that for small slits the vena contracta effect is overestimated in the model.
- $\tilde{p} > 1$ : As the reed is closed, the normalized residuals decrease, due to the correction for the residual flow. As the measured values for  $q$  are small and comparable to the measurement uncertainty, the normalized residuals are quite large ( $\pm 20\%$  for  $\tilde{p} > 1.2$ ).

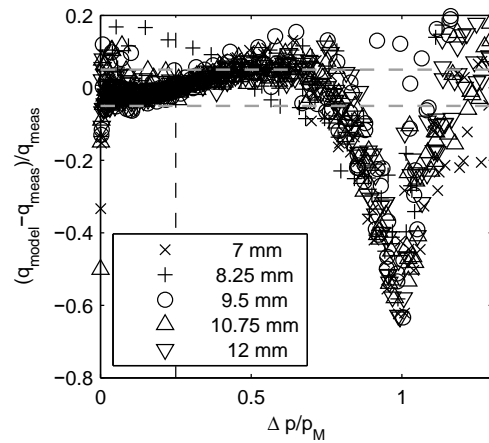


**Figure 4.24** Deviation of empirical flow model and experimental data. The model is given by Eqs.(4.28),(4.31a),(4.31b) with Eq. (4.29) and tables 4.1, 4.2. Normalized residuals are plotted versus the normalized differential pressure  $\tilde{p} = \Delta p/p_M$ . The dashed horizontal lines mark a 5% deviation, the vertical dashed line marks the saturation pressure  $\tilde{p}_{m,sat}$ .

A systematic influence is found neither for the lip position  $x_l$ , depicted by different markers in Fig. 4.24, nor for the slit height  $h_\infty$ . This leads to two conclusions:

- The quality of this empirical model is constant for the broad variety of embouchure configurations investigated here (lip position  $7 \text{ mm} < x_l < 12 \text{ mm}$ , initial slit height  $0.3 \text{ mm} < h_\infty < 1.4 \text{ mm}$ ).
- The flow-curves obtained for different embouchures scale with the slit height  $h_\infty$  but do not show qualitative differences in their shape

### Simplified Three-Parameter Model for the Reed-Slit Height

In analogy to the steps that led to an empirical model for the quasi-static reed flow, an empirical model for the reed-slit height can be defined:

The quasi-stationary slit-height  $h_\infty$  is, in analogy to Eq. (4.28), given by

$$h_0(\Delta p, F_l) = h_\infty(\Delta p, F_l) \left( 1 - \frac{\Delta p}{p_{M,h}(\Delta p, F_l)} \right)^{\frac{3}{2}}. \quad (4.32)$$

This model has the parameters  $h_\infty$  and  $p_{M,h}$ , which are the initial slit height in absence of a pressure difference (due to the pre-load applied to the reed by the lip), and the pressure to close the reed<sup>17</sup> respectively.

These two parameters are determined from the experimental slit-height vs. pressure characteristics using regression models analogous to Eq. (4.31)

$$h_\infty(\Delta p, F_l) = a_{0,h_\infty} + a_{1,h_\infty} \Delta p + a_{2,h_\infty} F_l + a_{3,h_\infty} (\Delta p)^2 + a_{4,h_\infty} F_l^2 \quad (4.33a)$$

$$p_{M,h}(\Delta p, F_l) = a_{0,p_{M,h}} + a_{1,p_{M,h}} \Delta p + a_{2,p_{M,h}} F_l + a_{3,p_{M,h}} (\Delta p)^2 + a_{4,p_{M,h}} F_l^2 \quad (4.33b)$$

with the following regression coefficients, depending on the position  $x_l$  of the lip with respect to the reed tip

<sup>17</sup>Note, that  $p_M$  is obtained from a fit to the flow vs. pressure-characteristics, while  $p_{M,h}$  is obtained from a fit to the slit-height vs. pressure-characteristics. Theoretically it should be  $p_M = p_{M,h}$ , but the fit parameter  $p_{M,h}$  is by 10 % larger than  $p_M$ .

**Table 4.3 Regression coefficients for  $h_{\infty}$ ; Eq. (4.33a)**

$h_{\infty}$	Lip distance $x_l$ from reed tip				
	7 mm	8.25 mm	9.5 mm	10.75 mm	12 mm
$a_0[]$	1.633	1.667	1.591	1.588	1.558
$a_1[(l/s)/kPa]$	-0.032	-0.026	-0.022	-0.019	-0.017
$a_2[(l/s)/N]$	-0.734	-0.639	-0.462	-0.383	-0.301
$a_3[(l/s)/kPa^2] \cdot 10^{-3}$	-0.336	-0.583	-0.316	-0.236	0.012
$a_4[(l/s)/N^2]$	0.081	0.064	0.035	0.025	0.017

**Table 4.4 Regression coefficients for  $p_{M,h}$ ; Eq. (4.33b)**

$p_{M,h}$	Lip distance $x_l$ from reed tip				
	7 mm	8.25 mm	9.5 mm	10.75 mm	12 mm
$a_0[mm]$	1.239	1.391	1.452	1.466	1.462
$a_1[mm/kPa]$	-0.020	-0.025	-0.019	-0.018	-0.015
$a_2[mm/N]$	-0.522	-0.390	-0.346	-0.275	-0.224
$a_3[mm/kPa^2] \cdot 10^{-3}$	-0.413	0.163	-0.061	0.086	0.167
$a_4[mm/N^2]$	0.065	0.231	0.021	0.014	0.010

## Discussion

An empirical model for the double-reed flow with respect to the embouchure configuration is presented. The embouchure is defined by the axial and perpendicular position of the lip module relative to the fixed reed. The axial position  $x_l$  is directly measured as the distance from the reed tip, the vertical position is monitored by measurement of the lip force  $F_l$ , which, in combination with the actual differential pressure  $\Delta p$ , determines the reed slit inlet height.

The model is given is given by Eqs.(4.28), (4.31a) and (4.31b).

The regression coefficients (4.31a) and (4.31b) for this model are valid for this specific double-reed used in the presented measurements of the quasi-stationary pressure-flow characteristics during which the lip force  $F_l$  is monitored. This set of experiments can be regarded as a “calibration procedure” of a reed to obtain its model parameters.

For the residual flow  $q_{res}$  when the reed is closed, a correction term scaling linearly with the mouth pressure is proposed.

For the reed used in this study values are given in Eq. (4.29) and tables 4.1 and 4.2.

With the calibrated model, the quasi-stationary flow-rate through the double-reed channel can be determined from the the artificial mouth's state variables  $x_l$ ,  $F_l$  and  $\Delta p = p_m - p_r$  with an accuracy of  $\pm 5\%$  within a range of normalized pressures  $0 < \tilde{p} < 0.4$ .

The model further allows to assign reed-model parameters  $q_A$  and  $p_M$  to an embouchure configuration directly from the actual setting of the experiment.

Thus, any working point of the artificial mouth can now be interpreted in the context of the reed model. This is useful for investigations on the bassoon in operating conditions as it allows measure subtle embouchure adjustments of the bassoonist needed to correct the intonation.

## 4.4 Summary

In this chapter, a model for the quasi-stationary flow-rate through the double-reed channel has been presented.

The double reed channel is a narrow, slightly diverging duct with sharp edges at the intake, which protrude into a large volume: the mouth cavity. If the steady pressure in the mouth is larger than in the reed, a quasi-stationary flow develops. This is described by the Bernoulli-equation extended by two pressure-loss terms accounting for energy losses related to flow phenomena in this type of duct: Flow separation at the sharp-edged intake and dissipation in the duct. Both terms are lumped into one global flow parameter.

The pressure difference between inside and outside of the reed channel does not only drives a flow, but also leads to a deflection of the reed blades. For the use in a lumped parameter model it is convenient to consider the displacement of the reed at its tip. The reed intake area is introduced as a scalar model variable dependent on the reed tip displacement, and the equivalent spring characteristics of the pressurized double-reed blade is experimentally obtained.

Including this simplified description into the flow-relation leads to a simple model for the reed. It has five parameters with respect to the flow-phenomena in the duct, the spring characteristics of the reed blade and the area ratio of input and output cross section in the diverging reed duct. This analytical model is used in a fitting procedure to estimate the influence of the respective phenomena on the global flow-rate and on the shape of the reed's valve-characteristics.

A simplified form of this model is further extended by an empirical relation to include a pre-deformation of the reed-duct, which occurs when the musician presses his lips against the reed blades to form an embouchure. The musician's embouchure is mimicked by use of a lip module in the artificial mouth, where an asymmetric configuration with only one lip pressed to the double-reed is practical. By measuring the axial lip position relative to the reed and the force exerted to it by the lip, realistic and well-defined embouchures can be precisely imposed.

The lip force, as a second control parameter of the artificial mouth, has been included into the reed model, by means of empirical relations obtained experimentally by a calibration procedure. This comprises for each reed a set of quasi-stationary flow measurements in several embouchure configurations. The necessary data has been obtained for a particular synthetic bassoon reed. With this calibrated model any embouchure configuration and working point of the artificial mouth can be expressed by reed parameters. This approach is validated for quasi-stationary regimes, but it may also provide an important link between experimental observations and physical models in the dynamical case.





# 5 Survey of Performance Characteristics of the Modern German Bassoon

## 5.1 Experimental Procedure and Data Analysis

The artificial mouth described in Chapter 3, makes possible the characterization of the double reed in quasi-stationary conditions as described in Chapter 4. This provides a framework to derive parameters from experimental configurations resembling realistic embouchures of a player.

Furthermore, the construction of the artificial mouth, and the precise adjustability of the lips in particular, is suited to carry out repeatable measurements on the bassoon under playing conditions. The experiments cover the complete playing range of the bassoon in frequency (notes) and dynamics (loudness). This chapter presents the experiment, a comprehensive overview on the parameter ranges and a discussion of some aspects of interaction between resonator and exciter under realistic playing conditions.

### 5.1.1 Description of the Experiment

When a reed wind instrument produces a sound, the periodic closing of the reed valve is triggered by reflections of pressure waves from the air column. In detail, the produced sound depends on the vibrational properties of the reed. The range of possible oscillatory states is very broad; depending on the player's interaction with the reed, many different sounds can be produced for one and the same air column.

While it is relatively intuitive even for a completely untrained person to start and maintain single notes on a bassoon, it is problematic to imitate this process with an artificial mouth: Even if such a device provides control over the relevant parameters, it is still demanding to determine ranges of these parameters, for which the whole system of blowing machine and instrument produces a sound. One systematic approach to study the operating regimes is to keep one playing parameter constant, while varying others. Scanning through the parameters in this way, the broad range of oscillatory and non-oscillatory states are explored, and the limits of the working range of the reed can be found. It should be noticed, that the playing regime for one set of parameters is not necessarily unique. Due to hysteresis effects, dependence on the history, different regimes can be established for one and the same set of playing parameters [150, 92]. This does not only involve instantaneous values of control parameters but also the rates of change in these parameters. These regime changes are found well within the playing range, but mostly for unusually high blowing pressures as will be shown later. Other more or less periodic and more or less stable regimes are found at the borders of the playing range, that is near the upper or lower threshold of oscillation. In modern playing styles, some musicians<sup>1</sup> explore these limits to achieve a special artistic expression. However, these unusual regimes and the playing range limits are not the focus of this study.

The aim is to investigate sustained notes in the usual playing range of the bassoon. These are the result of a periodic motion of the reed, having a stable fundamental frequency determining the perceived pitch. Transients like attacks, decays, note changes, vibrato, trills, note bendings as well as dynamical changes like *diminuendi* and *crescendi* are not studied here.

---

<sup>1</sup>E.g. the German bassoonist Johannes Schwarz, Ensemble Modern, Frankfurt a.M., Germany

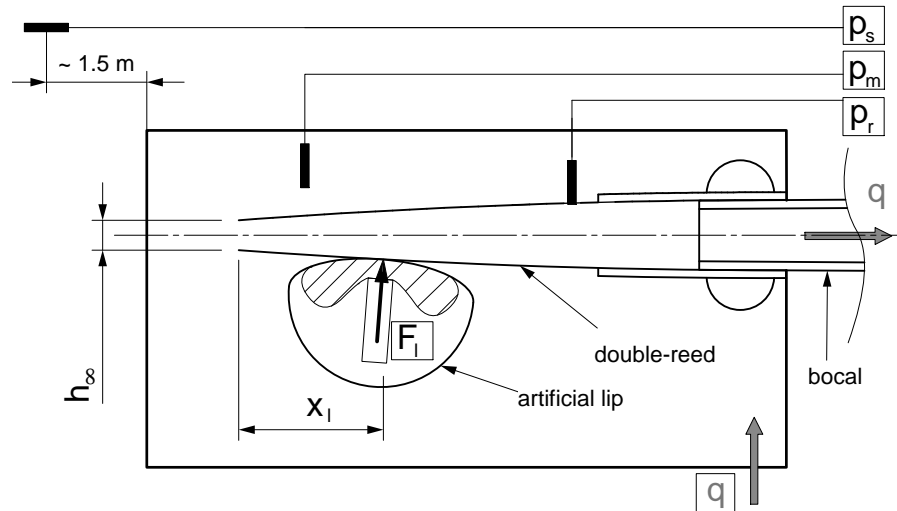


**Figure 5.1** Sketch of the experimental setup. Measured quantities in boxes ( $p_m$ ,  $p_r$ ,  $F_l$ ,  $q$ ,  $p_s$ ) are recorded instantaneously during the experiment.

For the artificial mouth in this study, the adjustment parameters are (see Fig. 5.1):

$x_l$  the position of the lip along the reed

$F_l$  the force of the lip

$p_m$  the blowing pressure in the “mouth” cavity.

Furthermore the resulting output data are

$p_r$  the unsteady reed pressure in the reed,

$p_s$  the sound pressure in the surrounding of the setup<sup>2</sup>

$q$  the mean volume flow-rate through the reed

Together with a given reed and resonator (which in case of the bassoon is set by the choice of a bocal fixed to the wooden corpus, and a fingering applied to the bassoon) the experimental situation is completely defined<sup>3</sup> Here, in contrast to previous studies [119, 3], only those oscillatory states have been studied, which produce the pitch, that a bassoonist expects when applying a fingering on the bassoon. This simplifying constraint is based on the assumption, that these operating regimes are the most relevant for the musical performance.

The experimental procedure was as follows: After initiating the tone, the blowing pressure  $p_m$  in the mouth and the lip force  $F_l$  were carefully balanced to play the note in tune at the softest possible dynamic level. The tuning was controlled by an electronic tuner, to be within  $\pm 5$  Cent around the fundamental frequency  $f_0$  corresponding to the fingering<sup>4</sup>. Subsequently, the blowing pressure was increased, followed by a readjustment of the lip force to maintain the tuning. This procedure was repeated to explore the complete parameter range for blowing pressure  $p_m$  and lip force  $F_l$  for which this note on the instrument could be sounded in tune. For each note the experiment was ended if the reed overblew (a sudden jump into a new stable regime with higher pitch), switched to another mode (a smooth and reversible turnover to a higher or lower pitch as the pressure is increased) or produced a multiphonic sound (a superposition of two non-harmonic sounds). In

<sup>2</sup>The external microphone was placed about 1.5 m perpendicular to the instruments longitudinal axis pointing to the “butt” end of the bassoon.

<sup>3</sup>Except for the acoustic surrounding, which certainly influences the sound pressure  $p_s$ .

<sup>4</sup>The tuning reference is the equally tempered scale for A4,  $f_0 = 443$  Hz. To the knowledge of the author, this is today’s convention among German orchestral musicians.

rare cases, the upper pressure threshold was reached and the reed closed permanently, or, to the other extreme, the lip was completely retracted from the reed blade. Some notes on the instrument could be still be sounded in tune at very high blowing pressures  $p_m > 12$  kPa. Without technical constraints of the experimental setup, these ranges were not studied, as the normal range of blowing pressures in bassoon playing is  $1 \text{ kPa} < p_m < 9 \text{ kPa}$  [68]. In this way, the complete musically relevant dynamical range of a note, available for the specific fingering at a fixed lip position, has been obtained experimentally.

For each of the intermediate steps in one experimental run, the parameters were held constant for several seconds to meet the assumption of quasi-stationarity for the recorded data<sup>5</sup>. The acquisition time was 1 second, sampled at  $f_s = 65.536$  kHz for the unsteady data (the reed pressure  $p_r$  and the sound pressure  $p_s$  in the measurement room), and  $f_s = 1$  kHz for the quasi-stationary data (the blowing pressure  $p_m$ , the flow-rate<sup>6</sup>  $q$  and the lip force  $F_l$ ), on two different measurement systems, which were synchronized by a pulse-train trigger signal. The lip position  $x_l = 10.75$  mm from the reed tip was adjusted<sup>7</sup> previous to the experiment and held constant in all measurements presented in this section.

For each acquired data set on a given configuration a meta-analysis has been performed, to extract additional features from the raw data.

### 5.1.2 Time Domain Analysis

In the normal playing regimes on the bassoon, the reed closes once per period<sup>8</sup>. Schematically, the reed performs a two-step motion, with an open and a closed episode. During one part of the period (duration  $\tau_o$ ), the reed remains open,  $p_r > 0$ ; in the subsequent part (duration  $\tau_c$ ) the reed is closed  $p_r < 0$ . The subscripts  $(.)_o$  and  $(.)_c$  mark respectively the open and closed period during one cycle. For a typical bassoon reed configuration, the measured reed pressure waveform ( $p_r$ ) is shown in Fig. 5.2. Within the two episodes of the pressure waveform  $p_r$  which are determined by the zero crossing of the reed pressure signal, the integral mean pressures are  $p_o$  and  $p_c$ , respectively. These pressures and the corresponding times  $\tau_o$  and  $\tau_c$  graphically represent the schematized two step motion of the reed predicted by analytical models [102, 125, 44, 136]. Note that in the ideal case described in these models the reed pressure mean value  $\bar{p}_r$  during one cycle must be zero. In a measurement, it is found that  $\bar{p}_r = \Delta p > 0$ . Hypothetically, this difference of several hundreds of Pascals indicates a pressure loss within the resonator. The determination of the episode durations  $\tau_o$  and  $\tau_c$  is done by an analysis of zero-crossings with subsample resolution, by linear interpolation between the measured samples before and after the zero crossing. Assuming, that the motion of the reed tip is nearly in phase with the reed pressure  $p_r$  and proportional to it [44, 102], the analysis of the pressure waveform in the time-domain introduces five more output data describing the operation point of the reed valve, which are:

$\tau_{o,c}$  the duration of reed opening and closure during one cycle,

$p_{o,c}$  the integral mean pressure in the reed during the opened and closed episode,

$\Delta p$  the pressure difference between the actual and ideal<sup>9</sup> mean reed pressure  $\bar{p}_{r,meas} - \bar{p}_{r,ideal}$

<sup>5</sup>After a mouth pressure change, a settling time was necessary for the volume-flow due to the large mouth cavity volume

<sup>6</sup>The flow rate has been determined from the output signal of a calibrated thermal mass-flow meter, a PT100 temperature sensor, and a sensor for the static pressure in line with the air supply system, close to the mouth cavity

<sup>7</sup>The offset lip position  $x_l = 0$  was adjusted by the eye, such that the center of the lip was flush with the reed tip. The frame carrying the lip was then moved downstream towards the bocal by a manual linear positioning stage for optical measurements. Millimeter-values for  $x_l$  are obtained from counting the turns of the spindle, a full turn corresponds to 0.5 mm.

<sup>8</sup>For cylindrical reed wind instruments, non-beating regimes can be obtained at low blowing pressures for standard playing techniques. Theoretically, in conical reed wind instruments a non-beating regime is also possible, but the range between the threshold pressures of these regimes is very small [44]. Another exception are multiphonics, where the reed closes two or more times during the (fundamental) cycle duration.

<sup>9</sup>In the ideal, loss-free case, the mean value  $\bar{p}_r = 0$ , since the zero-frequency impedance is zero [44]

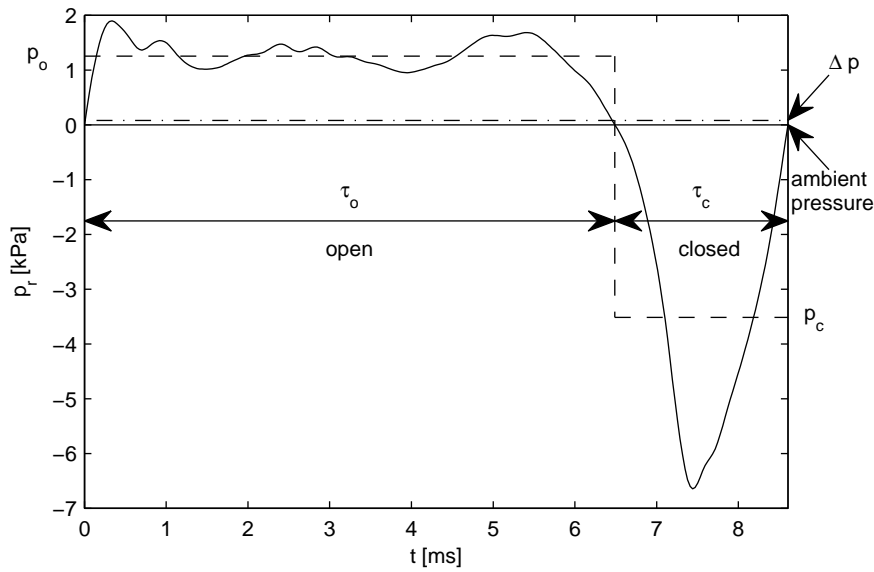


**Figure 5.2** Reed pressure (solid) and the corresponding simplified Helmholtz-pattern (dashed), and integral mean reed pressure  $\bar{p}_r > 0$ , for the note B2 ( $f_0 = 116$  Hz).

### 5.1.3 Spectral Analysis – Period Synchronized Sampling

The precise determination of zero-crossings carried out for the reed pressure waveform analysis is also useful for a harmonic spectral analysis of the reed pressure. The Discrete Fourier Transform (DFT) of a single pressure waveform, resampled in an odd number of equal time steps  $\delta t$  between the three zero crossings demarcating the cycle duration  $\tau = \tau_o + \tau_c$  results in a harmonic spectrum, where each spectral line corresponds to an integer harmonic  $n f_0$ , with  $n = 0, 1, 2, \dots, 1/(2\delta t f_0) + 1$ . This harmonic spectrum has a very low frequency resolution and assumes that all signal components are harmonic, which is a reasonable approximation for wind instruments [58]. Any inharmonic “noise” components in the signal are distributed over the harmonic spectral amplitudes. Despite the low frequency resolution, the pitch information is preserved with greatest possible accuracy<sup>10</sup>, thanks to the cumbersome analysis of zero crossings and resampling in the pre-processing. In this step subsample precision is needed, as a time step  $\delta t$  of  $1/(65536 \text{ Hz})$  corresponds to a tuning difference of  $1.5 \text{ Cent} < \Delta f_{cent} < 15 \text{ Cent}$  in the tonal range of the bassoon  $58 \text{ Hz} < f_0 < 622 \text{ Hz}$ . The analysis procedure<sup>11</sup> is called period-synchronized sampling in the following. This pre-processing to adapt the time signal to the inherent properties of the DFT is attractive for nearly perfectly harmonic signals as in the sustained part of a bassoon note: The fundamental frequency and the magnitudes of the harmonics are immediately available. The application of time-domain windowing, pitch detection and peak-picking algorithms to evaluate the spectral data become obsolete.

To characterize a single working point of the reed, the first eight magnitudes of the harmonic spectrum are used:

$f_0$  the fundamental frequency of the oscillation,

$|P_{r,i}|$   $i = 1..8$ , the magnitudes of the first eight harmonics<sup>12</sup> in the reed pressure spectrum

$|P_{s,i}|$   $i = 1..8$ , the corresponding magnitudes in the sound pressure spectrum

<sup>10</sup>This refers to “pitch” in a mathematical sense. The perceived pitch of a complex tone may be different.

<sup>11</sup>This analysis method has been proposed to the author by Johannes Baumgart

<sup>12</sup>including the fundamental

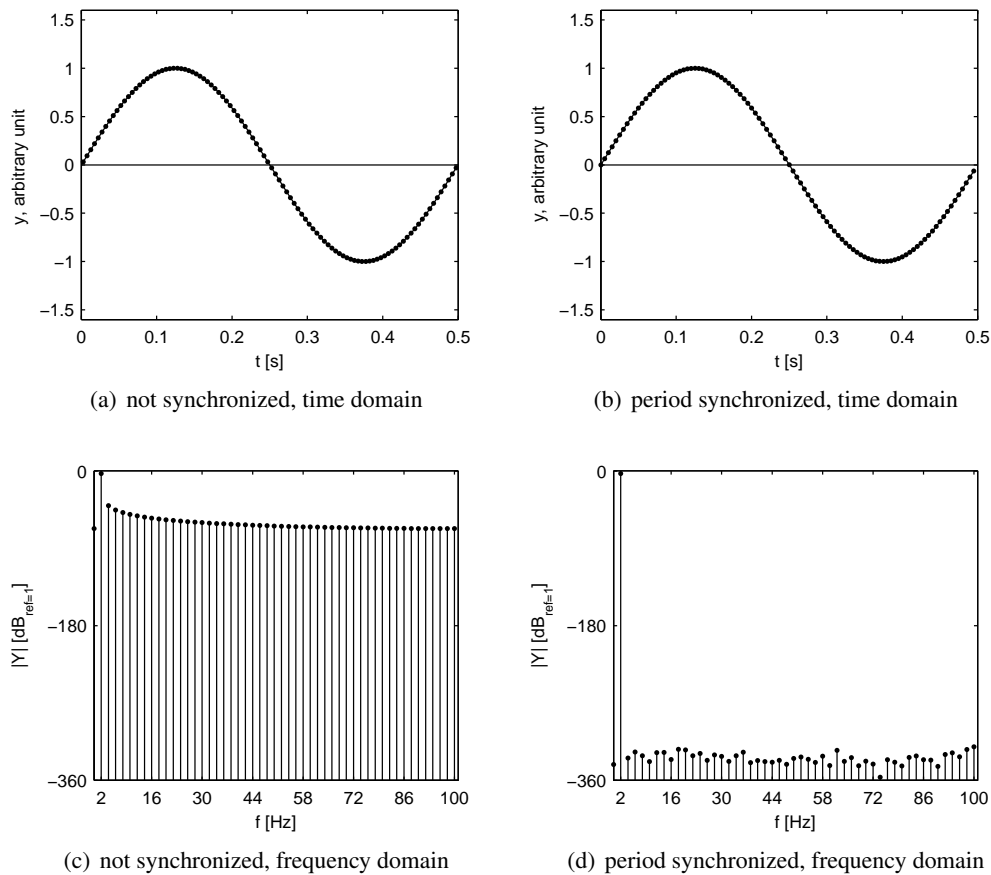


**Figure 5.3** Effect of period synchronized sampling on the DFT, demonstrated for a sampling duration of 0.5 seconds of the sine  $y = \sin(2\pi f_0 t)$ ; ( $f_0 = 2$  Hz), sampled at  $f_s = 200$  Hz.  
 Left:  $t_{start} = -\frac{1}{2f_s}$  s ( $n_{samples} = 101$ ); Right:  $t_{start} = 0$  ( $n_{samples} = 100$ )

### 5.1.4 Spectral Centroid and Formants

Characteristics of the spectrum of a sound are correlated with the perception of timbre, in the context of Music Information Retrieval, these spectral meta-data often are called timbre descriptors or audio descriptors [139]. Many acoustical parameters and “features” can be extracted from sound files, to certain aspects of timbre. The present work focuses only on a very basic, but standardized method of timbre description.

The international standard MPEG-7<sup>13</sup> defines so-called low-levels descriptors (LLD), some of which are used to characterize the timbral spectral characteristics of a sound. Three of those are purely spectral, they are calculated as one scalar per frame to be analyzed, and do not depend upon the evolution of the spectrum over time. Therefore they are useful within this study to characterize quasi-stationary states of the operating bassoon reed.

The three parameters are called the *harmonic spectral centroid* (*hsc*) in Hertz, the *harmonic spectral spread* (*hss*) and the *harmonic spectral deviation* (*hsd*). They are defined as the amplitude-weighted mean of the harmonic peaks of the spectrum (*hsc*), and the amplitude-weighted standard deviation of the harmonic peaks divided by the harmonic spectral centroid *hsc* (*hss*). The harmonic spectral deviation (*hsd*) is a measure for the deviation of the amplitudes of the partials from a global (smoothed) spectral envelope [139]. The algorithms to calculate these descriptors from a time-

<sup>13</sup>ISO Standard (ISO/IEC 15938)

domain signal of at least 125 ms is standardized, and the code is freely accessible [123]. Among those parameters the spectral centroid has been proven to correlate with the impression of brightness of a sound [145].

A similar spectral analysis method is the detection of formants. Formants are regions of higher amplitudes of the harmonics in the spectral envelope. The formant positions along the frequency axis are independent of the pitch. In speech, formants originate from the vocal tract which acts as a linear filter to the fluctuating air pressure. The shape of the vocal tract determines the formant frequencies. The relative frequencies of formants determine the vowels produced. Thus it is possible to recognize vowels independently of pitch<sup>14</sup>.

Formants are not only found in voice sounds, but also in the sound of conical wind instruments [121, 162]. The approach is largely similar to the spectral centroid, but has more subtlety, as a spectrum can exhibit more than one formant. Their relative position on the frequency axis is also relevant to the impression of timbre. Formants can be obtained by linear predictive coding (LPC) or from long-term averaged spectra (LTAS). Each formant is characterized by a center frequency  $\mathcal{F}i$  and a bandwidth  $Bi$ , where  $i$  is the ordinal number of the formant. In this study, the phonetics software *praat* [23] has been used to detect four formants for frequencies up to 5 kHz with the Burg-Algorithm from the recorded time-domain data of one second duration.

These spectral timbral descriptors are calculated for both the pressure inside the reed and the sound pressure in the surrounding of the instrument, as indicated by the subscripts  $(\cdot)_r$  and  $(\cdot)_s$ , respectively.

$hsc_{r,s}$  the harmonic spectral centroid

$hss_{r,s}$  the harmonic spectral spread,

$hds_{r,s}$  the harmonic spectral deviation,

$\mathcal{F}i_{r,s}$  ( $i = 1..4$ ), the center frequencies of the first four formants

$Bi_{r,s}$  ( $i = 1..4$ ), the band widths of the first four formants

### 5.1.5 Embouchure parameters

The quasi-static double-reed model introduced in Chapter 4 predicts the parameters  $p_M$  and  $q_A$  of the reed valve characteristics for any quasi-static working point of the reed defined by differential pressure  $\Delta p = p_m - p_r$  and lip force  $F_l$ . From the estimated values of  $p_M$  and  $q_A$ , the flow-rate  $q$  and the corresponding reed slit height  $h$  can be calculated.

Despite being based on many simplifications, the quasi-static model [172, 89, 102] of the reed is commonly used for the dynamic modeling of oscillating reed woodwinds up to now, for modeling in the time and frequency domain. As was recently proven that the model explains mode locking effects in the clarinet [129], it can be concluded that its application to dynamic cases is reasonable, to a large extent. Details of the unsteady flow at the reed intake have been quantified in recent studies, e.g. the change of the constriction coefficient (*vena contracta*) within one duty cycle [115] depending on the Reynolds number and reed intake geometry [39].

In this study, it will be shown experimentally, that the quasi-static model can provide useful information to characterize the operating point of the reed under playing conditions. In this quasi-stationary case, the model input  $\Delta p$  is a differential pressure calculated from  $p_r - \bar{p}_m$ , where  $p_r$  is the unsteady reed pressure measured inside the mouthpiece, and  $\bar{p}_m$  is the mouth pressure measured at a wall of the mouth cavity, averaged over one period. Similar to the mouth pressure, the lip force is assumed to be constant over one period  $F_l(t) = \bar{F}_l = \text{constant}$ . The averaging is obtained by the inertance of the artificial lip and the force sensor.  $\bar{F}_l$  is the sensor output.

<sup>14</sup>At very high pitches there is not a sufficient number of harmonics in each formant and the vowels cannot be distinguished

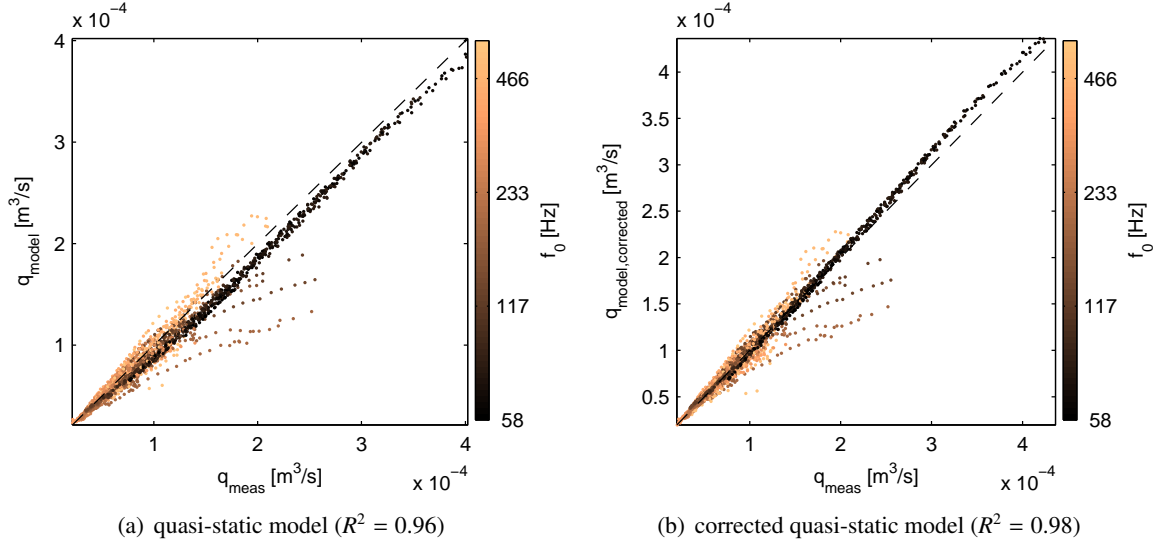


**Figure 5.4** Deviation between the measured mean flow-rate  $q_{meas}$  and the flow rate predicted by the quasi-static model. (a) before and (b) after correction for effects of the pressure efficiency and the non-dimensional lip force, by linear regression.

The applicability of the quasi-static model to dynamic cases can be assessed by using these two monitored mean values during playing and using them as input parameters to predict the mean-flow rate and the mean slit height. The empirical parameters for the models (Eq. 4.28) have been determined previously as described in Chapter 4, for the same lip position  $x_l$  used in the blowing experiment.

In Fig. 5.4(b) the model prediction  $q_{s,model} = f(\bar{F}_l, \Delta p)$  is compared with measured values. It is noticeable, that the quasi-static model applied in the dynamic case explains about 80% of the experimentally observed mean flow-rate ( $R^2 = 0.96$ ). For the residuals of the model a weak correlation with the ratio of mouth pressure over RMS reed pressure ( $R^2 = 0.18$ ) is observed (Fig. 5.5(a)). Although the correlation is weak, it can be observed, that the model tends to underpredict the flow-rate for “efficient” regimes, where  $p_m/p_{r,RMS}$  is larger than unity. Generally, for higher frequencies, the spread of residuals is significantly larger.

Another observation is, that the residuals correlate weakly with a non-dimensional lip force parameter  $F_l/(p_m w^2)$  (Fig. 5.5(b)). This can be seen for low oscillation frequencies, but globally the correlation is quite small ( $R^2 = 0.04$ ).

Surprisingly, no correlation could be found between the residuals and parameters such as the Reynolds or Strouhal number ( $R^2 < 0.001$ , data not shown.)<sup>15</sup>.

This analysis is based on a large number of independent experiments ( $n = 2212$ ), covering the complete tonal and dynamical range of three different bassoon-bocal combinations, using the same reed. It is remarkable, that for some notes in the middle register the model fails significantly by up to -50 %.

<sup>15</sup>One would have expected such a dependency because the model considers a limit for high Reynolds numbers and vanishing Strouhal number [88]. The Reynolds and Strouhal number are calculated here as quasi-stationary quantities  $Re(\frac{h_o}{w}) = \frac{u_{Bernoulli} h_o}{\nu} (\frac{h}{w})$  and  $St = \frac{f_0 w}{h_o}$ , respectively, where  $u_{Bernoulli} = \sqrt{\frac{2 p_m}{\rho}}$  is an estimate of the flow velocity,  $h_o(F_l, \Delta p)$  is embouchure dependent reed slit height during open episode (estimated from  $F_l$  and  $\Delta p = \bar{p}_m - p_o$  by use of the model),  $w = 14 \text{ mm}$  is the width of the reed channel (assumedly constant), and  $\nu = \frac{\eta}{\rho}$  is the kinematic viscosity.

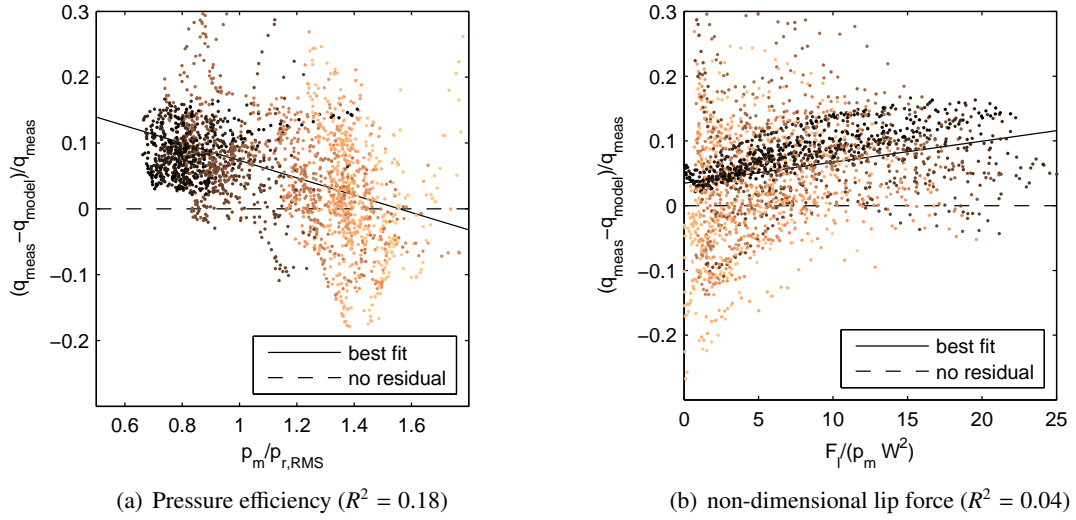


**Figure 5.5** Correlation of the residuals of the flow-model on (a) pressure efficiency  $p_m/p_{r,\text{RMS}}$  and (b) on the non-dimensional lip-force  $F_l/(p_m W^2)$ .

Applying a linear regression to correct for the two statistically weak effects, that the pressure efficiency and the non-dimensional lip force have on the model, improves the fit marginally by 5 % (fig. 5.4(b)). Reasons for the remaining discrepancy might be

- a change in the effective reed width for a change in the reed slit height (Fig. 4.12),
- an overestimation of the vena-contracta effect for very narrow slits (Fig. 4.24),
- an additional, lateral opening of the double-reed for high pressure regimes (and loose embouchures)
- a difference in quasi-static and dynamic reed blade movement.

These aspects should be studied more in detail by using time-resolved geometrical information of the oscillating reed slit.

Considering that the reed performs a two-step motion [136], an estimation of the reed slit height can be deduced from the monitored values of blowing pressure and lip force. The approach bases on an empirical model  $h_{\text{model}} = f(\bar{F}_l, \Delta p)$  (Eq.(4.33a)). Here, in contrast to the flow-rate estimation, the model input  $\Delta p$  is the differential pressure  $p_m - p_o$ , where  $p_o$  is the integral mean value of the reed pressure during the open phase of the oscillation cycle. Accordingly, the model then predicts the reed slit height  $h_o$  during the open episode. For the lowest notes of the bassoon, the open episode is up to ten times longer than the closed episode (more details are given below in section 5.2.3. This makes it easy to measure  $h_o$  optically, using a camera with a long shutter time to integrate over some periods (e.g. 1/30 sec). In this way, the averaging is performed directly in the image acquisition, as the amount of light on the sensor is integrated over some periods of the oscillation. Measurement and model show a reasonable agreement for the  $h_o$  of those notes, where the assumption of a rectangular two-step motion is met (Fig. 5.6).



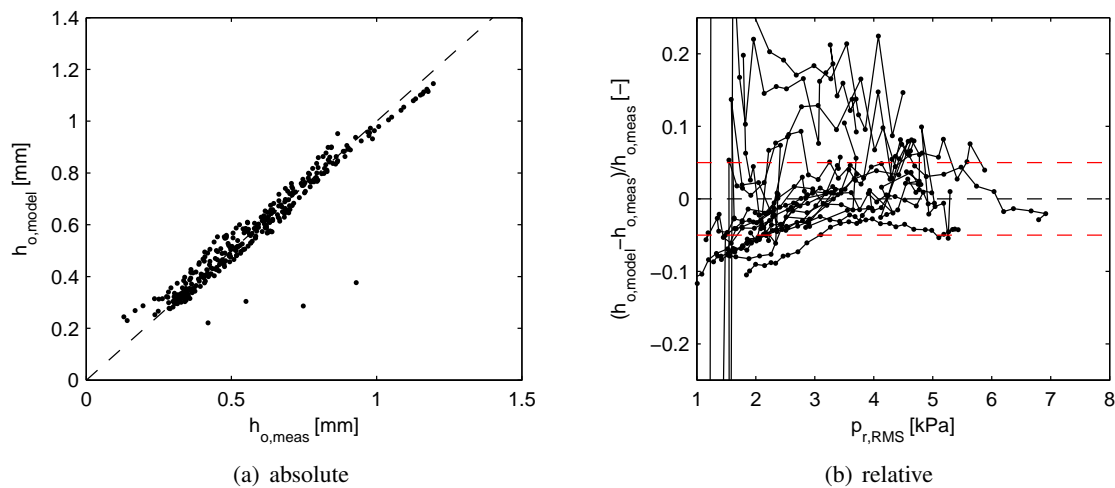


**Figure 5.6** Deviation between the measured slit height  $h_{o,meas}$  and the slit height predicted by the quasi-static model  $h_{o,model}$ . (a) absolute, (b) relative, plotted vs. the RMS-value of the reed pressure  $p_{r,RMS}$ . The dashed horizontal lines mark the 5% deviation.

For both mean flow-rate  $q$  and slit height  $h_o$ , the models underestimates the measurements, at low RMS-pressure. This is especially noticeable for the flow-rate, and is probably due to the reed motion induced flow. However, a general agreement is found, the most extreme outliers are still the within  $\pm 20\%$  for the flow-rate and less for the slit height.

In light of the considerable simplifications used in the quasi-static model, and the pronounced dynamics of the operating reed valve, the agreement is quite reasonable. Therefore it can be concluded, that the application of this model to characterize the quasi-stationary process at a single working point of the reed is acceptable.

Applying the model leads with the empirical relations Eq. 4.31b and Eq. 4.31a to an estimation of the reed closing pressure  $p_M$ , the flow parameter  $q_A$  and with Eq. 4.33a to an estimation of the reed slit height in the open episode. Especially  $p_M$  and  $q_A$  are important, as they can be used to characterize the working point with respect to an analytic model [102, 153]. The non-dimensional blowing pressure  $\gamma$  and non-dimensional embouchure parameter  $\zeta$  are defined as

$$\gamma = \frac{p_m}{p_M}, \quad (5.1)$$

and

$$\zeta = Z_c \frac{q_A}{p_M}, \quad (5.2)$$

where  $Z_c$  is the characteristic impedance of the air in the cross section at the bocal tip, where the reed is attached to the resonator.

The applicability of this analytic single-reed model to the case of the double-reed has been proven [4]. From  $p_M$  and  $q_A$  a reed equivalent stiffness  $K_s$  per unit area can be deduced as

$$K_s = \frac{p_M}{q_A} \sqrt{\frac{2p_M}{\rho}}, \quad (5.3)$$

where  $\rho$  is the air density<sup>16</sup>.

<sup>16</sup> $\rho \approx 1.2 \text{ kg/m}^3$

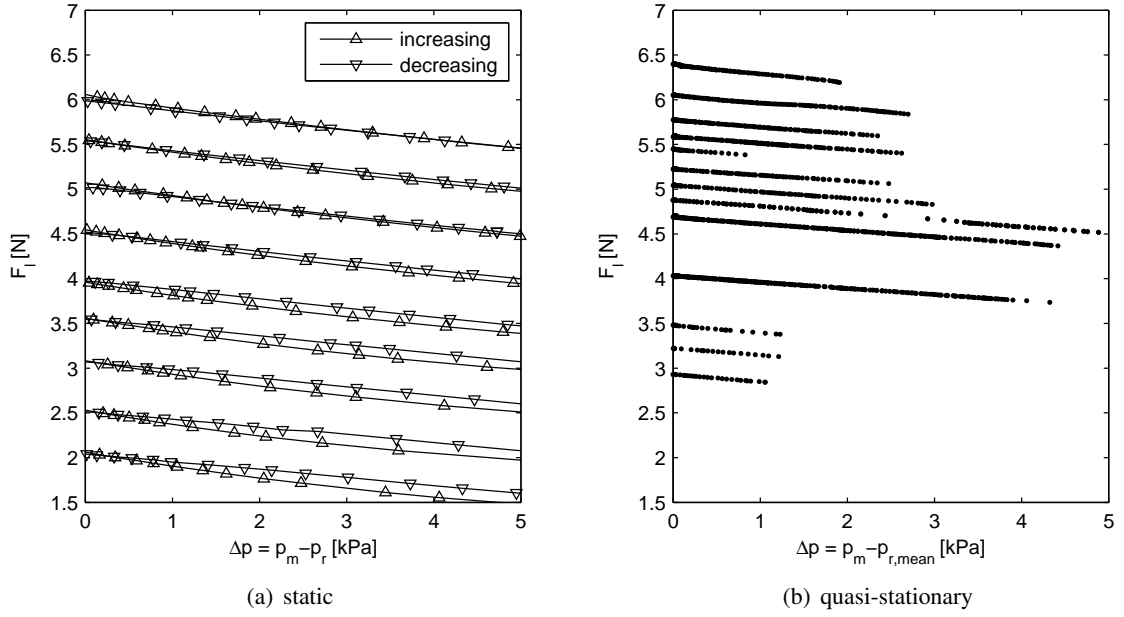


Figure 5.7 Lip force  $F_{l,initial}$  vs. mouth pressure change  $\Delta p$

### Pressure-induced lip force change

If the artificial lip block is fixed in one position and the artificial mouth is pressurized, the reed blades deflect and the lip force is reduced. The gradient of  $F_l$  with respect to  $\Delta p$  has the dimension of an area. The pressure difference  $\Delta p$  is  $\Delta p = p_m - \bar{p}_r$ , where  $p_m$  is the (constant) mouth pressure and  $\bar{p}_r$  is the time averaged pressure inside the reed. It was measured in both static (with blocked reed vibrations) and quasi-stationary (with vibrating reed) conditions, where  $\bar{p}_r$  is only a few dozens of Pascals.

The first case refers to the measurement of the reed-valve characteristics (see Chapter 4), the second case to a measurement under playing conditions with a resonator attached, where the mouth pressure is increased, without changing the lip position. This measurement is similar to artificial mouth measurements on the clarinet [42]. Interestingly, in the dynamic case investigated here, the relationship between force change and mouth pressure is linear ( $R^2 = 0.90 \dots 0.99$ ) and independent of both the initial lip force, and the frequency of oscillation (Fig. 5.7(b)).

As shown in Fig. 5.8, for the quasi-static measurement, the value clearly decreases with increasing initial lip force, probably as a consequence of the increased contact area between artificial lip and reed for higher lip forces. For the quasi-static case (infinitely slow reed deformation), the slope ( $F_l/d\Delta p$ ) is in the range between  $-1.1$  and  $-0.2 \text{ cm}^2$ . In the quasi-stationary case (reed blades beat with constant amplitude), the same pressure difference leads to less reduction of the lip force. In this case, the slope is  $-0.78 \pm 0.12 \text{ cm}^2$  (mean value  $\pm$  standard deviation for several configurations  $0.5 \text{ N} < F_l < 7 \text{ N}$ ).

The empirical, lip-position-dependent static model introduced in Chapter 4 is useful to interpret the artificial mouth adjustment parameters  $F_l$  and  $p_m$  together with the resulting reed pressure  $p_r(t)$  as non-dimensional parameters of an analytic reed model within reasonable accuracy. Furthermore, some equivalent physical properties such as the reed slit height and the reed stiffness can be derived.

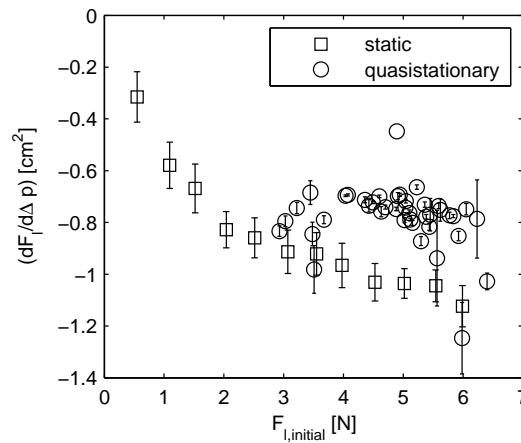


**Figure 5.8** Gradient  $(dF_l/d\Delta p)$  for several embouchure configurations characterized by the initial lip force  $F_{l,initial}$

These parameters describing a single working point are summarized below as

$\gamma$  the non-dimensional blowing pressure

$\zeta$  the non-dimensional embouchure parameter

$p_M$  the pressure to close the reed [Pa]

$q_A$  the reed flow-rate parameter [ $\frac{m^3}{s}$ ]

$K_s$  the reed equivalent stiffness per unit area [ $\frac{Pa}{m^2}$ ]

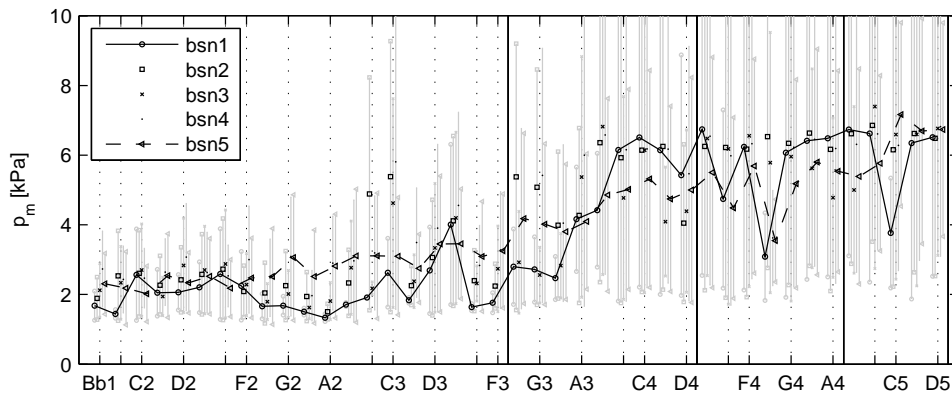
$h_o$  the reed slit height during the open episode [m]

Artificial mouth adjustment parameters, which are relatively easy to obtain with the present setup, can be used to characterize an experimental situation in the context of the elementary single-reed model [102].

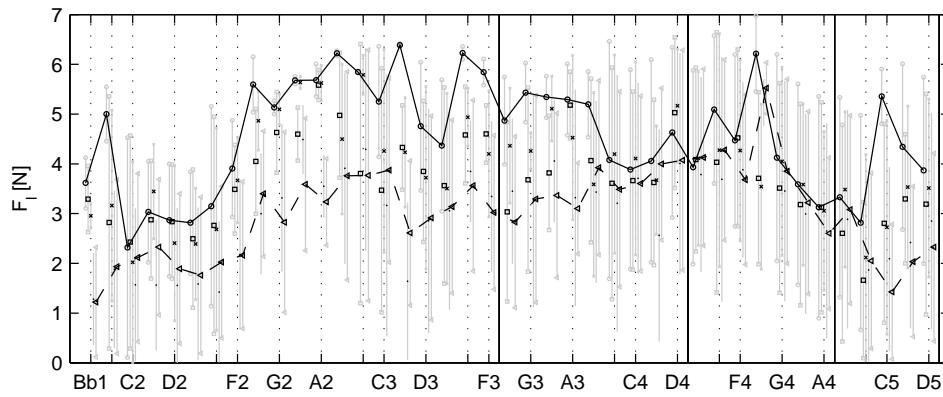
## 5.2 Observations on the Bassoon under Operating Conditions

In this section an overview will be given on the ranges of input parameters of the artificial mouth to produce musically relevant operating regimes, as well as the output parameters characterizing those regimes. The study covers the full tonal and dynamical range. The tested bassoons were modern German Bassoons from the manufacturers Adler, Hüller, and Heckel. From the latter manufacturer, a student model and a professional model have been used. One of the bassoons has been measured twice with two bocals of different length. The corresponding five bassoon-bocal combinations were excited with the same synthetic bassoon reed for fixed lip position ( $x_l = 10.75$  mm).

In the following plots of results and the observed ranges of parameters are plotted versus log-frequency. For better readability, this axis is labeled with the corresponding note names. The gray bars indicate the range of values observed for minimum and maximum dynamic level, at which the note was playable in tune. To display the variation between instruments, the corresponding mean values for each of the five the bassoon-bocal combinations are marked with different symbols  $\circ$ ,  $\square$ ,  $\times$ ,  $\cdot$ , and  $\triangleleft$ .



(a) Mouth pressure



(b) Lip force

**Figure 5.9** Input parameters  $p_m$  and  $F_l$ 

### 5.2.1 Excitation Parameter Ranges

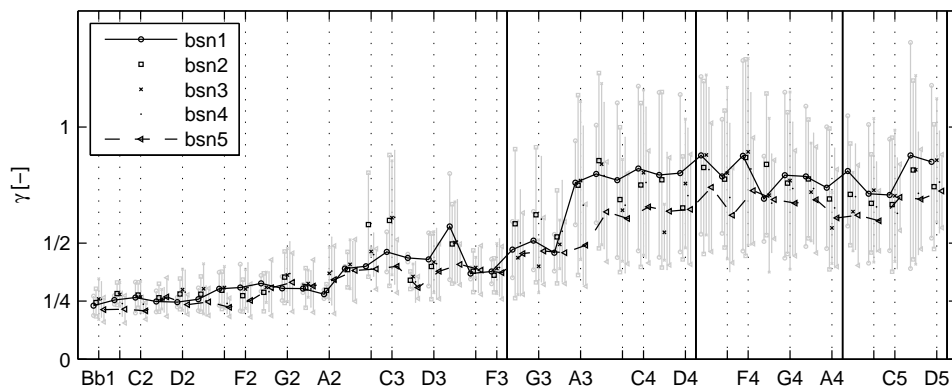
The artificial mouth adjustment parameters mouth pressure  $p_m$  and lip force  $F_l$  are regarded as *input* parameters to the coupled oscillatory system, to excite it at a fixed nominal frequency  $f_{0,nom}$  corresponding to the fingering applied to the resonator.

#### Artificial Mouth Input Parameters

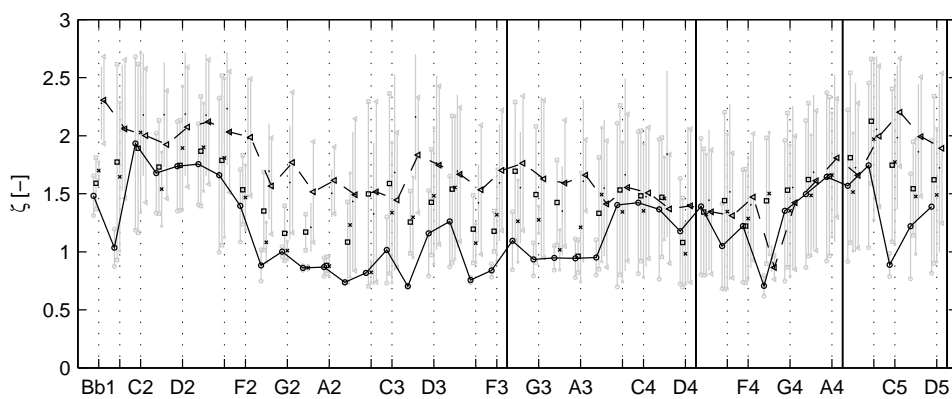
The mouth pressures  $p_m$  range from 1.5 kPa to more than 10 kPa (Fig. 5.9(a)). Blowing pressures larger than 10 kPa are unrealistically high [68]. Therefore, the vertical axis in Fig. 5.9(a) is cropped at this value, although notes could be played for even higher mouth pressures.

Ascending the scale, the minimum mouth pressure to sound a note in tune increases approximately linear with log-frequency: Lower notes require less blowing pressure than higher notes.

In general, two regions can be identified in Fig. 5.9(a): The lower notes (from Bb1 to A3) offer a smaller blowing pressure range ( $1 \text{ kPa} < \Delta p_m < 5.5 \text{ kPa}$ ) and are played at lower mean value of  $\bar{p}_m \approx 2.5 \text{ kPa}$ ; the higher notes (A3-D5) have a larger blowing pressure range ( $4.5 \text{ kPa} < \Delta p_m < 9 \text{ kPa}$ ) and a higher blowing pressure offset. Compared to the mouth pressure, the lip force characteristics to sound the notes in tune is irregular, no simple dependence on the log-frequency scale can be observed (Fig. 5.9(b)). Very generally speaking, the mean values  $\bar{F}_l$  are smaller at the lower and



(a) Non-dimensional mouth pressure



(b) Embouchure parameter

**Figure 5.10** Reed Model Input Parameters  $\gamma = \frac{p_m}{p_M}$  and  $\zeta = Z_c \frac{q_A}{p_M}$ .

upper limit of the tonal range, and larger in between. Adjacent notes may require a very different  $F_l$  offset. For each single note, the lip force range  $\Delta F_l$  indicates the adjustments needed to compensate for tuning when changing the dynamic level. This value reaches up to several Newtons and largely depends on the tuning properties of each instrument, and, naturally, on the position  $x_l$  of the lip on the reed, which was constant in all measurements presented here. Apparently the bassoon-bocal combination *bsn1* (open circles in the graphs) was tuned flat compared to the other bassoons and thus required globally a higher lip force, whereas for the combination *bsn5* (triangles in the graphs) the opposite trend is observed in Fig. 5.9(b).

### Reed Model Input Parameters

Using the quasi-static pressure-flow characteristics of the reed, the instantaneous lip force  $F_l$ , and blowing pressure  $p_m$ , each working point of the setup can be characterized by non-dimensional reed model parameters (see section 5.1.5), which are the non-dimensional blowing pressure  $\gamma$  (Fig. 5.10(a)) and an embouchure parameter  $\zeta$  (Fig. 5.10(b)) [102].

Both  $\gamma$  and  $\zeta$ -characteristics resemble the  $p_m$  and  $F_l$  characteristic in Fig. 5.16. A benchmarking value for bassoon embouchures is  $\zeta = 1.5 \pm 0.5$ . Regarding the spread of values with changes in the dynamic level, and the comparison of the five bassoons, the same observation as for the lip force qualitatively apply (see above paragraph). Note that  $\zeta$  is inversely related to the lip force

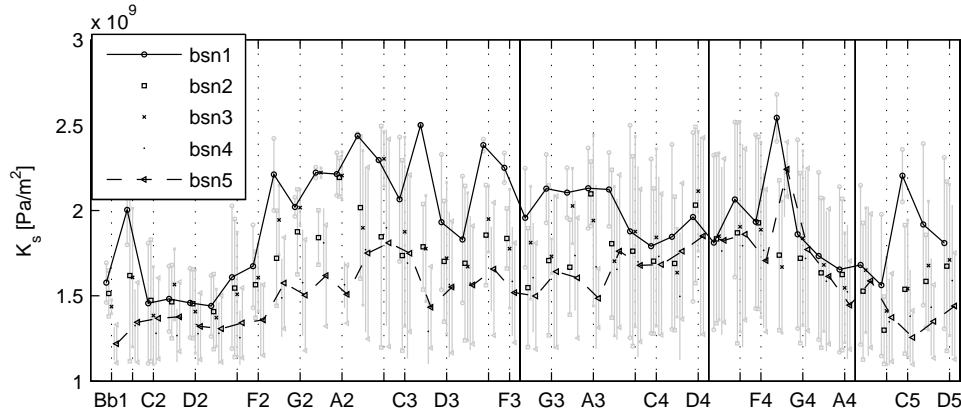


Figure 5.11 Reed stiffness  $K_s$  according to the quasi-static reed model.

$F_l$ . Large lip-forces correspond to a small slit-heights and thus small  $\zeta$ , because the pressure-flow characteristics (Fig. 4.22, Eq. (4.31)) is downscaled and shifted to lower values.

An interesting observation regarding the non-dimensional mouth pressure is, that for notes higher than A3,  $\gamma$  is larger than  $1/3$  (Fig. 5.10(a)). This means that those notes are played at mouth pressures above saturation  $p_{m,s}$  of the pressure-flow characteristics of the reed-valve (Tab. 3.1). On the other hand, the playing pressure range of the notes below G2 does hardly exceed saturation. Further it can be seen that in the upper tonal range oscillations are possible for  $\gamma > 1$ , for which the reed would be blocked under quasi-static conditions. Note, that  $\gamma > 1$  does not necessarily correspond to extremely high mouth pressures: For large lip force  $F_l > 6$  N, the pressure  $p_M$  to close the reed completely is smaller than 4 kPa (Fig. 4.22).

For each working point characterized by  $\gamma$  and  $\zeta$ , the corresponding reed effective stiffness  $K_s = p_M/q_A \sqrt{(2p_M)/\rho}$  can be calculated. It is a measure in Pa/m<sup>2</sup> indicating the pressure difference  $\Delta p$  in Pascal needed to reduce the reed's intake cross section  $S_{in}$  by one square meter. Typical values for the bassoon reed under playing conditions are  $K_s = (1.6 \pm 0.35) 10^9$  Pa/m<sup>2</sup> (Fig. 5.11). The reed stiffness  $K_s$  is related to the lip force  $F_l$ : large lip forces indicate a large pre-deflection and therefore an effective stiffening<sup>17</sup> of the reed.

The change in  $K_s$  with the dynamic level, and the observed spread in  $K_s$  between instruments is therefore mostly due to the tuning properties of the specific fingering, and the lip force applied to compensate for it. The presented measurement values of reed parameters under operating conditions provide ranges and limits for realistic embouchures on the reed, in which the sounding frequency of the coupled reed-resonator system is the desired fundamental frequency corresponding to the fingering on the resonator.

This information may be helpful for physical modeling, which has not been the scope of this work.

## Output Parameters

For each note, the oscillatory regime established for a combination of  $p_m$  and  $F_l$  is characterized by the output parameters RMS-value of the reed pressure  $p_{r,RMS}$  and the time-averaged volume flow-rate  $q$ . These may be called primary output parameters, because they are distinct measures at the operating reed, directly measurable without further analysis.

The RMS reed pressure  $p_{r,RMS}$  for musically relevant regimes ranges from 1 to 9 kPa, equivalent to 154 to 173 dB SPL (Fig. 5.12(a)). The minimum value for the softest regimes is  $\bar{p}_{m,min} = 2 \pm 0.5$  kPa, the differences on one note comparing between instruments exceed 1 kPa. This observation is

<sup>17</sup> Another possible explanation for the observed stiffness increase at high lip forces is, that an increasing extent of the reed area is covered by the lip when increasing the force.

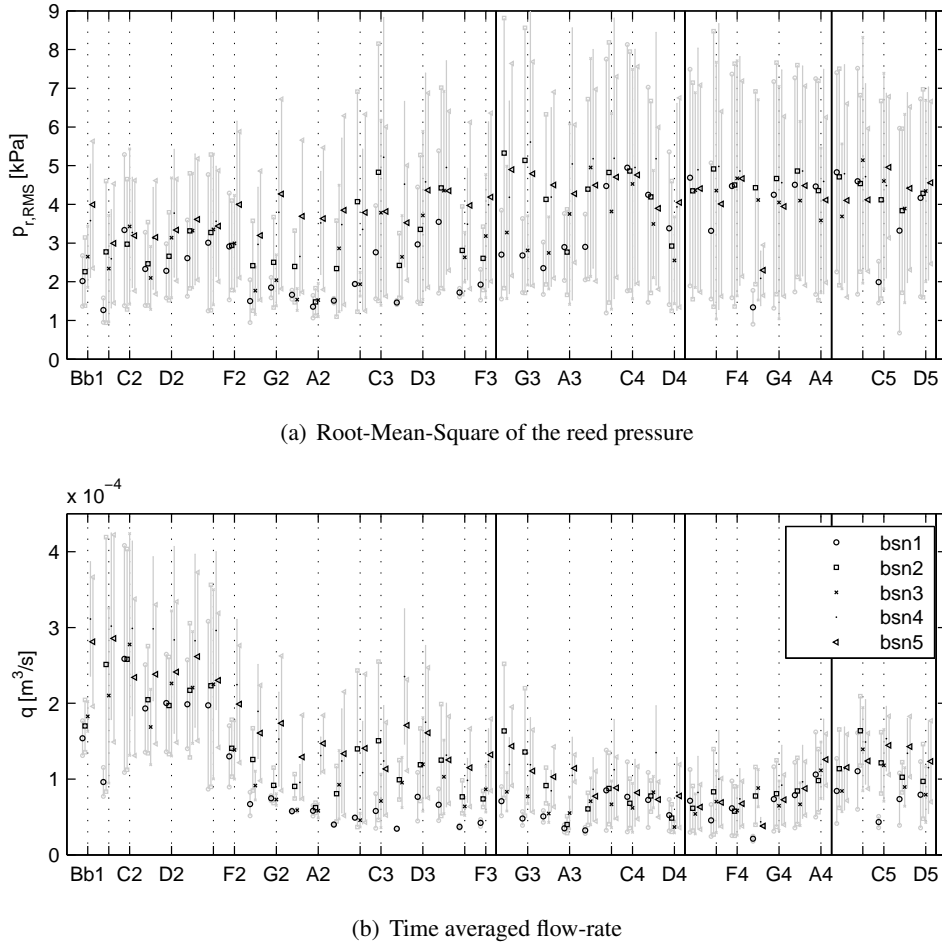


**Figure 5.12** Output parameters  $p_{r,RMS}$  and  $q$

largely influenced by the tuning of the instrument. Ascending the scale, the mean RMS reed pressure  $p_{r,RMS}$  tends to increase slightly. The notes of the lower register have a large fluctuation in  $\bar{p}_{r,RMS}$  across the log-frequency axis. This fluctuation is decreased for higher notes; apart from some outliers,  $\bar{p}_{r,RMS}$  is here around 4.2 kPa. The time-averaged volume flow-rate  $q$  ranges from up to  $4.5 \times 10^{-4} \text{ m}^3/\text{s}$  for C2 at the lower end of the tonal range, to less than a tenth of this value at F4 in the medium high register ( $0.25 \times 10^{-4} \text{ m}^3/\text{s}$ ). The notes Bb1 to E2 require the most volume flow ( $\bar{q} = 2 \times 10^{-4} \text{ m}^3/\text{s}$ ). From F2 to G4, the mean flow  $\bar{q}$  decreases from 2 to  $1 \times 10^{-4} \text{ m}^3/\text{s}$ . From A4 upwards in the note scale  $\bar{q}$  tends to increase again (Fig. 5.12(b)). These general trends in the flow-characteristics resemble the inverted lip force characteristics (Fig. 5.9(b)). The flow-rate tends to be increased for notes which are played at lower lip forces.

An interesting observation concerning the playing dynamics is, that the RMS reed pressure  $p_{r,RMS}$  scales with the mouth-pressure  $p_m$  in the highest register, independently of the mean flow  $q$ . On the contrary, the RMS reed pressure scales with the mean flow  $q$  in the lowest register, independently of the mouth pressure. The constant scaling factors are  $p_{r,RMS}/p_m = 0.75 \text{ kPa/kPa}$  and  $p_{r,RMS}/q = 18 \text{ kPa/(l/s)}$ , for the notes of the highest (above C4) and lowest register (below E2), respectively, as indicated by the light and dark dashed lines in Fig. 5.13. This leads to the conclusion, that the dynamics of low notes are flow-controlled, while being pressure controlled in the high notes. For the notes in the middle of the tonal range,  $p_{r,RMS}$  depends on both  $p_m$  and  $q$ .

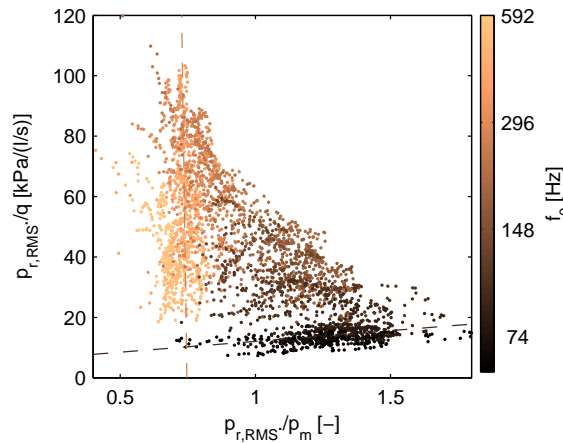


**Figure 5.13** Dependence of the dynamic level, characterized by the RMS mouthpiece pressure  $p_{r,RMS}$ , on the mouth pressure  $p_m$  and the time-averaged volume-flow rate  $q$ . Each dot is one working point of the reed, represented by one second of a sustained bassoon tone played with the artificial mouth. The color indicates the sounding frequency  $f_0$ , according to the colorbar to the right of the plot.

### 5.2.2 Characteristics of the radiated Sound

The radiated sound was recorded at a fixed position at about 1.5 m from the instrument, in a lab room with sound-reflecting walls. Thus, the measurements presented in this section are affected by the room acoustics, which in particular influence the absolute values of sound pressure level and loudness, to a lesser extent also the global spectral metrics like formant frequencies and harmonic spectral centroid. However, the results are comparable between measurements, because both positions of the microphone and the experimental setup with respect to the room were not changed. Even if not well-defined, this recording situation corresponds to realistic conditions of musical performance. In the blowing experiments, the external sound pressure levels ranged from around 71 dB SPL (notes A2, F#4) to 95 dB SPL (B3) at 1.5 m distance from the bassoon (Fig. 5.14(a)). The sound pressure level is very irregular over the semitones: Comparing the minimum SPL of single notes, the differences reach up to 15 dB SPL, which is more than the maximum dynamic range of a single note, 9 dB SPL. The general characteristics of SPL vs. log-frequency is approximately the same for all instruments, but some very large differences in SPL and dynamical range can be seen for a few individual notes when comparing between instruments (e.g. A2, C#3, F3, F#3, F#4, C#5). Despite the pronounced irregularity, which certainly is affected by the radiation pattern and room reflections, a general trend is observed that the dynamic range is doubled over the tonal range from 3 dB for low notes to 6 dB for the high notes. The characteristic of loudness<sup>18</sup>  $N$  vs. log-frequency (Fig. 5.14(b)) is very similar to the characteristic of  $SPL$  vs. log-frequency (Fig. 5.14(a)). Both curves are, however, very different compared to the reed internal pressure fluctuation amplitude  $p_{r,RMS}$  characteristic Fig. 5.12(a). This means that the radiated sound level does not scale directly with the sound pressure level near the sound source (in the reed mouthpiece). A more detailed insight by a study of the radiation characteristics (e.g. [121, 79]) would be helpful here. Roughly speaking, moderate bassoon playing produces sounds of  $44 \pm 12$  Sone at 1.5 m distance. The Sone-scale is linear with respect to the human perception; a doubling in Sone corresponds to a doubling in perceived loudness. In this light, the dynamical range of single notes in the blowing experiments was very small: Expressed in terms of loudness the *fortissimo* tones were only 30 to 50 % louder than the *pianissimo* tones. In general, the loudness follows the same trend as the SPL,

<sup>18</sup>Loudness is a psychoacoustical metrics to be calculated from a time series of sound pressure taking into account the signal processing in the human auditory system [54]. In contrast to the sound pressure level it characterizes the impression of loudness as perceived by a human. It is measured in Sone (according to the German standard DIN 45631), and a doubling in Sone corresponds to a doubling in perceived loudness.



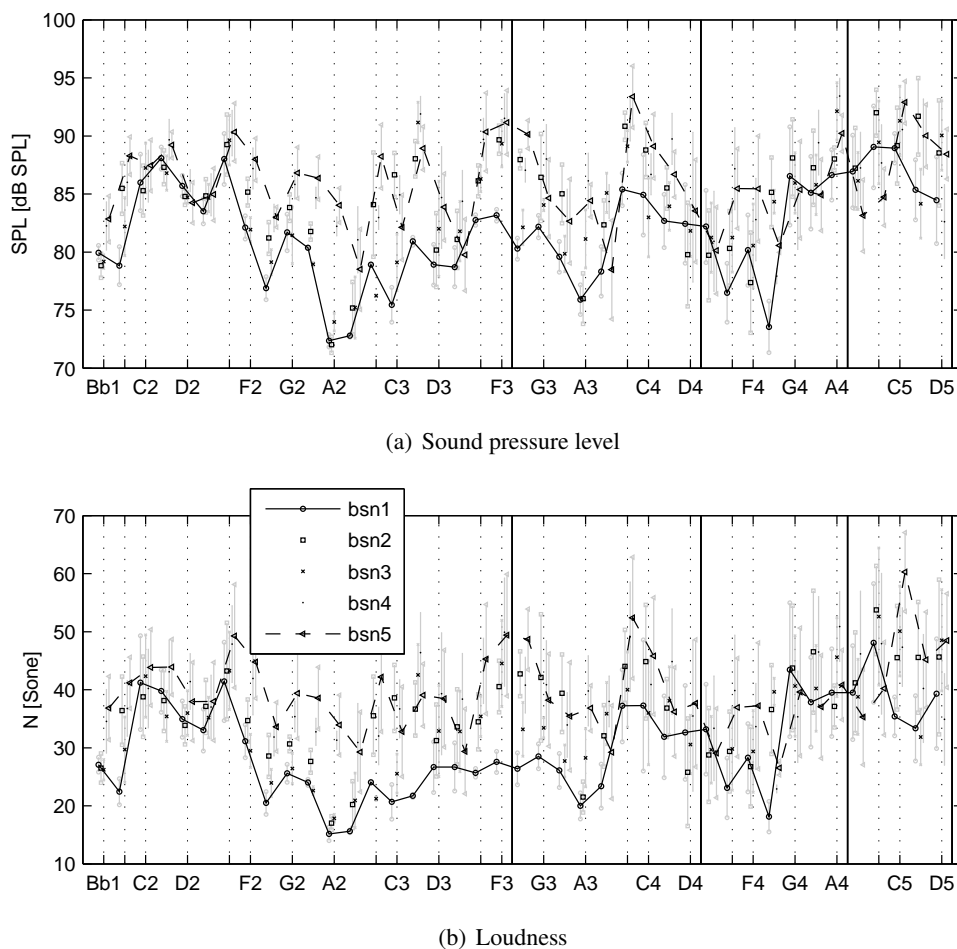


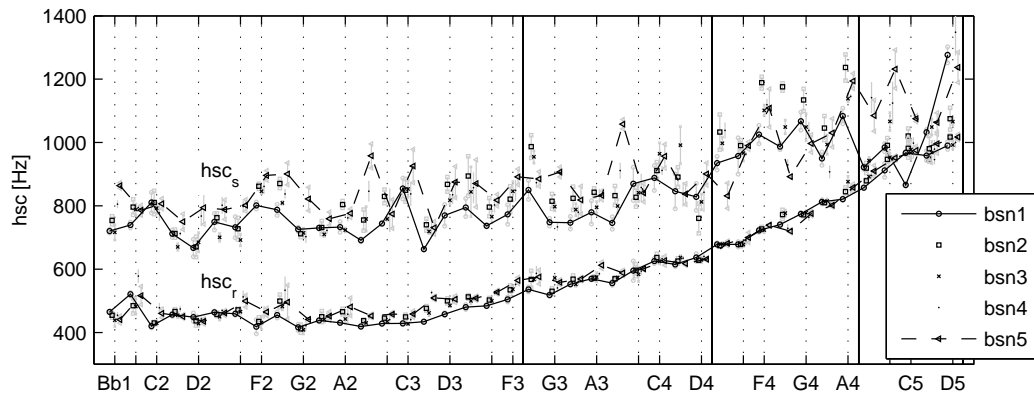
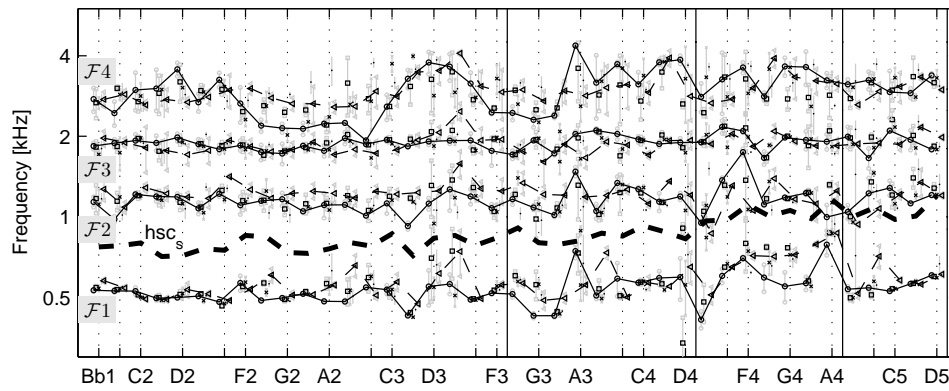
**Figure 5.14** Dynamic levels of the radiated sound in sound pressure level  $SPL$  and loudness  $N$ .

so the low notes have a smaller dynamic range than the higher notes. The largest dynamic range is observed for D4, for which the loudness could be doubled by blowing harder.

Note that the statements above on the dynamical limits refer to playing each of the notes at constant pitch.

The harmonic spectral centroid  $hsc_s$  of the sound radiated from the artificially blown bassoons is around 800 Hz for all notes up to D4 (Fig. 5.15(a)). Ascending the scale from D4,  $hsc_s$  tends to increase from 800 to 1100 Hz. The deviation from these global trends may be  $\pm 150$  Hz for individual notes. Regarding one single note, the differences in  $hsc$  between instruments is smaller than 100 Hz below D4 (except for Bb2), and slightly larger for higher notes. The range in which  $hsc_s$  varies with the dynamic level is 150 Hz at maximum.

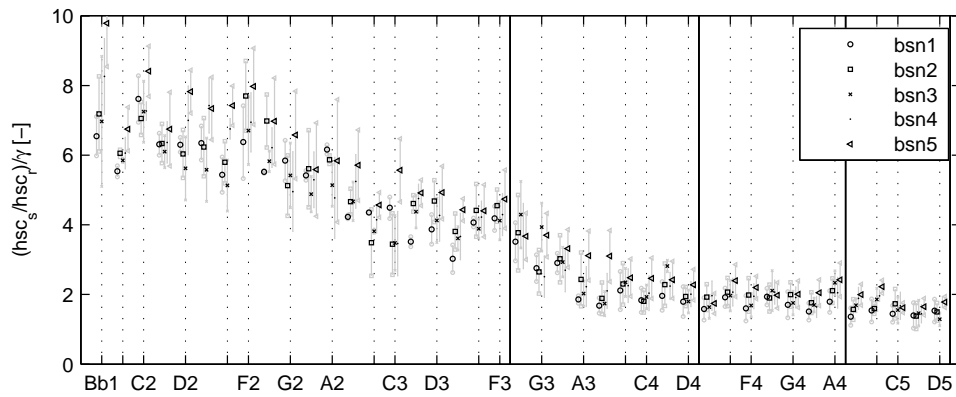
In contrast, the harmonic spectral centroid in the reed pressure  $hsc_r$  has a very narrow distribution of a few tens of Hertz only. The mean value is constant at 450 Hz for Bb1 to C3. For higher notes,  $hsc_r$  increases smoothly to reach 1 kHz at D5. Comparing spectral centroids measured in the reed and the surrounding (Fig. 5.15(a)) shows, that  $hsc_s$  is approximately twice as large as  $hsc_r$ . The vertical gray bars in this figure indicate, that the spectral centroid of the radiated sound  $hsc_s$  is largely influenced by the playing dynamics. In contrast to that, the centroid of the reed pressure spectrum  $hsc_r$  depends mostly on the fundamental frequency.

(a) Spectral centroids in the mouthpiece pressure ( $hsc_r$ ) and in the radiated sound ( $hsc_s$ ).(b) Formant center frequencies  $\mathcal{F}1$ ,  $\mathcal{F}2$ ,  $\mathcal{F}3$ ,  $\mathcal{F}4$  and  $hsc_s$  of the radiated sound.**Figure 5.15 Spectral metrics of the bassoon sound.**

There are four formants below 5 kHz in the sounds radiated from the artificially blown bassoon at the following mean values  $\pm$  standard deviation of center frequency:  $\mathcal{F}1 = 540 \pm 110$  Hz,  $\mathcal{F}2 = 1.2 \pm 0.18$  kHz,  $\mathcal{F}3 = 1.9 \pm 0.20$  kHz and  $\mathcal{F}4 = 3.0 \pm 0.60$  kHz (Fig. 5.15(b)). The center frequencies of second and third formant,  $\mathcal{F}2$  and  $\mathcal{F}3$ , respectively, appear to be mostly independent on the sounding frequency. The first and fourth formant,  $\mathcal{F}1$  and  $\mathcal{F}4$ , respectively, have quite irregular characteristics. The first formant changes at the acoustical register margins between second and third and, in particular, at the jump from the third to the fourth register. Except for some individual notes (e.g. Eb3, A3, D4) for who the  $\mathcal{F}1$  formant differs largely when comparing different instruments, the general  $\mathcal{F}1$  vs. log-frequency characteristic is the same for all five bassoon-bocal combinations under test. The effect of the dynamic level on the formant center frequencies increases with their ordinal number:  $\mathcal{F}1$  is for most notes unaffected by the dynamic level,  $\mathcal{F}4$  differs by several hundreds of Hertz. A further aspect of interest is the change in brightness of the sound due to adjustment of the dynamic level.

To evaluate the spectral enrichment of the sound with dynamics, the ratio  $(hsc_s/hsc_r)/\gamma$  is addressed, where the non-dimensional blowing pressure  $\gamma = p_m/p_M$  (Fig. 5.10(a)) characterizes the dynamic level. Thus, a large value in the dimensionless number  $(hsc_s/hsc_r)/\gamma$  indicates, that the spectral composition of radiated sound changes largely when increasing the blowing pressure.

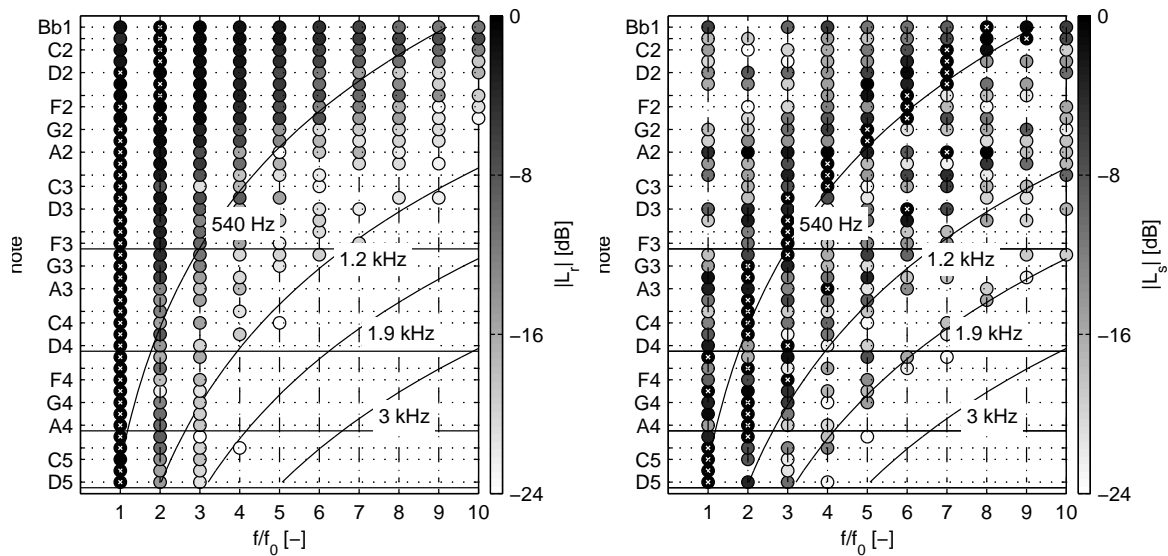
The sound color of the lower notes does change much more with the dynamics, than for the higher notes: Having a significantly larger range of blowing pressures (see Figs. 5.9(a) and 5.10(a)). For the notes above A3 the spectral enrichment with dynamics given by the parameter  $(hsc_s/hsc_r)/\gamma$  settles near 2 (Fig. 5.16(a)).



(a) Change in spectrum  $hsc_s/hsc_r$  with the blowing pressure  $\gamma = \frac{p_m}{p_M}$ .

**Figure 5.16** Spectral metrics of the bassoon sound

As indicated by Fig. 5.15(a), the spectral characteristics of the pressure near the sound source in the reed mouthpiece and the acoustic sound pressure outside of the instrument are quite different. A more detailed view is provided by the harmonic sound spectra presented in Fig. 5.17.



(a) Reed pressure spectra

(b) Sound pressure spectra at 1.5 m distance

**Figure 5.17** Comparison of harmonic pressure spectra inside the mouthpiece (a) and in the radiated pressure spectra (b) of a modern German bassoon. The curved black lines indicate the formant center frequencies. The color indicates the relative spectral pressure magnitudes in dB according to the colorbar left to the plots. The dB reference of each note is the strongest partial, marked with a white cross; the dynamic range is limited to -24... 0 dB. Each of the notes were blown with an artificial mouth at a moderate dynamic level,  $p_m \approx 0.5 (p_{m,max} + p_{m,min})$

For most of the tonal range, the spectral power in the mouthpiece pressure is concentrated below the first formant frequency. Usually, the first harmonic is the strongest, exceptions are found only for notes lower than G2.

Since the reed motion and the mouthpiece pressure resemble a rectangular two-step signal, some authors have related the presence of formants in the radiated sound of woodwinds to spectral “gaps” in the source spectrum [66]. These gaps stem from the fact that the amplitude spectrum of a periodic

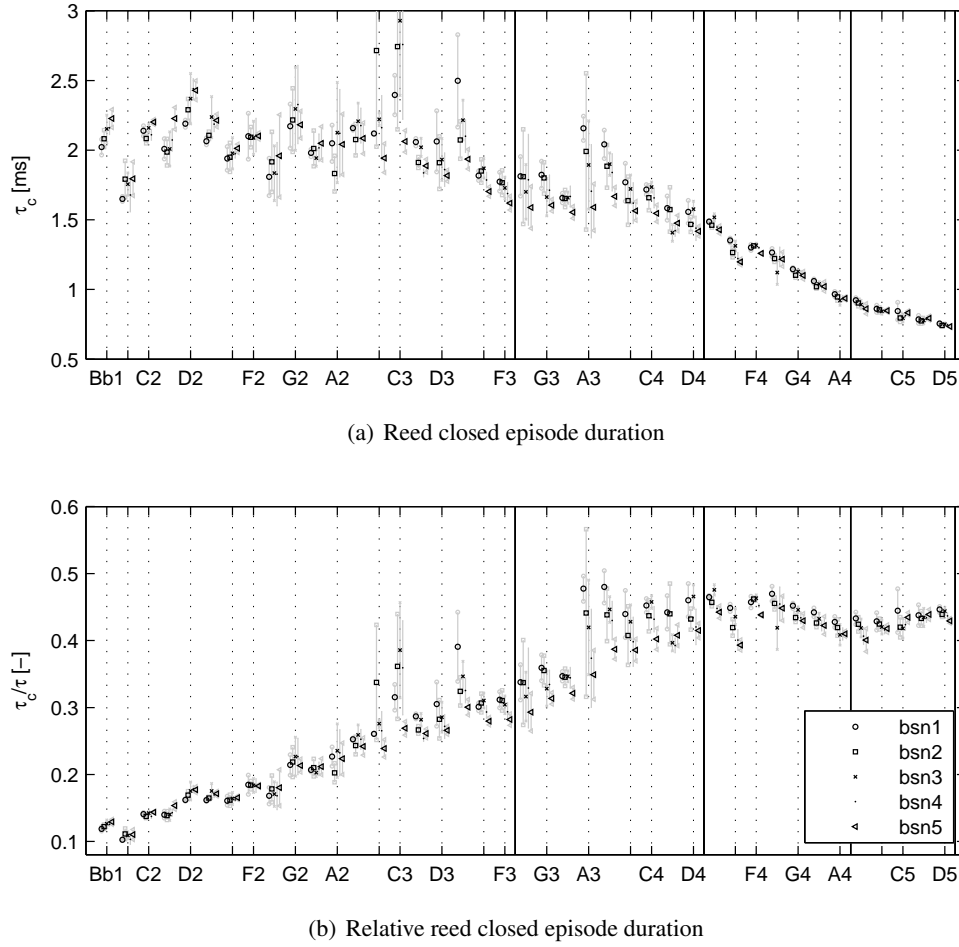


**Figure 5.18** Analysis of the duration  $\tau_c$  of the closed episode in one cycle of the reed tip oscillation

rectangular pulse train with a pulse duration  $\tau_c$  and a periodic time  $\tau$  is the modulus of a sinus cardinalis function. The amplitudes  $P_i$  of the harmonics with ordinal numbers  $i$  near  $n\tau_c/\tau$  are strongly attenuated ( $n$  integer).

Fransson has performed measurements on a bassoon excited by ionophone-generated sound pressure pulses, and found a good agreement in the radiated sound<sup>19</sup> with that of the instrument blown by a musician [63, 64]. Fricke and his co-workers have used this approach for analogue [66] and later digital pulse-forming techniques [134] to synthesize woodwind instrument sounds. Following their argumentation, the formants are already present in the reed pressure spectrum, halfway between the spectral gaps at  $1/\tau_c$  Hz.

According to their hypothesis, one would expect spectral gaps in the reed pressure spectrum at 360 and 720 Hz, which cannot be observed in the present measurements (Fig. 5.17(a)). Instead, the peaks in reed pressure spectrum decay monotonic by -24 dB up to 1.2 kHz. Only in the plot of radiated sound spectra (Fig. 5.17(b)), strong spectral peaks appear as dark shaded dots near the curved iso-frequency lines that mark the first three formant center frequencies (540 Hz, 1.2 kHz, 1.9 kHz): For many notes, the strongest partial coincides with the 540 Hz isoline indicating the main formant  $\mathcal{F}_1$ . The third formant  $\mathcal{F}_3$  is for most notes close to 1.9 kHz. Also, the larger fluctuations of the second formant  $\mathcal{F}_2$  around the 1.2 kHz isoline can be seen.

<sup>19</sup>The amplitudes of the ionophone-generated pressure pulses are however much smaller than in real blowing

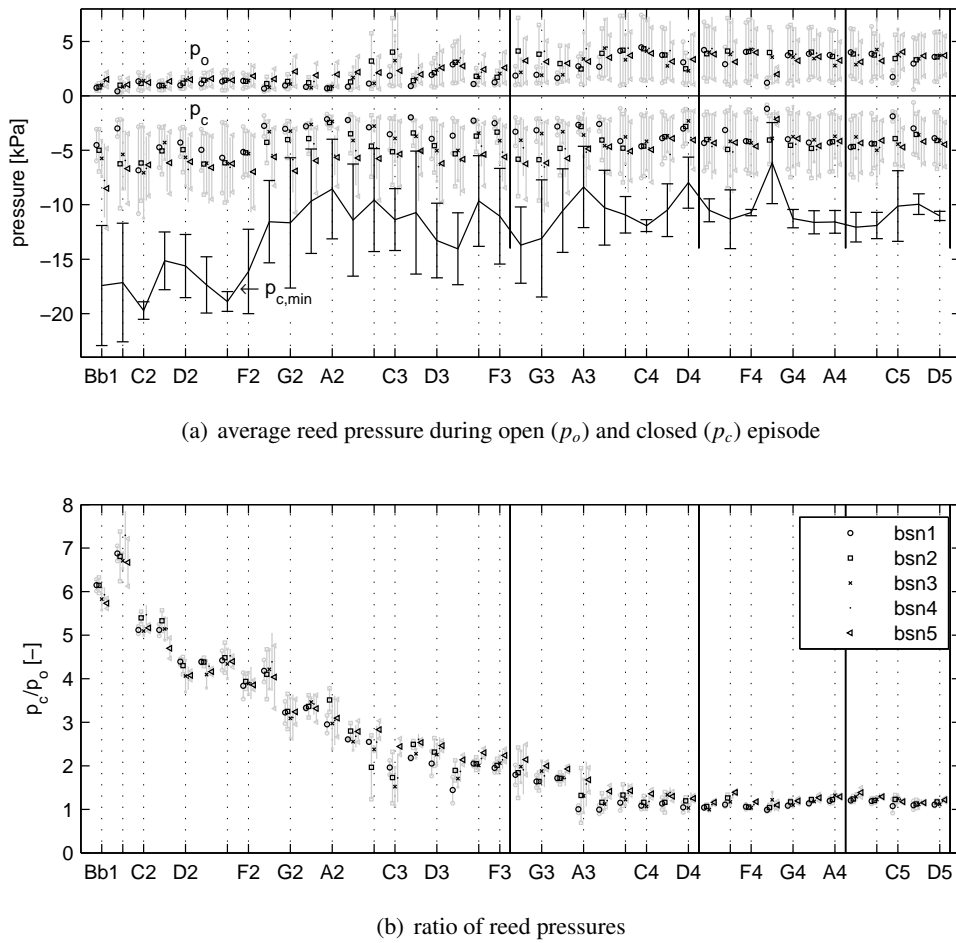


**Figure 5.19** Analysis of average reed pressures during the open ( $p_o$ ) and closed ( $p_c$ ) episode of one cycle of the reed tip oscillation. The straight black line indicates the minimum peak pressure  $p_{c,min}$  during the one period (mean value of five bassoons). The black errorbars on this curve indicate the spread of  $p_{c,min}$  observed on the five bassoons (standard deviation).

### 5.2.3 Reed Pressure Waveform Analysis

During one oscillation cycle, the reed closes once. The mouthpiece pressure  $p_r$  is approximately in phase with the reed tip motion [102, 44], so the durations of the open and closed episode can be estimated from the reed pressure waveform (see section 5.1.2).

Ascending the note scale, the reed closing time  $\tau_c$  is approximately constant in the lowest register (Bb1-F3) at a value of 2 ms (Fig. 5.18(a)). For higher notes,  $\tau_c$  tends to decrease with log-frequency, down to a value of 0.75 ms. The dynamic level has a slight influence of 10 % on  $\tau_c$ , for notes lower than D4. The same applies for the differences between instruments. For the higher notes in the third and fourth acoustical register<sup>20</sup>, the differences between instruments vanish, as well as the change in  $\tau_c$  with dynamics. This observation is especially interesting, because those notes have the largest playing range in which the instrument could be sounded in tune. A plausible explanation for this behaviour is, that the inertia of the reed blade becomes dominant in determining the reed motion. The relative duration of the closed episode,  $\tau_c/\tau$  ranges from 0.1 to 0.45 (Fig. 5.18(b)). Values higher than 0.5 indicate a mode-switch from standard to inverted Helmholtz motion pattern

<sup>20</sup>Acoustical register borders are marked by vertical straight lines in the plots

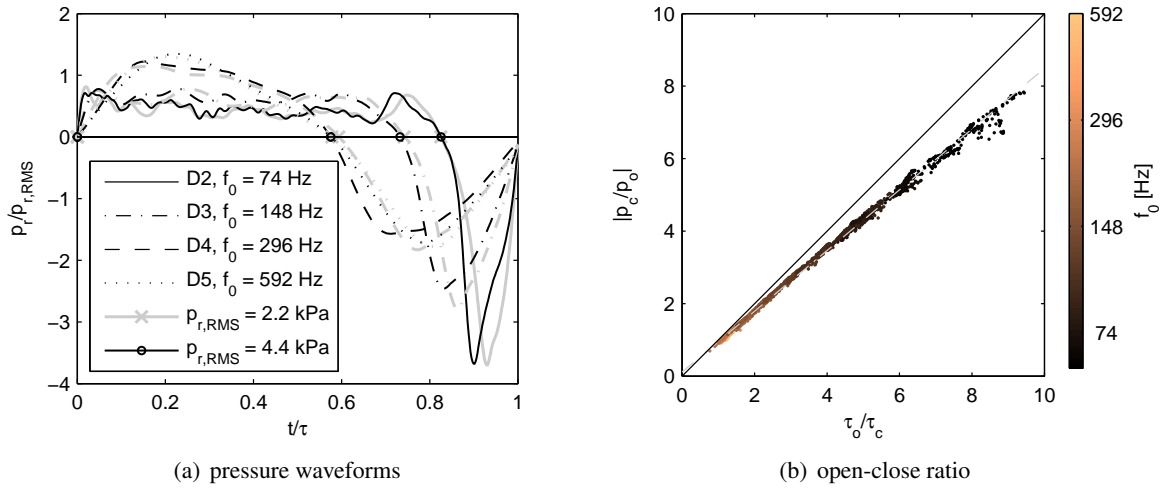


**Figure 5.20 Independence of the pressure waveform on the dynamic level.**

(a) Measured reed pressure signals  $p_r(t)$  during one oscillation cycle, normalized in pressure by the RMS-value  $p_{r,RMS}(\tau)$ , and in time by the periodic time  $\tau$ . The plot shows in 4 octaves the case of the note D at two dynamic pressure levels (gray: *piano*, black: *forte*).  
 (b) Ratio of open-close episode duration  $\frac{\tau_o}{\tau_c}$  versus the integral mean reed pressure ratio  $\frac{|p_c|}{p_o}$ . The slope of the dashed gray line is  $0.84 \pm 0.0027$ .

[44, 136], and are not observed in the standard playing range of the bassoon<sup>21</sup>. For most notes, the change of  $\tau_c/\tau$  with dynamic level is smaller than 10%, except for some individual notes in the middle of the tonal range (B2 to D4), where the variation can reach up to 40%. The spread in  $\tau_c/\tau$  is an indication for the frequency-stability of an oscillatory regime.

The two-step motion of the reed is further characterized by the average pressures  $p_o$  and  $p_c$  during the open and closed episode, respectively (see section 5.1.2). Sudden reed closure induces a negative pressure pulse due to the inertia of the flow. The integral mean pressure  $p_c$  during this episode ranges from -12 to -1 kPa; the corresponding pressure during the open episode  $p_o$  ranges from 0.2 to 8 kPa (Fig. 5.19(a)). Naturally, both averaged pressures depend strongly on the dynamic level and increase with the blowing pressure.

The change of both  $p_o$  and  $p_c$  with the mouth pressure  $p_m$  is linear, such that the ratio  $|p_c|/p_o$  does not change with the dynamics (Fig. 5.19(b)), which has analogously been observed for the relative reed closing duration  $\tau_c/\tau$  (Fig. 5.18(b)). Thus, increasing dynamic level affects the reed pressure, but the general shape of the wave pattern is preserved. As the fundamental frequency increases, the asymmetry in the waveform diminishes and point symmetry ( $\tau_c/\tau = 0.5$ ,  $p_o/p_c = 1$ ) with respect to the zero-crossing is approached. Besides these observations on the averaged reed pressures  $p_o$  and  $p_c$ , the independence of the general waveform on the dynamic level is directly evident in the time domain: Even for a doubling of the RMS reed pressure  $p_{r,RMS}$  subtle details in the reed pressure are preserved (Fig. 5.20). This confirms experimentally under realistic conditions, that the coupled non-linear system of reed and resonator has a linear adjustment range. This has been analytically predicted for ideal resonators [44].

For a lossless resonator, energy conservation states that  $\tau_o p_o = \tau_c p_c$  [136]. Therefore, the ratio  $\tau_o p_o/(\tau_c p_c) < 1$  indicates losses. In the experiments, this value<sup>22</sup> has been observed to be  $0.84 \pm 0.0027$  (Fig. 5.20(b)).

<sup>21</sup>Sudden regimes switch can be forced at the far end of the dynamic range for high blowing pressures on notes higher than C3, accompanied by a remarkable change in pitch, level and timbre. Apparently these regimes are not relevant for musical performance.

<sup>22</sup>The 95% confidence interval for the regression coefficient  $a_1$  of a model  $\frac{|p_c|}{p_o} = a_0 + a_1 \frac{\tau_o}{\tau_c}$  is [0.8370, 0.8397], ( $R^2 = 0.9984$ ,  $N = 3226$ )

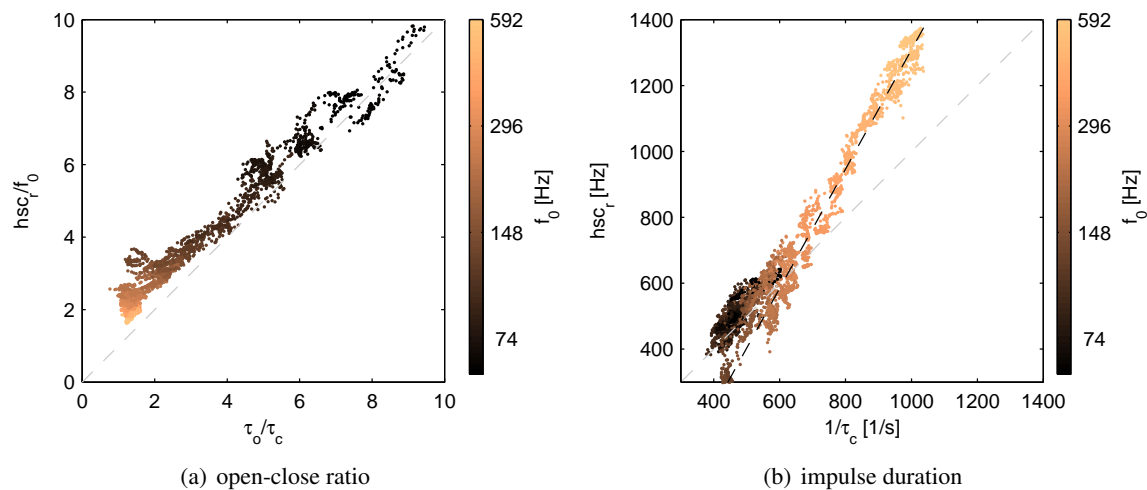


**Figure 5.21** Influence of the impulse duration  $\tau_c$  on the reed pressure spectral centroid (a)relative open-close duration  $\tau_o/\tau_c$  versus normalized spectral centroid  $hsc_r/f_0$  of the mouthpiece pressure. (b)impulse duration  $\tau_c$  versus spectral centroid  $hsc_r$ . The dashed black line has a slope of 1.81.

In general, the asymmetry in the reed pressure waveform determines the spectral centroid (Fig. 5.21(a)). For lower notes, the impulse duration  $\tau_c$  correlates with the spectral centroid in the reed (Fig. 5.21(b)); i.e.  $hsc_r/\tau_c \approx 1$ . For those notes, the harmonic spectral centroid in the reed coincides with the main formant. This experimental finding is in contradiction with the hypothesis on which the “pulse-forming theory” is based [66]. A significant deviation is found for the notes above A3, where  $hsc_r \cdot \tau_c \approx 1.8$ .

Ascending the note scale, the change of the reed pressure waveform with sounding frequency is due to the shortening of the resonator’s effective acoustic length. The shortening reduces the number of harmonic air column modes,  $n_{modes}$ , which contribute to the oscillation. Theoretically, these aspects have been discussed in detail for non-linearly excited ideal cylindrical and conical resonators [44, 136].

For real air-columns with tone holes, many air column modes largely varying in magnitude and harmonicity are present, and their possible contribution to the regime of oscillation is unclear at first glance.

To experimentally determine the number of relevant air-column modes  $n_{modes}$  for a real bassoon and to show its change with the fingering, a rescaling of the magnitude of the input impedance curve is helpful. Following Fletcher’s postulation [58], that air column modes must be strong to participate in a mode-locked regime of oscillation, the impedance peaks -6 dB lower than the maximum peak of each fingering are neglected. The second constraint, that the modes must be nearly harmonic is met by excluding all modes which are more than 100 Cent (one semitone) off the nearby harmonic frequency. The result looks very similar to the harmonicity map (Fig. 2.17), except for a modified color shading. For each fingering, the remaining peaks fulfilling the two criteria are added for each note to give  $n_{modes}$ .

The comparison of  $|p_c/p_o|$  from blowing experiments and  $n_{modes}$  obtained from the above analysis, shows their close relationship (Fig. 5.22). This very good agreement with the theoretical predictions [44, 136] indicates the proper choice of the thresholds  $\pm 100$  Cent for the harmonicity and -6 dB for the impedance magnitude, to determine the number of relevant air-column modes. Accordingly, in the subsequent analysis  $n_{modes}$  will be called the number of *supporting* air column-modes.

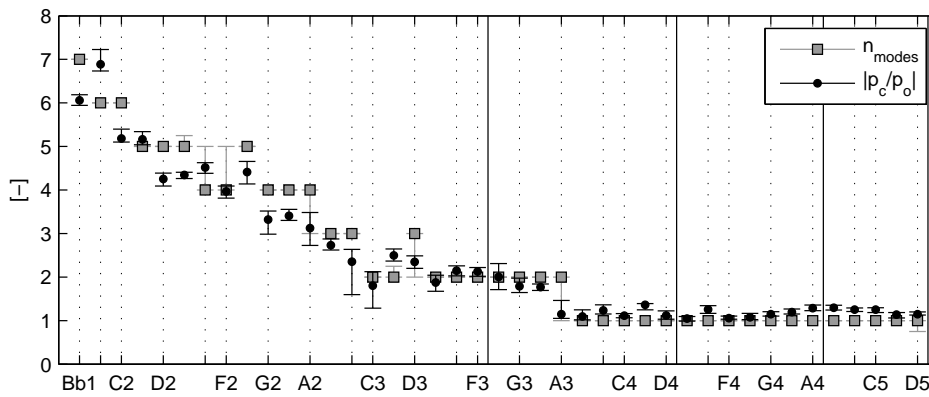


**Figure 5.22** Relation between the mouthpiece pressure waveform ( $|p_c/p_o|$ ) and the number of supporting resonator modes ( $n_{modes}$ ). The pressure waveform  $p_r(t)$  resembles a two step open-close function with the integral mean values  $p_o$  and  $p_c$  during the opening ( $p_r(t) > 0$ ) and closing ( $p_r(t) < 0$ ) episode, respectively.

#### 5.2.4 Summarizing Overview

Characteristic values of input and output parameters from the artificial mouth blowing experiments covering the tonal and dynamical range of the bassoon are given in Table 5.1. This table summarizes the results of the above sections, obtained for one synthetic bassoon reed on five different bassoon-bocal combinations. The lip was in an intermediate position  $x_l = 10.75$  mm from the reed tip. This distance was not changed during all measurements.



**Table 5.1** Overview on typical values of input and output parameters in artificial mouth blowing experiments on a modern German bassoon. The values are given as a range  $(\cdot)_{min} \dots (\cdot)_{max}$  or as a mean value  $(\cdot) \pm \sigma$ , where  $\sigma$  is the standard deviation. The right column gives references to figures with plots of the respective properties.

	Symbol	Measure	Unit	Range	Reference	
artificial mouth adjustment parameters	directly measured	$p_m$	mouth pressure <sup>a</sup>	[kPa]	1.1 ... 12	Fig. 5.9(a)
		$F_{l1,2}$	lip force <sup>a</sup>	[N]	0 ... 7	Fig. 5.9(b)
		$x_l$	lip position <sup>b</sup>	[mm]	0 ... 15	
$q$		averaged volume flow-rate <sup>a</sup>	[l/s]	0.02 ... 0.42	Fig. 5.12(b)	
$p_r(t)$		reed pressure inside mouthpiece <sup>c</sup>	[kPa]	-24 ... + 8	Fig. 5.20(a)	
$p_s(t)$		sound pressure at 1.5 m distance <sup>c</sup>	[Pa]	arbitrary	not shown	
$f_0$		sounding frequency <sup>d</sup>	[Hz]	58 ... 592	not shown	
$p_{r,RMS}$		RMS reed pressure <sup>d</sup>	[kPa]	1 ... 9	Fig. 5.12(a)	
$p_{s,RMS}$		RMS sound pressure <sup>e</sup>	[dB SPL]	72 ... 95	Fig. 5.14(a)	
$h_{SC_r}$		harmonic spectral centroid <sup>d,f</sup>	[Hz]	380 ... 1000	Fig. 5.15(a)	
reed pressure waveform parameters	meta-analysis	$\tau_c$	duration of closed episode <sup>a</sup>	[ms]	2.8 ... 0.75	Fig. 5.18(a)
		$\tau_o/\tau$	normalized duration of open episode <sup>d</sup>	[-]	0.9 ... 0.55	not shown
		$\tau_c/\tau$	normalized duration of closed episode <sup>d</sup>	[-]	0.1 ... 0.45	Fig. 5.18
		$p_o$	integral mean pressure, open episode <sup>d</sup>	[kPa]	0.2 ... 8	Fig. 5.19(a)
		$p_c$	integral mean pressure, closed episode <sup>d</sup>	[kPa]	-12 ... -2	Fig. 5.19(a)
		$p_{c,min}$	minimum pressure, closed episode <sup>d</sup>	[kPa]	-24 ... -5	Fig. 5.19(a)
timbral spectral parameters		$h_{SC_s}$	harmonic spectral centroid <sup>e,f</sup>	[Hz]	580 ... 1500	Fig. 5.15(a)
		$h_{SS}$	harmonic spectral spread <sup>e,f</sup>	[-]	0.2 ... 0.7	not shown
		$h_{SD}$	harmonic spectral deviation <sup>e,f</sup>	[-]	0.1 ... 0.3	not shown
		$\mathcal{F}1$	1st formant center frequency <sup>e,f</sup>	[Hz]	$540 \pm 110$	Fig. 5.15(b)
		$\mathcal{F}2$	2nd formant center frequency <sup>e,f</sup>	[kHz]	$1.2 \pm 0.18$	Fig. 5.15(b)
		$\mathcal{F}3$	3rd formant center frequency <sup>e,f</sup>	[kHz]	$1.9 \pm 0.2$	Fig. 5.15(b)
		$\mathcal{F}4$	4th formant center frequency <sup>e,f</sup>	[kHz]	$3.1 \pm 0.6$	Fig. 5.15(b)
		$B1$	1st formant bandwidth <sup>e,h</sup>	[Hz]	$220 \pm 160$	not shown
	$B2$	2nd formant bandwidth <sup>e,h</sup>	[Hz]	$470 \pm 280$	not shown	
	$B3$	3rd formant bandwidth <sup>e,h</sup>	[Hz]	$730 \pm 450$	not shown	
	$B4$	4th formant bandwidth <sup>e,h</sup>	[Hz]	$890 \pm 470$	not shown	
	$N$	Loudness at 1.5 m distance <sup>e,i</sup>	[Sone]	$44 \pm 12$	Fig. 5.14(b)	
quasi-static reed model parameters	$p_M$	pressure needed to close the reed <sup>j</sup>	[kPa]	$7.4 \pm 1.8$	not shown	
	$q_A$	flow parameter <sup>k</sup>	[m <sup>3</sup> /s]	$(0.6 \pm 0.3) 10^{-3}$	not shown	
	$K_s$	reed stiffness per unit area <sup>l</sup>	[Pa/m <sup>2</sup> ]	$(1.6 \pm 0.35) 10^9$	Fig. 5.11	
	$\gamma$	dimensionless blowing pressure <sup>m</sup>	[-]	0.16 ... 1.4	Fig. 5.10(a)	
	$\zeta$	embouchure parameter <sup>m</sup>	[-]	0.6 ... 2.7	Fig. 5.10(b)	
	$q_{model}$	flow-rate predicted by model <sup>n</sup>	[m <sup>3</sup> /s]	see: $q$	Fig. 5.4	
	$h_{o,model}$	max. slit height in open episode <sup>o</sup>	[mm]	0.1 ... 1.2	not shown	

<sup>a</sup> stationary measure<sup>b</sup> constant in all experiments (10.75 mm)<sup>c</sup> dynamic measure<sup>d</sup> from unsteady reed pressure<sup>e</sup> from unsteady sound pressure<sup>f</sup> MPEG7 (ISO/IEC15938)<sup>h</sup> praat (Burgers algorithm)<sup>i</sup> Zwicker (DIN 45631)<sup>j</sup> from quasi-static characteristics, Eq. (4.31b)<sup>k</sup> from quasi-static characteristics, Eq. (4.31a)<sup>l</sup>  $\frac{p_M}{q_A} \sqrt{\frac{2p_M}{\rho}}$ <sup>m</sup> elementary clarinet reed model [102]<sup>n</sup> estimate from empirical model; Eq. (4.28)<sup>o</sup> estimate from empirical model; Eq. (4.32)

### 5.3 Performance Control with the Embouchure

With the use of an artificial mouth, it is possible to independently adjust and measure the parameters lip force  $F_l$  and mouth pressure  $p_m$ . Within the standard playing range, for a given resonator setting, a steady-state regime of oscillation is fully set by a choice of these two<sup>23</sup> *input* parameters. This regime is further characterized by the resulting mean volume flow-rate  $q$ , the RMS-reed pressure  $p_{r,RMS}$  and the sounding frequency  $f_0 = 1/\tau$ , which are called *output* parameters.

In contrast to the artificial mouth experiments, where the input parameters are static, the musician adjusts the input parameters to achieve the desired output, so the output parameters are implicitly controlled by the embouchure.

In this section, the interplay of input and output parameters will be discussed with respect to some musician-related aspects of bassoon performance. In a concluding section, these findings will be reconsidered in light of the acoustical properties of the resonator.

#### 5.3.1 Register-dependent Embouchure Characteristics

The balance of input and output parameters characterizes the interplay of the resonator and embouchure and therefore provides information on the interaction of the resonator with the musician and his way of embouchure control. In the experiments, working points of the reed were adjusted to keep the output parameter  $f_0$  constant for each resonator setting.

As response variable  $p_{r,RMS}$  is chosen, which characterizes the dynamic level. Two controlled variables are proposed to describe the embouchure. The first is the blowing pressure  $p_m$ . The second is the logarithm of a non-dimensional lip force  $\tilde{F}_l$  defined as

$$\tilde{F}_l = \frac{F_l}{q\rho 2hf_0} \quad (5.4)$$

where  $q\rho$  is the mass flow-rate and  $2hf_0$  is the average velocity of the reed blade at the tip. The term in the denominator has the dimension of a force. For typical playing conditions  $\tilde{F}_l$  is  $10^2$  to  $10^6$ , for loose and tight embouchures, respectively.

It was shown by pressure waveform analysis in section 5.2.3, that the musically relevant oscillation regimes of the reed-resonator system in the time domain scale linearly with the dynamic level. The measurement results in Fig.5.23 reveal, that under playing conditions the response variable  $p_{r,RMS}$  is a linear combination of the controlled variables  $p_m$  and  $\log_{10} \tilde{F}_l$ . This analysis further indicates, that the slope  $\Delta p_{r,RMS}$  vs the controlled variables  $p_m$  and  $\log_{10} \tilde{F}_l$  depend on the sounding frequency  $f_0$ . By classification lines with a slope of unity and -3.27 kPa/decade, respectively, both plots can be split into two regions.

Both classification lines represent characteristics to discriminate the respective data into two groups, left and right to the vertical dashed line in Figs. 5.23(a) and 5.23(b). This classification will be interpreted in terms of two dimensions, which are orthogonal to the dashed lines and characterize the bassoon's blowing characteristics:

- i) the *pressure efficiency* dimension and
- ii) the *embouchure tightness* dimension

With the classification line  $p_{r,RMS}/p_m = 1$  in the first dimension  $p_{r,RMS}/p_m$  divides the notes into two groups according with a pressure efficiency smaller or larger than unity. The notes at the low end of the tonal range are efficient ( $p_{r,RMS}/p_m > 1$ ) whereas the higher notes are less efficient ( $p_{r,RMS}/p_m < 1$ ): To produce the same  $p_{r,RMS}$  the notes with a higher pitch require a larger mouth pressures.

The interpretation of the second dimension first requires a discussion of the non-dimensional

<sup>23</sup>For a given reed and a fixed lip position  $x_l$

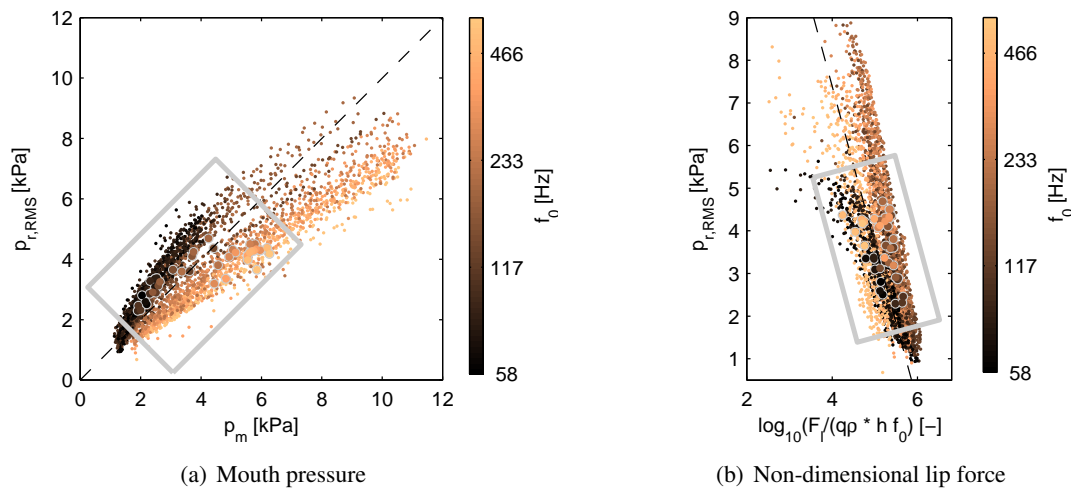


**Figure 5.23** Blowing characteristics of a modern German bassoon. Dependence of the response variable  $p_{r,RMS}$  on the controlled variables (a)  $p_m$  and (b)  $\log_{10} \tilde{F}_l$  (Eq.5.4) characterizing the embouchure. Each of the small dots marks one operation point, the large dots mark the centroids of several realizations of each note, with different dynamic levels, on all five bassoons under test (*bsn1 to bsn5*). The data are covering the full dynamical and tonal range, and stem from artificial mouth experiments ( $N_{total} = 3326$ ). The color indicates the sounding frequency, according to the colorbar to the right of the plots. The black dotted classification line has a slope of unity (a) and -3.27 kPa/decade (b).

lip force  $\tilde{F}_l$ . For a fixed fundamental frequency, low values of  $\tilde{F}_l$  correspond to low lip force and high flow rate. Following this interpretation  $\tilde{F}_l$  can be related to an effective slit height, in other words to the embouchure tightness. In this second dimension, the classification<sup>24</sup> line is  $p_{r,RMS} / \log_{10} \tilde{F}_l = -3.27$  kPa/decade. To produce tuned sounds of equal  $p_{r,RMS}$ , the notes in the middle of the playing range require a tighter embouchure ( $p_{r,RMS} / \log_{10} \tilde{F}_l > -3.27$  kPa/decade) compared to the notes in the lowest and highest registers which are played with a loose embouchure ( $p_{r,RMS} / \log_{10} \tilde{F}_l < -3.27$  kPa/decade). Contrary to the first pressure efficiency dimension, the second embouchure tightness dimension groups the lowest and highest notes.

The blowing characteristics of a modern German bassoon can be described by a scatterplot of  $\Delta p_{r,RMS} / \log_{10} \tilde{F}_l$  vs.  $p_{r,RMS} / p_m$ , where each point marks one operation regime of the reed (Fig. 5.24(a)). The classification lines of both dimensions divide this map of working points into four regions, according to their pressure efficiency and embouchure tightness (Fig. 5.24(b)). The proposed classification divides the playing range of notes into four regions, according to their blowing characteristics:

**group 1** (Bb1→E2): high pressure efficiency, loose embouchure

**group 2** (F2→G#3): high pressure efficiency, tight embouchure

**group 3** (A3→A4): low pressure efficiency, tight embouchure

**group 4** (Bb4→D5): low pressure efficiency, loose embouchure

<sup>24</sup>The classification line is obtained from statistical considerations, with the aim to obtain of a symmetric density function with a local minimum at the median. Half of all observed operating points have a lower value.

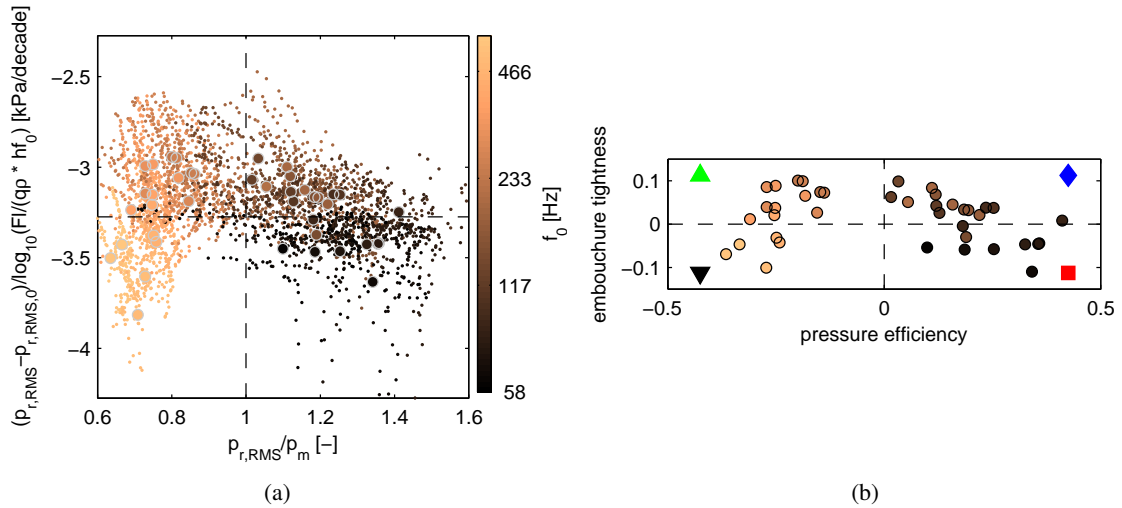


**Figure 5.24** (a) Grouping of operating regimes of a bassoon double-reed into four regions. Each of the small dots marks one operation point, the large dots mark the centroids of each note. The data are covering the full dynamical and tonal range, and stem from artificial mouth experiments on 5 German bassoons ( $n = 3326$ ). The colors indicate the fundamental frequency according to the colorbar to the right of the plot. (b) Mean centered and rescaled map showing only the centroids of operating regimes for each note, and their grouping (■,◆,▲,▼). The first dimension is the pressure efficiency  $p_{r,RMS}/p_m$  (horizontal axis), the second dimension  $\Delta p_{r,RMS}/\log_{10} \tilde{F}_l$  (vertical axis) is related to the embouchure tightness.

The quality of classification can be quantified by the effect size. A measure for the effect size is Cohen's  $D$ <sup>25</sup>. The border in the pressure efficiency dimension (between groups 1,2 and groups 3,4) is quite clear ( $D = 3.82$ ). The border in the embouchure tightness dimension (between groups 1,4 and groups 2,3) is less pronounced ( $D = 1.66$ ) (see Fig. 5.24(a)).

The above regime margins obtained from the analysis of blowing characteristics agree to some extent with the subjective judgements of bassoonists:

8 professional bassoonists, being asked to divide the tonal range on the bassoon into 4 regions according to their blowing characteristics, and to describe them in their own words<sup>26</sup>, gave the following responses

**low** (Bb1→E2): “loose support”, “large oscillation”, “much controlled air”, “loose embouchure”, “large opening”, “open embouchure”

**mid-low** (F2→G3): “medium support”, “medium embouchure”, “guided air”, “less loose embouchure”, “natural”, “convenient to play”, “medium blowing pressure”

**mid-high** (G#3→F#4): “much support”, “much embouchure”, “narrow blowing pressure”, “harder embouchure”, “fast air”, “straining, high blowing pressure”, “high lip tension”

**high** (G4→D5): “good support”, “little embouchure”, “loosened embouchure”, “free blowing pressure”, “very fast air”, “mouth is not narrow”, “medium-high tension”, “irregular”

<sup>25</sup> Assuming two independent observations  $X_1, X_2$ , normally distributed with mean values  $\mu_1, \mu_2$  and standard deviations  $\sigma_1^2, \sigma_2^2$ , Cohen's  $D$  is given by  $D = \frac{\mu_2 - \mu_1}{\sqrt{(\sigma_1^2 + \sigma_2^2)/2}}$ .

<sup>26</sup> The test persons were completely unaware of the objective of the study. A questionnaire was given to them showing a score of a chromatic scale of Bb1 to D5. The bar-less score switched from bass to tenor clef after B3. The questionnaire asked for two tasks: i) Divide the range into 4 groups A,B,C,D by making 3 vertical lines in the score! ii) How would you describe the four groups A,B,C,D in terms of blowing characteristics, embouchure and sound color? The test persons were 6 bassoon students and their teacher from a German university of music. They filled the questionnaire individually and simultaneously. The questionnaire was further handed out to one professional bassoon soloist who had graduated from a different school years ago.

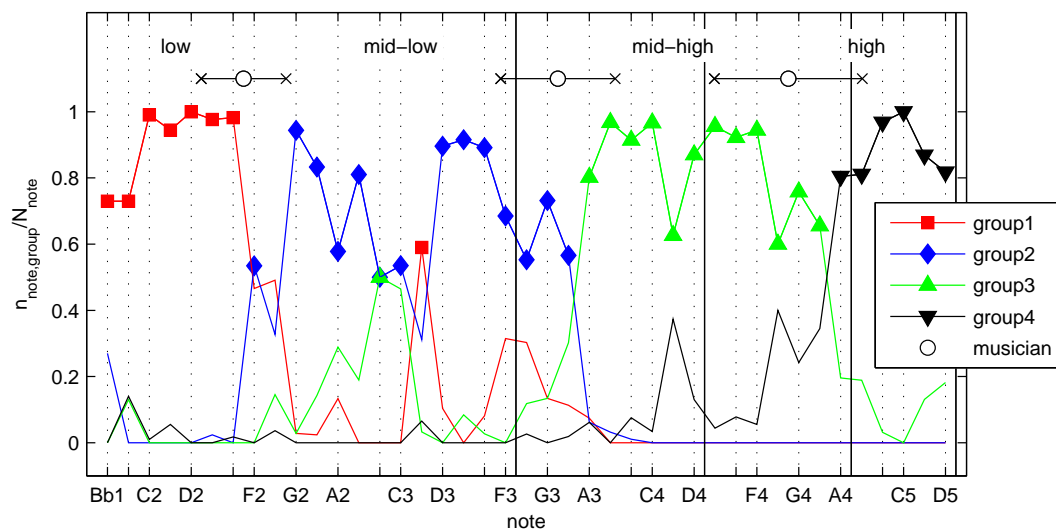


**Figure 5.25** Grouping of notes according to their embouchure characteristics. For each note, the ratio  $n_{note,i}/n_{note}$  is shown, where  $n_{note,i}$  is the number of operating points classified into the  $i^{th}$  group ( $i = 1, 2, 3, 4$ :  $\blacksquare, \blacklozenge, \blacktriangle, \blacktriangledown$ ), and  $n_{note}$  is the total number of operating points on that note. For each note, only the marker of the dominating group ( $n_i/n > 0.5$ ) is plotted. The data are covering the full dynamical range and stem from artificial mouth experiments on German 5 bassoons.

Markers  $\circ$  correspond to the median of regime margins as perceived by musician (according to a survey among 8 professional bassoonists).

The vertical straight black lines indicate the acoustical register margins.

The standard deviation of the regime margins in the responses of the musicians were 2.0, 2.7 and 3.5 semitones. Interestingly the regime margins observed under playing conditions, both with musicians and artificial mouth do not coincide with the acoustical register borders of the resonator (Fig.5.25).

One possibly would expect to see a change in blowing characteristics at the acoustical borders, e.g. at between F3 and F#3, which is the first overblown note, where the reed vibrates with a frequency near the second air column mode, but this is not the case.

The conclusion is, that careful artificial mouth experiments make some aspects of the embouchure control as perceived by musician comprehensible. Possible reasons for regime changes perceivable in the musicians embouchure can be found in the reed-resonator interaction. These aspects will be discussed in section 5.3.4.

### 5.3.2 Intonation Corrections

In the above section a classification of notes has been made, according to pressure efficiency and embouchure tightness. This classification bases on an analysis of blowing characteristics from the parameters lip force, mean flow-rate, mouth pressure and RMS reed pressure.

The rough classification into loose and tight embouchures needs to be reconsidered: Bassoonists report, that delicate embouchure corrections have to be made for each individual note. These nuanced adjustments of lip force to correct individual notes for their tuning are addressed in this section<sup>27</sup>.

The blowing pressure  $p_m$  is strongly correlated with the dynamic level of the sound, which, for the musician is an artistic constraint during the performance. For this reason, the lip force  $F_l$  is the free

<sup>27</sup>The results presented here have partly been published by the author in [75]

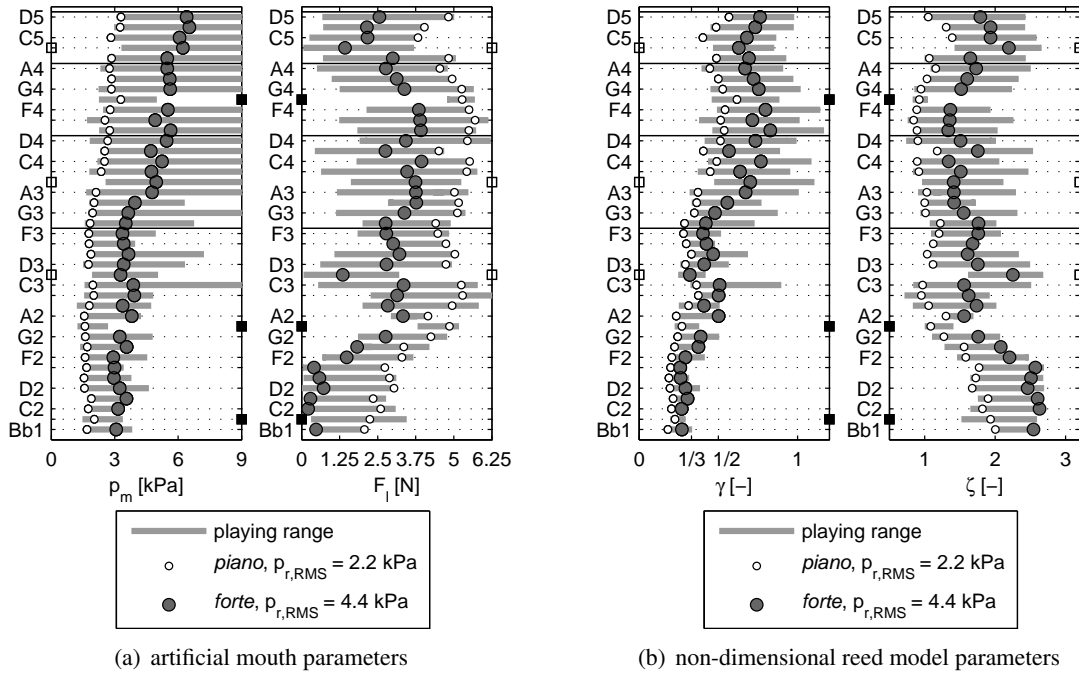


**Figure 5.26** Range of input parameters for bassoon playing to achieve clean tuning at small and large dynamic level (*piano* and *forte*). (a) measured values of lip force  $F_l$  and blowing pressure  $p_m$ ; (b) corresponding model parameters  $\gamma = p_m/p_M$  and  $\zeta = Z_c q_A/p_M$  of an elementary clarinet reed model [102]. Data from artificial mouth experiments on on bassoon (*bsn4*) with the same synthetic double-reed. Markers  $\circ$ ,  $\bullet$  correspond to the low and high reference level, respectively. Horizontal gray bars mark the maximum and minimum values on this bassoons. Markers  $\square$ ,  $\blacksquare$  on the vertical axis indicate those notes that could not be sounded in tune at the low and high reference level, respectively.

parameter used to adjust to the frequency. Actually, both parameters influence the tuning: Learning to play the bassoon means to train the blowing pressure dependent lip force correction for each note at each dynamic level.

To report the required embouchure corrections for playing each note in tune at a high and low dynamic level, values of mouth pressure and lip force are provided in Fig. 5.26. These two dynamic levels are given by the reference values of  $p_{r,RMS} = 2.2$  and  $4.4$  kPa, denoted as *piano* and *forte* in the plot. The RMS reed pressure might not be proportional neither to the radiated sound level nor to the perceived loudness (see Figs. 5.14 and 5.12(a)), but it is suited to compare the embouchures of adjacent notes and is independent of the room acoustics. The plots in Fig. 5.26 show, that the parameter ranges of some notes (e.g. B1, G $\sharp$ 2, G4), are considerably small compared to their neighbors. To a player, these notes may appear to be sharp, as they cannot be played loudly without changing their pitch. When blowing harder, the pitch increases, but a further reduction of lip force would let the tone break away.

In the higher registers, notes are found which cannot be played softly (e.g. C $\sharp$ 3, Bb, B4) at their nominal sounding frequency. Those notes appear to be flat. Playing them at low blowing pressure requires a high lip force to “push up” their tuning. Below a certain threshold of reed slit height<sup>28</sup> it is not possible to build up or maintain reed oscillations. Generally, the plot of lip forces indicates, that the notes in the low register have smaller and more demarcated ranges of playing parameters, compared to higher notes, whose pitches are more easy to bend as musicians report. Higher notes can be played at very high blowing pressures. Due to the observed generic irregularity, upwards

<sup>28</sup>The smallest initial slit height at which oscillations were still possible, was 0.1 mm

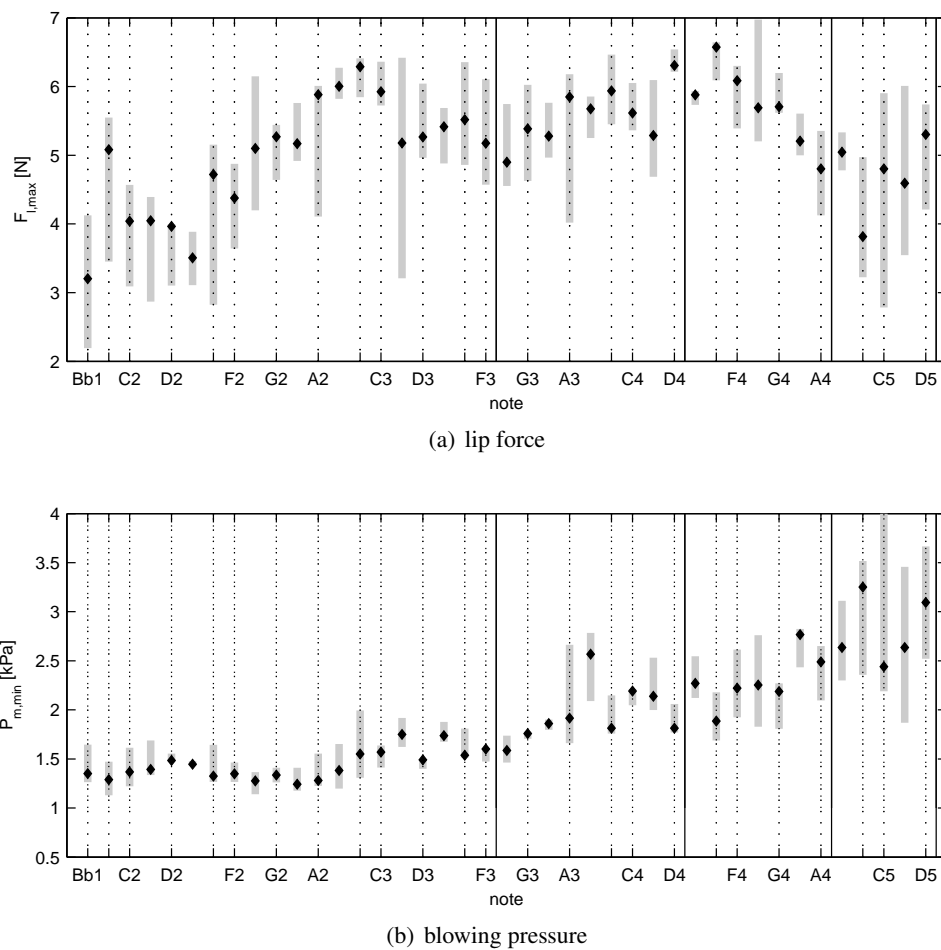


**Figure 5.27** Input parameters for bassoon playing to achieve clean tuning at the softest dynamic playing level (*pianissimo*).  
**a)** lip force  $F_{l,max}$  and  
**b)** blowing pressure  $p_{m,min}$ .  
 Data from artificial mouth experiments on five bassoons with the same synthetic double-reed. Markers are the median, vertical gray bars mark the maximum and minimum values from the five bassoons.

octave jumps may require a remarkable tightening (e.g. B1-B2, D2-D3) or loosening of (e.g. A3-A4, B3-B4) of the embouchure.

Although the lip force characteristics look similar for soft and loud playing in principle it differs in details. This indicates the need of incessant embouchure corrections not only between adjacent notes (e.g. E2-F2, C3-C#3, C4-C#4, F4-F#4), but also between different dynamic levels played on the same note.

As articulation and speed are excluded in this experiment, it can be guessed that in a real musical performance the proper dynamic adjustment of the embouchure is even more complicated.

The embouchure correction curves presented in Fig. 5.26 depend on the characteristics of the resonator. On each of the five bassoons some individual notes with tuning problems could be identified as outliers in the  $F_l$ -curve. However, the general lip force characteristics was the same for all bassoons, which range from instruments for students to instruments for professionals. Fig. 5.27 shows that the spread of values for maximum lip force  $F_{l,max}$  and minimum blowing pressure  $p_{m,min}$  needed to play the softest dynamic level on each note, is small compared to the absolute value.

Note, that the terms minimum and maximum do not refer to oscillation thresholds for one embouchure configuration as in previous studies [42]. Here the embouchure is readjusted for each working point, to find the lowest and highest pressures, where the respective note could be sounded in tune. At the lower limit of playing dynamics shown in Fig. 5.27, the artificial mouth parameters

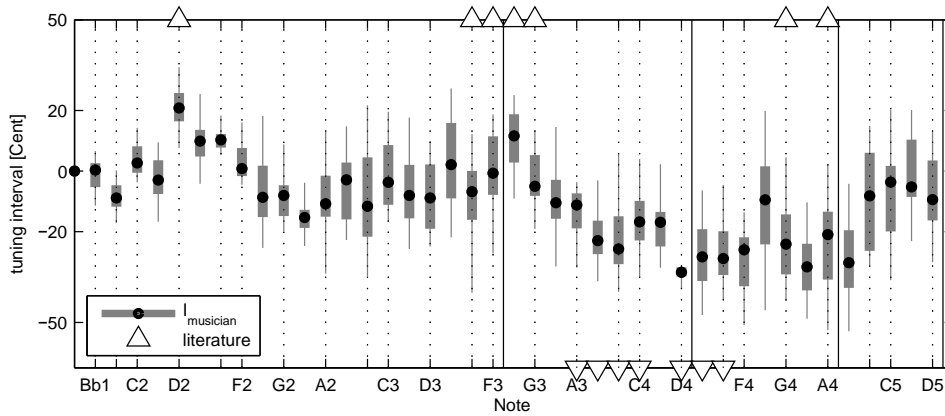


**Figure 5.28** Tuning discrepancy  $I_{\text{musician}}$  as perceived by one musician (black dots with gray errorbars). The markers ( $\Delta$ ,  $\nabla$ ) denote the tuning tendency (sharp, flat) of “some critical notes regarding special attendance”[34].

observed on all five bassoons have a relatively small spread and thus reveal the same general characteristics. This applies in particular to the blowing pressure. For the lip force, the variations are larger; they are most probably biased by a lip force offset compensating for the overall tuning. Nevertheless, it can be concluded that all five bassoons studied have quite similar playing characteristics, however a few outlier notes are observed on each instrument.

The lip force that needs to be applied to achieve the correct pitch can be regarded as an indirect measure of the intonation of a reed wind instrument as perceived by a player. The relation of lip force and tuning is inverse: notes which appear to be flat have to be adjusted by tightening the embouchure, while notes appearing to be sharp are played with a loose embouchure. The curve of the highest lip force  $F_{l,\max}(f_0)$  at which each note could be sounded in its nominal frequency  $f_{0,\text{nom}}$  can be regarded as a characteristic curve revealing the intonation properties of the bassoon<sup>29</sup> under playing conditions.

To investigate the perceived tuning discrepancy, a blowing experiment with a musician has been carried out: A professional bassoonist was asked to play all notes on a bassoon without embouchure corrections. All combinations of 3 bassoons, 3 bocals and 2 reeds (“hard” and “soft”, from natural cane) have been used in this investigation, the resulting sounding frequencies were obtained by autocorrelation from recorded audiodata of sustained notes [78]. The perceived tuning is then characterized by the interval  $I_{\text{musician}} = 1200 \log_2(f_0/f_{0,\text{nom}})$  Cent, where  $f_0$  is the actual sounding frequency, and  $f_{0,\text{nom}}$  is the nominal sounding frequency for that fingering, according to the equally tempered scale<sup>30</sup>. Comparing the mean values from this study (Fig. 5.28) with the lip force offset from the artificial blowing (Fig. 5.27(b)) a general agreement is found. The inverse proportionality of lip force and perceived tuning is examined by means of a regression model  $F_{l,\max} = a_0 + a_1 I_{\text{musician}}$  (Fig. 5.29). The regression coefficient<sup>31</sup> is  $a_1 = -0.37 \pm 0.16 \text{ N/(10 Cent)}$ . The coefficient of determination is  $R^2 = 0.37$ , which means that 20 % of the of the observed tuning discrepancy can be explained by assuming a simple linear correlation with the lip force offset.

Air columns, which are tuned flat<sup>32</sup> have to be played at higher lip forces. The choice of a bocal with proper dimension and the variation of its insertion length can be used to adjust the mean tuning in certain limits.

The observed correlation between  $F_l$  and  $I_{\text{musician}}$  is quite remarkable, taking into account that the measurements have been carried out on different bassoons, bocals and reeds; by real blowing and artificial mouth excitation.

<sup>29</sup>The term describes here the entity of a bassoon, bocal, and reed

<sup>30</sup>referenced to A4: 443 Hz

<sup>31</sup>The 95% confidence interval for the  $a_1$  estimate is  $[-0.53, -0.21] \text{ N/(10 Cent)}$

<sup>32</sup>Note “the tuning” is considered to be a property of the air-column, i.e. the entity of bocal and bassoon.



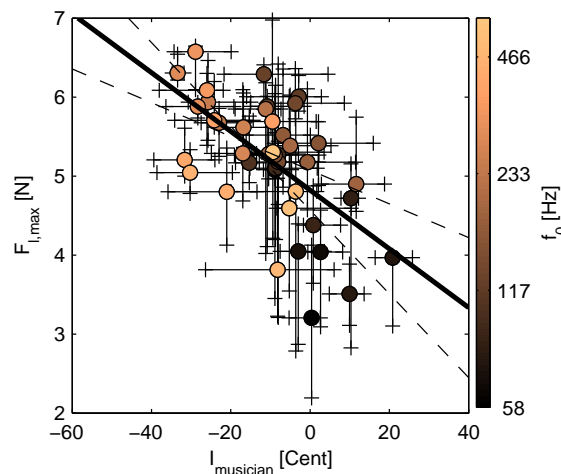


**Figure 5.29** Correlation between lip force  $F_{l,max}$  in artificial mouth blowing experiments and the tuning discrepancy  $I_{musician}$  as perceived by a musician. In the artificial mouth experiment the tuning was held constant and the adjusted lip force  $F_l$  was measured; in musician experiment, the embouchure was held constant by the musician and the resulting tuning  $I_{musician}$  was measured. Each of the 41 markers corresponds to a note within the chromatic playing range from B $\flat$ 1 to D5, the color indicates the sounding frequency  $f_0$  according to the colorbar on the left. Vertical errorbars mark the 25<sup>th</sup> and 75<sup>th</sup> percentiles of 18 measurements (full permutation of 3 bassoons, 3 bocals and 2 cane-reeds). Horizontal errorbars mark the maximum and minimum values from measurements on five bassoon-bocal combinations. Dashed lines correspond to the 95% confidence interval of the fit coefficients.

### 5.3.3 Sound Color Adjustments

According to the experience of woodwind players, the greatest influencing factor on the sound color are they themselves. For reed making players, which many bassoonists actually are, this may in particular be a firm conviction. Certainly, the complex of reed, lips and mouth is crucial in fine-tuning the sound color.

The setup used in the present study makes it is possible to study one aspect of this complex separately: The influence of the embouchure configuration on the sound color, for a fixed reed and lip position  $x_l$ .

To quantify the term sound color, the spectral metrics harmonic spectral centroid  $hsc$ , harmonic spectral spread  $hss$  and the center-frequencies  $\mathcal{F}1$ ,  $\mathcal{F}2$  and  $\mathcal{F}3$  of the formants, as well as their ratios are analyzed from the acoustical sound pressure recorded outside of the instrument. An embouchure configuration is given by the lip force  $F_l$  and the blowing pressure  $p_m$ , further, the RMS reed pressure  $p_{r,RMS}$  and the non-dimensional lip force  $F_l/(q\rho 2hf_0)$  are analyzed. The lip position  $x_l$  is the distance of the lip from the reed tip.

The influence of the dynamical level ( $p_{r,RMS}$ ) on the harmonic spectral centroid  $hsc_s$  and the harmonic spectral spread  $hss_s$  can be observed in the plot of standardized of output (sound) versus input (embouchure) data (Fig. 5.30). The standardization is  $z(X) = \frac{X-\mu}{\sigma}$ , where  $\mu$ ,  $\sigma$  are the mean and standard deviation, respectively, of the observations on  $X$  for each note.

Both spectral parameters  $hss$  and  $hsc$  increase with the dynamic level, which leads to the interpretation, that these sounds are perceived to be brighter [73, 145] and richer in overtones, when they are played louder.

The inverse effect is observed for the lip force  $F_l$ . This effect supposedly is a consequence of the observation that playing a note softer requires a raise in lip force to prevent a pitch change. The change in these spectral parameters with the blowing pressure is linear over most of the playing range, except near the upper and lower limits.

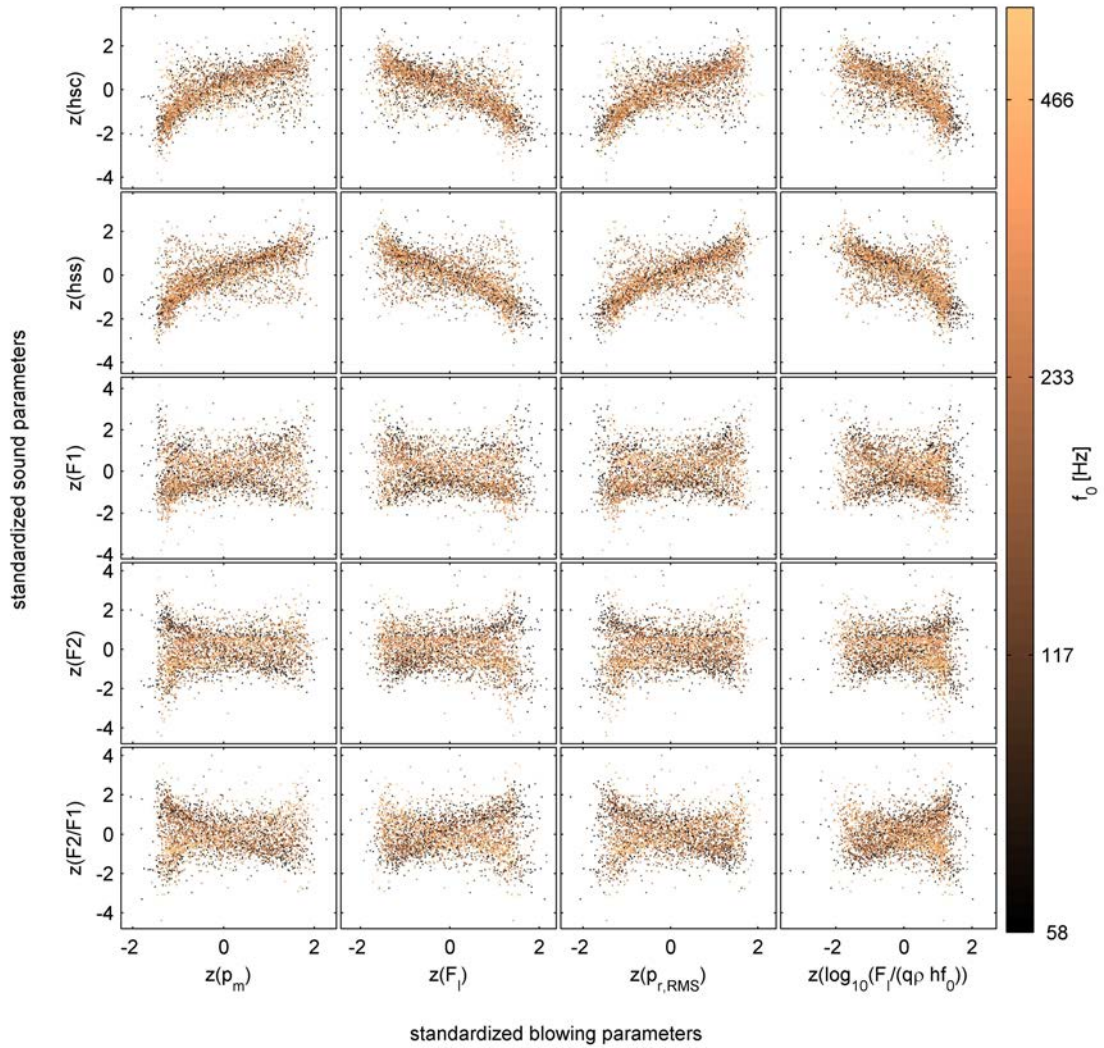


**Figure 5.30** Change of sound color related parameters with a change in the embouchure. Output data of the radiated sound are plotted versus input data of the artificial mouth.

**Input data**  $p_m$ : mouth pressure,  $F_l$ : lip force,  $p_{r,RMS}$ : root-mean-square reed pressure,  $F_l/(q\rho hf_0)$ : non-dimensional lip force;

**Output data:**  $hsc$ : harmonic spectral centroid,  $hss$ : harmonic spectral spread,  $F1, F2, F3$ : center frequencies of first, second and third formant, respectively.

For each note, measurement values have been standardized ( $z(X) = \frac{X-\mu}{\sigma}$ ). The data shown covers the tonal and dynamical range of five different bassoons.

The total number of experimental runs was  $n = 3226$ .

Formant analysis is a sound description concept similar to that of the global spectral centroid, but with a greater level of detail. An indication for a change in sound color with a change in the embouchure would be a shift in formant frequencies or a shift of their ratios. Both cannot clearly be observed in Fig. 5.30. In the low register notes, for the first two formant center frequencies  $F1$  and  $F2$ , an opposite trend can be observed:  $F1$  tends to increase, while  $F2$  tends to decrease with the dynamic level. A stronger indication for this weak trend is the plot of  $F2/F1$ . For higher notes, the trend is not visible, or even seems to be inverted.

The evidence for these global trends is not very strong. Reasons for the large spreading of the data may be generic differences in the overtone structure of single notes, and, to a smaller extent, influences of the room acoustics.

In general, the spectral centroid  $h_{sc}$  is much more affected by the playing dynamics, than the formant center frequencies  $\mathcal{F}1$ ,  $\mathcal{F}2$  and  $\mathcal{F}3$ .

To conclude, from the present experimental results the influence of embouchure on the sound color cannot be discussed independently of the playing dynamics. The generic sound color of a note as characterized by the formants does not depend strongly on the lip force applied at a fixed position relative to the reed tip. A superposed effect is, that the sounds become brighter as the dynamic level increases. These findings are evidence for the hypothesis, that the main influencing factors for the sound color are the acoustical properties of the resonator and the playing dynamics, for a given reed and a fixed lip position.

To investigate the remaining subtleties of sound color adjustments, which are certainly of great importance for the woodwind players, also the effect of the mouth cavity should be addressed. For the case of the bassoon, interesting experiments have been carried out by Hoekje [90].

The vocal tract influence has been proven to be relevant for the radiated sound in the saxophone, in a frequency range where the impedance amplitudes of the vocal tract and an air column mode are comparable [113].

Even if formant analysis has successfully been used to describe general aspects of timbre in stationary musical sounds [162, 121, 80], other global sound parameters such as sharpness, roughness and the harmonics to noise ratio and their relation to loudness, or more detailed concepts like an analysis of single complex partials should be taken into account. A crucial aspect to be studied further is the influence of the lip position on the reed.

### 5.3.4 Relation to the acoustical Properties of the Resonator

#### Intonation

In the previous sections, the input parameters to achieve a desired set of output parameters have been outlined. These provide some insight into how the musician controls his performance on single notes, namely intonation and dynamics, with his embouchure. His actions are consequences of the resonator's acoustics, namely the harmonicity and impedance peak magnitude of the air column modes.

This section links the previous performance-related results from the blowing experiments to the acoustical properties of the resonator. The discussion covers the aspects intonation, ease of playing, and sound color.

The *harmonicity map* (Fig. 2.17) introduced in section 2.4 is a contour plot of acoustic impedance curves, rescaled in frequency and magnitude.

Choosing a dB-threshold of -6 dB for the magnitude relative to the highest impedance peaks, and a tuning threshold of  $|100|$  Cent relative to the harmonic frequencies  $n f_0$  produces a plot focusing only on the strong nearly harmonic modes and their deviation in Cent from the corresponding harmonics (see Fig. 2.17). The choice of these thresholds is based on general statements of Fletcher [58] on conditions for mode-locking in non-linearly excited oscillators. Thresholding leads to a disregard of modes which are either out of tune or too weak, or both. The remaining modes are called "supporting modes". The observations on the reed pressure waveform in section 5.2.3, confirms that these thresholds are reasonable (see Fig. 5.22).

Assuming the proper selection of supporting modes, the favored sounding frequency can be thought to be a compromise of their peak frequencies  $f_n$ .

To account also their impedance magnitude  $|Z_n|$  in estimating the sounding frequency, the averaged

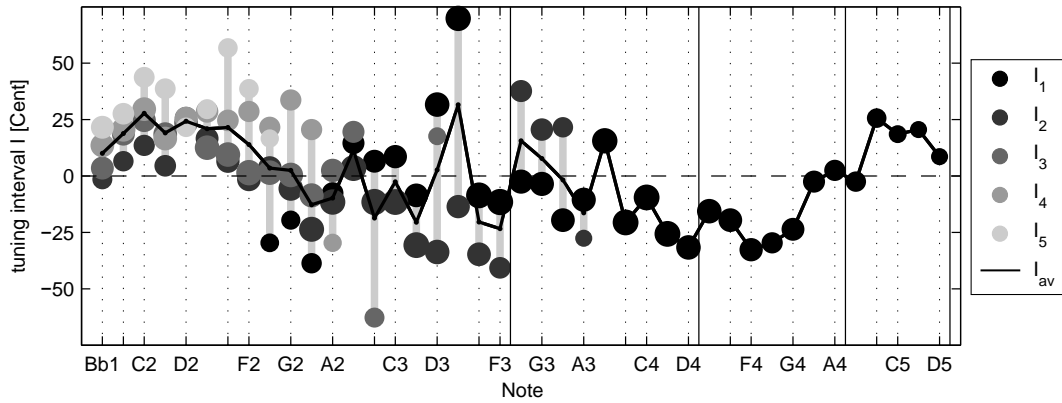


**Figure 5.31** Tuning discrepancy estimate from harmonicity considerations. Dots mark  $I_n$ , the intervals in Cent between supporting air-column modes  $n$  and the harmonic series  $n f_{0,nom}$ , the shading decreases with the ordinal number  $n$ . The marker size corresponds to the magnitude of  $|Z|$ . The black line  $I_{av}$  is the  $|Z|$ -weighted average of  $I_n$ .

tuning interval  $I_{av}$  is proposed as the weighted sum

$$I_{av} = \frac{1}{\sum_n |Z_n|} \sum_{n=1}^N I_n |Z_n|, \quad (5.5)$$

where  $I_n = 1200 \log_2(f_n/(n f_{0,nom}))$  is the interval in Cent between the  $n^{th}$  supporting air column resonance frequency  $f_n$  and the  $n^{th}$  harmonic, and  $Z_n = |Z(f_n)|$  are the corresponding impedance peak magnitudes. Note that  $|Z|$  is the measured impedance at the bocal tip, corrected for the mouthpiece effect.

This approach is similar to the “sum function” proposed by Wogram [173], but regards only strong modes and puts a strong emphasis on their harmonicity. This kind of approach is certainly simplistic in the light of the complexity of the coupling of the resonator to the non-linear excitation mechanism. However, it will be shown in the following that the approach provides reasonable results which deserve further discussions. Fig. 5.31 shows the  $|Z|$ -weighted average interval  $I_{av}$  versus the log-frequency corresponding to standard fingerings on the resonator. The vertical gray bars in this plot mark the range between these intervals, which may be related to the bending range: Fingerings with spread resonances would be easier to modulate in frequency than those with strictly aligned resonances. Following this argument, the latter would have a very stable tuning while others have a larger “bending range”. The term bending accounts for pitch changes by embouchure action. A bending range can be useful for a bassoonist for slight fine-tunings of their intonation while playing along with others. A stable, frequency-locked regime is only comfortable to the player, if the locked frequency corresponds to the desired tuning. The need for bending depends upon the mean value  $I_{av}$ . In this sense, also the number of participating air-column modes influences the bending behavior of a note, making it easier to bend a note between “competing” modes.

These hypotheses will be discussed for some characteristic notes which are known to bassoonists for being problematic in tuning: For example,  $D2$  is a note which is commonly regarded to be sharp [34]. For this note, Fig. 5.31 reveals, that all harmonics are about 25 Cent too high, which is an indication for a strongly locked regime, which is uncomfortable to be bend.

Another example is the note  $Eb3$  which is played with a fork fingering. The air column mode supporting the fundamental actually corresponds to the note  $D3$  and is therefore more than 50 Cent sharp (the first open tone hole of  $Eb3$  would produce  $D3$  without the forked fingering). The second harmonic however, gets strong support from a mode which is about 10 Cent flat (Fig. 5.31). This widespread configuration of modes allows to play the note in tune (with some effort, as bassoonists know), and also offers a huge bending range for this fingering.

A further statement commonly agreed upon bassoonists is, that the lowest notes in the first register

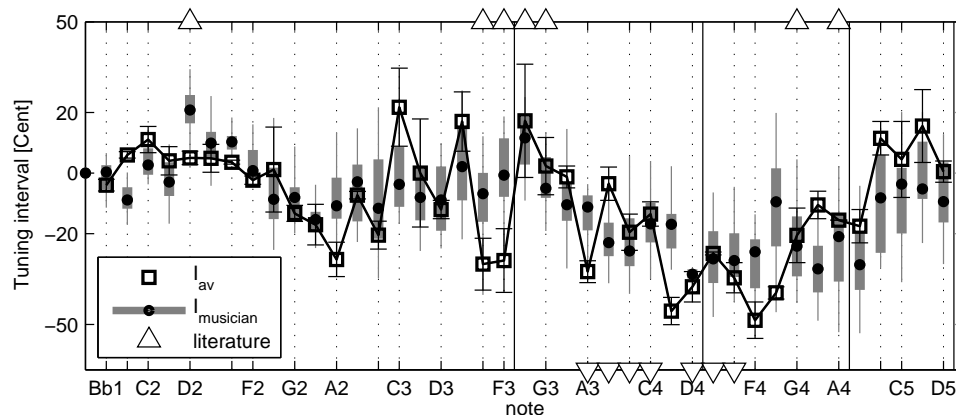


**Figure 5.32** Comparison of tuning estimates from a blowing test and from the harmonicity analysis. Black dots with gray errorbars mark the intonation discrepancy  $I_{\text{musician}}$  if the instrument is played by a musician advised not to use embouchure corrections. Squares mark the  $|Z|$ -weighted average  $I_{\text{av}}$  in Cent from the harmonicity analysis of measured impedance curves; the errorbars indicate the spread of measurements on  $I_{\text{av}}$  over five bassoons. The markers ( $\Delta$ ,  $\nabla$ ) denote the tuning tendency (sharp, flat) reported in bassoonist literature [34].

tend to be sharp and are not comfortably flattened with the embouchure (the D2 discussed above is a very pronounced example). Ascending the scale, the notes are better in tune, and are more easily adjusted. The notes of the upper half of the first register are the most comfortable to be played. In the middle of the second register (notes above the half-holed) to the middle of the third register, notes are rather flat and it is strenuous to bend them up.

All these statements are supported by Fig. 5.31: In the low register, up to five participating modes tend to be sharp and have a relatively small spreading being an indication for the difficulty in down-bending, that musicians report. From E2 to A3 the number of participating modes decreases from 4 to 2. Their spreading is relatively large, and for many fingerings the 0 Cent mark is within their range. For notes higher than A3, only one mode contributes to the regime of oscillations, and their frequency is rather flat, up to A4. This indicates the reported need of tight embouchures in this tonal region (see 5.3.1).

Another indication for the explanatory power of  $I_{\text{av}}$  can be found, when comparing this to intonation measurements with a player:

In the previously mentioned subjective study [78], the resulting sounding frequencies were obtained from a blowing experiment with a musician, advised to “blow straight” into several bassoons, i.e. to avoid any note-specific embouchure corrections. Comparing the mean values  $I_{\text{musician}}$  from this study with the intonation tendency estimate  $I_{\text{av}}$  from the harmonicity analysis of impedance curves, a good overall agreement is found (Fig. 5.32). The general agreement is quite remarkable, considering that  $I_{\text{av}}$  is only a scalar quantity of the passive linear behavior of the resonator, where as in the perceptual investigation of intonation the results are strongly influenced by the reed, the players abilities, preferences and also by the familiarization with his own instrument.

### Influence of the reed equivalent volume $V_{eq}$

Assuming a reed equivalent volume attached to the bore considers the effect that air is displaced by the vibrating reed blades. Thus,  $V_{eq}$  has a strong influence on the intonation tendency estimate  $I_{\text{av}}$ . Prolonging the resonator lowers the fundamental resonance and influences the inharmonicity of higher resonances. In the previous discussions, the reed equivalent volume  $V_{eq}$  has been taken to be 2.3 times the actual geometric volume of the reed ( $V_{reed}$ ). This is a reasonable guess, as will be shown in the following.

A correlation between the intonation tendency estimate  $I_{\text{av}}(V_{eq})$  and the subjective intonation

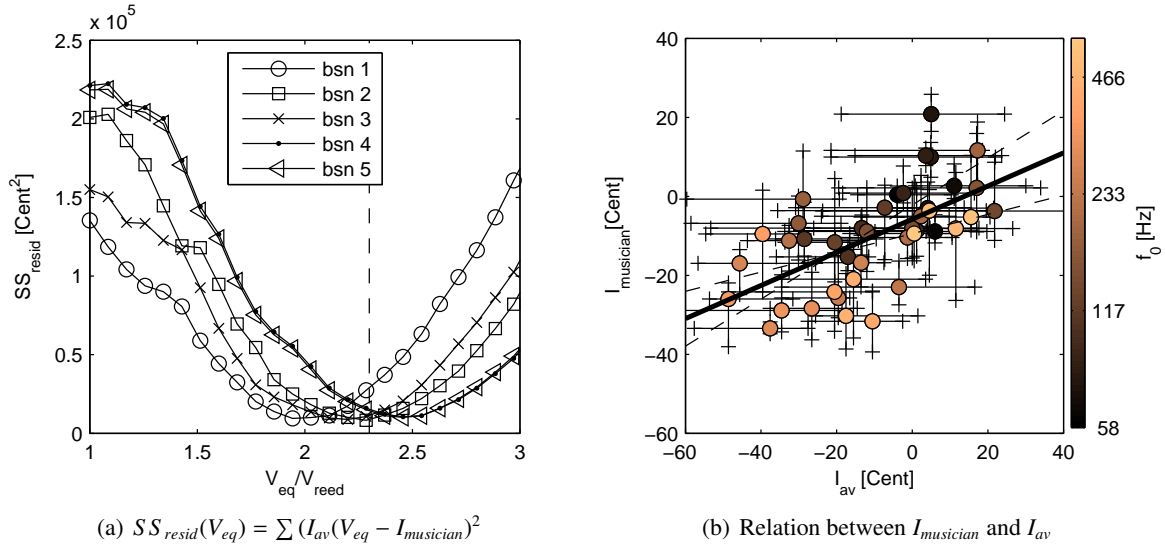


**Figure 5.33** Influence of the reed equivalent volume  $V_{eq}$  on the correlation between the perceived tuning  $I_{musician}$  and the intonation tendency estimate  $I_{av}$ .

**a)** Residual sum of squares as a function of the reed equivalent volume  $V_{eq}$  for five different bassoons.

**b)** Measurements and regression model  $I_{musician} = a_0 + a_1 I_{av}(V_{eq})$ , for  $V_{eq} = 2.3V_{reed}$  ( $a_0 = -5.8 \text{ Cent}$ ,  $a_1 = 0.42 \pm 0.18$ ,  $R^2 = 0.37$ ). Each of the 41 markers corresponds to the median of measurements of one note within the chromatic playing range from B $\flat$ 1 to D5, the color indicates the sounding frequency  $f_0$ , according to the colorbar at the right of the plot. Vertical errorbars mark the 25<sup>th</sup> and 75<sup>th</sup> percentiles of 18 measurements of  $I_{musician}$  (full permutation of 3 bassoons, 3 bocals and 2 cane-reeds). Horizontal errorbars mark the maximum and minimum values of  $I_{av}$  deduced from impedance measurements on five bassoon-bocal combinations.

discrepancy  $I_{musician}$  (Fig. 5.32) would indicate the proper choice of  $V_{eq}$ . In a parameter study,  $I_{av}(V_{eq})$  has been determined from a set of measured impedance curves of five bassoons using values of the reed equivalent volume ranging from 1 to 3 times the geometric reed volume  $V_{reed}$ . Evaluating the residual sum of squares  $SS_{resid}(V_{eq}) = \sum (I_{av}(V_{eq}) - I_{musician})^2$  minima are observed within the range  $2 \leq V_{eq}/V_{reed} \leq 2.5$  (Fig. 5.33). The observed correlation is moderate ( $a_1 = 0.42$ ) and in general, a model explaining 20 % of the total variation ( $R^2 = 0.37$ ) may not be regarded strong. However, it should be noticed that  $V_{eq}$  is introduced here as a constant, embouchure independent property, which is a very drastic simplification. The action of a lip force on the reed reduces the volume, and the mobility of the reed blades may be influenced by the elasticity of the lip cushions pressed to it. In the light of these effects, the significant dip in  $SS_{resid}$  (Fig. 5.33) is an indication for an optimum average size of  $V_{eq} \approx 2.3$  to observe a general similarity between the intonation perceived by a musician and the intonation estimate from the harmonicity analysis of the resonator, expressed in  $I_{musician}$  and  $I_{av}$ , respectively.

In the previous section 5.3.2, it has been found, that the lip force  $F_l$  correlates with the perceived tuning  $I_{musician}$  (Fig. 5.29). To further validate the guess made for the equivalent reed volume, the dependence of the correlation between  $F_l$  and the intonation estimate  $I_{av}$  on  $V_{eq}$  is examined in the following. To each equivalent volume on one of the five measured bassoon impedance curves, a linear regression analysis has been performed to relate the maximum lip force  $F_{l,max}$  to the intonation tendency estimate  $I_{av}(V_{eq})$ . For each regression model, the quality of fit is quantified by the coefficient of determination  $R^2$ . The plot of  $R^2$  versus  $V_{eq}$  clearly shows a sudden rise in  $R^2$  for values of  $V_{eq} > 2V_{reed}$  (Fig. 5.34(a)). The linear regression coefficient  $R^2$  as a function of  $V_{eq}$  has a maximum absolute value of  $-0.3 \text{ N}/(10 \text{ Cent})$  near  $V_{eq} \approx 2.5$  for all the bassoons (Fig. 5.34(b)). The agreement between the  $F_{l,max}$  and  $I_{av}$  is qualitatively the same as for  $I_{musician}$  and  $I_{av}$ . For the

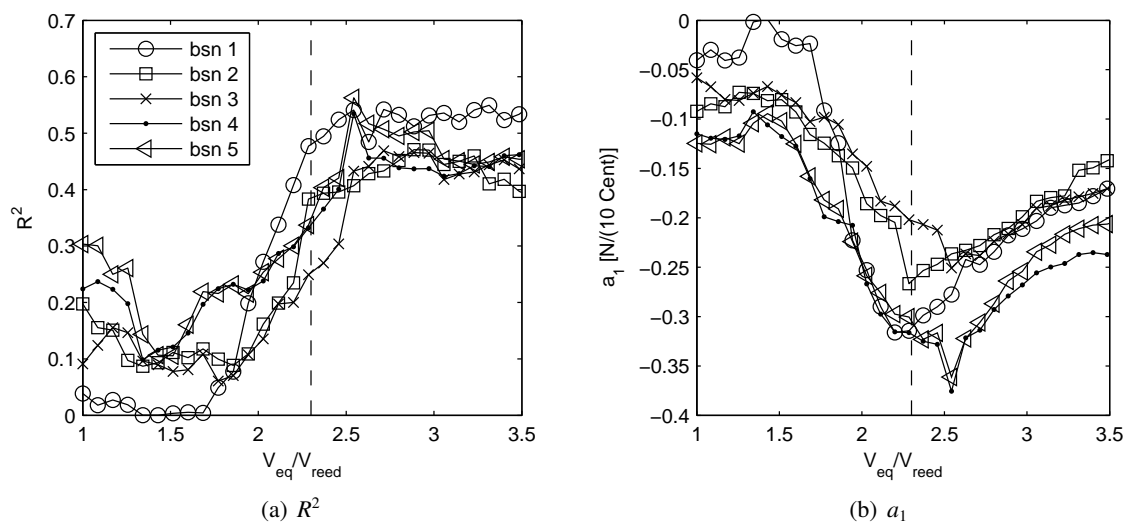


**Figure 5.34** Influence of  $V_{eq}$  on a regression model  $F_{I\max} = a_0 + a_1 I_{av}(V_{eq})$ , for five different bassoons.

chosen value  $V_{eq} = 2.3V_{reed}$ , the regression model parameters are  $a_1 = -0.24 \pm 0.11 \text{ N/(10 Cent)}^{33}$  with  $R^2 = 0.34$  (Fig. 5.35). To sum up: The harmonic properties of an air-column are related to its tuning properties under playing conditions. Both assessments with a musician and an artificial mouth give qualitatively the same results, using a different methodology.

To quantify the intonation discrepancy estimate, a scalar value  $I_{av}$  is proposed, which lumps both peak frequency and peak magnitude information from the input impedance curve. The contribution of each peak to  $I_{av}$  is determined by its relative position a) in frequency with respect to the nearest harmonic frequency and b) in magnitude with respect to the strongest mode in the spectrum. To the knowledge of the author, this proposal is new, though similar to the “sum function” proposed by Wogram [173].  $I_{av}$  explains about 20% of both the musicians perception of tuning and of the lip force needed to correct for tuning discrepancy, in artificial mouth experiments. In both cases, the dependence of  $I_{av}$  on the reed equivalent volume  $V_{eq}$  has been examined in terms of statistical determination, leading to the conclusion, that  $V_{eq} \approx 2.3V_{reed} = 2.2 \text{ cm}^3$  is a reasonable guess for the bassoon reed. A very similar value has been proposed in a previous study on the bassoon [107]. Due to the embouchure actions,  $V_{eq}$  might be quite different from note to note, depending on the mobility of the reed blade. The flow induced by the moving reed blade has been proven in numerical models as a property having a significant contribution to the sounding pitch [153, 35].

### Ease of playing

As shown in section 5.2.3, the acoustical properties of the resonator influences the reed pressure waveform and thus the spectral composition in the sound spectra. In this context the number of supporting air-column modes has been addressed (see Fig.5.22), but as hypothesized above, also their amplitude play a role.

This information is provided by the harmonicity map introduced in section 2.4. To show relations between the acoustics of the resonator, the reed pressure spectrum and the radiated sound, three contourplots of spectra are juxtaposed (Fig. 5.37). The reed- and sound pressure spectra shown here are obtained from experiments with a medium blowing pressure for the respective fingering to obtain a *mezzoforte* sound. For comparison reasons, the three plots have the same dynamic range of 6 dB. For each fingering (vertical axis), the strongest partial, or air column mode, respectively, is the 0 dB reference, which corresponds to the darkest color in the plot. To discriminate the strongest

<sup>33</sup>The 95% confidence interval for the  $a_1$  estimate is  $[-0.35, -0.12] \text{ N/(10 Cent)}$



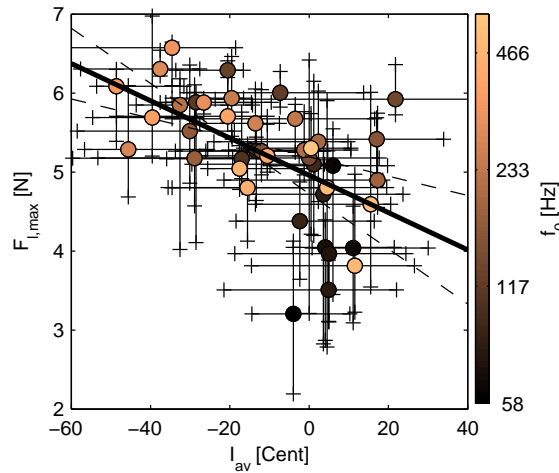


**Figure 5.35** Applied lip force  $F_{l,max}$  to achieve pure tuning in artificial mouth experiments on 5 bassoons with one synthetic double-reed as compared to the  $|Z|$ -weighted average tuning interval  $I_{av}$  of impedance peaks. Each of the 41 markers corresponds to the median of measurements on one note within the chromatic playing range from B $\flat$ 1 to D5. The color indicates the sounding frequency  $f_0$ , according to the colorbar to the right of the plot. Vertical and horizontal errorbars mark the maximum and minimum values from measurements on the same five bassoon-bocal combinations. Dashed lines correspond to the 95% confidence interval of the fit coefficients. In the calculation of  $I_{av}$  the reed equivalent volume was assumed to be  $V_{eq} = 2.3 V_{reed} = 2.2\text{cm}^3$  for all bassoons.

partial, or air column mode, they are marked with a white cross.

The comparison of Figs. 5.37(a) and 5.37(c) shows, that the harmonic content of the resonator impedance spectra is mirrored directly in the reed pressure spectra.

The ordinal number of the strongest air column mode decreases with increasing pitch, and a similar, but less pronounced effect is observed in the reed pressure spectrum. If the strongest mode in the resonator is the third or fourth, the strongest partial in the reed pressure signal is the second. If the strongest resonator mode is the first or second, the strongest partial is the fundamental. Note that in the highest register above G4, the strongest air column mode is lower than the fundamental frequency.

In section 5.3.1 a grouping of notes according to their blowing characteristics has been proposed. The dimensions underlying the classification are the pressure efficiency  $p_{r,RMS}/p_m$  and a non-dimensional parameter  $F_l/(q\rho 2hf_0)$ , named embouchure tightness. The grouping of notes from this artificial mouth embouchure analysis matches well the responses of musicians, being asked to divide the tonal range into four groups.

Possible reasons for the different behavior of the notes in these groups can be found in the acoustic resonance properties of the air-column. Not the ordinal number of the air column modes, but their count, strength and harmonic relation are important. This information is provided by the harmonicity map introduced in section 2.4. The harmonicity map (Fig. 5.37(a)) and the rescaled reed pressure spectra (Fig. 5.37(c)) allow for an interpretation of the observed classification into four groups with respect to the acoustics of the resonator:

**group 1** (B $\flat$ 1  $\rightarrow$  E2) Very weak fundamental mode. Number of supporting modes:  $> 4$ .

Strongest partial: 2<sup>nd</sup>

**group 2** (F2  $\rightarrow$  G $\sharp$ 3) Increasingly strong fundamental mode. Number of supporting modes: 4 to 2.

Strongest partial: 1<sup>st</sup>



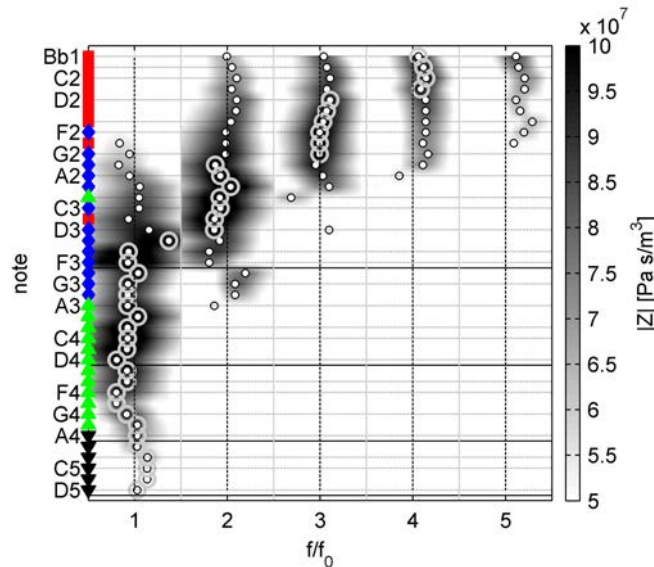


**Figure 5.36** Harmonicity map of the modern German Bassoon. Contourplot of impedance curves, rescaled in frequency and magnitude to show a range of  $\pm 100$  Cent around each harmonic in frequency and  $-6$  dB smaller than  $10 \times 10^6$  Pa s/m<sup>3</sup> in magnitude, respectively.

Markers ■, ◆, ▲, ▼ on the left vertical axis mark the grouping of notes according to the analysis in section 5.3.1.

White circles mark the strongest partial of each fingering.

**group 3** (A3→ G#4) Strong fundamental, tends to be flat. No supporting modes.

Strongest partial: 1<sup>st</sup>

**group 4** (A4→ D5) Weak fundamental, tends to be sharp. No supporting modes.

Strongest partial: 1<sup>st</sup>

Aided by the harmonicity information from Fig. 5.36 and Fig. 5.31, the playing characteristics can be interpreted to a large extent:

In the low register (Bb1→E2), many higher harmonics support a stable and efficient oscillation  $p_{r,RMS}/p_m > 1$ . The fundamental mode is very weak, and the strongest partial is the second. The tuning estimate  $I_{av}$  predicts a sharp tuning, which makes downbending difficult and necessitates a loose embouchure.

In the mid-low register (F2→G3), the fundamental mode is present (not lower than  $-6$  dB compared to the strongest mode). The tuning  $I_n$  of the participating air column modes have a large spread embracing the desired tuning (0 Cent) in most cases. These notes are most comfortable to play, with a tighter but comfortable embouchure. The relatively widespread supporting modes provide a efficient regimes of oscillation with easy frequency adjustment and large bending ranges.

The notes in the mid-high (G#3→F#4) and high (G4→D5) register lack the support of the second or higher air column modes and are played at low pressure efficiency ( $p_{r,RMS} < 1$ ). The reed pressure waveform becomes symmetrical  $\tau_c/\tau \approx 0.5$  and  $|p_c|/p_0 \approx 1$ , see Figs. 5.19(b) and 5.18(b). For the modern German Bassoon this border between low and high register is clearly found at the note A3, in both the harmonicity map (Fig. 5.37(a)) and the analysis of blowing characteristics (Fig. 5.24). With an accuracy of three semitones, this border is also confirmed by musicians. In the mid-high register, the remaining air-column mode is tuned rather flat for most notes, which requires tight embouchures to bend them up. Given the low pressure efficiency the musicians rating can be well understood, that the mid-high register is the most difficult to play.

The notes of the highest register have the same characteristics in general, but the embouchure can be released, because the one remaining mode is tuned sharp.

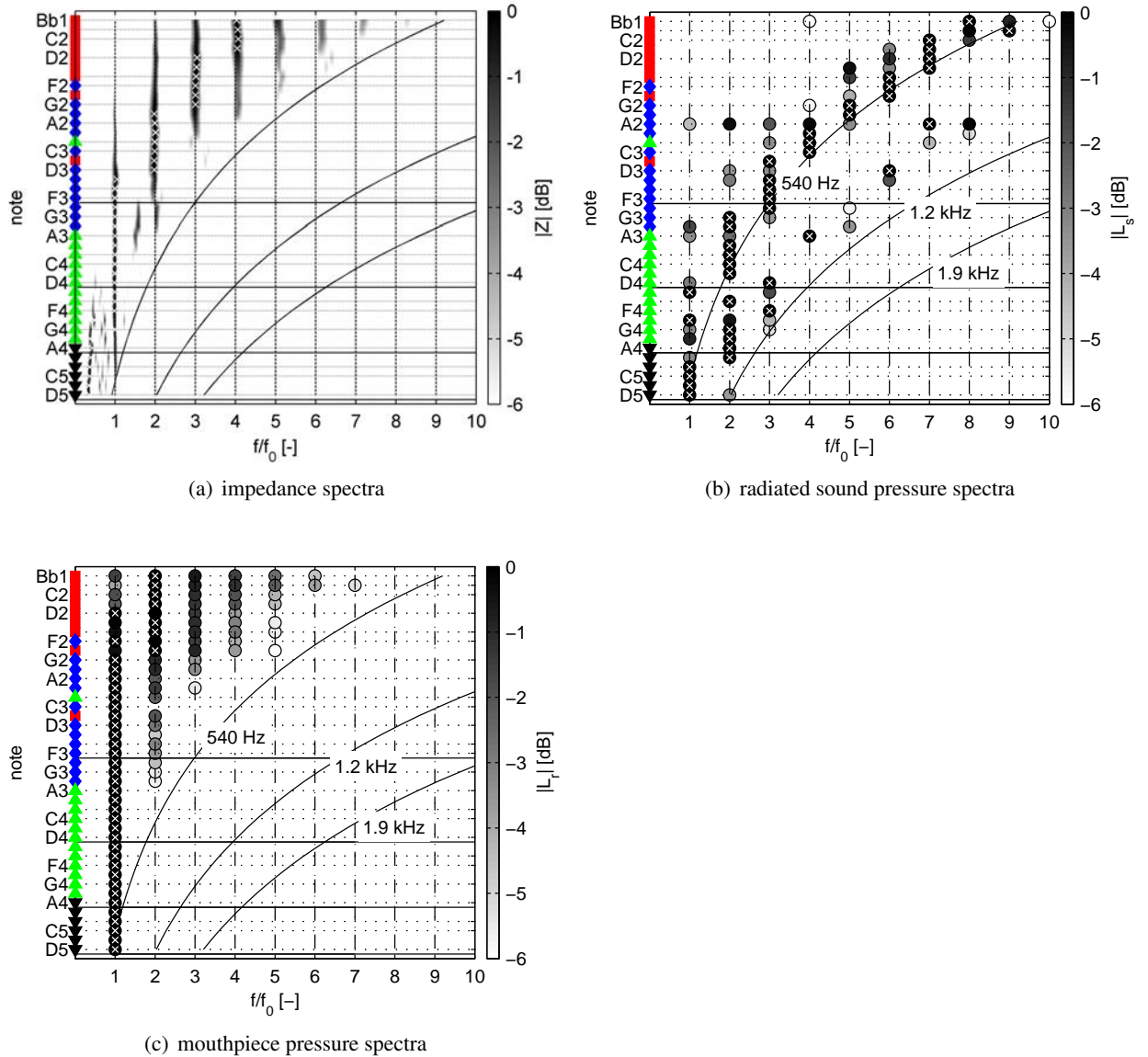


**Figure 5.37** Comparison of acoustic properties of the resonator and sound characteristics of a modern German bassoon. Measurements of acoustic impedance spectra corrected for mouthpiece volume (a), and pressure spectra inside the mouthpiece (c) and in the ambience (b), for standard fingerings played at a medium dynamic level (mouth pressure  $p_m \approx 1/2(p_{m,max} + p_{m,min})$ ). The color indicates the relative impedance magnitude (a) or relative spectral intensity (b,c) according to the colorscale left to the plots. For each note, the maxima are marked with a white cross. For all three plots, the dynamic range is limited to 0..-6 dB

Markers ■, ◆, ▲, ▼ on the left vertical axis mark the grouping of notes according to the analysis in section 5.3.1.

Solid curved lines are iso-frequency lines indicating the first three formants in the bassoon sound. Solid horizontal lines indicate the register limits of the resonator [104]. black

## Sound

From the previous considerations, the importance of the resonator for the tuning and the reed pressure waveform can be understood. Also for the discussion of the radiated sound characteristics, the acoustics of the resonator play an important role. It has been shown, that the general spectral characteristics of the radiated sound are fundamentally different compared to the pressure inside the mouthpiece. The formants in particular are not present in the reed pressure spectrum. By blowing harder, the spectral centroid increases, and the sounds become brighter but the formants center frequencies remain. The role of the embouchure seems to be mainly the adjustment of the correct frequency according to the desired dynamic level.

With these findings it can be concluded, that the spectral energy distribution in the radiated sound is a mostly invariant property of the resonator: The comparison of Figs. 5.37(a) and 5.37(b) reveals the importance of the cutoff frequency for the radiated sound. This frequency marks the limit of the harmonic alignment of the air column resonances, due to the open downstream tone-holes. It is clearly observed in Fig. 5.37(a) near the 540 Hz isoline. The sound pressure spectra appear inverse compared to the harmonicity map: The partials in the sound rise above the 6 dB threshold, where the air column modes are attenuated by this amount.

For almost all fingerings in the first, second and fourth register, the strongest partial is the one which is closest to the 540 Hz isoline. This is the reason for the main formant  $\mathcal{F}1$  in the bassoon sound which is located at 540 Hz in the present measurements (Fig. 5.15(b)). Exceptional are only some notes in the third register, where the partials are nearly half-way between the 540 and 1200 Hz isolines.

## 5.4 Summary

In this section it was shown, that the experimental apparatus developed for this thesis is suited to investigate the bassoon under realistic playing conditions. The possibility to precisely adjust the artificial lip and to measure the force it exerts to the reed allowed to carry out blowing experiments covering the full tonal and dynamical range of this instrument. A large set of benchmarking data describing the bassoon under quasi-stationary operation conditions was presented.

In particular, the lip adjustments during playing to correct the tuning with respect to the desired dynamic level became measurable. The quasi-static, lip force dependent model of the double-reed presented in Chapter 4 has been proven to explain to a surprisingly large extent the measured mean volume flow-rate under playing conditions. The applicability of this model makes it possible to “translate” artificial mouth adjustment parameters characterizing realistic embouchure configurations into reed model parameters in relevant playing regimes.

Furthermore, attempts have been made to relate aspects of the bassoon performance to the acoustics of the resonator. The presented experimental data confirmed, that the reed pressure waveform is determined by the number of supporting air column modes of the resonator, which ranges up to seven for the lowest notes. A method to estimate tuning tendencies for the sounding frequency of single notes from the impedance peaks of the resonator is presented. Being of purely empirical nature, it is yet supported by the presented experimental observations.

Investigation on the sound color of the bassoon were based on formant analysis. The main formant in the bassoon sound around 540 Hz is not present in the pressure spectrum measured near the sound source (inside the reed mouthpiece). It is a characteristics of the radiated sound, which depends to a large extent on the resonator. The analysis of artificial mouth parameters under playing conditions suggests a classification of the notes of a bassoon into four groups, according to their embouchure and blowing pressure characteristics. The classification fits well to subjective judgments of players. This is an indication that the blowing experiments carried out within the present work are quite close to the musical performance. Lacking a precise physical model, this experimental methodology can be helpful for user-centered design processes in musical instrument design. In a research cooperation with musical instrument makers and scientists, promising attempts have been made [174].



# 6 Conclusion

## 6.1 Summary

The general objective of this thesis is a quantitative, physical description of sound generation and radiation of a bassoon.

The scope ranges from an assessment of the acoustics of the resonator to a characterization of the mouthpiece and the interaction of both under realistic playing conditions, with respect to embouchure actions controlling the sounding frequency and dynamic level.

With a strong focus on experiments in the respective fields, the work relates experimental results to the existing, elementary models. Parameters describing the delicate situation at the double-reed, where the musician interacts with the instrument, have been derived from measurements covering the full tonal and dynamic range of the bassoon. The parameters link the experiment and the model domain and furthermore provide some insight into the embouchure control of the bassoon.

A description of the resonator based on a one-dimensional waveguide model in the transmission matrix notation is presented in **Chapter 2**. The derivation of the method is summarized and compact implementations to model the relevant acoustic elements are given. The incorporation of dissipation and dispersion at the walls of a conical frustum is discussed with respect to the formulation of a transfer matrix for a universal conical duct element (section 2.1.4). Given a known geometry, the resonance characteristics in woodwind air columns can be predicted by calculation of acoustic impedance spectra.

For the complementing experiments a commercial measurement system has been modified and recalibrated. Subsequent to a study of repeatability, the acoustic impedance spectra of five modern German bassoons from several makers are compared (section 2.3.1). The random errors observed in the measurements are  $\pm 5$  Cent in peak frequency and  $\pm 15$  % in peak magnitude. The differences between several individual instruments are larger. The comparison of measured and calculated impedance curves (section 2.3.2) shows a general family resemblance, but reveals discrepancies in peak frequency and magnitude that are large enough to be significant.

The graphical representation of impedance curves in a *harmonicity map* as suggested in section 2.4.3, provides a comprehensive overview on the resonance characteristics of an air-column. This representation may be very helpful in quantifying the global acoustical effect of geometrical modification of the air-column, e.g. in optimization routines.

At the beginning of **Chapter 3** the simplest analytical model for a single-reed is discussed, because it is commonly applied to double-reeds. It assumes harmonic oscillations for the pressure induced structural motion, quasi-stationary flow and the validity of the Bernoulli principle along a streamline in the flow.

To characterize the double-reed by a few scalar parameters in the context of this model, an artificial mouth has been constructed. It is equipped with a rigidly fixed commercial (synthetic) bassoon reed, accurately adjustable artificial lips, and force sensors to measure the force exerted to the reed (section 3.3.2). The design of this device makes the resonator interchangeable without affecting the embouchure. In its present and final design state, the artificial mouth permits to repeatedly carry out both quasi-static experiments to characterize the reed with lips pressed on it, and blowing experiments with the same embouchure configuration.

In **Chapter 4** measurements of the quasi-static pressure-flow valve characteristic of a double-reed are presented. A simple, but more general analytic model is proposed, taking account of separate parameters for i) flow effects like *vena contracta*, flow separation, and reattachment, ii) the non-linearity of the reed stiffness, and iii) the diffuser-like widening of the flow channel from reed tip to bocal tip (section 4.2.2). Varying these parameters within their physically relevant limits, it was shown, that the only parameter lowering the saturation pressure in the valve characteristics is the non-linearity of the stiffness of the reed. The proposed model agrees well with experimental observations for both the pressure dependent inlet slit height from optical measurements and the volume-flow rate as measured by a thermal flow meter (section 4.2.4).

The bassoon has been observed to be fully playable with an *oblique embouchure*, i.e. only one lip is pressed on the double-reed to adjust its inlet slit height (section 4.3.1). This finding constituted a major and crucial simplification of the experimental procedure in both dynamic and quasi-static measurements:

Modified only by a non-linear reed stiffness, the quasi-static single-reed model has been fitted to a set of characteristics' measurements with varying lip force applied to the reed (section 4.1.1). This yields an empirical relation between the artificial mouth parameters of lip force and blowing pressure, as well as the corresponding reed model parameters.

**Chapter 5** aims to bring the previous results together in steady blowing experiments with realistic embouchures. At first it is shown, that the empirical, lip-force dependent reed model presented in Chapter 4 applies under playing conditions as well. Despite its simplicity, the predicted mean flow-rate according to the quasi-static model matches surprisingly well the measurements. For a large number of experiments ( $N=2212$ ) one finds a good correlation ( $R^2=0.96$ ). The remaining discrepancy does not correlate with the Reynolds nor Strouhal number (section 5.1.5) and points rather to imperfections in the measurements.

Secondly, a comprehensive overview of the experimental data is given in order to benchmark the parameter ranges, at which the bassoon could be sounded at the expected nominal pitch corresponding to the fingering. This survey depicts the musically relevant dynamic range of each of the notes and the required lip force to correct for tuning. Providing the non-dimensional reed model parameters assigned to each of experimental situations, it may serve as a database for research in physical modeling of double-reed instruments.

Using one and the same reed, a variety of five bassoons of different quality and manufacture have been compared, revealing a generic similarity (section 5.2.1). In principle, the same has been observed in Chapter 2 concerning the acoustical properties of the resonator.

A meta-analysis of the mouthpiece pressure waveform confirmed, under realistic playing conditions, analytical predictions made by other authors for an idealized reed-resonator model: The reed pressure waveform depends on the number of air column modes supporting the reed oscillation (section 5.2.3). Ascending the scale, their count reduces: Above A3 ( $f_0 = 222$  Hz) the reed oscillation is mainly locked onto a single air-column mode.

The change in quantity and tuning of the supporting resonator modes leads to perceptible changes in the embouchure.

Analyzing measured artificial mouth data, a classification of notes into four groups according to their embouchure characteristics can be seen. Professional bassoonists asked independently from our measurements to classify the tonal range into four registers according to their *blowing sensation* chose nearly the same margins (section 5.3.1).

For a given reed the timbre of the radiated sound is to a large extent determined by the resonator, and secondly by the dynamic level: The formants around 0.5 and 1.2 kHz which are characteristic for the bassoon sound, do not vary notably with dynamics. However, a superposed effect is the rise in the spectral centroid when blowing harder (section 5.2.2). Whereas the reed pressure spectrum is determined mainly by the number of air-column modes and thus varies across the tonal range, the cut-off frequency of the resonator remains constant near 600 Hz. The data presented support the hypothesis, that the pressure inside the mouthpiece is determined by the harmonic resonator modes,

while the radiated sound is mostly influenced by the cut-off frequency.

The role of the lips on the mouthpiece is mainly to adjust the reed's inlet slit height to fine-tune the sounding frequency in accordance with the blowing pressure. The lip-force characteristics match the intonation rating of musicians, such that high levels of lip force are needed to bend up notes which appear to be flat (section 5.3.2). The intonation curve perceived by a musician furthermore correlates with a harmonicity indicator calculated from the impedance amplitude weighted tuning interval of the supporting impedance peaks (section 5.3.4).

This observation links the acoustics of the resonator, the sensation of the musician and the measurement data obtained with the artificial mouth. On the one hand, this demonstrates the usefulness of the artificial mouth presented in Chapter 3 for investigations on the bassoon which are of musical relevance; on the other hand, it supports the usefulness of the presented data and their interrelations to postulate user-centered optimization targets for woodwind design.

## 6.2 Outlook

The results in this thesis inspire many directions deserving further research:

Concerning the acoustics of the resonator, a careful investigation of losses in the waveguide is interesting. On the one hand, the limits of the one-dimensional waveguide approach should be investigated i) experimentally using accurately manufactured cones with small input diameter, and ii) numerically by a Finite-Element Model with visco-acoustic elements. On the other hand, losses at the sharp edges at the junctions of tone hole and main duct deserve further research, especially for small tone hole diameters. A high model accuracy certainly is crucial for the calculation based design of woodwind air-columns. Despite using a state-of-the-art input impedance measurement system validated with simple geometries, the agreement between theory and experiment for the case of the complex air column of a bassoon was not yet optimal. The reasons for that should be investigated.

The artificial mouth presented can be modified relatively easy to excite other reed wind instruments such as the oboe, or clarinet and saxophone. Once proven to be a powerful and versatile experimental tool in manual operation, further developments to automate the control of lip position, lip force and blowing pressure can speed up the experimental time significantly. To measure the reed's effective surface with respect to the embouchure, and generally in order to understand better the mechanics of the double-reed, displacement measurements at the reed tip using external acoustic excitation can be carried out. Furthermore, experiments with natural cane reeds at different stages of manufacture are interesting for both researchers and reed-making practitioners.

The thesis has provided experimental evidence that quasi-static valve characteristics can be applied in the dynamic case of the beating reed to predict the time-averaged volume-flow rate. The time-resolved simultaneous measurements of i) the reed blade using a high-speed camera, and ii) of the mean flow velocity inside the reed channel with a hot wire anemometer can provide further detailed insights into the fluid-structure interaction at the reed. In particular, a study of the influence of the edge radius at the reed blade tip on flow characteristics is interesting in order to investigate the role of the *vena contracta* in quasi-static and dynamic regimes.

Some aspects pointing to the interaction of musician and instrument have been investigated in this thesis through the analysis of careful artificial mouth measurements. Further studies can focus on details such as the functioning of auxiliary fingerings, reed pressure transients when switching the fingering or the appearance of multiphonic regimes. The possibility of measuring the mean flow

would allow an investigation of energy conversion in woodwinds in a reverberant chamber. Aiming at a detailed understanding of the reed-resonator interaction, and the role of the musician controlling the system with his or her embouchure, those measurements will help understanding of musicians' quality judgments. Such elucidation of the intersection between physics and performing arts is certainly demanding, but nonetheless essential in order to apply engineering methods in musical instrument research. Only multidisciplinary and communication between fields can provide a basis for suggesting improvements and postulate optimization targets for a systematic, customer specific redesign of woodwind instruments.

198 years after Weber's "Akustik der Blasinstrumente" and 43 years after the publication of his comprehensive book "Acoustical Aspects of Woodwind Instruments", Nederveen summarizes:

*"One has to stand in awe of builders of musical instruments, who have, by trial-and-error, designed optimally functioning instruments. Designing an instrument with the acoustic laws having perfect tuning, perfect flexibility and perfect sound quality still seems unattainable at the present state of the art." [129].*

These words of the distinguished expert may be both an encouragement and a consolation to scientists in the field.



# Acknowledgements

This work is dedicated to my friends and family who encouraged and supported me throughout the work<sup>1</sup>. To a large extent, it was their imperturbable belief in me that enabled me to start and finish this endeavour.

I owe my sincere gratitude to Prof. Roger Grundmann, who has supervised the development of this thesis, for the unconditional support he provided in many ways. The framework that he established and his inspiration made it possible for me to carry out this fascinating research, with a large amount of freedom. He not only enabled the present work to a paramount extent, but also enthused me to play bassoon and I am deeply thankful for both.

Further, it is a pleasure for me to thank my colleague and friend Dr. Johannes Baumgart who provided inestimable comprehensive support not only in the field of musical acoustics. It was a great pleasure to work with him and his views opened many times new perspectives for me. I am thankful for countless helpful discussions throughout the work, and also for the time shared during running, playing music or in the sauna.

I thank Prof. A. (Mico) Hirschberg, who gave me confidence in my results, spent a lot of time for helpful discussions and provided many helpful comments. I further would like to thank Dr. C.J. Nederveen for taking the time to discuss my results in depth. I thank them both for their work as external reviewers, and for not giving up on me...

I enjoyed crucial technical support from Timo Kirschke, Thomas Kaiser, Florian Orio (Fa. Diatest), Olaf Gerstner (Fa. Microepsilon), Brian Charles (Charles Double Reed Company), Harry Hartmann (Fa. Fiberreed), Raul Kränzler (Fa. Triole) and the team of the TUD wind tunnel.

I would like to thank my former colleagues at the institute of aerospace engineering at TUD: Dr. Kristina Koal, Catrin Mühlfriedel, Dr. Thomas Albrecht, Hans Metzkes, Dr. Gerd Mutschke, Dr. Andreas Richter, Dr. Fabian Schlegel, and Dr. Jörg Stiller.

I would like to express my gratitude to the bassoonists who contributed to this thesis by playing their instruments, volunteering in experiments, discussing, and teaching me to play the bassoon: Daniel Bätz, Stefan Pantzier, Ralf Rümker, Erik Reike, Rafael Staschik, Annette Falk, Prof. Tobias Pelkner and his students.

I enjoyed support by the German bassoon manufacturers Heckel, Moosmann, Püchner, Walter and Wolf. I especially would like to thank Ralf Reiter, Guntram and Peter Wolf.

I am grateful for the support provided by Robert Plöntzke, Sebastian Bozada, Dr. Hagen Domaschke, Dr. Matthias Hübner, Steffen Sturm, Raik Scheinpflug, Dr. Matthias Ehrlich, Wataru Ohno, Prof. Malte Kob, and Michael Johnson.

Many thanks to Matthias Schulz, Katrin Seifert and Paula for excellent typografism, catering and spirit in the last two night-shifts that this thesis required. Cheers!

To my parents: As you know, all of my work is built on the fundament of your love, the security and freedom that you provided, which enabled to develop and follow many and multiple interests. Thank you for the unconditional support, interest and sympathy with all my projects.

Above all, I owe my deepest gratitude to my beloved wife Karla. At a crucial moment it was her to inspire me to go further. Without her, I would definitely not be where I am now. Thank you for all your loving support and understanding.

---

<sup>1</sup>The work was supported by the German Federal Ministry of Economics and Technology (BMWi) (KF2229603-MF9)



# Bibliography

- [1] Almeida, A. (2006). *The Physics of Double-reed Wind Instruments and its Application to Sound Synthesis*. PhD thesis, Université Pierre & Marie Curie, Paris, France.
- [2] Almeida, A., George, D., Smith, J., and Wolfe, J. (2013). The clarinet: How blowing pressure, lip force, lip position and reed “hardness” affect pitch, sound level, and spectrum. *The Journal of the Acoustical Society of America*, 134(3):2247–2255.
- [3] Almeida, A., Lemare, J., Sheahan, M., Judge, J., Auvray, R., Dang, K. S., John, S., Geoffroy, J., Katupitiya, J., Santus, P., Skougarevsky, A., Smith, J., and Wolfe, J. (2010). Clarinet parameter cartography: automatic mapping of the sound produced as a function of blowing pressure and reed force. In *Proceedings of the International Symposium on Music Acoustics, Sydney*.
- [4] Almeida, A., Vergez, C., and Caussé, R. (2007a). Quasistatic nonlinear characteristics of double-reed instruments. *Journal of the Acoustical Society of America*, 121(1):536–546.
- [5] Almeida, A., Vergez, C., Caussé, R., and Rodet, X. (2004). Physical model of an oboe: comparison with experiments. In *Proceedings of the International Symposium on Musical Acoustics (ISMA), Nara Japan*.
- [6] Almeida, A., Vergez, C., and Caussé, R. (July/August 2007b). Experimental investigation of reed instrument functioning through image analysis of reed opening. *Acta Acustica united with Acustica*, 93:645–658(14).
- [7] Almenräder, C. (1837). Über Blasinstrumente mit Tonlöchern, besonders am Fagott. *Caecilia*, 19(74):77–87.
- [8] Backus, J. (1963). Small-vibration theory of the clarinet. *Journal of the Acoustical Society of America*, 35:305–313.
- [9] Backus, J. (1974). Input impedance curves for the reed woodwind instruments. *The Journal of the Acoustical Society of America*, 56(4):1266–1279.
- [10] Baines, A. (1991). *Woodwind Instruments and Their History*. Dover Publications, Inc., New York.
- [11] Bak, N. and Domler, P. (1987). The relation between blowing pressure and blowing frequency in clarinet playing. *Acustica*, 63:238–241.
- [12] Bamberger, A. (2008). Vortex sound of the flute and its interpretation. *Journal of the Acoustical Society of America*, 123(5):3239–3239.
- [13] Baumgart, J. (2010). *The Hair Bundle Fluid-Structure Interaction in the Inner Ear*. PhD thesis, Technische Universität Dresden.
- [14] Benade, A. (1960). On the mathematical theory of woodwind finger holes. *Journal of the Acoustical Society of America*, 32(12):1591–1608.
- [15] Benade, A. (1973). Trumpet acoustics (book chapter manuscript). Technical report, Case Western Reserve University.

- [16] Benade, A. (1990). *Fundamentals of Musical Acoustics*. Dover Publications, Inc., New York.
- [17] Benade, A. and Ibbi, M. (1987). Survey of impedance methods and a new piezo-disk-driven impedance head for air columns. *Journal of the Acoustical Society of America*, 81(4):1152–1167.
- [18] Benade, A. H. (1959). On woodwind instrument bores. *The Journal of the Acoustical Society of America*, 31(2):137–146.
- [19] Benade, A. H. (1968). On the propagation of sound waves in a cylindrical conduit. *The Journal of the Acoustical Society of America*, 44(2):616–623.
- [20] Benade, A. H. (1988). Equivalent circuits for conical waveguides. *The Journal of the Acoustical Society of America*, 83(5):1764–1769.
- [21] Bergeot, B., Almeida, A., Vergez, C., and Gazengel, B. (2012). Measurement of attack transients in a clarinet driven by a ramp-like varying pressure. In *Program of the 11th Congrès Français d'Acoustique and 2012 IOA annual meeting, Acoustics2012, Nantes*.
- [22] Böhm, T. (1871). *The flute and flute-playing in acoustical, technical, and artistic aspects*. Case School of Applied Sciences, Cleveland, Ohio.
- [23] Boersma, P. and Weenink, D. (2012). Praat: doing phonetics by computer [computer program]. version 5.1.34,. retrieved 22 April 2012 from <http://www.praat.org/>.
- [24] Bouasse, H. (1929a). *Instruments à Vent (Tome I)*. Libraire Delagrave, Paris.
- [25] Bouasse, H. (1929b). *Instruments à Vent (Tome II)*. Libraire Delagrave, Paris.
- [26] Braden, A. C. P., Newton, M. J., and Campbell, D. M. (2009). Trombone bore optimization based on input impedance targets. *The Journal of the Acoustical Society of America*, 125(4):2404–2412.
- [27] Bromage, S. (2007). *Visualisation of the Lip Motion of Brass Instrument Players, and Investigations of an Artificial Mouth as a Tool for Comparative Studies of Instruments*. PhD thesis, The University of Edinburgh.
- [28] Bromage, S., Campbell, M., and Gilbert, J. (July/August 2010). Open areas of vibrating lips in trombone playing. *Acta Acustica united with Acustica*, 96:603–613(11).
- [29] Carral, S. (2005). *Relationship between the physical parameters of musical wind instruments and the psychoacoustic attributes of the produced sound*. PhD thesis, University of Edinburgh.
- [30] Caussé, R., Kergomard, J., and Lurton, X. (1984). Input impedance of brass musical instruments – comparison between experiment and numerical models. *Journal of the Acoustical Society of America*, 75(1):241–254.
- [31] Chaigne, A. and Kergomard, J. (2008). *Acoustique des instruments de musique*. Belin.
- [32] Chen, J. M., Smith, J., and Wolfe, J. (2008). Experienced saxophonists learn to tune their vocal tracts. *Science*, 319(5864):776–776.
- [33] Chen, J.-M., Smith, J., and Wolfe, J. (2010). How players use their vocal tracts in advanced clarinet and saxophone performance. In *Proceedings of 20th International Symposium on Music Acoustics, Sydney and Katoomba*.
- [34] Corey, G. (1980). How to improve your tuning on the bassoon. *Journal of the International Double Reed Society*, 8.

- [35] Coyle, W., Kergomard, J., Guillemain, P., Vergez, C., and Guilloteau, A. (2013). An attempt at predicting the variation in playing frequencies for clarinets. In *Proceedings of the Stockholm Music Acoustics Conference 2013, SMAC 2013, Stockholm, Sweden*.
- [36] Craggs, A. (1989). The application of the transfer matrix and matrix condensation methods with finite elements to duct acoustics. *Journal of Sound and Vibration*, 132(3):393 – 402.
- [37] Cronin, R. H. and Keefe, D. H. (1996). Understanding the operation of auxiliary fingerings on conical double-reed instruments. In *Program of The 131st Meeting of the Acoustical Society of America*, volume 99, pages 2456–2457. ASA.
- [38] Cullen, J., Gilbert, J., and Campbell, D. (July/August 2000). Brass instruments: Linear stability analysis and experiments with an artificial mouth. *Acta Acustica united with Acustica*, 86:704–724(21).
- [39] da Silva, A. R., Scavone, G. P., and van Walstijn, M. (2007). Numerical simulations of fluid-structure interactions in single-reed mouthpieces. *Journal of the Acoustical Society of America*, 122(3):1798–1809.
- [40] Dalmont, J., Gilbert, J., and Ollivier, S. (2003). Nonlinear characteristics of single-reed instruments: quasistatic volume flow and reed opening measurements. *Journal of the Acoustical Society of America*, 114(4):2253–2262.
- [41] Dalmont, J.-P., Curtit, M., and Yahaya, A. F. (2012a). On the accuracy of bore reconstruction from input impedance measurements: Application to bassoon crook measurements. *The Journal of the Acoustical Society of America*, 131(1):708–714.
- [42] Dalmont, J.-P. and Frappé, C. (2007). Oscillation and extinction thresholds of the clarinet: Comparison of analytical results and experiments. *The Journal of the Acoustical Society of America*, 122(2):1173–1179.
- [43] Dalmont, J. P., Gazengel, B., Gilbert, J., and Kergomard, J. (1995). Some aspects of tuning and clean intonation in reed instruments. *Applied Acoustics*, 46(1):19 – 60. Musical Instrument Acoustics.
- [44] Dalmont, J.-P., Gilbert, J., and Kergomard, J. (July/August 2000). Reed instruments, from small to large amplitude periodic oscillations and the helmholtz motion analogy. *Acta Acustica united with Acustica*, 86:671–684(14).
- [45] Dalmont, J.-P., Guillemain, P., and Taillard, P.-A. (2012b). Influence of the reed flow on the intonation of the clarinet. In *Program of the 11th Congrès Français d’Acoustique and 2012 IOA annual meeting, Acoustics2012, Nantes*.
- [46] Dalmont, J.-P., Nederveen, C. J., Dubos, V., Ollivier, S., Vincent Meserette, V., and te Sligte, E. (July/August 2002). Experimental determination of the equivalent circuit of an open side hole: Linear and non linear behaviour. *Acta Acustica united with Acustica*, 88:567–575(9).
- [47] Dalmont, J.-P., Nederveen, C. J., and Joly, N. (2001). Radiation impedance of tubes with different flanges: Numerical and experimental investigations. *Journal of Sound and Vibration*, 244(3):505 – 534.
- [48] Dalmont, J.-P. and Roux, J. C. L. (2008). A new impedance sensor for wind instruments. *The Journal of the Acoustical Society of America*, 123(5):3014–3014.
- [49] Deverge, M., Pelorson, X., Vilain, C., Lagrée, P.-Y., Chentouf, F., Willems, J., and Hirschberg, A. (2003). Influence of collision on the flow through in-vitro rigid models of the vocal folds. *The Journal of the Acoustical Society of America*, 114(6):3354–3362.

- [50] Dickens, P., Smith, J., and Wolfe, J. (2007). Improved precision in measurements of acoustic impedance spectra using resonance-free calibration loads and controlled error distribution. *Journal of the Acoustical Society of America*, 121(3):1471–1481.
- [51] Durrieu, P., Hofmans, G., Ajello, G., Boot, R., Aurégan, Y., Hirschberg, A., and Peters, M. C. A. M. (2001). Quasisteady aero-acoustic response of orifices. *Journal of the Acoustical Society of America*, 110(4):1859–1872.
- [52] Elliott, S., Bowsher, J., and Watkinson, P. (1982). Input and transfer response of brass wind instruments. *The Journal of the Acoustical Society of America*, 72(6):1747–1760.
- [53] Ewell, T. and Hoyt, L. (1999). The bassoon-family fingering companion. <http://www.idrs.org/resources/BSNFING/BsnFingerings.pdf>, last viewed Februar 20th, 2012.
- [54] Fastl, H. and Zwicker, E. (2006). *Psychoacoustics - Facts and Models*. Springer.
- [55] Fellner, K. (2005). Transmission-Line Simulation meines Fagotts. Master's thesis, Institut für Angewandte und Numerische Mathematik eingereicht an der Technischen Universität Wien.
- [56] Ferrand, D. and Vergez, C. (2008). Blowing machine for wind musical instrument : toward a real-time control of the blowing pressure. In *Control and Automation, 2008 16th Mediterranean Conference on*, pages 1562 –1567.
- [57] Ferrand, D., Vergez, C., Fabre, B., and Blanc, F. (July/August 2010). High-precision regulation of a pressure controlled artificial mouth: The case of recorder-like musical instruments. *Acta Acustica united with Acustica*, 96:701–712(12).
- [58] Fletcher, N. H. (1978). Mode locking in nonlinearly excited inharmonic musical oscillators. *The Journal of the Acoustical Society of America*, 64(6):1566–1569.
- [59] Fletcher, N. H. and Rossing, T. D. (2005). *The Physics of Musical Instruments*. Springer.
- [60] Fletcher, N. H., Smith, J., Tarnopolsky, A. Z., and Wolfe, J. (2005). Acoustic impedance measurements—correction for probe geometry mismatch. *The Journal of the Acoustical Society of America*, 117(5):2889–2895.
- [61] Fletcher, N. H. and Thwaites, S. (1988). Obliquely truncated simple horns: Idealized models for vertebrate pinnae. *Acta Acustica united with Acustica*, 65(4):194–204.
- [62] Félix, S., Dalmont, J.-P., and Nederveen, C. J. (2012). Effects of bending portions of the air column on the acoustical resonances of a wind instrument. *The Journal of the Acoustical Society of America*, 131(5):4164–4172.
- [63] Fransson, F. (1966a). The source spectrum of double-reed woodwind instruments i. Technical report, Department for Speech, Music and Hearing, KTH, Stockholm, Sweden.
- [64] Fransson, F. (1966b). The source spectrum of double-reed woodwind instruments ii. Technical report, Department for Speech, Music and Hearing, KTH, Stockholm, Sweden.
- [65] Fréour, V., Caussé, R., and Buys, K. (2007). Mechanical behaviour of artificial lips. In *Proceedings of the International Symposium on Musical Acoustics, ISMA Barcelona 2007*.
- [66] Fricke, J. (1975). Formantbildende impulsfolgen bei blasinstrumenten. In *Fortschritte der Akustik, 13. Jahrestagung für Akustik (DAGA1975)*, Braunschweig.
- [67] Fuks, L. (1998). *From Air to Music - Acoustical, Physiological and Perceptual Aspects of Reed Wind Instruments Playing and Ventricular Fold Phonation*. PhD thesis, Kungl. Tekniska Högskolan.

- [68] Fuks, L. and Sundberg, J. (March/April 1999). Blowing pressures in bassoon, clarinet, oboe and saxophone. *Acta Acustica united with Acustica*, 85:267–277(11).
- [69] Gazengel, B. and Dalmont, J.-P. (2011). Mechanical response characterization of saxophone reeds. In *Proceedings of the Forum Acusticum 2011 - Aalborg - Denmark*.
- [70] Gazengel, B., Guimezanes, T., Dalmont, J. P., Doc, J. B., Fagart, S., and Leveille, Y. (2007). Experimental investigation of the influence of the mechanical characteristics of the lip on the vibrations of the single reed. In *Proceedings of the International Symposium on Musical Acoustics, ISMA, Barcelona*.
- [71] Gibiat, V. and Laloë, F. (1990). Acoustical impedance measurements by the two-microphone-three-calibration (tmte) method. *The Journal of the Acoustical Society of America*, 88(6):2533–2545.
- [72] Gilbert, J., Kergomard, J., and Ngoya, E. (1989). Calculation of the steady-state oscillations of a clarinet using the harmonic balance technique. *The Journal of the Acoustical Society of America*, 86(1):35–41.
- [73] Grey, J. M. and Gordon, J. W. (1978). Perceptual effects of spectral modifications on musical timbres. *The Journal of the Acoustical Society of America*, 63(5):1493–1500.
- [74] Grothe, T. (2012a). Das Bassoforte - ein Fagott für die Harmonie. *rohrblatt*, 27:83–87.
- [75] Grothe, T. (2012b). Investigation of bassoon embouchures with an artificial mouth. In *Program of the 11th Congrès Français d'Acoustique and 2012 IOA annual meeting, Acoustics2012, Nantes*.
- [76] Grothe, T. (2013). The bassoforte - a bassoon for wind bands. *Double Reed News-The magazine of the British Double Reed Society*, 103:8–12.
- [77] Grothe, T., Baumgart, J., and Grundmann, R. (2009). Effect of the structural dynamics of the bocal on the sound spectrum of a bassoon. In *Proceedings of the International Conference on Acoustics (NAG/DAGA 2009), Rotterdam; German Acoustical Society (DEGA)*.
- [78] Grothe, T., Baumgart, J., and Grundmann, R. (2010). Experimente zur Intonationsbestimmung beim Fagott. In *Fortschritte der Akustik, 36. Jahrestagung für Akustik (DAGA2010), Berlin*.
- [79] Grothe, T. and Kob, M. (2013). Investigation of bassoon directivity. In *Proceedings of the Stockholm Music Acoustics Conference 2013, SMAC 2013, Stockholm, Sweden*.
- [80] Grothe, T. and Wolf, P. (2013). A study of sound characteristics of a new bassoon as compared to a modern german bassoon. In *Proceedings of the Stockholm Music Acoustics Conference 2013, SMAC 2013, Stockholm, Sweden*.
- [81] Grundmann, R. (2005). S-Bogen für ein Holzblasinstrument, Deutsches Patent, DE10343437A1. neuartige S-Bogenkontur S27.
- [82] Grundmann, R. and Albrecht, T. (2003). Numerische Strömungsberechnung im S-Bogen des Fagotts (Computational fluid dynamics in the bassoon bocal). *Wissenschaftliche Zeitschrift der Technischen Universität Dresden*, 53(5-6).
- [83] Grundmann, R., Baumgart, J., Richter, A., and Krüger, H. (2005). Contribution of fluid dynamics to woodwind instruments investigations of timbre and pitch of bassoon bocals. *Journal of thermal science : JTS ; international journal of thermal and fluid sciences / Institute of Engineering Thermophysics, Chinese Academy of Sciences*, 14(3):264–266.

- [84] Guillemain, P., Vergez, C., Ferrand, D., and Farcy, A. (July/August 2010). An instrumented saxophone mouthpiece and its use to understand how an experienced musician plays. *Acta Acustica united with Acustica*, 96:622–634(13).
- [85] Heckel, W. (1899). *Der Fagott - Kurzgefasste Abhandlung über seine Entwicklung, seinen Bau und seine Spielweise*. Wilhelm Heckel Königlicher Hof-Instrumentenmacher, Biebrich am Rhein.
- [86] Hirschberg, A. (1995). *Mechanics of Musical Instruments*, chapter 7: Aero-Acoustics of Wind Instruments, pages 292–361. Springer Verlag Wien - New York.
- [87] Hirschberg, A. (2011). Personal communication.
- [88] Hirschberg, A. (2012). Personal communication.
- [89] Hirschberg, A., van de Laar, R., Marrou-Maurières, J., Wijnands, A., Dane, H., and Kruijswijk, S. (1990). A quasi-stationary model of air flow in the reed channel of single-reed woodwind instruments. *Acustica*, 70:146–154.
- [90] Hoekje, P. L. (1986). *Intercomponent exchange and upstream/downstream symmetry in nonlinear self-sustained oscillations of reed instruments*. PhD thesis, Case Western Reserve University, Cleveland, Ohio, USA.
- [91] Idelchik, I. (1960). *Handbook of Hydraulic Resistance*. Gosudarstvennoe Energeticheskoe Izdatke'stvo, Moskva-Leningrad.
- [92] Idogawa, T., Kobata, T., Komuro, K., and Iwaki, M. (1993). Nonlinear vibrations in the air column of a clarinet artificially blown. *Journal of the Acoustical Society of America*, 93(1):540–551.
- [93] Jang, S.-H. and Ih, J.-G. (1998). On the multiple microphone method for measuring in-duct acoustic properties in the presence of mean flow. *The Journal of the Acoustical Society of America*, 103(3):1520–1526.
- [94] Karkar, S., Vergez, C., and Cochelin, B. (2012). Oscillation threshold of a clarinet model: A numerical continuation approach. *The Journal of the Acoustical Society of America*, 131(1):698–707.
- [95] Kausel, W., Zietlow, D. W., and Moore, T. R. (2010). Influence of wall vibrations on the sound of brass wind instruments. *The Journal of the Acoustical Society of America*, 128(5):3161–3174.
- [96] Keefe, D. (1982a). Experiments on the single woodwind tone hole. *Journal of the Acoustical Society of America*, 72(3):688–699.
- [97] Keefe, D. (1982b). Theory of the single woodwind tone hole. *Journal of the Acoustical Society of America*, 72(3):676–687.
- [98] Keefe, D. H. (1983). Acoustic streaming, dimensional analysis of nonlinearities, and tone hole mutual interactions in woodwinds. *The Journal of the Acoustical Society of America*, 73(5):1804–1820.
- [99] Keefe, D. H. (1984). Acoustical wave propagation in cylindrical ducts: Transmission line parameter approximations for isothermal and nonisothermal boundary conditions. *The Journal of the Acoustical Society of America*, 75(1):58–62.
- [100] Keefe, D. H. (1989). Woodwind design algorithms to achieve desired tuning. *J. Catgut Acoust. Soc.*, 1:14–22.



- [101] Keefe, D. H. and Cronin, R. H. (1996). A linearized model of bassoon sound production: The role of auxiliary fingerings. In *Program of The 131st Meeting of the Acoustical Society of America*, volume 99, pages 2456–2457. ASA.
- [102] Kergomard, J. (1995). *Mechanics of Musical Instruments*, chapter 6: Elementary Considerations on Reed-Instrument Oscillations, pages 230–290. Springer Verlag Wien - New York.
- [103] Kinsler, L. E., Frey, A. R., Coppens, A. B., and Sanders, J. V. (2000). *Fundamentals of Acoustics*. John Wiley and Sons, Inc.
- [104] Kopp, J. (2006). The not quite harmonic overblowing of the bassoon. *The Double Reed*, 29(2):61–75.
- [105] Kopp, J. (2012). *The Bassoon*. Yale University Press.
- [106] Krüger, H. (2005). Konstruktion, Aufbau und experimentelle Verifizierung eines Fagottprüfstandes. Master’s thesis, Technische Universität Dresden.
- [107] Krüger, W. (1992). Untersuchungen am Fagott. Technical report, Institut für Musikinstrumentenbau, Zwota, Germany.
- [108] Kulik, Y. (2007). Transfer matrix of conical waveguides with any geometric parameters for increased precision in computer modeling. *The Journal of the Acoustical Society of America*, 122(5):EL179–EL184.
- [109] Le Vey, G. (2010). Optimal control theory: A method for the design of wind instruments. *Acta Acustica united with Acustica*, 96(4):722–732.
- [110] Lefebvre, A. (2010). *Computational Acoustic Methods for the Design of Woodwind Instruments*. PhD thesis, Mc Gill University, Montreal, Canada.
- [111] Lefebvre, A. and Scavone, G. (2010). Refinements to the model of a single woodwind instrument tonehole. In *Proceedings of the International Symposium on Music Acoustics, Sydney*.
- [112] Leppington, F. (1981). On the theory of woodwind finger holes. *Journal of Sound and Vibration*, 83:521–523.
- [113] Li, W., Chen, J.-M., Smith, J., and Wolfe, J. (2013). Vocal tract effects on the timbre of the saxophone. In *Proceedings of the Stockholm Music Acoustics Conference 2013, SMAC 2013, Stockholm, Sweden*.
- [114] Lighthill, J. (1978). *Waves in Fluids*. Cambridge Mathematical Library.
- [115] Lorenzoni, V. and Ragni, D. (2012). Experimental investigation of the flow inside a saxophone mouthpiece by particle image velocimetry. *The Journal of the Acoustical Society of America*, 131(1):715–721.
- [116] Macaluso, C. A. and Dalmont, J.-P. (2011). Trumpet with near-perfect harmonicity: Design and acoustic results. *The Journal of the Acoustical Society of America*, 129(1):404–414.
- [117] Mamou-Mani, A., Sharp, D. B., Meurisse, T., and Ring, W. (2012). Investigating the consistency of woodwind instrument manufacturing by comparing five nominally identical oboes. *The Journal of the Acoustical Society of America*, 131(1):728–736.
- [118] Mapes-Riordan, D. (1993). Horn modeling with conical and cylindrical transmission line elements. *Journal of the Audio Engineering Society*, 41:471–482.

- [119] Mayer, A. (2003). Riam (reed instrument artificial mouth) a computer controlled excitation device for reed instruments. In *Proceedings of the Stockholm Music Acoustic Conference*.
- [120] McGinnis, C. S. and Gallagher, C. (1941). The mode of vibration of a clarinet reed. *The Journal of the Acoustical Society of America*, 12(4):529–531.
- [121] Meyer, J. (2009). *Acoustics and the Performance of Music – Manual for Acousticians, Audio Engineers, Musicians, Architects and Musical Instruments Makers*. Springer.
- [122] Moers, E. and Kergomard, J. (2011). On the cutoff frequency of clarinet-like instruments - geometrical vs. acoustical regularity. arXiv:1101.4742v1.
- [123] MPEG (2012). MPEG-7: A suite of standards for description and search of audio, visual and multimedia content. <http://mpeg.chiariglione.org/standards/mpeg-7/mpeg-7.htm#E12E47>, last viewed April 22nd, 2012.
- [124] Munjal, M. L. (1987). *Acoustics of Ducts and Mufflers*. John Wiley and Sons, Inc.
- [125] Nederveen, C. J. (1998). *Acoustical Aspects of Woodwind Instruments*. Northern Illinois University Press.
- [126] Nederveen, C. J. (2009). Mode coupling in the sound generation in wind instruments. *NAG-DAGA 2009 Rotterdam*, pages 869–872.
- [127] Nederveen, C. J. and Dalmont, J.-P. (2007). Mode-locking effects in reed blown instruments. In *Proceedings of the International Symposium on Musical Acoustics, ISMA, Barcelona*.
- [128] Nederveen, C. J. and Dalmont, J.-P. (2008). Corrections to the plane-wave approximation in rapidly flaring horns. *Acta Acustica united with Acustica*, 94(3):461–473.
- [129] Nederveen, C. J. and Dalmont, J.-P. (2012). Mode locking effects on the playing frequency for fork fingerings on the clarinet. *The Journal of the Acoustical Society of America*, 131(1):689–697.
- [130] Nederveen, C. J., Jansen, J., and van Hassel, R. (1998). Corrections for woodwind tone-hole calculations. *Acta Acustica united with Acustica*, 84(5):957–966.
- [131] Newton, M. J., Campbell, M., and Gilbert, J. (2008). Mechanical response measurements of real and artificial brass players lips. *The Journal of the Acoustical Society of America*, 123(1):EL14–EL20.
- [132] Noreland, D., Kergomard, J., Laloë, F., Vergez, C., Guillemain, P., and Guilloteau, A. (2013). The logical clarinet: Numerical optimization of the geometry of woodwind instruments. *Acta Acustica united with Acustica*, 99(4):615–628.
- [133] Nurick, W. (2011). Flow characteristics and status of cfd hydrodynamic model development in sudden contraction manifold/ orifice configurations. Technical report, Nurick & Associates.
- [134] Oehler, M. (2007). *Die digitale Impulsformung als Werkzeug für die Analyse und Synthese von Blasinstrumentenklängen*. PhD thesis, Universität zu Köln.
- [135] Ohno, W. and Grothe, T. (2011). Analysis of uncertainty in input impedance measurements on woodwind instruments. In *Fortschritte der Akustik, 37. Jahrestagung für Akustik (DAGA2011)*, Duesseldorf.
- [136] Ollivier, S., Dalmont, J.-P., and Kergomard, J. (2004). Idealized models of reed woodwinds. part i: Analogy with the bowed string. *Acta Acustica united with Acustica*, 90(6):1192–1203.
- [137] Olson, H. F. (1940). *Elements of Acoustical Engineering*. D.Van Nostrand Company, Inc.

- [138] Ossman, T., Pichler, H., and Widholm, G. (1989). Bias: A computer-aided test system for brass wind instruments. In *Audio Engineering Society Convention 87*.
- [139] Peeters, G., Giordano, B. L., Susini, P., Misdariis, N., and McAdams, S. (2011). The timbre toolbox: Extracting audio descriptors from musical signals. *The Journal of the Acoustical Society of America*, 130(5):2902–2916.
- [140] Petiot, J.-F. and Tavard, F. (2008). Design and manufacturing of an artificial marine conch by bore optimisation. *The Journal of the Acoustical Society of America*, 123(5):3120–3120.
- [141] Pierce, A. D. (1989). *Acoustics*. The Acoustical Society of America.
- [142] Plitnik, G. and Strong, W. (1979). Numerical method for calculating input impedances of the oboe. *Journal of the Acoustical Society of America*, 65(3):816–825.
- [143] Poirson, E., Depince, P., and Petiot, J.-F. (2007). User-centered design by genetic algorithms: Application to brass musical instrument optimization. *Engineering Applications of Artificial Intelligence*, 20:511–518.
- [144] Raman, C. V. (1927). *Musical instruments and their tones*, chapter 8, pages 354–424. Handbuch der Physik. Springer.
- [145] Schubert, E. and Wolfe, J. (2006). Does timbral brightness scale with frequency and spectral centroid? *Acta Acustica united with Acustica*, 92(5):820–825.
- [146] Schubert, S. (2005). Experimentelle Bestimmung der Sekundärströmung und Wandschubspannung in einem optisch für die Messverfahren zugänglichen Musikinstrument, dem Fagott. Master’s thesis, Technische Universität Dresden.
- [147] Schumacher, R. (1981). Ab initio calculations of the oscillations of a clarinet. *Acustica*, 48(2):71–85.
- [148] Sharp, D. (1996). *Acoustic pulse reflectometry for the measurement of musical wind instruments*. PhD thesis, University of Edinburgh.
- [149] Sharp, D., Mamou-Mani, A., and van Walstijn, M. (2011). A single microphone capillary-based system for measuring the complex input impedance of musical wind instruments. *Acta Acustica united with Acustica*, 97(5):819–829.
- [150] Shimizu, M., Naoi, T., and Idogawa, T. (1989). Vibrations of the reed and the air column in the bassoon. *Journal of the Acoustical Society of Japan*, 10(5):269–278.
- [151] Silva, F. (2010). *Emergence des auto-oscillations dans un instrument de musique a anche simple*. PhD thesis, Universite de Provence - Aix - Marseille.
- [152] Silva, F., Guillemain, P., Kergomard, J., Vergez, C., and Debut, V. (2013). Some simulations of the effect of varying excitation parameters on the transients of reed instruments. hal-00779636.
- [153] Silva, F., Kergomard, J., Vergez, C., and Gilbert, J. (2008). Interaction of reed and acoustic resonator in clarinetlike systems. *The Journal of the Acoustical Society of America*, 124(5):3284–3295.
- [154] Smith, J., Rey, G., Dickens, P., Fletcher, N., Hollenberg, L., and Wolfe, J. (2007). Vocal tract resonances and the sound of the australian didjeridu (yidaki). iii. determinants of playing quality. *The Journal of the Acoustical Society of America*, 121(1):547–558.

- [155] Solis, J., Taniguchi, K., Ninomiya, T., Yamamoto, T., and Takanishi, A. (2009). Refining the flute sound production of the waseda flutist robot the mechanical design of the artificial organs involved during the flute playing. *Mechanism and Machine Theory*, 44(3):527 – 540. Special Issue on Bio-Inspired Mechanism Engineering.
- [156] Thompson, S. C. (1979). The effect of the reed resonance on woodwind tone production. *The Journal of the Acoustical Society of America*, 66(5):1299–1307.
- [157] van Walstijn, M. (2002). *Discrete-Time Modelling of Brass and Reed Woowind Instruments with Application to Musical Sound Synthesis*. PhD thesis, The University of Edinburgh.
- [158] van Walstijn, M. and Avanzini, F. (2007). Modelling the mechanical response of the reed-mouthpiece-lip system of a clarinet. part ii: A lumped model approximation. *Acta Acustica united with Acustica*, 93(3):435–446.
- [159] van Walstijn, M., Campbell, M., Kemp, J., and Sharp, D. (2005). Wideband measurement of the acoustic impedance of tubular objects. *Acta Acustica united with Acustica*, 91:590–604.
- [160] van Zon, J., Hirschberg, A., Gilbert, J., and Wijnands, A. P.J. (1990). Flow through the reed channel of a single reed music instrument. In *J. Phys. Colloques*, volume 51, pages C2–821–C2–824.
- [161] Vergez, C., Almeida, A., Caussé, R. E., and Rodet, X. (2003). Toward a simple physical model of double-reed musical instruments: influence of aero-dynamical losses in the embouchure on the coupling between the reed and the bore of the resonator. *Acta Acustica united with Acustica*, 89(6):964–973.
- [162] Voigt, W. (1975). *Untersuchungen zur Formantbildung in Klängen von Fagott und Dulzianen*. Gustav Bosse Verlag.
- [163] von Helmholtz, H. (1913). *Die Lehre von den Tonempfindungen als Physiologische Grundlage für die Theorie der Musik (On the Sensations of Tone as a Physiological Basis for the Theory of Music)*. Friedrich Vieweg & Sohn.
- [164] Weber, G. (1816). Versuch einer praktischen Akustik der Blasinstrumente (An attempt at functional wind instruments acoustics). *Allgemeine Musikalische Zeitung*, 18(3-6):33–44, 49–62, 65–74, 87–90.
- [165] Weber, G. (1825). Wesentliche Verbesserungen des Fagottes (Fundamental improvements to the bassoon). *Caecilia*, 2:123–140.
- [166] Weber, G. (1828). C. Almenräder’s weitere Fagott Verbesserungen (C.Almenrädgers further improvements to the bassoon). *Caecilia*, 9:128–130.
- [167] Weber, W. (1829a). Compensation von Orgelpfeifen (Pitch compensation of free-reed organ pipes). *Caecilia*, 43:181–202.
- [168] Weber, W. (1829b). Theorie der Zungenpfeifen. *Annalen der Physik und Chemie*, 17 (10):193–246.
- [169] Webster, J. C. (1947). An electrical method of measuring the intonation of cup-mouthpiece instruments. *The Journal of the Acoustical Society of America*, 19(5):902–906.
- [170] Werr, S. (2011). *Geschichte des Fagotts*. Wißner Verlag Augsburg.
- [171] Wikipedia (2013). Fagott — Wikipedia, the free encyclopedia. <http://de.wikipedia.org/wiki/Fagott>, last viewed September 22nd, 2013.

- [172] Wilson, T. A. and Beavers, G. S. (1974). Operating modes of the clarinet. *The Journal of the Acoustical Society of America*, 56(2):653–658.
- [173] Wogram, K. (1972). *Ein Beitrag zur Ermittlung der Stimmung von Blechblasinstrumenten*. PhD thesis, Technische Universität Carolo-Wilhelmina. SLUB Magazinb 1MB80 2585.
- [174] Wolf, G., Eppelsheim, B., Grothe, T., and Baumgart, J. (2013). Holzblasinstrument, Deutsches Patent DE102012006123A1.
- [175] Wolfe, J. (2012). Flute acoustics. <http://www.phys.unsw.edu.au/music/flute/>.
- [176] Wolfe, J. and Smith, J. (2003). Cutoff frequencies and cross fingerings in baroque, classical, and modern flutes. *The Journal of the Acoustical Society of America*, 114(4):2263–2272.
- [177] Wolfe, J., Smith, J., Tann, J., and Fletcher, N. H. (2001). Acoustic impedance spectra of classical and modern flutes. *Journal of Sound and Vibration*, 243(1):127 – 144.
- [178] Worman, W. (1971). *Self-Sustained Nonlinear Oscillations of Medium Amplitude in Clarinet-Like Systems*. PhD thesis, Case Western Reserve University.



# List of Figures

1.1	Corpus and bocal of a modern German bassoon. Picture taken from [171] . . . .	1
2.1	Schematic view of a conical woodwind instrument . . . . .	10
2.2	Schematic view of a conical duct element . . . . .	11
2.3	Schematic representation of a radiation boundary . . . . .	12
2.4	Schematic representation of a tone-hole in a woodwind instrument and its equivalent circuit. . . . .	13
2.5	Schematic representation of velocity profile and boundary layer in a conical duct	14
2.6	Deviation of fundamental frequency of the air column predicted by 4 plane-wave approximations. Conical waveguides with bassoon-like taper $z = 140$ and input radius $r = 2$ mm, and lengths $L$ within $100 \text{ mm} < L < 3000 \text{ mm}$ . . . . .	22
2.7	Sketch the adapter to connect a bassoon bocal to the BIAS measurement head. . .	24
2.8	Steps of the Calibration Procedure . . . . .	26
2.9	Deviation between measured and theoretical impedance extrema, from four cylindrical open tubes with radius $r = 2.1$ mm and varying length $l$ . . . . .	26
2.10	Temperature change at different positions in a bassoon bore after a temperature jump of the ambient temperature from 12 to 27 C° . . . . .	28
2.11	Influence of Temperature on the Input Impedance of Bassoons . . . . .	29
2.12	Dispersion of Input Impedance Peak Data (Frequency (-), Magnitude (x)) . . . .	30
2.13	Comparison of Input Impedance curves of 4 different Bassoons . . . . .	32
2.14	Comparison of numerical and experimental input impedance spectra of (a,b) a thin tube ( $r = 2.1$ mm, $l = 1002$ mm), (c,d) a straight bocal ( $r_1 = 2.1$ mm, $r_2 = 4.4$ mm $l = 328$ mm), (e,f) a bassoon with all holes closed (Bb <sub>1</sub> , $f_0 = 58$ Hz), (g,h) a bassoon with all holes open (F3, $f_0 = 175$ Hz), and (i,j) a bassoon with a fork fingering (F4, $f_0 = 353$ Hz). The impedance modulus is shown in the left column of graphs (a),(c),(d),(g),(i), the frequency deviation in Cent between the numerical and experimental impedance extrema is shown in the right column of graphs (b),(d),(f),(h),(j), for the respective cases. . . . .	33
2.15	Effect of the reed equivalent volume $V_{eq}$ . gray: measured input impedance at the bocal tip; black: measurement corrected by a reed equivalent volume. The vertical dashed lines mark the harmonic frequencies for Bb2, $f_0 = 117.3 \text{ Hz}$ .	36
2.16	Impedance map. The gray scale provides information about the magnitude of the impedance $ Z $ . . . . .	37
2.17	Harmonicity map. The vertical gray lines margin a frequency range of $\pm 100$ Cent left and right to each harmonic. The white dots mark the impedance peak frequencies and the grayscale provide information on the quality of the resonances. The dynamic range of the $ Z $ -axis is limited to 6 dB. . . . .	38
3.1	Terms used to describe double reeds . . . . .	41
3.2	Notation of variables and balance of forces on a mass segment of a reed blade . .	43
3.3	Schematic representation of the experimental setup of the artificial mouth (not to scale) . . . . .	49
3.4	Schematic representation of the reed admittance measurement (not to scale) . . .	50
3.5	Optional caption for list of figures . . . . .	54

3.6	Setup of the adjustable artificial lip module for Prototype II . . . . .	55
3.7	Front and side view of the lip module with possibility to adjust the lip position in 2 directions. Dimensions are in mm. . . . .	56
3.8	Assembling steps of the artificial lip. The air-balloon is subsequently filled with glycerin through tiny brass capillaries fitted in the PVC caps. . . . .	57
3.9	Bassoon artificial mouth setup . . . . .	59
4.1	Characteristic measures on a Bassoon Double-Reed . . . . .	62
4.2	Model parameters $w_A, h_A, sf$ for a Bassoon Double-Reed . . . . .	62
4.3	Geometrical Model of a Bassoon Reed Blade (measures taken from <i>Selmer Premium Plastic Medium 270M</i> ) . . . . .	63
4.4	Reed channel height and cross section profiles for several reed slit heights in the range $0.1 \text{ mm} < h < 1.6 \text{ mm}$ . . . . .	64
4.5	Reynolds number $Re$ and mean velocity $\bar{v} = \frac{q}{S}$ at three cross sections of the reed duct, as a function of the equivalent reed slit height $h_{eq}$ at the tip. The corresponding mouth pressure $p_m$ and reed pressure $p_r$ are given in the lower plot. . . . .	65
4.6	Sketch of the experimental setup . . . . .	66
4.7	Fit parameters for two writings of modified Bernoulli-equation describing the double-reed flow (Eqs. 4.15, 4.16). $\alpha = \frac{1}{C_{fu}^2} - \frac{S_{in}^2}{S_r^2}$ . . . . .	69
4.8	Relations between global fit parameter $\alpha$ , duct losses $\zeta$ and vena contracta-effect $C_c$ in double-reed flow. $\zeta = \alpha - 1 + \frac{2}{C_c} - \frac{1}{C_c^2}$ . Colors correspond to a variation of $C_c$ . . . . .	69
4.9	Volume flow through a double-reed channel as a function of pressure difference $\Delta p$ and inlet cross section $S_{in}$ . Comparison of measurement and model Eq. (4.15), with $\alpha = 1$ . Increasing (a) and decreasing (b) pressure regime. . . . .	70
4.10	Non-dimensionalized representation of the pressure-flow characteristics. The displayed measurement and model data correspond to Fig. 4.9 ( $p_{M,incr.} = 9.8 \text{ kPa}$ , $p_{M,decr.} = 8.9 \text{ kPa}$ , $S_{\infty,incr.} = 8 \text{ mm}^2$ , $S_{\infty,decr.} = 7.7 \text{ mm}^2$ ). . . . .	71
4.11	Schematic of the reed intake and characteristical measures of the reed-slit height. Three different deformation stadia: $h_0$ : $F_l = 0$ , $\Delta p = 0$ ; $h_\infty$ : $F_l > 0$ , $\Delta p = 0$ ; $h$ : $F_l > 0$ , $\Delta p > 0$ . . . . .	73
4.12	Hypothetical reed width $\bar{w} = \frac{3}{2} \frac{S_{in,meas}}{h_{meas}}$ versus measured reed slit height $h_{meas}$ . Data from 12 independent measurements . . . . .	74
4.13	Intake cross section $S_{in}$ of a bassoon double-reed, as a function of a measured pressure difference $\Delta p$ . Measurement and fit models Eq. (4.20a), with $S_\infty = 8.18 \text{ mm}^2$ , $p_M = 7.9 \text{ kPa}$ Eq. (4.20b), with $S_\infty = 8.40 \text{ mm}^2$ , $p_M = 6.6 \text{ kPa}$ and $C = 0.0336 \text{ (mm/kPa)}^2$ Eq. (4.20c), with $S_\infty = 8.44 \text{ mm}^2$ , $p_M = 9.5 \text{ kPa}$ and $\kappa = 1.47$ . . . . .	75
4.14	Impact of the model parameters $\alpha$ , $\kappa$ and $\epsilon$ on the non-dimensional pressure-flow characteristics according to a general model for the reed-flow Eq. (4.25). The classical single-reed flow curve corresponds to $\alpha = \kappa = 1$ and $\epsilon = 0$ (dashed line) . . . . .	77
4.15	Experimental data and fitted models for the intake cross section $S_{in}$ . Model parameters obtained by least-squares fitting are $S_\infty = 6.90 \text{ mm}^2$ , $p_M = 8.66 \text{ kPa}$ and $\kappa = 1.48$ . The points $S_{in,meas}$ are measured values (crosses), vertical lines show the uncertainty in $S_{in}$ (25 <sup>th</sup> and 75 <sup>th</sup> percentiles). $S_{in,model}(\Delta p)$ is calculated with identified model parameters for the range $0 < \Delta p < 10.8 \text{ kPa}$ (green solid line). Data from the increasing pressure regime. . . . .	79



4.16	Experimental data and fitted models for the flow-rate $q$ . The points $q_{meas}$ are measured values (crosses), vertical lines show the measurement uncertainty of the flow-meter. The model parameter obtained by least-squares fitting is $\alpha = 1.016$ . $q_{model}(S_{in}, \Delta p)$ is calculated with measured values for $S_{in}$ and $\Delta p$ (crosses), vertical lines show propagated uncertainty in $q$ due the uncertainty in $S_{in}$ . $q_{model}(\Delta p)$ is calculated with the model parameters $S_{\infty} = 6.90 \text{ mm}^2$ , $p_M = 8.66 \text{ kPa}$ , $\kappa = 1.48$ , $\alpha = 1.016$ for the range $0 < \Delta p < 10.8 \text{ kPa}$ (green solid line). Data from the increasing pressure regime. . . . .	79
4.17	Optional caption for list of figures . . . . .	80
4.18	Schematic representation of lip forces in a double-reed embouchure (longitudinal section) . . . . .	82
4.19	Effect of a static lip-force $F_{l,\infty}$ exerted to the reed in 5 different axial positions $x_l$ (measured from the reed-tip) . . . . .	83
4.20	Fitted model parameters $S_{\infty}$ , $p_M$ , $\alpha$ and $\kappa$ versus the initial reed-slit height $h_{\infty}$ . Experiments were performed with an axially and vertically adjustable artificial lip. Markers depict the axial lip positions $x_l$ with respect to the reed tip, vertical positions correspond to the initial slit height $h_{\infty}$ . . . . .	84
4.21	Lip force change $\Delta F_l$ due to the pressure induced reed blade deflection, for several embouchure configurations. Markers correspond to the lip position $x_l$ , colors correspond to the initial slit height $h_{\infty}$ . . . . .	86
4.22	Quasi stationary flow $q$ through a bassoon double-reed as a function of differential pressure $\Delta p$ and lip force $F_{lip}$ for several initial slit heights $h_{\infty}$ . Lip position $x_l = 10.75 \text{ mm}$ . Only the decreasing branch of the characteristics is shown. . . .	88
4.23	Residual flow $q_{res}$ as a function of mouth pressure. For the data shown here, the reed is assumed to be closed, i.e the image analysis algorithm failed to detect an intake area from the reeds front view. . . . .	89
4.24	Deviation of empirical flow model and experimental data. The model is given by Eqs.(4.28),(4.31a),(4.31b) with Eq. (4.29) and tables 4.1, 4.2. Normalized residuals are plotted versus the normalized differential pressure $\tilde{p} = \Delta p/p_M$ . The dashed horizontal lines mark a 5% deviation, the vertical dashed line marks the saturation pressure $\tilde{p}_{m,sat}$ . . . . .	91
5.1	Sketch of the experimental setup. Measured quantities in boxes ( $p_m$ , $p_r$ , $F_l$ , $q$ , $p_s$ ) are recorded instantaneously during the experiment. . . . .	96
5.2	Reed pressure (solid) and the corresponding simplified Helmholtz-pattern (dashed), and integral mean reed pressure $\bar{p}_r > 0$ , for the note B2 ( $f_0 = 116 \text{ Hz}$ ). . . . .	98
5.3	Optional caption for list of figures . . . . .	99
5.4	Deviation between the measured mean flow-rate $q_{meas}$ and the flow rate predicted by the quasi-static model. (a) before and (b) after correction for effects of the pressure efficiency and the non-dimensional lip force, by linear regression. . . .	101
5.5	Correlation of the residuals of the flow-model on (a) pressure efficiency $p_m/p_{r,RMS}$ and (b) on the non-dimensional lip-force $F_l/(p_m w^2)$ . . . . .	102
5.6	Deviation between the measured slit height $h_{o,meas}$ and the slit height predicted by the quasi-static model $h_{o,model}$ . (a) absolute, (b) relative, plotted vs. the RMS-value of the reed pressure $p_{r,RMS}$ . The dashed horizontal lines mark the 5% deviation. .	103
5.7	Lip force $F_{l,initial}$ vs. mouth pressure change $\Delta p$ . . . . .	104
5.8	Gradient ( $dF_l/d\Delta p$ ) for several embouchure configurations characterized by the initial lip force $F_{l,initial}$ . . . . .	105
5.9	Input parameters $p_m$ and $F_l$ . . . . .	106
5.10	Reed Model Input Parameters $\gamma = \frac{p_m}{p_M}$ and $\zeta = Z_c \frac{q_A}{p_M}$ . . . . .	107
5.11	Reed stiffness $K_s$ according to the quasi-static reed model. . . . .	108
5.12	Output parameters $p_{r,RMS}$ and $q$ . . . . .	109

5.13	Dependence of the dynamic level, characterized by the RMS mouthpiece pressure $p_{r,RMS}$ , on the mouth pressure $p_m$ and the time-averaged volume-flow rate $q$ . Each dot is one working point of the reed, represented by one second of a sustained bassoon tone played with the artificial mouth. The color indicates the sounding frequency $f_0$ , according to the colorbar to the right of the plot. . . . .	110
5.14	Dynamic levels of the radiated sound in sound pressure level $SPL$ and loudness $N$ . . . . .	111
5.15	Spectral metrics of the bassoon sound. . . . .	112
5.16	Spectral metrics of the bassoon sound . . . . .	113
5.17	Comparison of harmonic pressure spectra inside the mouthpiece (a) and in the radiated pressure spectra (b) of a modern German bassoon. The curved black lines indicate the formant center frequencies. The color indicates the relative spectral pressure magnitudes in dB according to the colorbar left to the plots. The dB reference of each note is the strongest partial, marked with a white cross; the dynamic range is limited to -24. . . 0 dB. Each of the notes were blown with an artificial mouth at a moderate dynamic level, $p_m \approx 0.5 (p_{m,max} + p_{m,min})$ . . . . .	113
5.18	Analysis of the duration $\tau_c$ of the closed episode in one cycle of the reed tip oscillation	114
5.19	Analysis of average reed pressures during the open ( $p_o$ ) and closed ( $p_c$ ) episode of one cycle of the reed tip oscillation. The straight black line indicates the minimum peak pressure $p_{c,min}$ during the one period (mean value of five bassoons). The black errorbars on this curve indicate the spread of $p_{c,min}$ observed on the five bassoons (standard deviation). . . . .	115
5.20	Independence of the pressure waveform on the dynamic level. (a) Measured reed pressure signals $p_r(t)$ during one oscillation cycle, normalized in pressure by the RMS-value $p_{r,RMS}(\tau)$ , and in time by the periodic time $\tau$ . The plot shows in 4 octaves the case of the note D at two dynamic pressure levels (gray: <i>piano</i> , black: <i>forte</i> ). (b) Ratio of open-close episode duration $\frac{\tau_o}{\tau_c}$ versus the integral mean reed pressure ratio $\frac{ p_c }{p_o}$ . The slope of the dashed gray line is $0.84 \pm 0.0027$ . . . . .	116
5.21	Influence of the impulse duration $\tau_c$ on the reed pressure spectral centroid (a) relative open-close duration $\tau_o/\tau_c$ versus normalized spectral centroid $hsc_r/f_0$ of the mouthpiece pressure. (b) impulse duration $\tau_c$ versus spectral centroid $hsc_r$ . The dashed black line has a slope of 1.81. . . . .	117
5.22	Relation between the mouthpiece pressure waveform ( $ p_c/p_o $ ) and the number of supporting resonator modes ( $n_{modes}$ ). The pressure waveform $p_r(t)$ resembles a two step open-close function with the integral mean values $p_o$ and $p_c$ during the opening ( $p_r(t) > 0$ ) and closing ( $p_r(t) < 0$ ) episode, respectively. . . . .	118
5.23	Blowing characteristics of a modern German bassoon. Dependence of the response variable $p_{r,RMS}$ on the controlled variables (a) $p_m$ and (b) $\log_{10} \tilde{F}_l$ (Eq.5.4) characterizing the embouchure. Each of the small dots marks one operation point, the large dots mark the centroids of several realizations of each note, with different dynamic levels, on all five bassoons under test ( <i>bsn1 to bsn5</i> ). The data are covering the full dynamical and tonal range, and stem from artificial mouth experiments ( $N_{total} = 3326$ ). The color indicates the sounding frequency, according to the colorbar to the right of the plots. The black dotted classification line has a slope of unity (a) and -3.27 kPa/decade (b). . . . .	121

- 5.24 (a) Grouping of operating regimes of a bassoon double-reed into four regions. Each of the small dots marks one operation point, the large dots mark the centroids of each note. The data are covering the full dynamical and tonal range, and stem from artificial mouth experiments on 5 German bassoons ( $n = 3326$ ). The colors indicate the fundamental frequency according to the colorbar to the right of the plot.  
 (b) Mean centered and rescaled map showing only the centroids of operating regimes for each note, and their grouping ( $\blacksquare, \blacklozenge, \blacktriangle, \blacktriangledown$ ). The first dimension is the pressure efficiency  $p_{r,RMS}/p_m$  (horizontal axis), the second dimension  $\Delta p_{r,RMS}/\log_{10} \tilde{F}_l$  (vertical axis) is related to the embouchure tightness. . . . . 122
- 5.25 Grouping of notes according to their embouchure characteristics. For each note, the ratio  $n_{note,i}/n_{note}$  is shown, where  $n_{note,i}$  is the number of operating points classified into the  $i^{th}$  group ( $i = 1, 2, 3, 4$ :  $\blacksquare, \blacklozenge, \blacktriangle, \blacktriangledown$ ), and  $n_{note}$  is the total number of operating points on that note. For each note, only the marker of the dominating group ( $n_i/n > 0.5$ ) is plotted. The data are covering the full dynamical range and stem from artificial mouth experiments on German 5 bassoons.  
 Markers  $\circ$  correspond to the median of regime margins as perceived by musician (according to a survey among 8 professional bassoonists).  
 The vertical straight black lines indicate the acoustical register margins. . . . . 123
- 5.26 Range of input parameters for bassoon playing to achieve clean tuning at small and large dynamic level (*piano* and *forte*). (a) measured values of lip force  $F_l$  and blowing pressure  $p_m$ ; (b) corresponding model parameters  $\gamma = p_m/p_M$  and  $\zeta = Z_c q_A/p_M$  of an elementary clarinet reed model [102].  
 Data from artificial mouth experiments on on bassoon (*bsn4*) with the same synthetic double-reed. Markers  $\circ, \bullet$  correspond to the low and high reference level, respectively. Horizontal gray bars mark the maximum and minimum values on this bassoons. Markers  $\square, \blacksquare$  on the vertical axis indicate those notes that could not be sounded in tune at the low and high reference level, respectively. . . . . 124
- 5.27 Input parameters for bassoon playing to achieve clean tuning at the softest dynamic playing level (*pianissimo*).  
 a) lip force  $F_{l,max}$  and  
 b) blowing pressure  $p_{m,min}$ .  
 Data from artificial mouth experiments on five bassoons with the same synthetic double-reed. Markers are the median, vertical gray bars mark the maximum and minimum values from the five bassoons. . . . . 125
- 5.28 Tuning discrepancy  $I_{musician}$  as perceived by one musician (black dots with gray errorbars). The markers ( $\Delta, \nabla$ ) denote the tuning tendency (sharp, flat) of “some critical notes regarding special attendance”[34]. . . . . 126
- 5.29 Correlation between lip force  $F_{l,max}$  in artificial mouth blowing experiments and the tuning discrepancy  $I_{musician}$  as perceived by a musician. In the artificial mouth experiment the tuning was held constant and the adjusted lip force  $F_l$  was measured; in musician experiment, the embouchure was held constant by the musician and the resulting tuning  $I_{musician}$  was measured.  
 Each of the 41 markers corresponds to a note within the chromatic playing range from B $\flat$ 1 to D5, the color indicates the sounding frequency  $f_0$  according to the colorbar on the left. Vertical errorbars mark the 25<sup>th</sup> and 75<sup>th</sup> percentiles of 18 measurements (full permutation of 3 bassoons, 3 bocals and 2 cane-reeds). Horizontal errorbars mark the maximum and minimum values from measurements on five bassoon-bocal combinations. Dashed lines correspond to the 95% confidence interval of the fit coefficients. . . . . 127

- 5.30 Change of sound color related parameters with a change in the embouchure. Output data of the radiated sound are plotted versus input data of the artificial mouth. Input data  $p_m$ : mouth pressure,  $F_l$ : lip force,  $p_{r,RMS}$ : root-mean-square reed pressure,  $F_l/(q\rho hf_0)$ : non-dimensional lip force; Output data:  $hsc$ : harmonic spectral centroid,  $hss$ : harmonic spectral spread,  $\mathcal{F}1, \mathcal{F}2, \mathcal{F}3$ : center frequencies of first, second and third formant, respectively. For each note, measurement values have been standardized ( $z(X) = \frac{X-\mu}{\sigma}$ ). The data shown covers the tonal and dynamical range of five different bassoons. The total number of experimental runs was  $n = 3226$ . . . . . 128
- 5.31 Tuning discrepancy estimate from harmonicity considerations. Dots mark  $I_n$ , the intervals in Cent between supporting air-column modes  $n$  and the harmonic series  $n f_{0,nom}$ , the shading decreases with the ordinal number  $n$ . The marker size corresponds to the magnitude of  $|Z|$ . The black line  $I_{av}$  is the  $|Z|$ - weighted average of  $I_n$ . . . . . 130
- 5.32 Comparison of tuning estimates from a blowing test and from the harmonicity analysis. Black dots with gray errorbars mark the intonation discrepancy  $I_{musician}$  if the instrument is played by a musician advised not to use embouchure corrections. Squares mark the  $|Z|$ - weighted average  $I_{av}$  in Cent from the harmonicity analysis of measured impedance curves; the errorbars indicate the spread of measurements on  $I_{av}$  over five bassoons. The markers ( $\Delta$ ,  $\nabla$ ) denote the tuning tendency (sharp, flat) reported in bassoonist literature [34]. . . . . 131
- 5.33 Influence of the reed equivalent volume  $V_{eq}$  on the correlation between the perceived tuning  $I_{musician}$  and the intonation tendency estimate  $I_{av}$ .  
a) Residual sum of squares as a function of the reed equivalent volume  $V_{eq}$  for five different bassoons.  
b) Measurements and regression model  $I_{musician} = a_0 + a_1 I_{av}(V_{eq})$ , for  $V_{eq} = 2.3 V_{reed}$  ( $a_0 = -5.8$  Cent,  $a_1 = 0.42 \pm 0.18$ ,  $R^2 = 0.37$ ). Each of the 41 markers corresponds to the median of measurements of one note within the chromatic playing range from Bb1 to D5, the color indicates the sounding frequency  $f_0$ , according to the colorbar at the right of the plot. Vertical errorbars mark the 25<sup>th</sup> and 75<sup>th</sup> percentiles of 18 measurements of  $I_{musician}$  (full permutation of 3 bassoons, 3 bocals and 2 cane-reeds). Horizontal errorbars mark the maximum and minimum values of  $I_{av}$  deduced from impedance measurements on five bassoon-bocal combinations. . . . . 132
- 5.34 Influence of  $V_{eq}$  on a regression model  $F_{l,max} = a_0 + a_1 I_{av}(V_{eq})$ , for five different bassoons. . . . . 133
- 5.35 Applied lip force  $F_{l,max}$  to achieve pure tuning in artificial mouth experiments on 5 bassoons with one synthetic double-reed as compared to the  $|Z|$ - weighted average tuning interval  $I_{av}$  of impedance peaks. Each of the 41 markers corresponds to the median of measurements on one note within the chromatic playing range from Bb1 to D5. The color indicates the sounding frequency  $f_0$ , according to the colorbar to the right of the plot. Vertical and horizontal errorbars mark the maximum and minimum values from measurements on the same five bassoon-bocal combinations. Dashed lines correspond to the 95% confidence interval of the fit coefficients. In the calculation of  $I_{av}$ , the reed equivalent volume was assumed to be  $V_{eq} = 2.3 V_{reed} = 2.2\text{cm}^3$  for all bassoons. . . . . 134

- 5.36 Harmonicity map of the modern German Bassoon. Contourplot of impedance curves, rescaled in frequency and magnitude to show a range of  $\pm 100$  Cent around each harmonic in frequency and -6 dB smaller than  $10 \times 10^6$  Pa s/m<sup>3</sup> in magnitude, respectively.  
 Markers ■,◆,▲,▼ on the left vertical axis mark the grouping of notes according to the analysis in section 5.3.1.  
 White circles mark the strongest partial of each fingering. . . . . 135
- 5.37 Comparison of acoustic properties of the resonator and sound characteristics of a modern German bassoon. Measurements of acoustic impedance spectra corrected for mouthpiece volume (a), and pressure spectra inside the mouthpiece (c) and in the ambience (b), for standard fingerings played at a medium dynamic level (mouth pressure  $p_m \approx 1/2(p_{m,max} + p_{m,min})$ ). The color indicates the relative impedance magnitude (a) or relative spectral intensity (b,c) according to the colorscale left to the plots. For each note, the maxima are marked with a white cross. For all three plots, the dynamic range is limited to 0..-6 dB  
 Markers ■,◆,▲,▼ on the left vertical axis mark the grouping of notes according to the analysis in section 5.3.1.  
 Solid curved lines are iso-frequency lines indicating the first three formants in the bassoon sound. Solid horizontal lines indicate the register limits of the resonator [104]. black . . . . . 136
- 1 Flow-rate  $q$  through a loss-free reed channel neglecting the *vena contracta* effect (dashed: tube, solid: diffuser), according to Eq.(4.15) for typical measurement values of  $\Delta p_{meas}$ ,  $p_M$ ,  $S_\infty$ , and  $S_r$  . . . . . 172
- 2 Optional caption for list of figures . . . . . 173
- 3 Optional caption for list of figures . . . . . 174



# List of Tables

3.1	An elementary physical model for the double-reed (“Raman-Model” [102]) Model parameters $h_\infty = 1$ mm, $w = 14$ mm, $p_M = 9.5$ kPa, $f_r = 1300$ Hz, $Q_r = 3$ .	48
3.2	Parameter estimation for the “Raman-Model” [102] on the basis of measurements on the double-reed . . . . .	51
4.1	Regression coefficients for $q_A$ ; Eq. (4.31a) . . . . .	90
4.2	Regression coefficients for $p_M$ ; Eq. (4.31b) . . . . .	90
4.3	Regression coefficients for $h_\infty$ ; Eq. (4.33a) . . . . .	92
4.4	Regression coefficients for $p_{M,h}$ ; Eq. (4.33b) . . . . .	92
5.1	Overview on typical values of input and output parameters in artificial mouth blowing experiments on a modern German bassoon. The values are given as a range $(\cdot)_{min} \dots (\cdot)_{max}$ or as a mean value $(\bar{\cdot}) \pm \sigma$ , where $\sigma$ is the standard deviation. The right column gives references to figures with plots of the respective properties.	119





# Appendix

## A1: Remarks on Modeling Wall Losses in a Conical Waveguide

The inclusion of losses by means of an effective wavenumber deserves some discussion.

It is not obvious, that the approach of modifying the wave-number in the solution of the wave-equation is correct for the case of the conical duct with varying cross section. Though this is straightforward for the cylindrical duct segment, for the case of the cone it is not, due to the occurrence of a loss-dependent pressure gradient in propagation direction.

Instead of modifying the wavenumber in the solution of the ideal case, it appears to be more elaborate to include loss terms in the wave-equation, and derive solutions to satisfy this modified equation. This path has been followed by Nederveen, who scaled flow and pressure in the equation of motion and continuity by means of loss coefficients [125]. The result is a modified Webster-equation, extended by loss terms. From solving this, an explicit formula for the input impedance of the conical waveguide is obtained, based on several assumptions.

In two steps this approach will be outlined, with the notation introduced here, to make it comparable. First, Nederveens formula for the loss-free cone is rearranged to match the transmission-line formalism. The rearrangement shows, that both approaches are mathematically identical.

Second, Nederveens formula for the lossy cone, which he derived from extending the Webster-equation by loss-terms, is rearranged. Written in the same notation, the simple loss-modeling by the effective, complex wavenumber can be compared to Nederveens more elaborate approach, and discrepancies will be discussed. Numerical examples are given for several configurations.

### Loss-free Cone

Derived from the Webster Horn equation, Nederveen [128] gives a formulation for the admittance  $Y = 1/Z$  of a cross section within a conical duct with apical distance  $x$ , for the loss-free case. In the notation used in the present work  $((\cdot)_{a,b} = (\cdot)_{1,2}; R = x; L_{ba} = L)$ , this formulation<sup>1</sup> can be written

$$Y = \frac{1}{jZ_c} \left[ \frac{1}{kx} - \frac{1}{\tan(kx + \Psi)} \right] \quad (1)$$

The impedance  $Z_1$  at the input cross section  $(\cdot)_1$  of a conical duct segment with input and output radii  $r_{1,2}$  at apical distances  $x_{1,2}$  and length  $L = x_2 - x_1$  (see Fig. 2.2) is found from relating Eq.(1) at input and output. With some calculus [128] it can be written for the input impedance

$$Z_1 = \left( \frac{1}{jZ_{c1}} \left[ \frac{1}{kx_1} - \frac{\left( \frac{1}{kx_2} - j\frac{Z_{c2}}{Z_2} \right) + \tan(kL)}{1 - \left( \frac{1}{kx_2} - j\frac{Z_{c2}}{Z_2} \right) \tan(kL)} \right] \right)^{-1}, \quad (2)$$

where  $Z_2$  is the load impedance at the output end of the cone ( $1/Y_b$  in Nederveens nomenclature). With the substitution

$$a = \left( \frac{1}{kx_2} - j\frac{Z_{c2}}{Z_2} \right) \quad (3)$$

---

<sup>1</sup>(Eq.(8) in [128])

this becomes

$$Z_1 = j Z_{c1} \frac{1 - a \tan(kL)}{\frac{1}{k x_1} - \frac{a}{k x_1} \tan(kL) - a - \tan(kL)} = \frac{\cos(kL) - a \sin(kL)}{\frac{1}{k x_1} \cos(kL) - \frac{a}{k x_1} \sin(kL) - a \cos(kL) - \sin(kL)}. \quad (4)$$

Inserting Eq.(3), the numerator  $\mathcal{N}$  of  $Z_1 = \mathcal{N}/\mathcal{D}$  becomes

$$\mathcal{N} = \frac{1}{Z_2} \left( Z_2 \cos(kL) - Z_2 \frac{1}{k x_2} \sin(kL) + j Z_{c2} \sin(kL) \right). \quad (5)$$

Inserting Eq.(3), the denominator  $\mathcal{D}$  of  $Z_1 = \mathcal{N}/\mathcal{D}$  becomes

$$\mathcal{D} = \frac{k x_2 - k x_1}{k x_1 k x_2} \cos(kL) - \frac{1}{k x_1 k x_2} \sin(kL) + j \frac{Z_{c2}}{Z_2} \left( \cos(kL) + \frac{1}{k x_1} \sin(kL) \right) - \sin(kL), \quad (6)$$

which can be further rearranged, with  $L = x_2 - x_1$

$$\mathcal{D} = -\frac{1}{j Z_2} \left( j Z_2 \sin(kL) + j Z_2 \frac{1}{k x_2} \left( \frac{1}{k x_1} \sin(kL) - \frac{L}{x_1} \cos(kL) \right) + Z_{c2} \left( \cos(kL) + \frac{1}{k x_1} \sin(kL) \right) \right). \quad (7)$$

Using  $x_2/r_2 = x_1/r_1$  and  $Z_{c2}/Z_{c1} = r_1^2/r_2^2$  for some further rearrangement in  $\mathcal{N}$  and  $\mathcal{D}$ , the input impedance of the cone can be written

$$Z_1 = \frac{Z_2 \left( \frac{r_2}{r_1} \cos(kL) - \frac{1}{k x_1} \sin(kL) \right) + j Z_{c1} \frac{r_1}{r_2} \sin(kL)}{Z_2 \frac{1}{Z_{c1}} \left[ \frac{r_2}{r_1} j \sin(kL) + j \frac{1}{k x_1} \left( \frac{1}{k x_1} \sin(kL) - \frac{L}{x_1} \cos(kL) \right) \right] + \frac{r_1}{r_2} \left[ \cos(kL) + \frac{1}{k x_1} \sin(kL) \right]}, \quad (8)$$

which has the form

$$Z_1 = \frac{Z_2 A + B}{Z_2 C + D} \quad (9)$$

where

$$\begin{aligned} A &= \frac{r_2}{r_1} \cos(kL) - \frac{1}{k x_1} \sin(kL) \\ B &= Z_{c1} \frac{r_1}{r_2} j \sin(kL) \\ C &= \frac{1}{Z_{c1}} \left[ \frac{r_2}{r_1} j \sin(kL) + j \frac{1}{k x_1} \left( \frac{1}{k x_1} \sin(kL) - \frac{L}{x_1} \cos(kL) \right) \right] \\ D &= \frac{r_1}{r_2} \left[ \cos(kL) + \frac{1}{k x_1} \sin(kL) \right]. \end{aligned} \quad (10)$$

This is identical with the transmission matrix coefficients that Benade gave to describe the transmission characteristics of an “equivalent circuit for conical waveguides” [19].

Although Benades approach and his equations are sometimes regarded as an approximate solution [59], they are in fact mathematically identical with the analytic solution Eq.(2.21) given by Fletcher [61], as will be shown here: By use of the identities

$$\begin{aligned} \frac{r_1}{r_2} &= \frac{x_1}{x_2} \\ x_2 - x_1 &= L \\ \frac{Z_{c2}}{Z_{c1}} &= \left( \frac{r_1}{r_2} \right)^2 \\ \sin(\arctan(kx)) &= \frac{kx}{\sqrt{1+(kx)^2}} \\ \cos(\arctan(kx)) &= \frac{1}{\sqrt{1+(kx)^2}}, \end{aligned} \quad (11)$$

the cosine-terms in Eq.(2.21)

$$\cos\left(kL - \left(\theta - \frac{\pi}{2}\right)\right) = -\sin(kL) \cos(\theta) + \sin(\theta) \cos(kL) \quad (12)$$

can be written

$$-\sin(kL) \frac{1}{\sqrt{1+(kx)^2}} + \frac{kx}{\sqrt{1+(kx)^2}} \cos(kL). \quad (13)$$

Thus, denoting the transmission coefficients in Fletchers Eq.(2.21) and Benades Eq.(10) with  $(\cdot)_F$  and  $(\cdot)_B$ , respectively, it follows:

$$\begin{aligned} A_F &= \frac{r_2}{r_1} \left( -\sin(kL) \frac{1}{\sqrt{1+(kx_2)^2}} + \frac{kx_2}{\sqrt{1+(kx_2)^2}} \cos(kL) \right) \frac{\sqrt{1+(kx_2)^2}}{kx_2} \\ &= \frac{r_2}{r_1} \left( \cos(kL) - \frac{1}{kx_2} \sin(kL) \right) \\ &= \frac{r_2}{r_1} \cos(kL) - \frac{1}{kx_1} \sin(kL) = A_B \end{aligned} \quad (14)$$

In analogy to this rearrangement, it can be shown that  $B_F = B_B$ ,  $C_F = C_B$  and  $D_F = D_B$ .

The conclusion of this rearrangement is, that three well-known formulations for the input impedance of the cone provided by Nederveen Eq.(2), Benade Eq.(10) and Fletcher Eq.(10) are identical. All three are different writings for the analytic solution to the Webster-equation for the sound propagation in a conical horn, which is probably not obvious at first glance.

### Lossy Cone

To include losses into his formulation for the wave propagation, Nederveen [125] modified the Webster-equation to introduce two dimensionless loss parameters  $\epsilon_v$  and  $\beta$ , which can be written in the nomenclature used in the present work as

$$\begin{aligned} \epsilon_v &= \frac{1}{1 + \left( \frac{\gamma-1}{\sqrt{Pr}} \right)}, \\ \beta &= (1-j) k x \frac{1}{2} \sqrt{2} \frac{\delta_v}{r} \left( 1 + \frac{\gamma-1}{\sqrt{Pr}} \right), \\ &= (1-j) k x \frac{1}{2} \sqrt{2} \frac{\delta_v}{r} \frac{1}{\epsilon_v}, \\ &= (1-j) k x \frac{\alpha'}{r}, \end{aligned} \quad (15)$$

where  $\delta_v$ ,  $\gamma$ ,  $Pr$ ,  $\alpha'$  have been introduced above.

The solution for the admittance, that Nederveen derived from the modifying the Webster-equation to add additional loss terms in  $\beta$  and  $\epsilon_v$  can be written

$$Y = \frac{1}{jZ_c} \left[ \frac{1 - \tilde{\alpha}_g}{kx} - \frac{1 + \tilde{\alpha}_f}{\tan(kx + \Psi + \tilde{\alpha}\xi)} \right] \quad (16)$$

for a cross section with apical distance  $x$  in conical duct. Here,  $\tilde{\alpha}$  are frequency and position dependent loss terms given by

$$\begin{aligned} \tilde{\alpha}(r) &= kx \frac{\alpha'}{r} \\ \tilde{\alpha}_f(r, x) &= kx \frac{\alpha'_f}{r} (1-j), \\ \tilde{\alpha}_g(r, x) &= (kx)^2 \frac{\alpha'_g}{r} (1-j) \\ \text{and} \\ \xi &= \ln(kx) + g. \end{aligned} \quad (17)$$

There are three loss parameters  $\alpha'$  which analogously to Eq.(2.38) represent effective boundary layer thicknesses

$$\begin{aligned} \alpha'(\omega) &= \frac{1}{2} \sqrt{2} \delta_v \left( 1 + \frac{\gamma-1}{\sqrt{Pr}} \right), \\ \alpha'_f(\omega, x) &= f \sqrt{2} \delta_v \left( 1 + \frac{1}{f \cdot (kx)} + \frac{\gamma-1}{\sqrt{Pr}} \right), \\ \alpha'_g(\omega, x) &= g \sqrt{2} \delta_v \left( 1 + \frac{1}{2g \cdot (kx)^2} + \frac{\gamma-1}{\sqrt{Pr}} \right), \end{aligned} \quad (18)$$

where  $f$  and  $g$  are factors from a combination of with sinus cardinalis and Cosine integral<sup>2</sup> functions evaluated at the position  $2 k x$  given by

$$\begin{aligned} f &= \text{Ci}(2 k x) \sin(2 k x) - \text{si}(2 k x) \cos(2 k x), \\ g &= - \text{Ci}(2 k x) \cos(2 k x) - \text{si}(2 k x) \sin(2 k x), \end{aligned} \quad (19)$$

which stem from approximations to solutions of the extended wave-equation.

After some rearrangement, to eliminate  $\Psi$  from Eq.(16) [128], for the input impedance of the lossy cone it can be written

$$Z_1 = \left( \frac{1}{j Z_{c1}} \left[ \frac{1 - \tilde{\alpha}_{g1}}{k x_1} - \frac{(1 + \tilde{\alpha}_{f1}) \left( \frac{1 - \tilde{\alpha}_{g2}}{k x_2} - j \frac{Z_{c2}}{Z_2} \right) + (1 + \tilde{\alpha}_{f1}) (1 + \tilde{\alpha}_{f2}) \tan(k L + \tilde{\alpha}_2 \Delta \xi)}{(1 + \tilde{\alpha}_{f2}) - \left( \frac{1 - \tilde{\alpha}_{g2}}{k x_2} - j \frac{Z_{c2}}{Z_2} \right) \tan(k L + \tilde{\alpha}_2 \Delta \xi)} \right] \right)^{-1}, \quad (20)$$

where  $\Delta \xi = \xi_2 - \xi_1 = \ln(r_2/r_1) + g_2 - g_1$ . The subscripts  $(\cdot)_{1,2}$  in the loss terms  $\tilde{\alpha}$  stand for input and output cross section, thus  $\tilde{\alpha}_{f1} = \tilde{\alpha}_f(r_1, x_1)$ .

It is obvious, that for the loss free case with  $\delta_v = 0$  the loss terms  $\tilde{\alpha}, \tilde{\alpha}_f, \tilde{\alpha}_g$  become zero and Eq.(20) becomes Eq.(2).

---

<sup>2</sup> $\text{si}(x) = \frac{\sin x}{x}$  and  $\text{Ci}(x) = \gamma_E + \ln x + \int_0^x \frac{\cos t - 1}{t} dt$ , with  $\gamma_E = 0.57721$  being the Euler-Mascheroni-constant.

## A2: Influence of Model Parameters

The model Eq.(4.15) derived above provides a general expression for the flow-rate in any lossy duct with different cross sections at inlet and outlet, given that the preceding assumptions remain valid. In this equation, there are two parameters

$m$ : A geometrical parameter given by the cross section ratio  $S_{in}/S_r$ , which expresses the conicity in a tubular duct of fixed length.

$\alpha$ : A global flow parameter representing phenomena as flow separation and dissipation of kinetic energy at the intake and in the duct flow, respectively.

For the cases of interest here,  $S_{in} \leq S_r$  is given, hence the limits of  $m$  are  $0 < m < 1$ .

The limits for the parameter  $\alpha$  are  $0 \leq \alpha < \infty$ , where the lower limit corresponds to the ideal case ( $C_c = 1$ ,  $\zeta = 0$ ), where Eq.(4.15) equals the Bernoulli Equation Eq.(4.2), and  $\alpha \rightarrow \infty$  corresponds to a hypothetical case with infinitely large losses in the duct.

Both cases will be examined for a given pressure difference  $\Delta p$  between the output cross section  $S_r$  and the constant pressure  $p_m$  in a large reservoir to which the duct is attached.

### Geometrical parameter $m$

First the ideal case  $\alpha = 0$  is discussed:

If in this loss-free case the reed channel were uniform, i.e.  $m = 1$ , the pressures  $p_1$  and  $p_r$  would be the same. This corresponds to the case of an ideal tube, in other words to neglecting the existence of the reed channel. This situation is equivalent to a large pressure reservoir with an opening of size  $S_{in}$ , through which the mean flow-rate is given by  $q = S_{in} \sqrt{2\Delta p/\rho}$ .

On the other hand, if the reed channel were not uniform, i.e.  $m < 1$ , the duct is an ideal diffuser, where the pressures at input and output are different  $p_1 < p_r$ . For a given pressure difference  $\Delta p = p_m - p_r$ , the flow is then completely governed by the conditions at the duct output and the duct geometry, in particular the input cross section  $S_{in}$ , has no effect on the flow-rate. The mean flow-rate is then given by  $q = S_r \sqrt{2\Delta p/\rho}$ .

For these two idealized cases the flow-rate  $q$  as predicted by Eq.(4.15) is plotted in Fig. 1, where experimental data for  $\Delta p$ ,  $p_M$ ,  $S_\infty$ , and  $S_r$  from a measurement of a typical bassoon reed have been used. The intake cross section  $S_{in}$  is here assumed to scale linearly with the pressure difference, according to  $S_{in} = S_\infty (1 - (\Delta p_{meas}/p_M))$  (Eq. 3.14, where  $p_M = 8.2$  kPa is the pressure needed to close the reed and  $S_\infty = 8$  mm<sup>2</sup> is the initial cross section in absence of mouth pressure).

The cross section ratio  $m = S_{in}/S_r$  has a constant value  $m = 1$  for the tube case (dashed line), and varies with  $\Delta p$  for the diffuser case (solid line). In this loss free case,  $S_{in}$  vanishes from Eq.(4.15), the flow depends only on  $S_r$  and the pressure difference  $\Delta p$ .  $S_r$  is the cross section at the sensor position, here  $S_r = 21$  mm<sup>2</sup>.

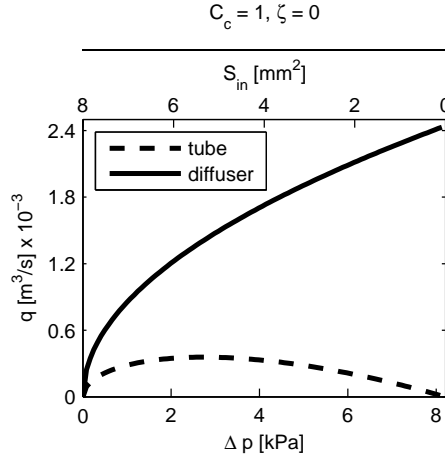


**Figure 1** Flow-rate  $q$  through a loss-free reed channel neglecting the *vena contracta* effect (dashed: tube, solid: diffuser), according to Eq.(4.15) for typical measurement values of  $\Delta p_{meas}$ ,  $p_M$ ,  $S_\infty$ , and  $S_r$

It is obvious, that both idealized models with  $\alpha = 0$  are not reasonable to calculate the flow through the reed channel. On the one hand, the mean flow-rate in fact is certainly related to the intake cross section in the real reed flow. On the other hand, the assumption of  $m = 1$  assuring this relation is clearly not met for the bassoon reed, as the reed blades are deformed at the tip, but not at the outflow end. From  $S_{in} = S_{in}(\Delta p)$  and  $S_r = const.$  it follows that  $m = m(\Delta p) < 1$  (see Fig. 4.4). As stressed by Hirschberg [86], a key finding from this basic analytic model is, that the intake cross section controls the flow if, and only if, the energy dissipating flow phenomena are present, thus  $\alpha > 0$ .

This in turn means that the existence of either the vena contracta effect or duct losses, or a combination of both is essential in the double-reed flow.

### Flow Parameter $\alpha$

Both the constriction coefficient  $C_c$  and the loss coefficient  $\zeta$  contribute to the flow parameter  $\alpha$  according to Eq.(4.14). As shown above, only for values of  $\alpha > 0$ , the flow predicted by the model Eq.(4.15) is linked to the intake cross section. This condition is satisfied for  $0 < C_c < 1$  and  $0 < \zeta < 1$ . The change of the mean flow-rate predicted by the model when varying these model parameters separately is shown in Fig. 2(a) and Fig. 2(b). A qualitative and quantitative change is observed, as the flow-curve is downscaled and its maximum shifted to the left for  $C_c \rightarrow 0$  and  $\zeta \rightarrow 1$ , which means that the saturation pressure  $p_{m,sat}$ , where the flow reaches its maximum  $q_{max}$ , is lowered.

As both  $C_c$  and  $\zeta$  contribute to the flow parameter  $\alpha$ , the change of the flow-curve predicted by the model Eq.(4.15) due to a variation of one coefficient within its limits depends upon the respective value of the other coefficient.

**$C_c$ :** For  $\zeta = 0$ , a variation of the constriction coefficient within  $1 > C_c > 0$  shifts the flow-curve between three theoretical cases: The loss-free diffuser case is given for  $C_c = 1$ . For  $C_c \rightarrow 0.5$  the flow-characteristics approaches the loss-free tube case. For a decrease  $0.5 > C_c \rightarrow 0$ , the curve is further downscaled with a very small shift of the saturation pressure  $p_{m,sat}$  and the hypothetical limit  $C_c = 0$  corresponds to a completely blocked flow (Fig. 2(a)).

**$\zeta$ :** For  $C_c = 0.5$ , which is given as a typical value in the literature [89, 160, 39, 115], the variation of the loss parameter within  $0 < \zeta < 1$  downscales the flow-maximum, but has a negligible impact on location of the flow curves maximum (Fig. 2(b)).

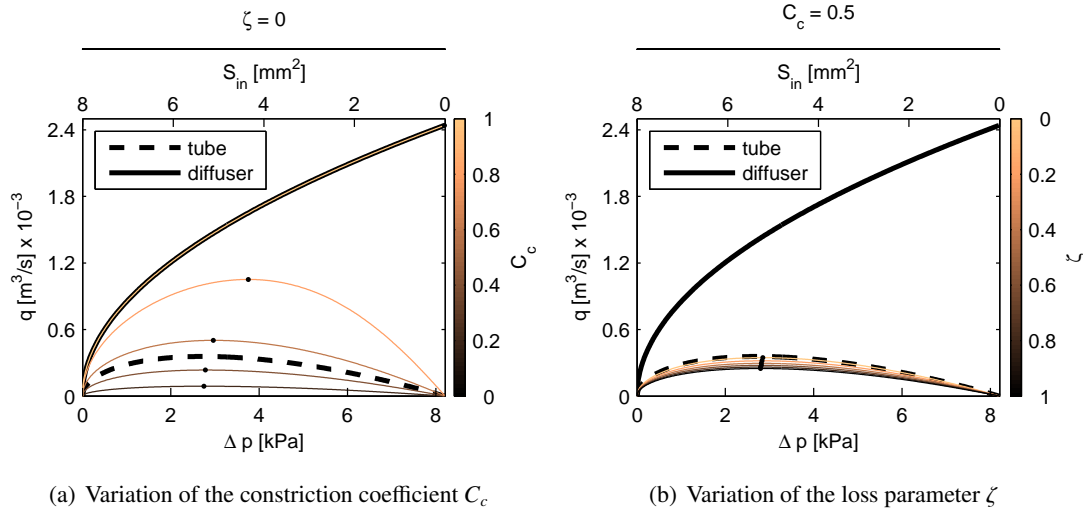


**Figure 2** Influence of the constriction coefficient (a) and the loss parameter (b) on the flow-rate  $q$  predicted by the model Eq.(4.15) for the same experimental data used in Fig. 1. Dots mark the flow maximum. The colours of the lines indicate the value of the variable parameter, according to the colorbar right of the graph

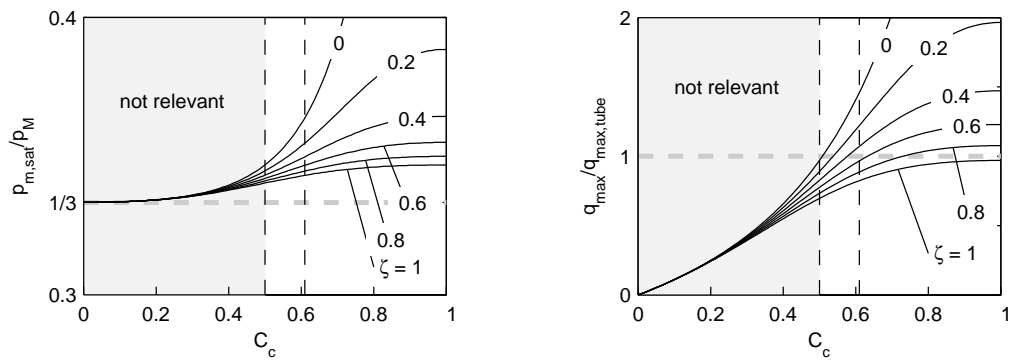
The relative position of the maximum of the flow-curve  $\{p_{m,s}, q_{max}\}$  with respect to  $C_c$  and  $\zeta$  within their limits is shown in Fig. 3. Here, non-dimensionalized data are plotted, referenced to  $p_M$  and  $q_{tube,max}$ , the pressure to close the reed and the maximum flow-rate for the loss-free tube case, respectively.

There are two key findings in the plots of Figs. 3(a) and 3(b) which characterize the quasi-stationary flow model Eq.(4.15) as derived above:

- The maximum of the flow curve is located in the range  $0.34 < \frac{p_{m,sat}}{p_M} < 0.37$  for any value  $0 < \zeta < 1$  within the limits  $0.5 < C_c < 0.61$ . For very sharp edges, these limits are given as theoretical limits in the literature [89] and have been confirmed numerically [39] and experimentally [115]. Moreover, the normalized saturation pressure  $\frac{p_{m,sat}}{p_M}$  is never lower than  $\frac{1}{3}$  within the limits  $1 > C_c > 0$ .
- The scaling range of the flow curve indicated by the maximum flow rate  $q_{max}$  is within  $0.69 < \frac{q_{max}}{q_{max,tube}} < 1.43$  for any parameter combination within  $0.5 < C_c < 0.61$ ,  $0 < \zeta < 1$ .

The experimental setup used here employs only one pressure measurement inside the duct, and thus the global flow parameter  $\alpha$  can be estimated by fitting the model Eq.(4.15) to experimental data. It is not possible to distinguish the contributions of the *vena contracta* effect and the dissipative pressure loss. However, since the limits of  $C_c$  can be narrowed down [89], from Eq.(4.14) pairs of values for  $C_c$  and  $\zeta$  within their respective range of validity can be identified to meet the obtained value for  $\alpha$ .

A juxtaposition of model and measurement data is given in section 4.1.3.



(a) Influence of  $C_c, \zeta$  on the saturation pressure  $\frac{p_{m,sat}}{p_M}$  (b) Influence of  $C_c, \zeta$  on the flow-rate maximum  $\frac{q_{max}}{q_{max,tube}}$

**Figure 3** Influence of model parameters  $C_c, \zeta$  on the general shape of the flow curve indicated by the flow-maximum at saturation. This characteristic point given in normalized coordinates  $(p_{m,sat}(C_c, \zeta)/p_M, q_{max}(C_c, \zeta)/q_{max,tube})$ . The variation of parameters  $C_c, \zeta$  is carried out for a typical bassoon reed configuration ( $p_M = 8$  kPa,  $q_{max,tube} = 0.33 \cdot 10^{-3}$  m<sup>3</sup>/s). The shaded region  $0 < C_c < 0.5$  marks the physically not relevant parameter range.



# Selbständigkeitserklärung

Hiermit erkläre ich, dass ich die am heutigen Tage eingereichte Schrift zum Thema *Experimental Investigations of Bassoon Acoustics* unter Betreuung von Prof. (em) Dr.-Ing Roger Grundmann selbstständig erarbeitet, verfasst und Zitate kenntlich gemacht habe.

Dr.-Ing. Johannes Baumgart wies mich auf die Methode des periodensynchronen Samplens hin und schlug die Steifigkeitsmatrix-Methode zur Berechnung des Druckverlaufs im Wellenleiter mit Seitenabzweigen vor.

Prof. Dr. Ir. A. (Mico) Hirschberg diskutierte mit mir die Details des vorgestellten Rohrblattmodells.

Teile der Einleitung stammen aus einem von mir verfassten Artikel, welcher von Michael Johnson ins Englische übersetzt wurde [76]. Andere Hilfsmittel als die genannten wurden von mir nicht benutzt.

Dresden, 25.November2013

Timo Grothe

